



**HAL**  
open science

# Dynamically reduced spaces in condensed matter physics: Quantum Hall bilayers, dimensional reduction, and magnetic spin systems

Gunnar Möller

► **To cite this version:**

Gunnar Möller. Dynamically reduced spaces in condensed matter physics: Quantum Hall bilayers, dimensional reduction, and magnetic spin systems. Condensed Matter [cond-mat]. Université Paris Sud - Paris XI, 2006. English. NNT: . tel-00121765

**HAL Id: tel-00121765**

**<https://theses.hal.science/tel-00121765>**

Submitted on 21 Dec 2006

**HAL** is a multi-disciplinary open access archive for the deposit and dissemination of scientific research documents, whether they are published or not. The documents may come from teaching and research institutions in France or abroad, or from public or private research centers.

L'archive ouverte pluridisciplinaire **HAL**, est destinée au dépôt et à la diffusion de documents scientifiques de niveau recherche, publiés ou non, émanant des établissements d'enseignement et de recherche français ou étrangers, des laboratoires publics ou privés.

Université Paris XI  
UFR Scientifique d'Orsay

**Dynamically reduced spaces in condensed matter physics:  
Quantum Hall bilayers, dimensional reduction, and  
magnetic spin systems**

THÈSE

présentée à l'Université Paris XI  
pour l'obtention du grade de  
*Docteur en Sciences de l'Université de Paris XI Orsay*

par

Gunnar MÖLLER

de

Hagen (Allemagne)

Soutenue le 21 septembre 2006 devant la Commission d'examen

M. Benoît DOUÇOT	Rapporteur
M. Pascal LEDERER	Président du Jury
M. Thierry MARTIN	Rapporteur
Mme. Cristiane de MORAIS SMITH	Examineur
M. Stéphane OUVRY	Directeur de Thèse

Numéro d'ordre de la thèse:  
8371

The only tyrant I accept in this world is the still voice within.  
*Mahatma Gandhi*

## Remerciements

Je voudrais remercier Benoît Douçot et Thierry Martin d'avoir accepté de rapporter sur cette thèse doctorale, d'autant plus qu'ils disposaient d'un délai très bref pour effectuer cet important travail. Merci également à Cristiane de Morais Smith et Pascal Lederer pour leur participation dans le jury de cette thèse, et surtout pour le grand intérêt qu'ils ont porté à mon travail et leurs remarques critiques sur son contenu.

Le plaisir de tout chercheur est évidemment sa fascination pour la science, qui est encore plus enrichissante quand elle est partagée. J'ai eu souvent l'occasion d'apprécier ce plaisir au cours des dernières années dans les deux laboratoires qui m'ont accueillis au cours de cette thèse, notamment le Laboratoire de Physique Théorique et Modèles Statistiques à Orsay, et les Bell Laboratories à Murray Hill, New Jersey.

Tandis que l'entourage dans les laboratoires a créé une ambiance agréable, c'est grâce à mes collaborateurs que mon travail a pu être aussi enseignant, riche et stimulant. Un grand merci à Steven Simon qui m'a généreusement accueilli aux Bell Labs, et qui m'a introduit avec beaucoup d'enthousiasme à la physique de l'effet Hall quantique. Notre collaboration n'a pas seulement été fructueuse et très instructive sur le plan scientifique. Elle a surtout été une source de plaisir alimentée par la créativité, l'engagement et l'esprit amical de Steven. Aussi, ses encouragements dans les phases difficiles de notre travail étaient beaucoup appréciés. Mes remerciements vont aussi à Edward Rezaei qui a contribué à mon projet non seulement par l'apport de nombreuses données numériques mais aussi par sa bonne humeur lors des conférences téléphoniques qui ont accompagnés notre collaboration.

Je tiens aussi à remercier Thierry Jolicoeur et Nicolas Regnault pour nos collaborations, et j'espère que le travail que nous avons effectué ensemble sera le point de départ pour de nombreux projets à venir. Les discussions stimulantes avec Thierry et son avis scientifique incontournable ont été très porteurs pour mon travail. De même que les échanges aussi réguliers qu'intenses sur le calcul scientifique avec Nicolas. Merci à Sergey Matveenko d'avoir partagé la passion pour les systèmes d'anyons.

Je suis particulièrement heureux d'avoir trouvé en Roderich Moessner un excellent tuteur qui m'a rendu service avec ses conseils avant même de commencer de cette thèse. C'était alors un grand plaisir de pouvoir entreprendre notre projet de recherche qui m'a ouvert de nouveaux horizons scientifiques.

Je voudrais remercier Stéphane Ouvry à la fois d'être soucieux de proposer le meilleur accueil à tous les chercheurs qui ont, comme moi, le plaisir d'intégrer l'équipe du Laboratoire de Physique Théorique et Modèles Statistiques, et plus particulièrement pour son engagement dans la direction de mes travaux de thèse. Notre travail commun m'a appris à garder l'esprit ouvert tout en appliquant la rigueur mathématique à l'analyse des problèmes scientifiques. Je suis également très heureux d'avoir toujours pu compter sur son soutien pour mes collaborations aussi bien à Paris comme au Bell Laboratories.

Finalement, il faut admettre que le travail que je présente en ces pages repose en grande partie sur l'adorable support de ma famille et de mes amis. Je voudrais remercier très chaleureusement tous ceux qui ont éclairés mes journées avec leur amitié. Sans eux, je n'aurais pu réussir cette quête scientifique.

My last acknowledgments are dedicated to Joy Cunningham for her care, support and love during these years of my doctoral studies, and for her tireless efforts to correct the present document.



# Contents

<b>1</b>	<b>Introduction</b>	<b>10</b>
<b>2</b>	<b>Paired States in Quantum Hall Systems</b>	<b>15</b>
2.1	Introduction . . . . .	16
2.1.1	Two dimensional electron gas . . . . .	17
2.1.2	Classical Hall voltage . . . . .	18
2.1.3	Integer Quantum Hall Effect . . . . .	18
2.1.4	Fractional quantum Hall effect . . . . .	23
2.1.5	Internal degrees of freedom . . . . .	32
2.2	CF pairing in the QH Bilayer . . . . .	35
2.2.1	Introduction . . . . .	35
2.2.2	Wave functions for the quantum Hall bilayer . . . . .	38
2.2.3	Numerical Results . . . . .	48
2.2.4	Conclusion . . . . .	65
2.3	Paired Hall states in the single layer . . . . .	67
2.3.1	Paired wave functions . . . . .	69
2.3.2	Pairing of Composite Fermions . . . . .	71
2.3.3	Composite fermions in negative flux . . . . .	72
2.3.4	Realizations of pairing in the single layer . . . . .	77
2.3.5	Conclusions . . . . .	87
2.4	Summary . . . . .	88
<b>3</b>	<b>Dimensional Reduction on a Sphere</b>	<b>90</b>
3.1	Introduction . . . . .	91
3.2	Review of the anyon model . . . . .	94
3.2.1	Multivalued wave functions . . . . .	94
3.2.2	Lagrangian theory . . . . .	94
3.2.3	Hamiltonian theory . . . . .	96
3.2.4	Anyon spectrum . . . . .	97
3.3	Dimensional reduction of free models . . . . .	98

3.3.1	A Reminder: Harmonic Dimensional Reduction . . . . .	98
3.3.2	Free Particle on the Circle . . . . .	101
3.3.3	Free Particle on the Sphere . . . . .	102
3.4	Generalized spherical Aharonov-Bohm model . . . . .	104
3.4.1	Symmetric single-particle case . . . . .	105
3.4.2	Tilted single-particle case . . . . .	107
3.4.3	Generalization to the N-Body Case . . . . .	110
3.4.4	The Two-Body Case and its Ground State . . . . .	111
3.5	Conclusion . . . . .	112
<b>4</b>	<b>Frustrated Magnetic Systems and Spin Ice</b>	<b>113</b>
4.1	Introduction . . . . .	114
4.1.1	A historical perspective . . . . .	115
4.1.2	Spin Ice . . . . .	116
4.1.3	Emergent gauge structure in spin ice . . . . .	117
4.1.4	Spin Ice Materials . . . . .	118
4.1.5	Projective Equivalence . . . . .	119
4.1.6	Square Ice . . . . .	120
4.2	Artificial spin ice . . . . .	121
4.3	Models for artificial ice . . . . .	125
4.3.1	Spectra in Fourier space . . . . .	125
4.3.2	Mean Field Theory . . . . .	141
4.3.3	Thermodynamics: Numerical Algorithms . . . . .	143
4.3.4	Thermodynamics: Observed quantities . . . . .	150
4.3.5	Thermodynamics: Results . . . . .	151
4.3.6	Models for Dynamics and Annealing . . . . .	158
4.4	Summary and Outlook . . . . .	163
<b>A</b>	<b>Monte Carlo Algorithms and the Detailed Balance</b>	<b>165</b>
A.1	General Principle . . . . .	165
A.2	Applicability . . . . .	166
A.3	Towards efficient MC algorithms . . . . .	167
A.3.1	Ising Spin Systems . . . . .	167
A.3.2	Strongly Correlated Electron Systems . . . . .	168
A.4	Estimation of errors . . . . .	170
A.4.1	Time-correlation function . . . . .	170
A.4.2	Binning . . . . .	172



<b>B Appendices to Chapter 2</b>	<b>173</b>
B.1 Paired CF wave functions on the sphere . . . . .	173
B.2 Mixed CF-CB states with filled CF shells . . . . .	176
B.3 Numerical Methods . . . . .	180
B.4 The Pfaffian . . . . .	183
<b>Bibliography</b>	<b>185</b>
<b>Abstract/Résumé</b>	<b>196</b>



# Chapter 1

## Introduction

In the course of the 20<sup>th</sup> century, physics has undergone a series of internal revolutions. The beginning of this century was marked by profound ruptures in the understanding of several fundamental aspects of physics, notably—as officially commemorated with the world year of physics 2005 taking place in the course of this thesis—with Einstein’s discovery of the theory of relativity [Einstein (1905b)], his fundamentally important insights into Brownian motion [Einstein (1905c)], and the photoelectric effect [Einstein (1905a)]. These were followed in the “golden years” of physics by the development of quantum mechanics [Schrödinger (1926a,b)], which has provided the basis for an advanced understanding of the world on atomic scales in the course of the last 80 years. Initially motivated by the necessity to explain the discrete structure of atomic levels, the same concepts were used and complemented appropriately, such as to explore both smaller length-, or higher energy scales and inversely larger length scales at smaller energies. While atoms are the building blocks of all materials that surround us, the understanding of these materials required not only a theory capable of describing individual atoms, but also a means of formalizing the additional complexity arising from ensembles of a large number of these, as found in solid state or condensed-matter systems.

In as far as the electronic properties in common metals are concerned, these could be understood as a gas of electrons subject to the periodic potential of the underlying lattice of atomic cores and more firmly bound electrons on their inner shells. The collective behavior of the electronic liquid has been successfully understood via Landau’s Fermi liquid theory [Landau and Lifshitz (1980)]. This theory, in which interactions between electrons could be described in a perturbative approach starting from free particles, is a prime example of a reductionistic theory which deduces the properties of a phys-

ical system from those of its elementary constituents. The renormalization treatment of this theory states that the quasi-particles in the Fermi liquid behave essentially like electrons with an altered set of physical parameters. The superconductivity of metals, one of the few examples for macroscopic quantum phenomena known by the mid century, could also be understood based on Fermi-liquid theory [Bardeen *et al.* (1957)]; it takes the existence of a Fermi-surface as the starting point.

Around the year 1980, several discoveries caused a rupture within the previous theoretical framework for the electronic structure of solids. So-called heavy fermion compounds were found in which strong electronic interactions cause a fundamental change of the conduction properties of the material [Steglich *et al.* (1979)]. Soon afterwards, the discovery of the quantum Hall effect [v. Klitzing *et al.* (1980)] introduced a new macroscopic quantum effect to the condensed matter community. When the fractional quantum Hall effect (FQHE) was unveiled [Tsui *et al.* (1982)], it became clear that electronic interactions play a key role for these physics. The third effect in this line of discoveries was high temperature superconductivity [Bednorz and Müller (1986)], which was just another step towards the era of strongly correlated electron systems in condensed matter physics.

Both high temperature superconductivity and the quantum Hall effects are intimately related to physics in two dimensions, the former being observed in complex oxides with mobile electrons confined to stacked CuO planes, and the latter taking place in man-made two-dimensional electron gases (2DEG).<sup>1</sup> While the particular physics of two dimensions gives rise to the fantastically complex low-temperature magnetotransport of 2DEGs that is known as the ensemble of quantum Hall effects, the high magnetic field and reduced dimension of these systems can equally be regarded as simplifications to their theoretical understanding: the relevant Hilbert spaces, so-called Landau levels, have a very simple structure. These circumstances allowed to obtain an almost exact analytic form of the many-body wave function of the FQHE states at filling factors  $\nu = 1/(2m + 1)$  [Laughlin (1983)], the importance of which was rewarded by a Nobel-price.

Though more fundamental field theories have been developed to provide a deeper understanding of the FQHE [Murthy and Shankar (2003)], the trial wave function approach may serve as the final test for analyzing the energetics of competing quantum phases described by varying field theories. This is the philosophy deployed in our analysis of a phase transition occurring

---

<sup>1</sup>The integer quantum Hall effect has also been observed in a bulk three-dimensional crystal in the field induced spin density wave phase (FISDW) of the Bechgaard salts (TMTSF)<sub>2</sub>X [Cooper *et al.* (1989); Hannahs *et al.* (1989)].

in the quantum Hall bilayer system that is presented in chapter 2 of this thesis. In comparison to the single layer systems in which the QHE was initially discovered, the bilayer system discussed here is enriched by a supplementary internal degree of freedom. By providing additional complexity and a new set of parameters that can be tuned in experiments while probing the according response, the bilayer system has stimulated an active field of experimental and theoretical analysis [Eisenstein and Girvin/MacDonald in Das Sarma and Pinczuk (1997)]. The particular bilayer state occurring at filling factor  $\nu_T = 1$  can be established through spontaneous interlayer coherence between the two layers [Eisenstein and MacDonald (2004)], each of which would realize a compressible state with Fermi liquid-like behavior when isolated from the other layer. Both the compressible and the incompressible bilayer state can be realized, according to the effective separation between the two layers. However, the nature of the phase transition between these two regimes has been contested, and contradictory statements can be found in the respective literature [e.g. Schliemann *et al.* (2001); Shibata and Yoshioka (2006)].

Here we propose a study based on trial wave functions to gain further insight into the regime intermediate between the Fermi-liquid and interlayer coherent phase, as well as the phase transition between them. To this end, we develop a new class of wave functions that are based on paired composite fermions (CF). One can understand the relevance of CF wave functions by noting that they naturally describe (many-particle) states with low interaction energy. Formally, one can derive a set of CF orbitals that represent a reduced basis for many-particle states with inherently ‘good’ correlations [Jain and Kamilla (1997a)]. We use this dynamically reduced basis to analyze superconducting states of composite fermions analogous to those introduced by Bardeen, Cooper and Schrieffer. This allows us to identify a paired CF phase, and we conclude that it should be separated by a second order phase transition from the interlayer-coherent incompressible state residing at smaller layer separation. We then also pursue the long-standing question of whether pairing might cause an incompressible quantum Hall state at half filling in the single layer.

One of the fascinating aspects of complex systems is the emergence of inherently new behavior at a certain scale of organization. A prime example of such a phenomenon is given by the elementary excitations of the fractional quantum Hall states. These are anyons, particles with fractional statistics which come into life through the subtle collective interplay of electrons in two dimensions. In chapter 3 of this thesis, we consider the anyon-model that describes the properties of such entities, idealized as point-like particles

[Leinaas and Myrheim (1977)], which we can think of as an effective low-temperature theory describing quasi-particle excitations of a quantum Hall state. Though the quantum Hall effect serves as excellent proof of the contrary, in some cases reduced dimensions represent a true simplification of the initial problem. In the context of the anyon model, we can find an instance for such a simplification. While the spectrum of the anyon model is very complicated, parts of it can be mapped on that of a particular integrable one-dimensional model, the Calogero model [Hansson *et al.* (1992)]. More specifically, we analyze the possibility of an analogous mapping between anyon models on the sphere and the Calogero-Sutherland model. As for the physics of the FQHE, a projection to the LLL (or a suitable generalization on the sphere) plays a central role in this analysis [Ouvry (2001)].

In a fourth chapter, a different subject is analyzed that, upon first sight, appears disjointed from the other questions touched upon in this thesis. However, there are multiple connections between the physics of the quantum Hall effect and the frustrated spin systems discussed there. More precisely, the spin ice model is thus named due to a mapping with the arrangements of hydrogen atoms in ice, i.e. the solid phase of water [Anderson (1956)]. The ground state configurations of this spin system form a macroscopically degenerate manifold. Thinking of spins as arrows indicating the direction of a fictitious flux, these ground states of spins on a three-dimensional pyrochlore lattice are characterized by the ice rules. These rules dictate that the flux is conserved at every point of the lattice: there are two spins pointing towards each node of the lattice, and two pointing away from it. This model can be represented as a two dimensional model of spins on the links of a square lattice, also known as the six vertex model. Furthermore, the square ice model is integrable [Lieb (1967a)], and it can even be related to the concept of fractional statistics [Ihm (1995)]. The ice model can be regarded as the low-temperature limit or effective model of a more general system in which spins may take any configuration, but where those of the ice model are the energetically most favorable ones. The particular research project undertaken in the course of this thesis was motivated by an attempt to realize square ice in an artificial structure [Wang *et al.* (2006)]. Such a strong interplay between technological developments and advances in theory has also frequently occurred within the world of the quantum Hall effect. In order to obtain low-temperature physics as in the ice model, a particular type of interactions between neighboring spins is required. The interactions found in the experimentally realized system are long-range dipolar interactions. Whereas such interactions are self screening for spin ice in three dimensions [Isakov *et al.* (2005)] such that the low temperature physics obtained is that

of the ice model, we find that this is not true for the two dimensional version. However, we show how an ice regime may also be obtained for spins with dipolar interactions in two dimensions for a modified sample geometry. Furthermore, we discuss a phenomenological model for the dynamics realized in the experimental system and explain the results in terms of a dynamical bottleneck for the diffusion of defects or non-ice rule vertices.

### **Structure of this thesis**

Regarding the organization of this thesis, each of the chapter is begun with a short abstract illustrating the contents therein and our corresponding publications. Furthermore, each chapter contains an introduction that discusses knowledge required for full appreciation and understanding of the studies. The introductions include a discussion of the integer and fractional quantum Hall effect in chapter 2, an introduction to the anyon model in chapter 3, as well as a discussion of spin ice in chapter 4. Appendix A includes notes on those Monte Carlo methods discussed recurrently throughout this thesis.

## Chapter 2

# Paired States in Quantum Hall Systems

The content of this chapter revolves around a discussion of paired quantum Hall states, mainly based upon arguments on the level of the respective wave functions. An introduction is given to familiarize the reader with the basic ideas of the quantum Hall effect. Our analysis explores the role of paired composite fermions. First, the importance of pairing of composite fermions is explored in the context of bilayer systems at filling factor  $1/2 + 1/2$ . We also show how a mixed fluid picture generalizes the paired state wave functions which yield a proper description of the bilayer system at arbitrary layer separations. Second, we construct paired wave functions in the single layer and undertake a discussion of a possible paired state at half-filling. This construction is based on composite fermions at negative flux, a subject that has been thoroughly discussed in our paper:

G. Möller and S. H. Simon, Phys. Rev. B **72**, 045344 (2005).



## 2.1 Introduction

The quantum Hall effect, discovered in 1980 by Klaus v. Klitzing [v. Klitzing *et al.* (1980)] has provided a constant source of rich physical phenomena, and has given rise to a series of new developments in both theory and experiment [Das Sarma and Pinczuk (1997)]. Due to this history, many introductory works treating the subject matter are already available, and we will therefore refer to the respective textbooks for a comprehensive introduction [Prange and Girvin (1987); Das Sarma and Pinczuk (1997); Heinonen (1998); Comtet *et al.* (1998)]. However, some essential features of the quantum Hall effect and the theory used to describe this phenomenon will be given.

What we designate as the quantum Hall effect manifests itself as peculiar transport properties of two-dimensional electron gases in a strong magnetic field at cryogenic temperatures. Low temperature measurements of the longitudinal resistivity  $\rho_{xx}$  and the transverse Hall resistivity  $\rho_{xy}$  of such systems<sup>1</sup> reveal a series of plateaus in  $\rho_{xy}$  at quantized values

$$\rho_{xy} = \frac{h}{\nu e^2} \quad (2.1)$$

accompanied by vanishing dissipation

$$\rho_{xx} \rightarrow 0, \text{ and } \sigma_{xx} \rightarrow 0. \quad (2.2)$$

In relation (2.1), we introduced the quantum number  $\nu$  which takes integer values for the most marked plateaus that are appropriately referred to as the integer quantum Hall effect (IQHE) [v. Klitzing *et al.* (1980)]. Measurements have revealed that the Hall resistivity is given by (2.1) with  $\nu$  integer to a remarkable 10 digit accuracy—limited by the present possibilities of resistance metrology. This fact is exploited accordingly and the resistivity of the Hall plateau at  $\nu = 1$  is taken as the reference in order to define current standard of resistance at the precise value of  $25,812.80700 \Omega$  [v. Klitzing (2004)].

When observed in even higher magnetic fields and within samples with less disorder, Hall plateaus with fractional values of  $\nu$  can be found. This phenomenon, known as the fractional quantum Hall effect (FQHE) was discovered by Tsui *et al.* (1982). In contrast to the IQHE which can be explained entirely in terms of one-body quantum mechanics, the description of the FQHE requires taking into account the interactions between

---

<sup>1</sup>While the QHE was first discovered in 2DEG's, similar evidence was also found in the FISDW phase of the Bechgaard salts (TMTSF)<sub>2</sub>X [Cooper *et al.* (1989); Hannahs *et al.* (1989)].

the electrons. The fractions  $\nu$  at which the quantum Hall effect occurs are universal, and do not depend on the particularities of the material of the sample, etc. A variety of different fractional quantum Hall states are known, each of which represents unusual properties, e.g. excitations with fractional charge and statistics (anyons). The possibility of even more exotic excitations with non-abelian statistics at  $\nu = \frac{5}{2}$  and  $\nu = \frac{12}{5}$  is currently being studied with respect to its application to topological quantum computing [Kitaev (1997); Das Sarma *et al.* (2005); Stern and Halperin (2006); Bonderson *et al.* (2006a,b); Chung and Stone (2006)]. Actually performing such computations would require manipulation of only a single quasi-particle [Simon *et al.* (2006)].

### 2.1.1 Two dimensional electron gas

The physics of the quantum Hall effect crucially depends on the dimensionality of the system. The ability to effectively manufacture two-dimensional electron gases (2DEG) is an achievement of semiconductor technology [Fowler *et al.* (1966)]. Recent quantum Hall experiments are generally performed on semiconductor devices consisting of sandwiched structures of GaAs and AlGaAs. These devices, grown by molecular beam epitaxy (MBE) [Joyce (2001)], exploit the fact that  $\text{Al}_x\text{Ga}_{1-x}\text{As}$  has a larger band gap than pure GaAs, while their lattices are characterized by approximately identical lattice spacings. Thus, one may draw potential landscapes with atomically smooth interfaces. In a junction between these two materials, conduction electrons from the weakly  $n$ -doped AlGaAs flow towards the GaAs until the electric field generated in this dipole layer compensates for the potential differences between the bulk conduction bands in both materials. This creates a potential perpendicular to the interface (that we will call the  $z$ -direction) with the ability to confine the motion of electrons trapped in the inversion layer to the directions parallel to the interface. At sufficiently low temperatures, only the lowest localized state is accessible to the carriers and an effectively two-dimensional system is obtained.

As an important experimental detail, note that the probability density of the equilibrium charge distribution has its maximum well inside the GaAs layer, whereas its value right at the interface is small, such that scattering from impurities in this interface becomes relatively less important. Furthermore, dopants (donors) needed to enhance the carrier density in the 2DEG are typically placed far from the actual 2DEG, such that the resulting impurity potential is weak. The final mobility of electrons in the 2DEG provides a measure indicating how clean a sample is. The numbers attained for the mobility of carriers in the cleanest samples are impressive, the present mo-

bility record being  $3.1 \times 10^7 \text{cm}^2/\text{Vs}$  [Xia *et al.* (2004)]. This corresponds to a mean free path of approximately 0.3mm, i.e. about  $10^6$  lattice sites.

### 2.1.2 Classical Hall voltage

The transport experiment proposed by Hall (1879) consists in observing the voltage drop in a sample immersed in a homogeneous magnetic field  $\mathbf{B} = B\mathbf{e}_z$  while observing the voltage drop  $V_L$  along the direction of the current  $I$  and the voltage  $V_H$  perpendicular to both the current and the magnetic field—known as the Hall voltage. Neglecting disorder and the periodic potential of the underlying atomic lattice,  $V_H$  is most easily derived by boosting the system to the moving frame in which electrons are at rest, the velocity of which is obtained from the current density  $\mathbf{j} = -en_e\mathbf{v}$ . In that inertial system, the equilibrium state of electrons is attained if all electric fields vanish, i.e.  $\mathbf{E}_{\text{moving}} = 0$ . Considering the situation in the laboratory frame by applying a boost with  $-\mathbf{v} = -v\mathbf{e}_x$  yields electric fields

$$\mathbf{E}_{\text{lab}} = -\frac{1}{c}\mathbf{v} \times \mathbf{B}. \quad (2.3)$$

Given the definition of the resistivity  $\mathbf{E} = \rho\mathbf{j}$ , the resistivity tensor is

$$\rho = \begin{pmatrix} \rho_{xx} & \rho_{xy} \\ \rho_{yx} & \rho_{yy} \end{pmatrix} = \frac{B}{n_e e c} \begin{pmatrix} 0 & 1 \\ -1 & 0 \end{pmatrix}. \quad (2.4)$$

For two dimensional samples, measurements actually determine the Hall resistivity of the sample directly rather than a Hall resistance, as long as  $\sigma_{xx} = 0$ . In other words, resistivity measurements in 2D are entirely unaffected by the geometrical details of the probe. The conductivity, obtained as the inverse tensor  $\sigma = \rho^{-1}$  equally yields vanishing elements on its diagonal which is a sign of dissipationless transport.

A phenomenological Drude theory, adding a drag force on the electrons, adds field-independent diagonal values to the resistivity tensor, while the off-diagonal ‘Hall’ elements remain unmodified.

### 2.1.3 Integer Quantum Hall Effect

Invoking translational invariance, we showed that the Hall resistivity is proportional to the magnetic field. However, low temperature measurements under a high magnetic field show an entirely different behavior with plateaus in the Hall resistance at magnitudes given by (2.1) associated to different values of the quantum number  $\nu$  (see Fig. 2.1). Thus, the presence of disorder breaking the translational invariance is a necessary condition for the universal quantization of the Hall conductivity.

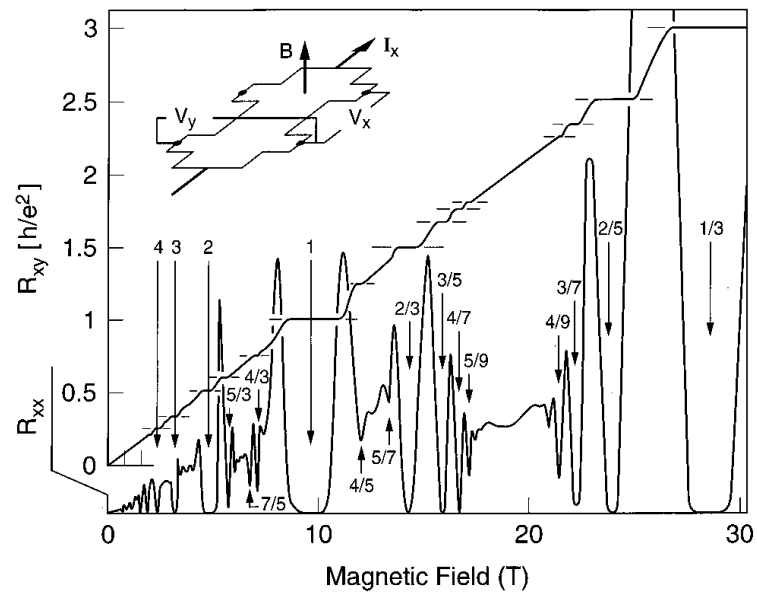


Figure 2.1: Hall resistivity and longitudinal resistivity measured on a two-dimensional electron gas in a GaAs structure taken from Eisenstein and Stormer (1990). The filling factors of the respective states are marked in the figure, and both integer and fractional quantum Hall states are visible. The inset displays the measurement geometry.

In this section, we will focus on the cases with  $\nu$  integer. From (2.1) and (2.4), the carrier densities at the observed Hall plateaus are found to be

$$n_e = \nu \frac{eB}{hc} = \nu \frac{B}{\Phi_0}, \quad (2.5)$$

where

$$\Phi_0 = \frac{hc}{e} \quad (2.6)$$

is the elementary flux quantum.<sup>2</sup> With these indications towards the quantum nature of the phenomenon, let us analyze the quantum mechanics of a single electron in a magnetic field, as given by the Hamiltonian

$$H = \frac{1}{2m_b} [\mathbf{p} + e\mathbf{A}(\mathbf{r})]^2 \equiv \frac{1}{2m_b} \hat{\Pi}^2, \quad (2.7)$$

where  $m_b$  is the band mass reflecting the underlying crystal structure. We defined the kinetic momentum  $\hat{\Pi}$  and the problem is formulated in two dimensions,  $\mathbf{r} = (x, y)$ . The homogeneous magnetic field  $\mathbf{B} = B\mathbf{e}_z$  is represented by the vector potential  $\mathbf{A}(\mathbf{r})$  in a suitable gauge. In analogy to the harmonic oscillator, the problem can be solved by introducing ladder operators

$$a = (2eB\hbar)^{-1/2} [\hat{\Pi}_x + i\hat{\Pi}_y] \quad (2.8)$$

with commutation relations  $[a, a^\dagger] = 1$ . These operators allow reformulation of the Hamiltonian as

$$H = \hbar\omega_C \left( a^\dagger a + \frac{1}{2} \right) \quad (2.9)$$

with the cyclotron frequency  $\omega_C = eB/m_b c$ , in complete analogy to a harmonic oscillator. However, unlike the harmonic oscillator, there is a second pair of ladder operators with commutation relations  $[b, b^\dagger] = 1$  and  $[a^{(\dagger)}, b^{(\dagger)}] = 0$ , thus commuting with the Hamiltonian, indicating a degeneracy of its energy eigenstates, that are also called Landau levels (LL). In a semiclassical formulation of this problem, we understand that electrons move on quantized cyclotron orbits, the center point of which may be arbitrarily displaced in the plane and is a conserved quantity of motion. The first pair of ladder operators  $a, a^\dagger$  is related to the cyclotron motion relative to the guiding center, and the second pair  $b, b^\dagger$  to the guiding center coordinates themselves. The eigenstates  $|n, m\rangle$  are obtained by repeated application of the creation operators to the vacuum  $|0, 0\rangle$  characterized by

$$a|0, 0\rangle = b|0, 0\rangle = 0, \quad (2.10)$$

---

<sup>2</sup>given in the *cgs* system; in SI units  $\Phi_0 = h/e$ , instead.

such that the eigenstates can be computed as

$$|n, m\rangle = \frac{(a^\dagger)^n (b^\dagger)^m}{\sqrt{n!} \sqrt{m!}} |0, 0\rangle. \quad (2.11)$$

The degeneracy of the Landau levels can be obtained by equating the free partition function to the partition function of the system in presence of a magnetic field in the vanishing field limit. Neglecting the electron spin, we have

$$Z_B = d_{LL} \sum_{n=0}^{\infty} e^{-\beta \hbar \omega_C n} = d_{LL} \frac{1}{1 - e^{-\beta \hbar \omega_C}} \xrightarrow{\omega_C \rightarrow 0} \frac{d_{LL}}{\beta \hbar \omega_C}, \quad (2.12)$$

where  $d_{LL}$  is the degeneracy of each LL. In the absence of a magnetic field, we have

$$Z_0 = \int d^2x \frac{d^2p}{(2\pi\hbar)^2} e^{-\beta \frac{p^2}{2m_b}} = \frac{\mathcal{S} m_b}{2\pi\beta\hbar^2} \quad (2.13)$$

where  $\mathcal{S}$  is the surface of integration. Since the limit of (2.12) should recover (2.13), we find the degeneracy per unit surface to be

$$\frac{d_{LL}}{\mathcal{S}} = \frac{eB}{hc} = \frac{B}{\Phi_0}. \quad (2.14)$$

We thus identify the density (2.5) as the degeneracy per unit surface of the one-particle eigenstates of the Schrödinger equation, i.e. each Landau level contains exactly one state per flux quantum of the magnetic field. Inversely, we recognize  $\nu$  as the Landau level filling factor given by

$$\nu = \frac{n_e}{n_\Phi} = \frac{\#\text{electrons}}{\#\text{states}} \quad (2.15)$$

The surface  $S_\phi$  occupied by a single quantum state is related to the natural length scale of a particle in a magnetic field, the magnetic length given by

$$\ell_0 = \sqrt{\hbar/(eB)}. \quad (2.16)$$

The surface per quantum state  $S_\phi = 2\pi\ell_0^2$ , is related to the commutation relation of the guiding center coordinates of a single electron  $[X, Y] = i\ell_0^2$ , which represents an uncertainty relation that affects two coordinates in real space. This particularity relates the QHE to non-commutative field theories [Douglas and Nekrasov (2001)].

Thus far, we have neglected the influence of the electron spin in the discussion of the spectrum. The spin causes an additional two-fold degeneracy of the Landau levels, which is lifted by the coupling of electrons to the

magnetic field inducing the Zeeman splitting  $\Delta_Z = g\hbar eB/m$ . Though this expression looks very similar to the energy scale of the Landau-level spacing, the Zeeman splitting is set by the bare electron mass  $m$ , whereas the cyclotron energy is set by its band mass  $m_b$  which is strongly reduced in the typical GaAs host semiconductor. Thus, the cyclotron energy is typically at least an order of magnitude larger than the Zeeman splitting.

While the above analysis explains why situations are special where the electron density is (2.5) with integer  $\nu$ , the question remains why the system continues to exhibit the same conductivity when the electron density differs slightly from this value such as to form a plateau in  $\sigma_{xy}$ . A possible explanation based on a semiclassical picture is that no transport occurs in the bulk of a filled Landau level, where electrons circle around in stationary cyclotron orbits without a net current. Conversely, electrons at the edge of the sample follow skipping orbits and do contribute to transport, which is uni-directional. Regarding the problem in quantum mechanics amounts to considering scattering amplitudes between states accessible to carriers. Let us point out again, that each edge mode transports electrons only in one direction. Then, overlap with oppositely directed edge modes is vanishingly small for a wide sample, and scattering processes can only induce forward scattering—adding a trivial phase to the electron wave function. However, the absence of possibilities for scattering relies crucially on the existence of an excitation gap in the bulk of the electron state. For a filled LL configuration, it is easy to see that the lowest excitations are available at energies as large as the LL spacing (or that of the respective spin-subband). The conductivity for an ideal quantum channel with a transmission probability equal to unity equals  $\sigma = e^2/h$  according to the Landauer-Büttiker picture for ballistic quantum transport [Büttiker (1986); Landauer (1989); Imry and Landauer (1999)]. If several LL's are filled, each of them contributes an independent transport channel, which yields precisely the quantized Hall resistivity. Finally, if  $\nu$  differs from an integer  $n$  by a small amount  $\bar{\nu} = \nu - n$  the resulting electrons or holes will not contribute to transport, but rather will be trapped by impurities: in an external potential, electron guiding centers follow a drift motion along its equipotential lines. For a low density of such defects, these will accumulate in the deepest valleys of the potential landscape, where they may only follow closed itineraries. Only when extended orbitals become accessible, diffusive transport sets in, and consequently a finite longitudinal resistivity is found in the transitions between Hall plateaus. Jumps between these plateaus can thus be understood as percolation transitions in a scaling theory [Huckestein (1995)], or, taking into account tunneling processes between neighboring localized orbits, in the framework of an improved theory

known as the network model [Chalker and Coddington (1988)].

#### 2.1.4 Fractional quantum Hall effect

At very high magnetic fields, the 2DEG can be driven into a regime where all electrons occupy states in the lowest Landau level (LLL), i.e.  $\nu < 1$ . From the point of view of the single particle theory invoked above, one would expect a large number of degenerate states in this regime that are prone to featuring dissipative transport. However, more quantized Hall states with dissipationless transport exist under this condition, the first example of which was discovered by Tsui *et al.* (1982) at the filling factor  $\nu = \frac{1}{3}$ .

With increasingly clean samples, more fractional quantum Hall states were discovered where  $\nu$  is given by small rational fractions. Common fractions involve the most marked series of states at  $\nu = p/(2mp + 1)$  with  $p$  and  $m$  integer, and some states are also found in higher Landau levels. All of the previous fractions have in common that they are odd-denominator states, though there are exceptions to this rule, e.g.  $\nu = \frac{3}{8}$  and  $\nu = \frac{5}{2}$  [Willett *et al.* (1987)] which is discussed in more detail below.

All states of the fractional quantum Hall effect (FQHE) have a commonality that they occur when the Fermi energy resides within a Landau level, implying that the existence of a gap may be explained solely as an interacting many particle problem. In other words, the FQHE is driven by the tendency to minimize the Coulomb interaction energy  $V_{e-e}$  between electrons. Consequently, it is observed under conditions where variations of the Coulomb energy between different possible quantum states  $\delta V_{e-e}$  set the dominating energy scale in the problem, in particular such that  $\delta V_{e-e} \gg k_B T, V_{\text{disorder}}$ . This requires very clean samples as well as typical measurement temperatures of the order of the transport gap of the respective state. The gap can attain some Kelvin for  $\nu = \frac{1}{3}$  and a lower end for possible gaps remains speculation: Each time cleaner samples and lower measurement temperatures were achieved, a number of new incompressible states have been observed.

From the point of view of any standard textbook of quantum mechanics, the FQHE is a difficult problem, since the Coulomb interaction between electrons occupying the degenerate states of the partially filled Landau level does not provide a small parameter that would allow to treat this problem in perturbation theory. Instead, the full Coulomb Hamiltonian has to be diagonalized in order to find the ground state of this system. Yet, the size of the  $N$ -body Hilbert space grows exponentially in the system size  $N$ . Consequently, a direct diagonalization of the Hamiltonian may be pursued to obtain numerical solutions to this problem [Fano *et al.* (1986)], but is restricted to very small systems. Surprisingly, theory has cast light upon



the phenomena of the FQHE using a much simpler approach. This approach consists of guessing a candidate for the many-body wave function describing the ground state of the system.

### The Laughlin wave function

An educated guess for ground state wave functions in the FQHE regime was first proposed by Laughlin for the states at  $\nu = \frac{1}{2m+1}$  [Laughlin (1983)]. The basis of his approach is that writing a wave function that is confined to the LLL imposes strong limitations on the type of function that one could possibly write.

The LLL eigenstates are particularly simple when expressing the vector potential in the symmetric gauge  $\mathbf{A} = -\frac{1}{2}B \mathbf{r} \times \mathbf{e}_z$ . The differential equation (2.10) for the states in the LLL then becomes

$$(z + 4\ell_0^2 \bar{\partial})\phi(z, \bar{z}) = 0, \quad (2.17)$$

where electron positions are described as complex coordinates  $z = x + iy$  and  $\bar{\partial} = \frac{\partial}{\partial \bar{z}}$ . The conclusion is that the LLL wave functions are harmonic functions  $f(z)$ , up to an exponential factor

$$\phi(z, \bar{z}) = f(z)e^{-z\bar{z}/4\ell_0^2}. \quad (2.18)$$

Since the symmetric gauge conserves rotational invariance, the  $z$ -component of the angular momentum is a valid quantum number. In pursuit of an eigenfunction of the operator  $L_z = -i\hbar \frac{\partial}{\partial \phi}$  with eigenvalue  $m$ , we assume their angular behavior is  $e^{im\phi}$ . Given (2.18), this yields the single possible solution  $r^m e^{im\phi} e^{-z\bar{z}/4\ell_0^2} = z^m e^{-z\bar{z}/4\ell_0^2}$ . These functions represent a convenient basis for the LLL in the symmetric gauge.

Interestingly, the above reasoning generalizes to the two-particle problem. Given a central interaction that ensures the relative angular momentum  $2m + 1$  is a conserved quantity, the only 2-particle LLL wave function at center of mass angular momentum  $M$  is given by

$$\Psi_{2m+1, M}(z_1, z_2) = (z_1 - z_2)^{2m+1} (z_1 + z_2)^M e^{-(z_1 \bar{z}_1 + z_2 \bar{z}_2)/4\ell_0^2} \quad (2.19)$$

up to a normalization factor. We restricted the relative angular momentum to odd values since only these yield fermionic wave functions. As there is a unique 2-particle LLL eigenstate satisfying the boundary conditions, (2.19) is an eigenstate of the Hamiltonian for any interaction potential  $V(r)$  (as long as this potential remains smaller than the cyclotron energy  $\hbar\omega_C$  such that the admixture of higher LL's can be neglected). The radial part of the Schrödinger equation is trivial due to the LLL condition.

Consequently, any interaction can be entirely specified in the LLL via the matrix elements of the two particle eigenstates (2.19)

$$V_{2m+1} = \langle 2m+1, M | V | 2m+1, M \rangle, \quad (2.20)$$

which are independent of the center of mass momentum  $M$  and which are known as the Haldane pseudopotentials [Haldane (1983)]. Evaluated for the Coulomb interaction, these coefficients yield a monotonically decreasing series. A general form of a many particle wave function in the lowest Landau level can be similarly described by the relative angular momenta of particle pairs  $2m_{ij} + 1$ . In order to minimize the interaction energy in the Coulomb potential, the relative angular momentum should then be as large as possible for each particle pair. The resulting trial wave functions are in the form proposed by Laughlin [Laughlin (1983)]

$$\Psi_{\frac{1}{2m+1}} = \prod_{i < j}^N (z_i - z_j)^{2m+1} e^{-\frac{1}{4\ell_0^2} \sum_k |z_k|^2}. \quad (2.21)$$

For  $m = 0$ ,  $\Psi_1$  yields the *exact* ground state wave function of an entirely filled Landau level, which is all angular momentum eigenstates filled up to the orbital with  $m = N - 1$ . For  $m > 0$ , (2.21) yields very good trial states for repulsive interactions. It can be shown in numerical simulations of small systems that the Laughlin wave functions are almost identical to the exact ground state of the Coulomb Hamiltonian [Fano *et al.* (1986)]. It is the exact ground state for the particular short range interactions with pseudopotentials that verify  $V_k = 0 \forall k > 2m$  [Haldane (1983); Trugman and Kivelson (1985); Pokrovsky and Talapov (1985)].

An intuitive way to understand the physics of (2.21) can be achieved by writing the probability  $|\Psi_{1/q}|^2$  for realizing a given configuration  $z_1, \dots, z_N$  as an equivalent Boltzmann probability

$$|\Psi_{\frac{1}{q}}(z_1, \dots, z_N)|^2 = e^{-\beta H_{\text{eff}}^q} \quad (2.22)$$

with  $q = 2m + 1$  and  $\beta = \frac{2}{q}$  and the effective Hamiltonian is given by

$$H_{\text{eff}}^q = q^2 \sum_{i < j} \ln |z_i - z_j| - \frac{q}{4\ell_0^2} \sum_j |z_j|^2. \quad (2.23)$$

This problem is analogous to a classical plasma at the inverse temperature  $\beta$  and composed by particles of charge  $q$  interacting via logarithmic 2D Coulomb interactions. The last term in the Hamiltonian expresses the interaction with a uniform neutralizing background charge attracting charges

to the origin, as is easily shown by 2D electrostatics. At equilibrium, the density of this background charge  $n_{BG} = [2\pi\ell_0^2]^{-1}$  is precisely screened by the freely moving plasma. The resulting distribution of charges yields a circular droplet with an electron density of  $1/q$  times the background charge or a filling factor  $\nu = \frac{1}{2m+1}$ . Furthermore, we learn from this analogy that the Laughlin state describes a translationally invariant liquid [Laughlin (1983)], except at very large  $q$  where a Wigner crystal minimizes the energy of (2.23) [Caillol *et al.* (1982)].

### Quasiparticle excitations - fractional charge and statistics

The crucial question remains of why the Laughlin state is gapped. In the representation of the pseudo-potentials, we understand that the Laughlin form represents a delicate way to escape paying a high price for particle pairs with low relative angular momentum. Conversely, it is not possible to increase the relative angular momentum at a given filling factor  $\nu$ , as the filling fixes the total number of zeros of  $\Psi$ . Indeed, by examining the Aharonov-Bohm phase of a single particle wandering around a large circle of area  $\mathcal{S}$  in the quantum liquid, we see that it picks up an Aharonov-Bohm phase of

$$\exp \left\{ i \frac{2\pi}{\Phi_0} \oint \mathbf{A} \cdot d\mathbf{l} \right\} = \exp \left\{ i \frac{2\pi\Phi}{\Phi_0} \right\}, \quad (2.24)$$

therefore the corresponding loop must enclose  $\mathcal{S}B/\Phi_0$  ‘vortices’ of the wave function, i.e. points where the wave function goes to zero and a phase  $2\pi$  is acquired going around each such point. Now the Laughlin state is the optimal way of distributing the vortices on top of the particle positions, thus keeping the particles at distance, or equivalently, maintaining a large relative angular momentum.

Creating a density fluctuation inside the electron droplet by adding or subtracting a vortex to the wave function costs a finite amount of energy. Envision the process where a flux tube is adiabatically introduced into the system at a position  $z_0$ . Adding one more flux in this manner yields the quasi-hole wave function [Laughlin (1983)]

$$\Psi_{\text{qh}} = \prod_k (z_k - z_0) \Psi_{\frac{1}{q}}. \quad (2.25)$$

The subtraction of a flux quantum leads to the slightly more complicated quasi-electron wave function

$$\Psi_{\text{qe}} = e^{-\frac{1}{4\ell_0^2} \sum_k |z_k|^2} \prod_k \left( 2\ell_0^2 \frac{\partial}{\partial z_k} - \bar{z}_0 \right) \prod_{i < j} (z_i - z_j)^q. \quad (2.26)$$

Both these objects are localized defects of the quantum liquid, and their energy gives the transport gap for the system. Both carry a charge which can be obtained once more in the plasma analogy by the screening argument. One obtains  $q_{\text{qh/qe}} = \pm \frac{e}{q}$ , and the existence of these fractionally charged objects has indeed been confirmed experimentally [Clark *et al.* (1988); Simmons *et al.* (1989)]. Finally, the transport behavior of the FQHE states can be explained in terms of the edge states where the carriers are the fractionally charged quasi-particles [Kane and Fisher (1995)].

The statistics of the quasi-particles can be calculated from a Berry's phase calculation [Arovas *et al.* (1984)], and is obtained directly from the trial wave function. In essence, when a quasi-particle is moved around a large closed circle adiabatically, the resulting Berry's phase  $\beta$  is related to the number of electrons that the path  $\mathcal{C}$  encloses

$$\beta(\mathcal{C}) = e^{\pm 2\pi i \langle N \rangle}. \quad (2.27)$$

If  $\mathcal{C}$  encloses a bulk region of the quantum Hall liquid, some number of electrons  $N_0$  will be contained in this area on average. This situation must be compared to the one where a quasi-particle has been added inside the path  $\mathcal{C}$ . Provided the path is much larger than the extension of the quasi-particle,  $\mathcal{C}$  will then enclose a total number of  $\langle N \rangle = N_0 + q_{\text{qh/qe}}/e$  particles. Given that the charge is fractional, the interchange of two Laughlin quasi-holes or quasi-electrons causes the wave function to pick up a phase factor  $\exp[i\pi q_{\text{qh/qe}}/e]$  [Halperin (1984)]. Numerical tests of the above statements successfully confirmed the statistics of the Laughlin quasi-hole, but noted problems with the definition of the statistics parameter for the quasi-electron [Kjønsgberg and Myrheim (1999)]. Nonetheless, the quasi-particle statistics are confirmed also by Chern-Simons theory [Zhang *et al.* (1989)] independently of particular trial wave functions. A generalization of bosonic and fermionic statistics is possible only in two dimensions and is referred to as fractional statistics. Particles with such statistics are also called anyons, as will be discussed in more detail in chapter 3.

### Composite Fermions

The Laughlin wave functions provide a satisfactory and simple theoretical approach to the understanding of the FQHE at filling factors  $\nu = 1/(2m+1)$ . However, many other fractions are observed. A first approach to their understanding was the hierarchy model [Haldane (1983); Halperin (1984)] which considers the condensation of quasi-particles of the Laughlin states into incompressible quantum states similar to the original Laughlin state. Then

the quasi-particles of the states thus obtained may again form incompressible states with their own quasi-particle excitations, etc. While the hierarchy explains the existence of all incompressible states that have in fact been observed, some states occur that are many levels down the hierarchy whereas much higher lying states have never been observed.

The composite fermion (CF) picture [Jain (1989)] proposes an alternative explanation of the quantum Hall states that has predictive power regarding the stability of the fractions described. As the starting point to understand the CF picture, consider the following reinterpretation of the Laughlin wave function:

$$\begin{aligned}\Psi_{\frac{1}{2m+1}} &= \prod_{i<j} (z_i - z_j)^{2m} \prod_{i<j} (z_i - z_j) e^{-\frac{1}{4\ell_0^2} \sum_k |z_k|^2} \\ &= \prod_{i<j} (z_i - z_j)^{2m} \Psi_1.\end{aligned}\quad (2.28)$$

Decomposed in this fashion as the fermionic wave function of a single filled Landau level and a Jastrow factor describing the attachment of  $2m$  vortices to the particles, we can interpret the  $\nu = 1/3$  state as the IQHE of composite fermions. The composite particles obtained by attaching two vortices to each electron are fermions just as the bare electrons, since the Jastrow factor is symmetric and conserves the symmetry of the wave function. To generalize the CF construction, replace  $\Psi_1$  by a wave function  $\Psi_p$  describing  $\nu = p$  filled Landau levels. By definition, the density of zeros (or flux) in  $\Psi_p$  is  $n_\Phi = n_e/p$ . The total flux including that associated to the supplementary zeros then adds up to  $\Phi_T = n_e/p + 2mn_e$ . Inversely, for a given external flux the CF experience the reduced effective flux  $\Phi_{\text{eff}} = \Phi_T - 2mN$ . The filling factors corresponding to CF configurations with filled LLs, i.e. susceptible for an IQHE of CF's are

$$\nu = \frac{1}{2m + 1/p} = \frac{p}{2mp + 1}, \text{ with } m, p \in \mathbb{N}.\quad (2.29)$$

Incompressible states have been found experimentally at these filling factors [e.g. Eisenstein and Stormer (1990)], and their gaps are decreasing with  $p$ .

The recipe described above nearly yields suitable trial wave functions for states at these  $\nu$ . However, in addition to replacing  $\Psi_1$  by the wave function of a higher filled LL, one needs to repair the defect that such a wave function will contain non-analytic terms and have a non-zero overlap with higher Landau levels. Formally, this is achieved by the projection  $\mathcal{P}$  to the LLL

$$\Psi_{\frac{p}{2mp+1}} = \mathcal{P} \prod_{i<j} (z_i - z_j)^{2m} \Psi_p.\quad (2.30)$$

This construction may seem confusing, since the action of the projection to the LLL is unintuitive. Another way to think about this construction is to notice that it yields a LLL wave function at the appropriate particle-number to flux relation. The involvement of higher Landau levels is not required for this construction. Analogous to the Laughlin wave function, one needs to distribute the zeros of the wave function so as to maximally reduce the interaction energy of electrons. Yet, in contrast to the filling factors  $1/(2m+1)$ , the number of zeros available is not a multiple of the particle number. One may construct wave functions at the fillings of the Jain series starting with the closest Laughlin wave function at a smaller filling factor. This means placing vortices on all other particles. To attain the wanted filling factor, one then needs to introduce defects by reducing the number of zeros to the required number. This can be realized by applying differential operators. Demanding that the resulting states be eigenstates of the total angular momentum and that the number of defects be identical for all electrons, this approach has been shown to be equivalent to the construction involving a LLL projection [Jain and Kamilla (1997b)]. Alternatively, it has been argued that wave functions at filling factor  $\frac{p}{2mp+1}$  can be obtained by writing wave functions in which electrons are arranged by clusters of  $p$  particles [Ginocchio and Haxton (1996)]. In between the electrons within different clusters the correlations remain optimal as in the Laughlin state, however, there are defects increasing the interactions between electrons in the same cluster.

### Chern-Simons theory

The Laughlin and Jain wave functions are founded on the observation that it is favorable to attach vortices of the wave function to the positions of the particles. However, the wave function approach has the inherent difficulty that it depends on being able to guess the right wave function, which is generally difficult. Also, it is not completely satisfactory from a theoretical point of view since it is not starting from first principles.

Even before composite fermions were introduced, the concept of statistical transmutation via a Chern-Simons transformation was exploited to describe the Laughlin state in a composite boson approach [Girvin *et al.* (1985); Girvin and MacDonald (1987); Zhang *et al.* (1989)], aiming to apply the framework of Ginzburg-Landau theory. Such a transformation permits consideration of the statistics of particles as an interaction via a gauge field. Though any unit of flux can be attached in this way to yield particles with intermediate statistics (see chapter 3), a Chern-Simons theory for the composite fermion picture [Lopez and Fradkin (1991); Halperin *et al.* (1993)]

only requires the attachment of even multiples of the elementary flux quantum  $\Phi_0$ . Conceptually, the Chern-Simons transformation corresponds to applying the singular gauge transform

$$\Psi'(z_1, \dots, z_N) = \prod_{i < j} \left[ \frac{(z_i - z_j)}{|z_i - z_j|} \right]^{2m} \Psi(z_1, \dots, z_N), \quad (2.31)$$

such that if the initial wave function is a solution of the Schrödinger equation  $\mathcal{H}\Psi = E\Psi$ , then the transformed wave function is described by  $\mathcal{H}'\Psi' = E\Psi'$  with the transformed CS-Hamiltonian  $\mathcal{H}'$ . In the Hamiltonian  $\mathcal{H}'$  an additional magnetic field corresponding to flux tubes at the positions of the particles (and referred to as Chern-Simons magnetic field) appears. The corresponding vector potential is

$$\mathbf{A}'(\mathbf{r}) = \mathbf{A}(\mathbf{r}) + \frac{2m\Phi_0}{2\pi} \sum_{i < j} \frac{\mathbf{e}_z \times (\mathbf{r} - \mathbf{r}_j)}{|\mathbf{r} - \mathbf{r}_j|^2} \equiv \mathbf{A}(\mathbf{r}) + \mathbf{a}(\mathbf{r}), \quad (2.32)$$

and the gauge transformed fermions are described by the Hamiltonian

$$\mathcal{H}' = \frac{1}{2m_b} \sum_j [\mathbf{p}_j + e\mathbf{A}(\mathbf{r}) + e\mathbf{a}(\mathbf{r})]^2 + \sum_j U_{\text{ext}}(\mathbf{r}_j) + \sum_{i < j} V(\mathbf{r}_i - \mathbf{r}_j), \quad (2.33)$$

including the Chern-Simons magnetic field  $b(\mathbf{r}) = \nabla \times \mathbf{a}(\mathbf{r})|_z$ , that acts exclusively on the transformed particles and is not physically observable exterior to the system. It is coupled to the particle density via

$$b(\mathbf{r}) = \nabla \times \mathbf{a}(\mathbf{r}) = 2m\Phi_0 n(\mathbf{r}). \quad (2.34)$$

Choosing the Chern-Simons field opposite in direction to the external magnetic field, the gauge transformed fermions experience a reduced effective magnetic field at the mean-field level

$$B_{\text{eff}} = B - \langle b \rangle, \quad (2.35)$$

which strongly resembles the analogous expression for the effective field of composite fermions. However, the Chern-Simons theory is a precise reformulation of the initial problem and permits one to calculate the perturbations around this mean field approach. These perturbations are particularly important for the case  $\nu = \frac{1}{2}$  since the effective field is exactly zero in the mean field under that condition, as was discussed in detail by Halperin *et al.* (1993). A cornerstone of this work was the calculation of the electromagnetic response functions that allow calculation of a variety of transport

phenomena in the quantum Hall regime. The existence of a Fermi surface at half filling, equally predicted by Halperin *et al.* (1993) has been confirmed experimentally via the study of surface acoustic waves [Willett *et al.* (1993)]. Finally we should note that a main difficulty of the Chern-Simons theories is in showing how an effective mass  $m^*$  replaces the band mass  $m_b$  that is present in the Hamiltonian used to obtain the proper energy scales of excitations which are set by the Coulomb interactions in the LLL [Simon in Heinonen (1998)].

### Extended Hamiltonian theories

Though this subject is not touched upon in the present document, given the importance of these new developments it would be a serious shortcoming not to mention the Hamiltonian theories developed to overcome some of the problems inherent to the Chern-Simons approach [Murthy and Shankar (2003)], notably the difficulty in calculating activation gaps.

The starting point of the extended Hamiltonian theory is a Chern-Simons transformation. This is complemented by enlarging the given Hilbert space artificially, introducing a new set of conjugate dynamical variables at each point in space. In a second unitary transformation, these additional fields may be used to compensate for the Chern-Simons vector potential. However, this leaves a new constraint  $\bar{\chi}(\mathbf{q})|\phi\rangle = 0$  behind that physical states  $|\phi\rangle$  must obey. The Hamiltonian, projected to the LLL may be expressed entirely in terms of the projected density operators

$$\bar{\mathcal{H}} = \frac{1}{2} \sum_{\mathbf{q}} \bar{\rho}(\mathbf{q}) v(q) e^{-q^2 l^2 / 2} \bar{\rho}(-\mathbf{q}), \quad (2.36)$$

where the projected density operators  $\bar{\rho}$  are a function of the electron guiding center coordinates  $\mathbf{R}_e$ . By contrast, the constraint  $\bar{\chi}$  is described by the pseudovortex field of charge  $-c^2 = 2mp/(2mp + 1)$  and given by the expansion

$$\bar{\chi}(\mathbf{q}) = \sum_j e^{-i\mathbf{q}\mathbf{R}_{vj}} \quad (2.37)$$

with vortex guiding center coordinates

$$\mathbf{R}_v = \mathbf{r} + \frac{l^2}{c(c+1)} \mathbf{e}_z \times \hat{\Pi}, \quad (2.38)$$

which are distinct from those of the electrons. An elegant way to solve the constraint imposed by  $\bar{\chi}$  is to introduce the composite fermion space as a



weighted combination of the electron and vortex coordinates, such that

$$\bar{\rho}^{\text{CF}}(\mathbf{q}) = \bar{\rho}(\mathbf{q}) - c^2 \bar{\chi}(\mathbf{q}), \quad (2.39)$$

which is the choice giving the proper long-wavelength limit of the matrix elements of this density operator. One of the virtues of this theory is that the structure of the Hamiltonian remains exactly that of the initial one (2.36), including the form of the commutation relations of the density operators which we have omitted here for brevity. This includes the possibility to iterate an identical procedure for describing a second generation of composite fermions [Goerbig *et al.* (2004)]. These can be exploited to explain the FQHE at new fractions like  $\nu = 4/11, 5/13, 5/17,$  and  $6/17$ . In view of the following discussion of the bilayer system at total filling one, we should also draw attention to the application of the extended Hamiltonian formalism to the interlayer coherent state in this system [Stanic and Milovanovic (2005)].

### 2.1.5 Internal degrees of freedom

Thus far, we have hardly made reference to the electron spin. This is due to the fact that electron spins are largely polarized under a high magnetic field, and the dynamics in the highest orbital/spin band may be considered as that of spinless particles. This is not generally true, and in situations where the Zeeman energy is small enough, new problems arise as competition between fully and partially polarized spin states opens up the possibility for an even richer structure of phase transitions between these [Eisenstein in Das Sarma and Pinczuk (1997)].

Internal degrees of freedom are also present in other materials in which the QHE may be observed. A classical example silicon, in which a valley degeneracy introduces such a degree of freedom. The very recent discovery of the QHE in graphene has provided a new material with such degeneracies. In addition to the valley degeneracy, graphene also has a second discrete degeneracy owing to the band structure having two equivalent points in the Brillouin zone of the hexagonal graphene structure.

Bilayer systems may be regarded as an alternative means to obtain an additional internal degree of freedom in two-dimensional electron systems, where system parameters may be manipulated with less experimental difficulties. Indeed, the physics of these two internal degrees of freedom resemble each other, and the layer degree of freedom is also called pseudospin, accordingly. However, one should point out some important differences. In particular, the interaction of electrons in the double layer system is not the same between particles with equal and different pseudospin respectively,

thus there is no full  $SU(2)$  symmetry for rotations of the internal degree of freedom. The second important difference is the existence of interlayer tunneling in the bilayer case—this hybridizes states between the layers and introduces an additional energy scale to the problem.

Experimentally, two different methods have been employed such as to obtain bilayer systems. The most intuitive approach consists of producing a double quantum well structure, which then provides two 2DEGs [Pfeiffer *et al.* (1991)]. However, it is also possible to obtain effective bilayer structures in a single wide quantum well, where electrons accumulate close to the upper and lower interfaces, attracted by the positive charges of donors above and below this structure. The potential barrier separating these two layers emerges merely from the Hartree potential of the electrons themselves [Suen *et al.* (1991)]. Both systems are well characterized by the layer separation  $d$  and the splitting of the symmetric and antisymmetric states due to the interlayer tunneling  $\Delta_{SAS}$ .

The parameter  $\Delta_{SAS}$  largely determines whether the bilayer system can be analyzed as two independent systems interacting via the Coulomb interactions of the electrons in each of the layers, or whether it is more appropriate to consider individual electrons as delocalized between the layers which may occupy the previously mentioned (single-particle) symmetric and antisymmetric states  $|S\rangle = |\downarrow\rangle + |\uparrow\rangle$  and  $|AS\rangle = |\downarrow\rangle - |\uparrow\rangle$ .

Obtaining samples with weak tunnelling, or small  $\Delta_{SAS}$ , is an experimental challenge to the versatility of molecular beam epitaxy [Eisenstein (2003)]. The tunneling strength  $\Delta_{SAS}$  is decreased by increasing the barrier height as well as its width. Since the mean carrier separation at fixed filling factor is proportional to the magnetic length  $\ell_0$ , working with systems at low particle density allows one to obtain lower tunneling strengths at the same effective layer separation  $d/\ell_0$ .

As to the new physics observed in bilayer systems, much excitement has been created by even denominator states found at total fillings (given by the sum of the filling factors in the individual layers)  $\nu_T = \frac{1}{2}$  and  $\nu_T = \frac{3}{2}$  in double layer systems, fractions which are considerably simpler than the more exotic cases of even denominator states in the single layer. As a side-note, the first of these two states,  $\nu_T = \frac{1}{2}$  had been predicted in advance of the experiments [Rezayi and Haldane (1987)], and suitable wave functions were proposed even longer before [Halperin (1983)]. This should also be contrasted with the prominent single layer state at a half filled second Landau level,  $\nu = 5/2$ , the nature of which is still a matter of controversy years after its discovery [Willett *et al.* (1987)].

New phenomena in the bilayer also include total filling fractions that are

formed through a spontaneous charge imbalance in the system, thus choosing energetically more favorable internal states at the cost of capacitive charging energy. An example of such a state is  $\nu = 11/15 (= 1/3 + 2/5)$  [Manoharan *et al.* (1997)].

An incompressible state at total filling  $\nu_T = 1$ , first observed by Eisenstein *et al.* (1992) was not deemed important at first, since it was thought of as a state that could be understood simply in terms of an IQHE of electrons in the symmetric channel of the hybridized double well state. However, this state persists even when the tunneling  $\Delta_{SAS}$  becomes very small, and is negligible on the scale of Coulomb interaction energies. In this case, the explanation for the existence of this quantum state becomes highly non-trivial, as the individual half-filled layers would be compressible. Indeed, at larger layer separation, such a compressible state is observed. The following section is devoted to reviewing the existing literature on this question, as well as our own analysis of this system in the idealized case of vanishing tunneling strength.

## 2.2 A composite particles description for the quantum Hall bilayer system at $\nu_T = 1$

### 2.2.1 Introduction

In bilayer quantum Hall systems at filling fraction  $\nu = \frac{1}{2} + \frac{1}{2}$ , at least two different quantum states of matter are known to occur, depending upon the spacing  $d$  between the layers [Das Sarma and Pinczuk (1997)]. For large enough spacing, the two layers interact very weakly and must be essentially independent  $\nu = \frac{1}{2}$  states, which can be described as compressible composite fermion (CF) Fermi seas [Heinonen (1998)]. So long as the distance between the two layers is very large, there are very strong intralayer correlations but very weak interlayer correlations (although, as we will discuss below, even very weak interlayer correlations may create a pairing instability at exponentially low temperatures [Bonesteel *et al.* (1996)]). Inversely, for small enough spacing between the two layers the ground state is known to be the interlayer coherent “111 state”, which we can think of as a composite boson (CB), or interlayer exciton condensate [Eisentein and MacDonald (2004)], with strong interlayer correlations and intralayer correlations which are weaker than that of the composite fermion Fermi sea [Das Sarma and Pinczuk (1997)]. While the nature of these two limiting states is reasonably well understood, the nature of the states at intermediate  $d$  is less understood and has been an active topic of both theoretical [Joglekar and MacDonald (2001); Schliemann *et al.* (2001); Schliemann (2003); Stern and Halperin (2002); Park (2004); Nomura and Yoshioka (2002); Kim *et al.* (2001)] and experimental interest [Murphy *et al.* (1994); Spielman *et al.* (2000, 2001); Kellogg *et al.* (2002, 2003); Spielman *et al.* (2004)]. Although there are many interesting questions remaining that involve more complicated experimental situations, within the current work we always consider a zero temperature bilayer system with zero tunnelling between the two layers and no disorder. Furthermore, we only consider the situation of  $\nu = \frac{1}{2} + \frac{1}{2}$  where the electron density in each layer is such that  $n_1 = n_2 = B/(2\phi_0)$  with  $\phi_0 = hc/e$  the flux quantum and  $B$  the magnetic field. Finally we assume that electrons are fully spin-polarized, we neglect the finite extension of the wave functions in the  $z$ -direction, and we always assume that the magnetic field is precisely perpendicular to the plane of the sample.

Our main focus in this work is on the nature of the transition between intralayer 111 (CB) state and the interlayer fermi liquid (CF) state. Currently, contradictory conclusions about the nature of the transition may be drawn from the literature. The experiments are complex and are frequently hard to interpret (and may require assumptions beyond the simplifying assumptions

made in the current investigation). While some of the experiments [Murphy *et al.* (1994); Spielman *et al.* (2000, 2001); Kellogg *et al.* (2002, 2003); Spielman *et al.* (2004)] point towards a continuous transition between two phases, it is not clear whether this could actually be a first order transition smeared by disorder [Stern and Halperin (2002)]. There is no doubt, however, that a notable change of behavior takes place in the approximate vicinity of  $d/\ell_0 \approx 1.7$  with  $\ell_0 = \sqrt{\phi_0/B}$  as the magnetic length.

Theoretically, the situation is no clearer. Several very influential theoretical works [Schliemann *et al.* (2001); Joglekar *et al.* (2004); Moon *et al.* (1995)] found indications of a first order transition near  $d/\ell_0 \approx 1.3$ , whereas other studies have found no indication for a first order transition and evoke continuous evolution of correlation functions [Nomura and Yoshioka (2002)], and indications of a continuous transition occurring near  $d/\ell_0 \approx 1.6$  [Shibata and Yoshioka (2006)]. Some very influential works have pointed to the possibility that a number of more exotic phases could also be lurking within this transition as well [Kim *et al.* (2001); Park (2004); Bonesteel *et al.* (1996); Bonesteel (1993); Nomura and Yoshioka (2002)]. In particular, it has been suggested [Bonesteel *et al.* (1996); Kim *et al.* (2001); Morinari (1999)] that the bilayer CF Fermi sea is always unstable to pairing from weak interactions between the two layers (due to gauge field fluctuations). Some of these works [Kim *et al.* (2001); Morinari (1999)] further concluded that the pairing should be in the  $p_x - ip_y$  channel, which would be analogous to the pairing that occurs in single layer CF systems to form the Moore-Read Pfaffian state [Moore and Read (1991); Greiter *et al.* (1992)] from the CF Fermi sea. As discussed later, we do believe that CF pairing plays a crucial role in the crossover, though we find that the channel is  $p_x + ip_y$ .

A somewhat different approach has been proposed in a previous construction of a quasi-particle description for the bilayer system [Simon *et al.* (2003)]. In this work, a set of trial wave functions were constructed to attempt to describe the crossover between phases. This theory (which will be described in detail below) has provided an intuitive picture for the transition from the CF-liquid product state to the 111-state in terms of an energy trade-off between intralayer interaction energy and interlayer interaction energy. At large layer separation  $d$ , CF's fill a Fermi sea. These CF's can be thought of as an electron bound to correlation holes within the same layer. At small layer separation the 111-state can be thought of as a condensate of interlayer excitons or composite bosons. These composite bosons are formed by electrons bound to a correlation hole in the opposite layer (as well as a single correlation hole in the same layer). Within the theory of Simon *et al.* (2003), at intermediate  $d$  wave functions were introduced with some amount

of CF's with particle-hole binding within the layer and some amount of CB's with particle-hole binding between layers. As the distance  $d$  between the layers is continually reduced, the CF's are continually replaced by CB's and the intralayer correlation is replaced by interlayer correlations.

While physically appealing, this description of the transition is clearly incomplete in that it considers CF's and CB's as independent types of particles, though in reality all of the electrons must be identical. Both the CF's and CB's consist of electrons bound to correlation holes or vortices, or with "flux attached" in the Chern-Simons language. The difference between the CB's and CF's is whether they are bound to correlation holes in the opposite layer (CB's) or only within the same layer (CF's). However, nothing prevents electrons from breaking free from their correlation holes and becoming bound to a different correlation hole—which could then change the identity of a particle from a CB to a CF and vice versa. Indeed, whenever two composite bosons in opposite layers approach the same coordinate position, they can "trade" their accompanying correlation holes (vortices or flux quanta), and emerge as two composite fermions. In terms of a second quantized notation, with  $\psi$  representing a composite fermion annihilation operator, and  $\phi$  representing a composite boson annihilation operator, such scattering processes would be described by an interaction term

$$\lambda_{\mathbf{k}_1, \mathbf{k}_2, \mathbf{k}_3, \mathbf{k}_4} \psi_{\uparrow, \mathbf{k}_1}^\dagger \psi_{\downarrow, \mathbf{k}_2}^\dagger \phi_{\uparrow, \mathbf{k}_3} \phi_{\downarrow, \mathbf{k}_4} + h.c. \quad (2.40)$$

with  $\uparrow$  and  $\downarrow$  representing the two layers and  $\lambda$  as a coupling constant (and *h.c.* denoting the hermitian conjugate). If the bosons happen to be condensed there is a large expectation for the CB's to be in a  $\mathbf{k} = 0$  state. Invoking momentum conservation, the most prominent such interaction term is then of the form

$$\lambda_k \psi_{\uparrow, \mathbf{k}_1}^\dagger \psi_{\downarrow, -\mathbf{k}_1}^\dagger \langle \phi_{\uparrow, \mathbf{k}=\mathbf{0}} \phi_{\downarrow, \mathbf{k}=\mathbf{0}} \rangle + h.c. \quad (2.41)$$

which we immediately recognize as a pairing term for the composite fermions. Although it may not be obvious at this point, we will argue that the CF pairing likely occurs in the  $p_x + ip_y$  channel. An equivalent statement is that the two-electron pair wave function acquires a phase of  $+2\pi$  as two paired electrons in opposite layers are taken in a clockwise path around each other. The argument rests on the fact that for the 111 wave function, taking any electron around any other electron in the opposite layer will result in a  $+2\pi$  phase. As will be further illustrated, compatibility of CB's that make up the 111 state with the CF's that make up the p-wave paired CF state requires that these phases match, and hence that the p-wave pairing is of  $p_x + ip_y$  type.

In the current work, we consider explicit wave functions for interlayer paired CF states. As in BCS theory, the shape of the pairing wave function is treated in terms of a set of (a very small number of) variational parameters. We find that for interlayer spacings  $d \gtrsim \ell_0$  our trial states are exceedingly good representations of the ground state. It is particularly intriguing that these paired states work well at interlayer spacings far below the putative transition. However, at spacings below  $d \approx \ell_0$  we find that the simple paired CF states are no longer accurate. We then return to the above described idea of CF-CB mixtures. With only one additional variational parameter representing the probability that an electron is a CB versus being a CF, we obtain a family of wave functions that nearly match the exact ground state for all values of  $d/\ell_0$ .

The general structure of this study is as follows. In section 2.2.2, we will discuss in detail the particular wave functions that we were studied. First, in section 2.2.2.1 we review the composite fermion fermi liquid in single layer systems, and focus on some particular aspects that help us construct bilayer states with paired CF in section 2.2.2.2. We then turn to the discussion of the interlayer coherent 111-state in section 2.2.2.3 and how it too can be interpreted as both a state of composite bosons (CB's) and as a paired state. Finally, in section 2.2.2.4 we discuss the merging of the physics of CB's with that of the paired CF states to yield a mixed fluid wave function which incorporates both types of physics. We show in this section that  $p_x + ip_y$  is the only pairing symmetry of CF's that can coexist with CB's. We note that wave functions discussed in section 2.2.2.4 include the mixed CB-CF wave function introduced by Simon *et al.* (2003) as a special case.

Having constructed the wave functions which are at the core of our discussion, we have tested the validity of our approach based on numerical calculations on the sphere. To this end, in section 2.2.3 we present data from Monte Carlo simulations of the paired CF (2.2.3.1) and mixed fluid (2.2.3.2) wave functions and study these results in comparison to exact numerical diagonalizations of the Coulomb Hamiltonian for small model systems of up to 14 electrons.

In Appendix B.1, we discuss in detail how to adapt the mixed fluid wave functions to obtain a representation on the sphere. More numerical results for a restricted class of wave functions, corresponding to filled CF shells on the sphere, are discussed in Appendix B.2.

## 2.2.2 Wave functions for the quantum Hall bilayer

In this section we review the various trial wave functions that we will be focusing on. For some the discussion of the composite fermion liquid (Section

2.2.2.1) and the 111 state (Section 2.2.2.3) may be mostly review. This material is nonetheless included in depth to emphasize a few key points that guide our reasoning.

For simplicity, in this section we will consider infinite-sized systems on a planar geometry so that we can write wave functions in the usual complex coordinate notation. As a reminder  $z_i = x_i + iy_i$  is used as the complex representation of the particle coordinates of particle  $i$  (with the overbar representing the complex conjugate), and the usual Gaussian factors of  $e^{-\sum_i z_i \bar{z}_i / (2\ell_0)^2}$  are understood to be included in the measure of the Hilbert space and will not be written explicitly for simplicity of notation. For bilayer states, we note coordinates in the second layer as  $w_j$ , using the same complex representation. In section 2.2.3 below, we will convert to considering wave functions on the sphere, where we actually perform our numerical calculations. The changes required to adapt our theory to the spherical geometry are discussed in Appendix B.1.

### 2.2.2.1 Composite Fermion Liquid

For bilayer systems at infinite layer spacing, the interlayer interaction vanishes and the two layers can be considered as independent  $\nu = \frac{1}{2}$  systems. For such single layer  $\nu = \frac{1}{2}$  systems, the composite fermion approach [Heinonen (1998)] has been remarkably successful in describing a great deal of the observed physics. In this picture [Jain (1990); Heinonen (1998)], the wave function for interacting electrons in magnetic field  $B$  is written in terms of the wave function for free (composite) fermions in an effective magnetic field  $\mathcal{B} = B - 2n\phi_0$  with the density of electrons  $n$ . Each fermion is also attached to two vortices (or correlation holes) of the wave function (Jastrow factors) resulting in the following type of wave function:

$$\Psi^{CF} = \mathcal{P} \prod_{k < p} (z_p - z_k)^2 \det [\phi_i(z_j, \bar{z}_j)]. \quad (2.42)$$

where  $\phi_i$  are the orbitals for free fermions in the effective magnetic field  $\mathcal{B}$ , and  $\mathcal{P}$  is the projection operator that projects to the lowest Landau level.

For the special case  $\nu = \frac{1}{2}$  the CF's experience zero effective field and behave similarly as electrons at zero field, forming a Fermi sea [Willett *et al.* (1993); Heinonen (1998)]. For an infinitely extended plane, plane waves form a basis of single particle orbitals for particles in zero effective magnetic field such that

$$\phi_i(z_j) = e^{i\mathbf{k}_i \cdot \mathbf{r}_j}. \quad (2.43)$$

Since  $\mathbf{k} \cdot \mathbf{r} = \frac{1}{2}(k\bar{z} + \bar{k}z)$  (with  $k$  being the complex representation of the vector  $\mathbf{k}$ ) and the projection on the LLL transforms  $\bar{z} \rightarrow -2\frac{\partial}{\partial z}$ , the plane



wave factors become translation operators under projection [Read (1994)]. This yields

$$\Psi_{\frac{1}{2}} = \mathcal{A} \left\{ \prod_{i < j} ([z_i + 2\ell_0^2 k_i] - [z_j + 2\ell_0^2 k_j])^2 \prod_i e^{i\bar{k}_i z_i / 2} \right\}, \quad (2.44)$$

where  $\mathcal{A}$  is the antisymmetrizing operator that sums over all possible pairings of the  $z_i$ 's with the  $k_j$ 's, odd permutations added with a minus sign. We see that the fermions are still bound to zeros of the wave function, but the positions of the zeros (correlation holes) are moved away from the electrons by a distance  $2\ell_0^2 k$ , which is given in terms of “momentum”  $k$ . In order to minimize the Coulomb energy, these distances should be minimized, but simultaneously, all the  $k_i$  have to be different or the wave function will vanish on antisymmetrization. Thus, to minimize potential energy, the  $k_i$ 's fill up a Fermi sea of minimal size. This is how the potential energy becomes the driving force for establishing the Fermi sea. Although this naive picture of charged dipole dynamics is not strictly true in the way that it is presented here [Graham *et al.* (2003)], there are several ways to more rigorously embody this type of dipolar Fermi sea dynamics in a theory of the lowest Landau level, which give credibility to this type of simplified argument [Murthy and Shankar (2003); Read (1998); Stern *et al.* (1999)].

Unfortunately, the projection  $\mathcal{P}$  in Eq. 2.42 is exceedingly difficult to implement numerically for large systems. To circumvent this problem, Jain and Kamilla (1997a) proposed a rewriting of the composite fermion wave function as

$$\Psi^{CF} = \prod_{k < p} (z_p - z_k)^2 \det [\tilde{\phi}_i(z_j)], \quad (2.45)$$

where

$$\tilde{\phi}_i(z_j) = J_j^{-1} \mathcal{P} [\phi_i(z_j, \bar{z}_j) J_j], \quad (2.46)$$

with  $J_j = \prod_{k \neq j} (z_k - z_j)$  and the  $\phi_i$  chosen such as to represent wave functions corresponding to a filled Fermi sea. This form, while not strictly identical to the form of Eq. 2.42, is extremely close numerically and has equally impressive overlaps with exact diagonalizations [Jain and Kamilla (1997a)] and is therefore an equally good starting point for studying composite fermion physics. However, in contrast to the form of Eq. 2.42, the form of Eqs. 2.45 and 2.46 are comparatively easy to evaluate numerically and therefore allow large system quantum Monte Carlo calculations [Jain and Kamilla (1997a)]. Here, we have used this type of approach.

In order to obtain a wave function for the bilayer system at  $\nu = \frac{1}{2} + \frac{1}{2}$  and infinite layer separation, a simple product state of two composite fermion

liquids (CFL) is appropriate.

$$\Psi(d \rightarrow \infty) = |CFL\rangle \otimes |CFL\rangle \quad (2.47)$$

At finite layer separation, however, correlations between the layers are expected to exist and have been suspected to resemble a paired state [Bonesteel (1993); Bonesteel *et al.* (1996); Morinari (1998, 1999); Kim *et al.* (2001)]. As we will see below, the product state (2.47) may be regarded as a particular paired state whenever the Fermi-surface is inversion symmetric with respect to the center of the Brillouin zone. In these cases, for each particle in layer one occupying a state with momentum  $\mathbf{k}$ , there exists its partner in layer two occupying a state with momentum  $-\mathbf{k}$ .

### 2.2.2.2 Paired CF bilayer state

We now consider how to write a trial wave function for an interlayer paired composite fermion state, which we suggest should be an accurate description of the bilayer system when the spacing between the layers is large. As a starting point, let us take the well known BCS wave function in the grand canonical ensemble [de Gennes (1966)]

$$|\Psi\rangle = \prod_{\mathbf{k}} \left( u_{\mathbf{k}} + v_{\mathbf{k}} e^{i\varphi} a_{\mathbf{k}\downarrow}^{\dagger} a_{-\mathbf{k}\uparrow}^{\dagger} \right) |0\rangle \quad (2.48)$$

with the normalization  $|u_{\mathbf{k}}|^2 + |v_{\mathbf{k}}|^2 = 1$  and where  $a_{\mathbf{k}\uparrow}^{\dagger}$  creates a particle in layer  $\uparrow$  with momentum  $\mathbf{k}$ . Note that the  $u$ 's and  $v$ 's are properly understood here as variational parameters of the BCS wave function. Next, we rewrite this wave function in an unnormalized form by multiplying all factors by  $u_{\mathbf{k}}^{-1}$  and defining  $g_{\mathbf{k}} = v_{\mathbf{k}}/u_{\mathbf{k}}$ , so

$$|\Psi\rangle = \prod_{\mathbf{k}} \left( 1 + g_{\mathbf{k}} e^{i\varphi} a_{\mathbf{k}\downarrow}^{\dagger} a_{-\mathbf{k}\uparrow}^{\dagger} \right) |0\rangle. \quad (2.49)$$

Finally, we project to a fixed number  $2N$  of particles (i.e, switch to canonical ensemble) by integration over  $\int d\varphi \exp(-iN\varphi)$  such that we retain exactly  $N$  pair creation operators. This yields

$$|\Psi\rangle = \sum_{\{\mathbf{k}_1, \dots, \mathbf{k}_N\}} \prod_{\mathbf{k}_i} g_{\mathbf{k}_i} a_{\mathbf{k}_i\downarrow}^{\dagger} a_{-\mathbf{k}_i\uparrow}^{\dagger} |0\rangle. \quad (2.50)$$

The Fourier transform into real space then reads

$$\Psi = \det [g(\mathbf{r}_{i\downarrow}, \mathbf{r}_{j\uparrow})] \quad (2.51a)$$

with

$$g(\mathbf{r}_{i\downarrow}, \mathbf{r}_{j\uparrow}) = \sum_{\mathbf{k}} g_{\mathbf{k}} e^{i\mathbf{k}(\mathbf{r}_{i\downarrow} - \mathbf{r}_{j\uparrow})}. \quad (2.51b)$$

Note that the exponential factor of the Fourier transform can be regarded as a product of two basis functions  $\phi_{\mathbf{k}}(\mathbf{r}) = e^{i\mathbf{k}\mathbf{r}}$  on the plane, i.e.

$$e^{i\mathbf{k}(\mathbf{r}_{i\downarrow} - \mathbf{r}_{j\uparrow})} = e^{i\mathbf{k}\mathbf{r}_{i\downarrow}} e^{-i\mathbf{k}\mathbf{r}_{j\uparrow}} = \phi_{\mathbf{k}}(\mathbf{r}_{i\downarrow}) \phi_{-\mathbf{k}}(\mathbf{r}_{j\uparrow}). \quad (2.52)$$

With this in mind, similar paired wave functions can be written for more general geometries with arbitrary basis functions. In this study, we construct paired states for composite fermions in the bilayer system denoting particles in the upper layer as  $z$  and those in the lower layer as  $w$ . As in section 2.2.2.1 we will multiply our fermion wave function with composite-fermionizing Jastrow factors and project to the lowest Landau level yielding

$$\begin{aligned} \Psi &= \mathcal{P} \prod_{i<j} (z_i - z_j)^2 \prod_{i<j} (w_i - w_j)^2 \det [g(z_i, w_j)] \\ &\equiv \mathcal{P} \det [J_i^{zz} J_j^{ww} g(z_i, w_j)], \end{aligned} \quad (2.53)$$

where we have defined “single particle” Jastrow factors

$$J_i^{zz} = \prod_{k \neq i} (z_i - z_k) \quad (2.54a)$$

$$J_i^{ww} = \prod_{k \neq i} (w_i - w_k). \quad (2.54b)$$

In order to handle the projection numerically, we follow the recipe of Jain and Kamilla (2.46) discussed above, multiplying the Jastrow factors inside the determinant and projecting individual matrix entries. This prescription applies to the bilayer case in a similar manner as for the single layer case (since the total Hilbert space of the bilayer system may be represented as a direct product of the space for each layer and projection in one space does not affect the other). We then obtain the final paired wave function:

$$\Psi^{\text{paired}} = \det [g_F(z_i, w_j)] \quad (2.55a)$$

where

$$g_F(z_i, w_j) = \sum_{\mathbf{k}} g_{\mathbf{k}} J_i^{zz} J_j^{ww} \tilde{\phi}_{\mathbf{k}}(z_i) \tilde{\phi}_{-\mathbf{k}}(w_j). \quad (2.55b)$$

By convention, the single particle Jastrow factors  $J_i$  are kept inside the function  $g_F$  so that  $g_F(z_i - w_j)$  is actually a function of all of the  $z$ 's and  $w$ 's through the  $J$ 's. The subscript  $F$  here has been chosen to indicate that these

are paired composite Fermions. Note that in the above expressions  $\mathbf{k}$  may stand for a general set of orbital quantum numbers (this will be important for spherical geometry where the free wave functions are spherical harmonics rather than plane waves).

The  $g_{\mathbf{k}}$ 's defining the shape of the pair wave function are variational parameters, analogous to the usual  $u$ 's and  $v$ 's. These parameters must be optimized as usual, though the optimal solution in this case is a function of the layer separation  $d$ . It is also to be noted that the expression (2.55a) can describe pairing in arbitrary pairing channels depending upon the choice of  $g_{\mathbf{k}}$  and the basis set  $\{\phi_{\mathbf{k}}\}$ . As a general definition, when the pair wave function has the short distance form

$$g(z_i, w_j) \propto (z_i - w_j)^l \times h(|z_i - w_j|), \quad (2.56)$$

we say this is  $l$ -wave pairing. However, note that  $g(z, w)$  should asymptotically approach zero for  $|z - w| \rightarrow \infty$ , such that the pair wave function can be normalized. We also frequently use the atomic physics nomenclature where  $l = 0$  is termed  $s$ -wave,  $l = 1$  is the  $p$ -wave, and so forth. Furthermore,  $l = +1$  is denoted as  $p_x + ip_y$  pairing, whereas  $l = -1$  is  $p_x - ip_y$  pairing. The pairing symmetry is independent of whether we move the  $J^{zz}$  and  $J^{ww}$  factors inside or outside of the function  $g_F$ .

As a simple example, consider the variational parameters  $g_{\mathbf{k}}$  defined as follows:

$$g_{\mathbf{k}} = \begin{cases} \text{anything nonzero,} & |\mathbf{k}| \leq k_F \\ 0, & \text{otherwise} \end{cases} \quad (2.57)$$

It is easy to show that in this scenario one recovers the product state of two composite fermion liquids (2.47).

### 2.2.2.3 111-state

When the spacing between the two layers becomes small, the bilayer system forms an interlayer coherent state. A number of different approaches have been used to understand this state and a large amount of progress has been made using a mapping to an iso-spin easy-plane ferromagnet [Moon *et al.* (1995); Yang *et al.* (1996)]. In this work, however, we will follow the Laughlin approach of considering trial wave functions in a first quantized description. When the distance between the two layers becomes zero, the exact ground state wave function of  $\nu = \frac{1}{2} + \frac{1}{2}$  is known to be the so-called 111-state [Halperin (1983); Moon *et al.* (1995)]

$$\Psi_{111} = \prod_{i < j} (z_i - z_j)(w_i - w_j) \prod_{i, j} (z_i - w_j), \quad (2.58)$$

where again we use  $z$  to represent particles in the upper layer and  $w$  to represent particles in the lower layer. In contrast to the CF state, (2.58) contains only one Jastrow factor between particles in the same layer so that the wave function is properly antisymmetric under exchange of particles in the same layer. Thus, no additional determinant is needed to fix the symmetry as was the case in the CF state. In addition, (2.58) includes a Jastrow factor between particles in opposite layers. Consequently, there is no amplitude for finding two particles at the same position in opposite layers. This can be interpreted as particles carrying correlation holes in the neighboring layer. One can say the 111-state is composed of interlayer excitons [Eisentein and MacDonald (2004)]. Another terminology is the Chern-Simons language where the electrons are transformed into bosons bound to flux quanta, where each flux quantum penetrates both layers. These "composite bosons" can be thought of as an electron bound to a vortex of the wave function in each layer. Condensing these bosons gives the wave function  $\Psi_{\text{CB}} = 1$  for the composite particles and the transform back to an electron wave function upon reattaching the Jastrow factors yields (2.58).

However, it is also useful to rewrite the 111 wave function using the Cauchy identity

$$\prod_{i < j} (z_i - z_j) \prod_{i < j} (w_i - w_j) = \prod_{i, j} (z_i - w_j) \det \frac{1}{z_i - w_j} \quad (2.59)$$

which yields

$$\Psi_{111} = \det \left[ \frac{1}{z_i - w_j} \right] \prod_{i, j} (z_i - w_j)^2. \quad (2.60)$$

This notation resembles the form of a general paired bilayer state as discussed above in section 2.2.2.2. This resemblance has been noted previously [Kim *et al.* (2001); Ho (1995)], and from the form of the  $1/(z_i - w_j)$  factor, it has been concluded that the pairing symmetry is  $(p_x - ip_y)$  [Kim *et al.* (2001)]. However, we claim that this is an incorrect interpretation. Since Jastrow factors outside the determinant cancel this apparent singularity, the phase obtained by taking an electron around its partner is actually  $+2\pi$  rather than  $-2\pi$ . In fact, for the 111 state it is clear from the explicit form (2.58) that as any electron is taken around another electron in either layer, one accumulates a phase of precisely  $+2\pi$ . For clarity, it is useful to move the Jastrow factors in Eq. 2.60 inside the determinant. We obtain

$$\Psi_{111} = \det [g_{\text{B}}(z_i, w_j)] \quad (2.61)$$

where

$$g_{\text{B}}(z_i, w_j) = \frac{J_i^{zw} J_j^{wz}}{z_i - w_j} \quad (2.62)$$

and the interlayer partial Jastrow factors are defined by

$$J_i^{zw} = \prod_k (z_i - w_k) \quad (2.63a)$$

$$J_i^{wz} = \prod_k (w_i - z_k). \quad (2.63b)$$

Here, the subscript  $B$  means that we have a pairing wave function for composite **B**osons. In this form, it is quite clear that  $g_B(z_i, w_j)$  represents pairing of  $p_x + ip_y$  type since a phase of  $+2\pi$  is obtained when  $z_i$  moves around  $w_j$  rather than  $-2\pi$ . Nonetheless, as suggested by Kim *et al.* (2001), it seems natural to have the same pairing symmetry for  $d > \ell_B$  and  $d \lesssim \ell_B$ . This then suggests that the relevant pairing symmetry for the composite fermions is  $p_x + ip_y$  rather than  $p_x - ip_y$ .

#### 2.2.2.4 Mixed CF-CB state

In section 2.2.2.2, we found the general expression for an interlayer-paired CF state in the bilayer (2.55a) which we believe should be appropriate ground state wave functions when  $d/\ell_0$  is large. Furthermore, in section 2.2.2.3 we determined a way to write the 111 (CB) state, which is exact at small  $d/\ell_0$  as a paired state. Both these types of wave functions could be written as determinants of pairing functions  $g_F$  and  $g_B$ , respectively. Now, following the ideas of Simon *et al.* (2003), we considered transitional wave functions that include both the physics of the CF's and the physics of the CB's. We propose the following extremely simple generalized form

$$\Psi^{\text{CF-CB}} = \det[G(z_i, w_j)] \quad (2.64)$$

with

$$G(z_i, w_j) = g_F(z_i, w_j; \{g_k\}) + c_B g_B(z_i, w_j), \quad (2.65)$$

where  $c_B$  is an additional variational parameter representing the relative number of CB's versus CF's. Note that as above  $g_F$  is a function of the variational parameters  $\{g_k\}$  which describe the shape of the pairing wave function.

To elucidate the meaning of this linear interpolation between composite fermion and composite boson pairing functions, it is useful to consider more carefully the physics of the fermion pairing described by Eq. 2.55a. Each entry in the matrix  $g_F(z_i, w_j)$  is a sum of many terms (See Eq. 2.55b) with each term representing the filling of particles  $z_i$  and  $w_j$  into a particular pair of CF orbitals (one in each layer). Upon multiplying out the entire determinant,

each term will include precisely  $N$  occupied CF orbitals, and as directed by Pauli exclusion, no orbital may be occupied more than once. Terms with double occupation of the same orbital cancel out by antisymmetry of the determinant, even for non-orthogonal base functions  $\phi_i$ . The amplitude that a particular orbital is occupied is determined by the coefficients  $g_{\mathbf{k}}$  (See also Eq. 2.50). Now, let us consider instead the pairing function  $G(z_i, w_j)$  which has both the fermionic  $g_{\text{F}}$  terms as well as the bosonic  $g_{\text{B}}$  terms (See Eq. 2.65). When we calculate the determinant in Eq. 2.64, each  $G(z_i, w_j)$  will be the sum of a term where the CB orbitals are filled for particles  $z_i$  and  $w_j$  (the  $g_{\text{B}}$  terms) and several terms where  $z_i$  and  $w_j$  instead fill a pair of CF orbitals. When we multiply out the entire determinant it results in a linear combination of all possible choices of filling  $M$  CF orbitals and  $N - M$  CB orbitals. As with the case for the paired CF wave function, the amplitude of different orbitals being filled is determined by the coefficients  $g_{\mathbf{k}}$  for the fermions and  $c_{\text{B}}$  for the bosons.

With this reasoning, we can actually reconstruct the mixed CB-CF wave functions introduced by Simon *et al.* (2003) as a special case of Eq. 2.64. To this end, let us fix  $c_{\text{B}}$  to some constant value, e.g.  $c_{\text{B}} = 1$ , and for all other variational parameters  $g_{\mathbf{k}}$  let us use a step function (analogous to Eq. 2.57 where we represented the filled Fermi sea as a paired state), but with a reduced Fermi-momentum  $(k_{\text{F}})_{\text{F}}$ :

$$g_{\mathbf{k}} = \begin{cases} \infty, & |\mathbf{k}| \leq (k_{\text{F}})_{\text{F}} \\ 0, & \text{otherwise} \end{cases} . \quad (2.66)$$

Where a very large  $g_{\mathbf{k}}$  is chosen, the corresponding state is forced to be occupied (the resulting normalization suppresses anything that does not include the maximal possible number of  $g_{\mathbf{k}}$  terms). Due to the Pauli exclusion principle, every CF state may be occupied only once, and consequently the particles remaining once the CF-sea is filled up to the reduced Fermi momentum  $(k_{\text{F}})_{\text{F}}$  can only occupy composite boson orbitals. The choice (2.66) results in the probability for a CF to occupy a state with  $|k| \leq (k_{\text{F}})_{\text{F}}$  to be equal to unity, which corresponds to a filled shell configuration. This construction is “equal” to the mixed CF-CB construction by Simon *et al.* (2003). (By “equal” here we mean that the two constructions are equivalent up to the differences between projection prescriptions in the original Jain construction Eq. 2.42 and the Jain-Kamilla construction Eq. 2.45). In Appendix B.2, we show explicitly that the filled shell states among those analyzed by Simon *et al.* (2003) can be reproduced accurately by choosing  $g_{\mathbf{k}}$  as in Eq. 2.66.

In contrast to the formula for the mixed fluid states given by Simon *et al.* (2003), the present form (Eq. 2.64) with  $g_{\mathbf{k}}$  according to Eq. 2.66

allows for an efficient numerical calculation. In our present approach, as explained below, the antisymmetry of the wave function is a natural result of the determinant (requiring  $\propto N_1^3$  numerical operations), whereas the aforementioned wave functions require explicit antisymmetrization, an operation that requires much computation power with an operation count scaling as  $N!$  with the system size.

We emphasize again that while Simon *et al.* (2003) considered a limited family of wave functions without CF pairing, the current approach (Eq. 2.64) allows for the handling of both nontrivial CF pairing and CF-CB mixtures simultaneously.

We now focus upon the question of whether, or under which circumstances, Eq. 2.64 is a valid lowest Landau level wave function. First, to test the requirement of antisymmetry, consider the interchange of 2 particles in the same layer, e.g.  $z_i \leftrightarrow z_j$ , thus in all columns  $k$ :

$$\begin{cases} g_B(z_i, w_k) \leftrightarrow g_B(z_j, w_k), & \text{lines } i, j \\ g_B(z_l, w_k) \rightarrow g_B(z_l, w_k), & \forall \text{ lines } l \notin \{i, j\} \end{cases} \quad (2.67a)$$

$$\begin{cases} g_F(z_i, w_k) \leftrightarrow g_F(z_j, w_k), & \text{lines } i, j \\ g_F(z_l, w_k) \rightarrow g_F(z_l, w_k), & \forall \text{ lines } l \notin \{i, j\} \end{cases} \quad (2.67b)$$

In other words, exchanging two particles amounts to interchanging two lines of the matrix  $(G)_{ij}$ .

The second condition to be checked is whether the proposed wave function is properly homogeneous, implying that it is an angular momentum eigenstate as required for the ground state of any rotationally invariant system. This condition is known to be true for both limiting cases—the 111 and the paired CF states. For it to remain true for the mixed CF-CB state, it is sufficient to require that  $(g_F)_{ij}$  and  $(g_B)_{ij}$  be of identical order in all variables. To check this it is sufficient to count the order (or number of zeros) that occur for a given variable in  $g_{ij}$ . For example, let us choose to look at the variable  $z_1$ . For  $i \neq 1$  we have  $g_B(z_i, w_j) = J_i^{zw} J_j^{wz} / (z_i - w_j)$ . The variable  $z_1$  occurs only inside of  $J_j^{wz}$  and occurs only once. Therefore, it is first order in  $z_1$ . Similarly for  $i \neq 1$ , in  $g_F(z_i, w_j) = g(z_i, w_j) J_i^{zz} J_j^{ww}$  the variable  $z_1$  occurs only inside of  $J_i^{zz}$  and occurs only one time, so that it is also first order. Let us now look at the term  $i = 1$ . In this instance, we have  $g_B(z_1, w_j) = J_1^{zw} J_j^{wz} / (z_1 - w_j)$  which has  $z_1$  occurring  $N$  times in  $J_1^{zw}$ , once in  $J_j^{wz}$  and once in the denominator, resulting in a total order  $N$ . For  $g_F(z_1, w_j) = g(z_1, w_j) J_1^{zz} J_j^{ww}$  there are  $N - 1$  powers of  $z_1$  in  $J_1^{zz}$  and additional  $l$  powers in  $g(z_1, w_j)$  if we have  $l$ -wave pairing (See Eq. 2.56), giving a total number of powers of  $z_1$  equal to  $N - 1 + l$ . Thus, in order for this to match the degree of  $g_B(z_1, w_j)$ , we must choose  $l = +1$  or  $p_x + ip_y$



pairing of the Fermions. It is clear that choosing any other pairing symmetry would result in a wave function that is nonhomogeneous (therefore not an angular momentum eigenstate) upon mixing fermions with bosons. While we cannot rule out some first order phase transition between some other pairing symmetry for the CF's and a coherent CB phase, it appears to us that  $p_x + ip_y$  is the only symmetry compatible with coexistence of CB's and CF's.

In the following sections and Appendix B.1 we will translate these wave functions onto spherical geometry for which we have performed detailed numerics.

### 2.2.3 Numerical Results

In this section, we study the variational wave functions discussed previously. In particular we focus upon Eq. 2.64, which includes Eq. 2.53 as an important special case. Using Monte-Carlo, we numerically evaluated the ground state energy of these trial wave functions and the electron-electron position correlation functions. These results were then compared to similar results calculated using exact diagonalization methods. We have found that our trial wave functions provide extremely accurate representation of the exact ground states.

To avoid complications associated with system boundaries, we chose to work with a spherical geometry [Haldane (1983)] with a monopole of flux  $N_\phi \equiv 2S$  flux quanta at its center. We gave each electron not only a positional coordinate, but also a layer index which may be either  $\uparrow$  or  $\downarrow$ .  $N$  electrons were put on the surface of the sphere where half of them occupy each layer ( $N = 2N_\uparrow = 2N_\downarrow$ ). We have assumed no tunnelling between the two layers, therefore, these can be thought of as distinguishable electrons. We focused upon filling fraction  $\nu = \frac{1}{2} + \frac{1}{2}$  which corresponds to  $N_\phi = 2N_\uparrow - 1 = N - 1$ . This is precisely the flux at which the 111 state occurs. Note, however, that for a single layer the composite Fermion liquid state with no effective flux occurs at  $N_\phi = 2(N_\uparrow - 1)$ , which differs from what we consider by a single flux quantum. This difference in "shift" means that we are actually considering a crossover from the 111 state to a Fermi liquid state with one additional flux quantum. It turns out that this one additional flux quantum is appropriate here since precisely such a shift is induced by the nature of the p-wave pairing.

The interaction between electrons is taken to be of the Coulombic form

$$V_{\uparrow\uparrow}(r) = V_{\downarrow\downarrow}(r) = e^2/(\epsilon r) \quad (2.68)$$

$$V_{\uparrow\downarrow}(r) = V_{\downarrow\uparrow}(r) = e^2/(\epsilon\sqrt{r^2 + d^2}) \quad (2.69)$$

where  $r$  is the chord distance between the electrons,  $\epsilon$  is a dielectric constant, and  $d$  represents the distance between the layers (measured in units of the magnetic length  $\ell_0$ ). Note that for simplicity, finite well width is not taken into account.

Since our Hamiltonian is rotationally symmetric on the sphere, we can decompose all states into angular momentum eigenstates. Our exact diagonalization calculations determined the ground state to be in the angular momentum  $L = 0$  sector. The trial ground state wave functions are also  $L = 0$ . In addition to rotational symmetry, the Hamiltonian exhibits a symmetry under exchange of the two layers. The ground state was found in the subspace with parity  $(-1)^{N_1}$ . Again, it is simple to check that this is also the symmetry of our trial wave functions.

Exact diagonalization calculations were performed for system sizes of  $N = 10, 12$  and  $14$  electrons for a large range of values of the interlayer spacings  $d$ . In order to evaluate the significance of our results it is useful to examine the size of the Hilbert space in which the Hamiltonian resides. While the full Hilbert space is large (even for 10 electrons), once the space is reduced to states of  $L = 0$ , the space is quite a bit smaller. In Table 2.1 we show the dimensions of the  $L = 0$  Hilbert space (and the dimensions of the even and odd parity parts of that space) for the different size systems. While these sizes may appear small we note that they are typical sizes for  $L = 0$  subspaces for what are considered to be relatively large exact diagonalizations. For comparison in Table 2.1 we show the dimensions of the  $L = 0$  spaces for a number of other typical quantum Hall calculations in the literature.

For a given interlayer spacing  $d$ , we first performed exact diagonalization to find the ground state, and then determined how “close” we could get to this state with our trial variational wave functions. The trial variational wave functions are a function of the parameters  $\{g_{\mathbf{k}}\}$  (for both Eq. 2.64 and Eq. 2.53) and one additional parameter  $c_B$  (which we can think of as being set to zero in Eq. 2.53). While it is clear that with enough variational parameters one can fit any result, the actual number of variational parameters we use is quite small. First of all  $g_{\mathbf{k}}$  can be assumed to be a function of  $|\mathbf{k}|$  only. More accurately, on the sphere the orbital states are indexed by the quantum numbers  $n$  (the shell index) and  $m$  (the  $z$  component of the angular momentum in the shell), and by rotational invariance of the ground state we can assume that the variational parameters are independent of  $m$ . In other words, there is a single parameter per composite fermion shell (or composite fermion Landau level); we noted these parameters as  $g_n$ . For the system sizes available in our exact diagonalizations, no more than 5 such variational

$\nu$	$N$	$N_\phi$	$D(L=0)$	$[E_{\text{trial}} - E_G]/E_G$
$\frac{1}{2} + \frac{1}{2}$	5+5	9	<b>29</b> +9	$< 1.5 \times 10^{-3}$
	6+6	11	155+ <b>97</b>	$< 2 \times 10^{-3}$
	7+7	13	<b>844</b> +715	$< 2.2 \times 10^{-3}$
$\frac{1}{3}$	6	15	6	$5 \times 10^{-4}$
	7	18	10	$5 \times 10^{-4}$
	8	21	31	$5 \times 10^{-4}$
	9	24	84	$5 \times 10^{-4}$
	10	27	319	$6 \times 10^{-4}$
$\frac{2}{5}$	8	16	8	$4 \times 10^{-5}$
	10	21	52	$2 \times 10^{-4}$
	12	26	418	$2 \times 10^{-4}$

Table 2.1: Hilbert space dimensions of the  $L = 0$  subspace for the examined bilayer systems and several reference states. For bilayer states two values are indicated corresponding to the fraction of states with odd and even parity under layer exchange. The respective subspace containing the groundstate is typeset in bold. Exact diagonalization calculations for the bilayer system were performed by E. H. Rezayi for the purpose of this collaboration. Data on the exact energies of single layer states was collected from the FQHE database [Regnault (b)].

parameters were necessary to obtain satisfactory trial states. Considering the dimensions of the symmetry reduced Hilbert space (shown in Table 2.1) which is much larger than 5, we conclude that the agreement of our states with the exact ground state is nontrivial.

In order to compare our trial states to the exact diagonalizations, we calculate the trial state energy as well as the electron-electron pair correlation functions,<sup>3</sup> defined as

$$h_{\sigma\sigma'}(\theta) = \frac{\mathcal{N}_{\sigma\sigma'}}{\langle\rho_\sigma\rangle\langle\rho_{\sigma'}\rangle} \langle\rho_\sigma(\vec{r})\rho_{\sigma'}(\vec{r}')\rangle \quad (2.70)$$

where  $\rho_\sigma(\vec{r})$  is the density in layer  $\sigma$  at position  $\vec{r}$ , and  $\theta$  is defined as the great circle angle between positions  $\vec{r}$  and  $\vec{r}'$ . The normalization is chosen such that  $h(r \rightarrow \infty) = \mathcal{N}_{\sigma\sigma'}$ , with

$$\mathcal{N}_{\sigma\sigma'} = \frac{N_1 - \delta_{\sigma\sigma'}}{N_1}. \quad (2.71)$$

<sup>3</sup>We choose to represent the pair correlation function using the unusual symbol  $h(r)$  for the entirety of this chapter, since  $g(r)$  is used as a symbol for the pair wave function.

This choice yields the proper count of interacting particle pairs when calculating the energy in terms of the pair correlation functions as

$$E = \frac{N_1^2 e^2}{2\epsilon} \int d\mu(r) \sum_{\sigma, \sigma'=\uparrow, \downarrow} (h_{\sigma, \sigma'}(r) - \mathcal{N}_{\sigma\sigma'}) V_{\sigma\sigma'}(r), \quad (2.72)$$

with  $\mu(r) = \sin(r/2\pi R)$  for the sphere.

This variational procedure attempts to find the lowest energy trial state at each interlayer spacing  $d$ . Since the energy differences are small (which is a test to the validity of our wave functions), it turns out to be substantially easier to try to make the pair correlation function of the trial state match that found in the exact diagonalization. Details of the optimization procedure for the variational parameters can be found in Appendix B.3.

For larger system sizes where we were unable to perform exact diagonalization, we are nonetheless still able to study this system by Monte Carlo. In such cases, the variational parameters must be optimized by simply attempting to minimize the energy of the trial state, though we are uncertain of the proximity of the results to the exact ground state. At present, this possibility has not yet been exploited, and we limit our study of bigger systems to filled shell states. This study is presented in Appendix B.2.

### 2.2.3.1 Paired CF results

In this section, we discuss the results for the paired CF wave functions (2.55a) with pairing in the  $p_x + ip_y$  channel. In Figure 2.2, the relative errors of the trial state energies with respect to the ground state energy  $[E^\gamma(d) - E^G(d)]/E^G(d)$  for two different system sizes of  $N = 10$  and  $N = 14$  particles are represented. In both cases, the paired CF states yield excellent trial states for large  $d$ , whereas there is a layer separation  $d^{\text{CB}}$  below which the paired CF picture yields no good trial states. We find  $d^{\text{CB}} \approx 0.9\ell_0$  and  $d^{\text{CB}} \approx 1.1\ell_0$  for 10 and 14 particles respectively.

These results are surprising, since the regime where paired CF states yield very good trial states extends from infinite layer separation down to  $d \sim \ell_0$ , well below the point where experiments observe the set-in of the various phenomena that are thought to be associated with spontaneous interlayer coherence and the presence of CB's or interlayer excitons. Given the large increase in  $d^{\text{CB}}$  between the systems with  $N = 10$  and  $N = 14$  particles, it is not clear at present how to extrapolate to the thermodynamic limit. A naïve extrapolation over  $N^{-1}$  based on the above values yields  $d^{\text{CB}} \approx 1.6$  in the thermodynamic limit, which is rather close to where a transition is observed experimentally. For the system sizes we analyzed, there might also

be closed shell effects that come into play. In particular,  $N = 12$  corresponds to a pair of two filled CF shells with 6 electrons each (see Appendix B.2). Thus, it is imaginable that it is particularly unfavorable to have a single electron (per layer) in the highest shell which happens when  $N = 14$ . In this context, note also that  $N = 10$  obtains a nearly perfect representation of the ground state at very large separation, whereas a small error remains for  $N = 14$  electrons. The magnitude of these errors will be discussed more in the following section.

Incidentally, in a recent numerical study [Shibata and Yoshioka (2006)], it was shown that the character of the low-lying excited states changes at around  $d = 1.2\ell_0$  for a finite system with  $N_1 = 12$ . In light of our theory, this might correspond to the layer separation  $d^{\text{CB}}$  which separates states where CB's do or do not play a role.<sup>4</sup> We shall come back to this point later when discussing the impact of our numerical results with respect to the nature of the phase transitions that occur in the bilayer system.

### 2.2.3.2 Mixed CF-CB results

In order to obtain a complete description of the ground-state evolution starting from vanishing layer separation, we need to consider the mixed fluid description of the quantum Hall bilayer. Upon addition of CB's to the paired CF description, one obtains the family of mixed CF-CB states (2.64). Technically this corresponds to adding one more variational parameter to the previously discussed case of paired CF. Consequently, using this extended family of trial states yields at least as good results as with composite fermions only.

Numerical simulations confirm that the mixed fluid description of bilayer trial wave functions (2.64) achieves an impressively precise description of the ground state for all  $d$ . This is exhibited in the numerical results shown in Fig. 2.3, once more displaying data for the systems with  $N = 10$  and  $N = 14$  electrons.

In both cases, we have found the largest relative error for the prediction of the ground-state energy at intermediate distances close to  $d = 1.5\ell_0$ . These “worst case errors” are listed in Table 2.1. Upon comparing of these errors to those prevailing for selected hierarchy states, notably  $\nu = 1/3$  and  $\nu = 2/5$ , we find that the errors for our bilayer states are about 3-4 times as large as those of the Laughlin state at  $\nu = 1/3$  for Hilbert-spaces of comparable dimension. Given that this state is often referenced as a standard for its

---

<sup>4</sup>Remark that the value predicted from a linear extrapolation of the results for  $N_1 = 5$  and  $N_1 = 7$  is  $d^{\text{CB}}(N_1 = 12) \approx 1.3\ell_0$ .

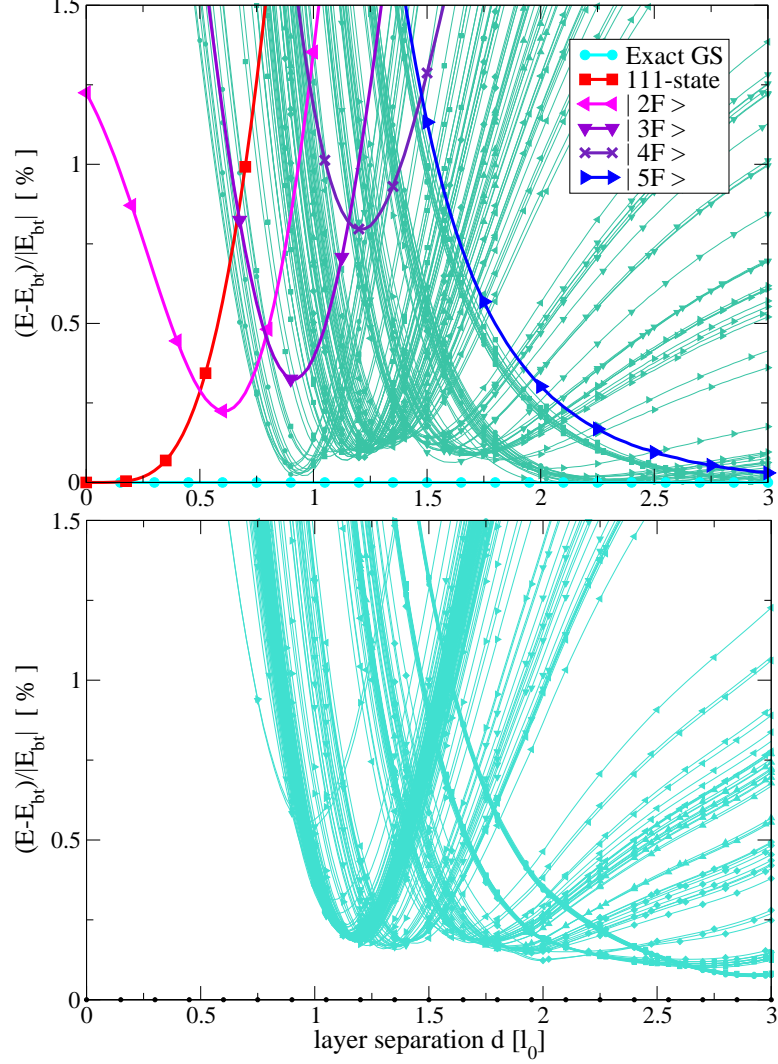


Figure 2.2: (color online) Relative errors in energy of p-wave paired CF trial states (2.55a) in the bilayer for  $N = 5+5$  particles (top) and  $N = 7+7$  particles (bottom). Each of the represented curves corresponds to a different trial state, i.e. a different choice of parameters  $\{g_n\}$ . By definition, the exact ground state defines the zero point line. The largest errors are of order  $1.5 \times 10^{-3}$  and  $2.2 \times 10^{-3}$  for  $N_1 = 5$  and  $N_1 = 7$  respectively, when regarding only those layer separations greater than  $d = d^{\text{CB}}$ , where the paired CF Ansatz yields “good” trial states. For comparison, the mixed fluid trial states from Simon *et al.* (2003) are represented as bold lines in the upper panel (see legend).

accurate description of the ground-state energy, this is a satisfying result. The results at  $\nu = 2/5$  are even more accurate, however, the bilayer states also approach the exact ground state energy much closer than the maximal error just cited, especially for  $N = 10$  particles.

The above results for the energies represent a strong indication that the trial states are very close to the exact ground states. A second comparison that is often referred to in the literature of the quantum Hall effect is the overlap integral  $O$  between the exact ground state and trial states, where

$$O = \langle \Psi_{\text{trial}} | \Psi_{\text{exact}} \rangle = \int d(z_1, \dots, z_{N_1}, w_1, \dots, w_{N_1}) \Psi_{\text{trial}}^* \Psi_{\text{exact}}. \quad (2.73)$$

The overlaps of the mixed fluid states with an *a priori* given number of CF have been examined by Simon *et al.* (2003). For the state that comes closest in energy to the exact ground state, the state with 2 composite fermions (termed  $|2 \text{ Fermions}\rangle$  by Simon *et al.* (2003)), a maximal overlap  $|\langle 2 \text{ Fermions} | \text{GS}(d = 0.625) \rangle|^2 \approx 98\%$  is reached. For the mixed fluid states with CF pairing that yield energy differences well below the minimal difference for  $|2 \text{ Fermions}\rangle$  over the whole interval of  $d$ , overlaps even closer to one are expected, however, overlaps were not calculated in this study. Instead, we compared the correlation functions of various trial states with respect to those of the exact numerical diagonalization. A series of such comparisons, shown in Fig. 2.4, confirms the close match of the mixed fluid trial states.

Naturally, nearly exact trial states are obtained at  $d \rightarrow 0$ , where the appearance of CF's may be regarded as a perturbation of the 111-state (which is obtained by the particular choice of parameters  $g_k = 0$  and  $c_B = 1$ , and which is the exact ground state at  $d = 0$ ). However, the admixture of CF's becomes important at rather small  $d$ . This fact is unveiled by analyzing the correlation functions shown in Fig. 2.4 for  $N = 5 + 5$  electrons. For  $d$  as small as  $d = 0.5\ell_0$ , the correlation hole for small  $r$  in the intralayer correlation function  $h_{\downarrow\downarrow}$  is noticeably enlarged, and the correlation hole in the interlayer correlation function  $h_{\uparrow\downarrow}$  is reduced accordingly, with  $h_{\uparrow\downarrow}(0) > 0$ . Any such change is exclusively due to the admixture of CF to the quantum state. To highlight the evolution just described, the upper left panel of Fig. 2.4 allows a joint representation of the correlation functions at  $d = 0$  and  $d = 0.5\ell_0$ .

Since we know the overlap for the states  $|n \text{ Fermions}\rangle$ , as explained above, it is instructive to focus upon the points where these states yield the best approximation to the ground-state. For the state  $|2 \text{ Fermions}\rangle$ , this occurs at approximately  $d = 0.625\ell_0$ . Whereas the mixed fluid states reproduce the correlation functions of the exact solution well, the correla-

tion functions belonging to  $|2 \text{ Fermions} \rangle$  give good approximations for the short-distance correlations, but show inappropriate oscillations for larger  $r$ .

With growing  $d$ , the anti-correlations described by the correlation hole in  $h_{\uparrow\downarrow}$  continue to decrease and the correlation hole in  $h_{\downarrow\downarrow}$  expands to its full size. For choices of  $g_n$  that correspond to sufficiently large numerical values such that the correlation hole in  $h_{\downarrow\downarrow}$  has reached its full size, the shape of the intralayer correlation function is relatively insensitive to these parameters. This means that intralayer correlations are coded into the Jastrow factors regardless of the specific (projected) CF orbital. Contrarily, the interlayer correlation function  $h_{\uparrow\downarrow}$  has a strong dependence on the shape of  $g_n$ .

In the previous section, we highlighted that paired states without an admixture of CB correlations reproduce exact solutions down to  $d \sim \ell_0$ . Accordingly, the correlation function  $h_{\uparrow\downarrow}$  in the middle left panel of Fig. 2.4 features a strong anti-correlation of electrons in both layers. This correlation hole can thus be explained entirely in terms of CF-pairing, which is counterintuitive since one would expect pairing to enhance correlations between the layers. With regard to the shape of the pair wave functions (2.56) where  $g(z, w) \propto (z - w)$  for  $p$ -wave pairing, we can more clearly understand this feature. By virtue of this property,  $p_x + ip_y$  pairing introduces *anti*-correlations on short length scales. As the pair wave function is forced to have a maximum and to decay for  $r \rightarrow \infty$ ,  $g$  is guaranteed to describe a bound state of pairs with some finite typical distance between the bound particles. Correspondingly, the correlation hole in  $h_{\uparrow\downarrow}$  is accompanied with an enhanced correlation function around  $r \approx 2\ell_0$ .

Furthermore, it should be noted that the number of variational parameters required to obtain good agreement of  $h(r)$  becomes maximal at intermediate layer separations  $d \sim 1.5\ell_0$ , where the influence of CF pairing is strongest. This is where CF may occupy orbitals in CF shells higher than the Fermi momentum of a filled CF Fermi sea. Numerical optimization is most difficult at those layer separations, and the largest deviations from the exact solution are observed.

Note that residual correlations between both layers remain present even at  $d = 3\ell_0$ , the largest layer separation we examined. Even for the system with  $N = 6 + 6$  electrons, which corresponds to two filled CF-shells, residual correlations remain. Even at layer separations as large as  $3\ell_0$ , the state does not factorize into two independent composite fermion liquid states. Instead, the observed correlations remain well-characterized by interlayer CF pairing.

Lastly, we confirmed numerically that the mixed fluid trial states introduced by Simon *et al.* (2003) may be obtained in the described approach for the filled shell cases. The general phenomenology that may be obtained



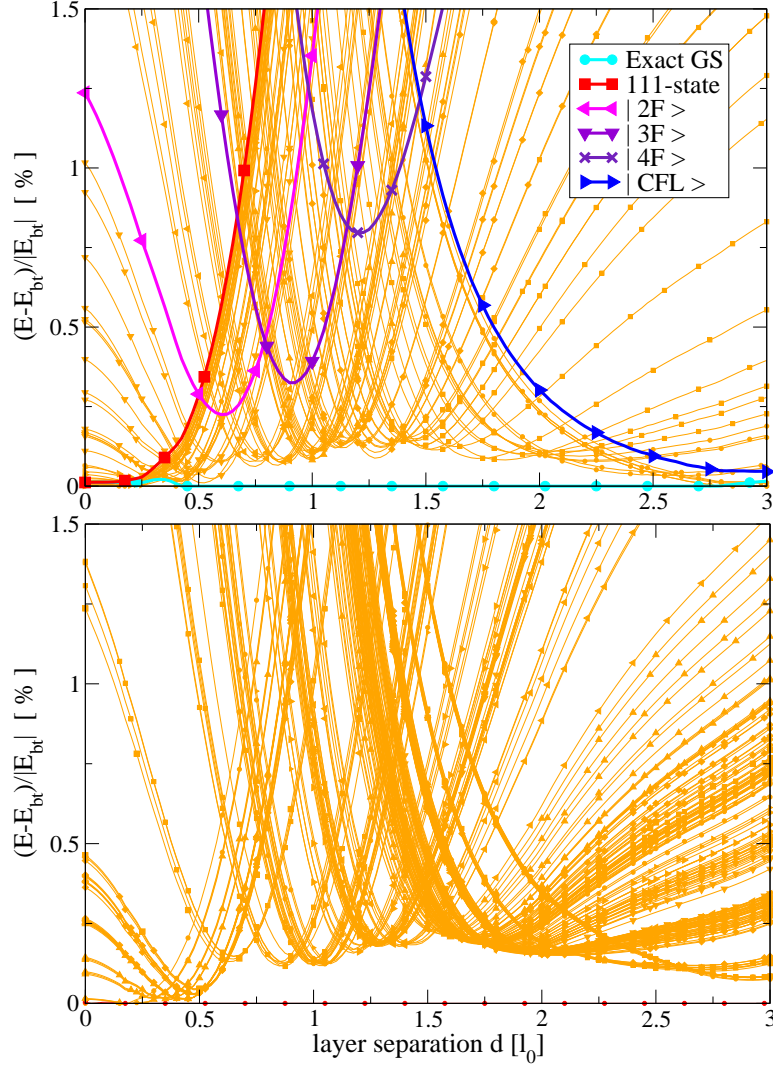


Figure 2.3: Comparison of relative errors in energy for mixed CB-CF fluid with interlayer p-wave paired CF model systems with  $N = 10$  (top) and  $N = 14$  electrons (bottom). As in Fig. 2.2, each curve represents a different trial state. The mixed fluid states from Simon *et al.* (2003) are highlighted in bold in the upper panel. Over the entire range of  $d$ , extremely good trial states are obtained, with a remaining error  $\delta\epsilon < 2.2 \times 10^{-3}$ . For intermediate  $d$ , where the states  $|n \text{ Fermions}\rangle$  do not perform very well, considerable improvements are realized.

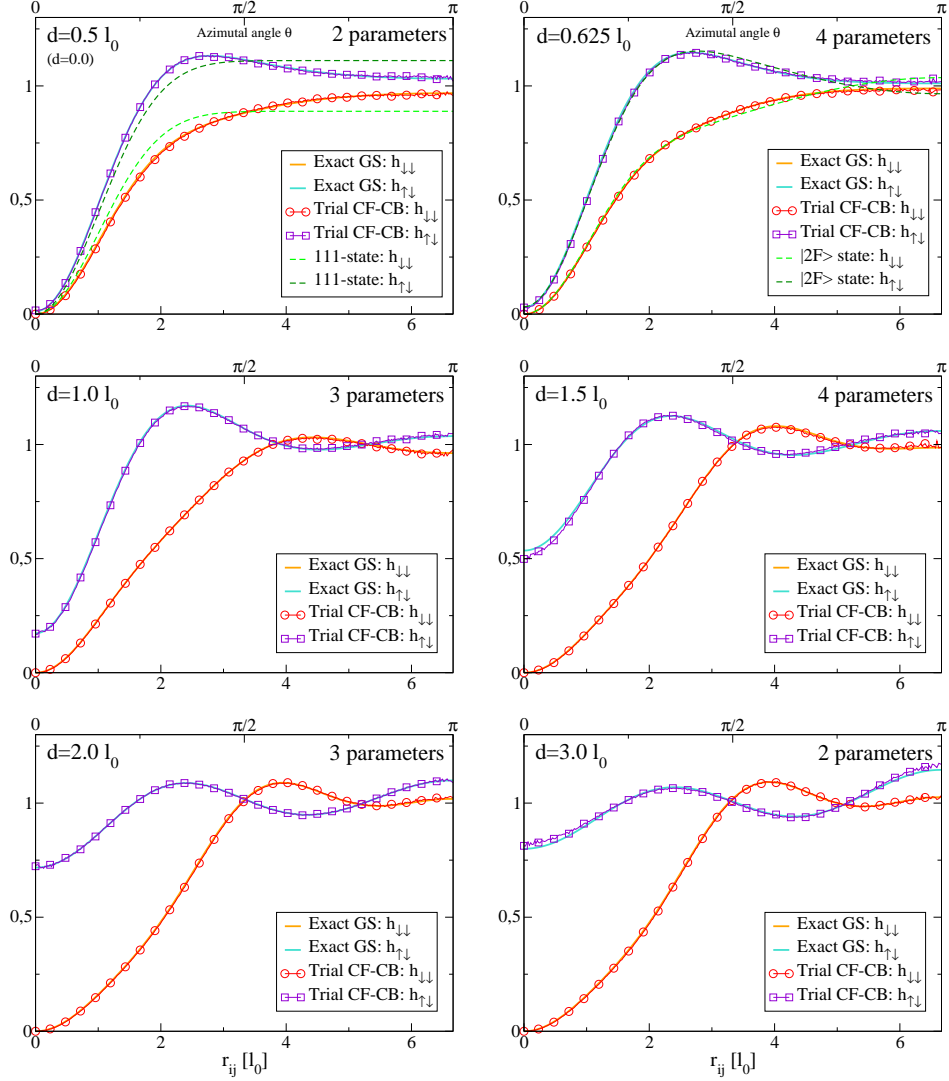


Figure 2.4: Correlation functions  $h_{\uparrow\downarrow}(r)$  of the respective “best” trial states at selected layer separations  $d$  for a system with  $5+5$  electrons. The agreement between the trial wave-functions (thin lines with symbols) and the exact results (bold lines) is significant for any value of  $d$ . Even at small finite  $d$ , the functions  $h_{\sigma\sigma'}(r)$  differ noticeably from the case of the 111-state (upper left). The correlation functions of the [2 Fermions) mixed fluid state [Simon *et al.* (2003)] exhibit discrepancies upon comparison to the exact solution despite the large overlap of 98% at the given  $d$  (upper right). The number of variational parameters employed here is indicated in each case.

from the analysis of filled CF shell states is discussed in Appendix B.2.

### 2.2.3.3 Occupation probabilities of CF shells

With the mixed fluid wave functions (2.55a), a vast family of trial states is available. Furthermore, the above results confirm that the mixed fluid wave functions allow for an accurate description of ground-state properties. As a step towards an understanding of the numerical results just presented, it is interesting to analyze the occupation probabilities of the various CF-LL that correspond to the most successful trial states.

In Figures 2.2 and 2.3, the individual trial states were anonymous, and revealing the explicit values of the variational parameters  $\{g_n\}$  would not have been very meaningful for two reasons. First, these parameters can be arbitrarily rescaled. Secondly, the normalization of the corresponding orbitals is unknown, if defined at all—the projection to the LLL provides a basis of correlated wave functions that are not orthogonal.

Though related to the variational parameters  $g_k$ , the occupation probability of orbitals with momentum  $k$  non-trivially depends upon the ensemble of  $g_k$ 's, since these are also involved in the total normalization of the wave function. For Monte-Carlo simulations, it is not required to normalize the wave function. Instead, the unnormalized wave function is utilized, such that  $\int d(z, w) |\Psi|^2$  remains a function of  $g_k$ . This dependence may be used to calculate an estimate for the occupation probabilities of the different CF-shells via the following relation:

$$p(k) = \frac{g_k}{2N} \frac{1}{\langle |\Psi(g_k)|^2 \rangle} \frac{\partial \langle |\Psi|^2 \rangle}{\partial g_k}, \quad (2.74)$$

where  $\langle \cdot \rangle$  notes  $|\Psi(g_k)|^2$ -weighted averages, and  $p(k)$  gives the approximate probability that an electron occupies a CF orbital with momentum  $k$ . The relation (2.74) may be explained with the example of a simple one-particle two-state model with wave function  $\Psi = a_1\phi_1 + a_2\phi_2$ , which we allow to be unnormalized. Expanding the square of this wave function,

$$|\Psi|^2 = |a_1|^2 |\phi_1|^2 + a_1 a_2^* \phi_1 \phi_2^* + a_1^* a_2 \phi_1^* \phi_2 + |a_2|^2 |\phi_2|^2 \quad (2.75)$$

we can see that Eq. (2.74) yields the proper occupation probabilities of both levels, provided that the overlap integral  $\langle \phi_1 \phi_2^* \rangle$  vanishes. This is the case for the scalar product of wave functions in a regular orthogonal basis. This argument generalizes to the N-body case simply by applying the rule for the derivation of products.

For the mixed bilayer states, however, we use the non-orthogonal basis of the LLL-projected CF orbitals. Nonetheless, we could verify that the

occupation probabilities for states with filled CF shells (where we know the occupation probabilities (Appendix B.2)) are obtained from (2.74) with high accuracy, showing that the respective overlap integrals are small.

Surprisingly, upon applying the same philosophy to the composite boson degrees of freedom of the bilayer wave functions (2.64), the procedure fails. Differentiating with respect to  $c_B$  in (2.74), the occupation of the CB orbitals is over- or underestimated. This indicates that the overlap integrals between the CF- and CB- orbitals are not small—which supports our idea that scattering processes between these two species of composite particles are important. However, it is not clear why the same terms do not affect the values of the CF occupation numbers in a similar way.

Let us now turn to the results obtained for the two selected systems sizes that we discussed in the previous sections. Taking the best trial state as a reference at each  $d$ , we may extract from our calculation the  $d$ -dependence of the occupation probability  $p(n)$  to find an electron in CF shell  $n$ . The resulting data is displayed in Fig. 2.5.

Upon looking at large layer separations, it is first noticed that the distribution at  $d = 3\ell_0$  is that of the CF Fermi sea. For example, in the lower panel for  $N = 7 + 7$  electrons, the probability that an electron is in the lowest CF shell is  $p(0) \approx 2/7 \approx 0.28$ . For the next higher shell, which is fourfold degenerate, one finds  $p(1) \approx 4/7 \approx 0.57$ . The third shell amounts for the remaining probability. Upon going to intermediate layer separation, the onset of pairing is realized as one would expect by analogy with BCS theory: electrons are lifted above those orbitals within the equivalent of a Fermi-sea and occupy states at higher momentum, instead. Correspondingly, the occupations in the lowest two shells drop to the advantage of the higher ones,  $n = 3$  included, which is occupied by a single electron initially. For  $N = 5 + 5$ , we follow an analogous trend of redistribution among the occupation of CF-levels, noting that the total probability of finding a particle in one of the excited orbitals is quite important, with absolute values close to 25%. Only at lower layer separation does the occupation of the CB orbital become important. Conversely, the occupation of CF orbitals plays an important role down to very low layer separations.

Now, the occupation of the CB orbital  $p_B$  may be analyzed. First, it is important to note that this data was obtained by subtracting the CF occupation probabilities from 1:

$$p_B = 1 - \sum_n p(n). \quad (2.76)$$

At large layer separation, the value thus obtained dropped slightly below zero. However, this error is not very large, amounting to approximately 1%,

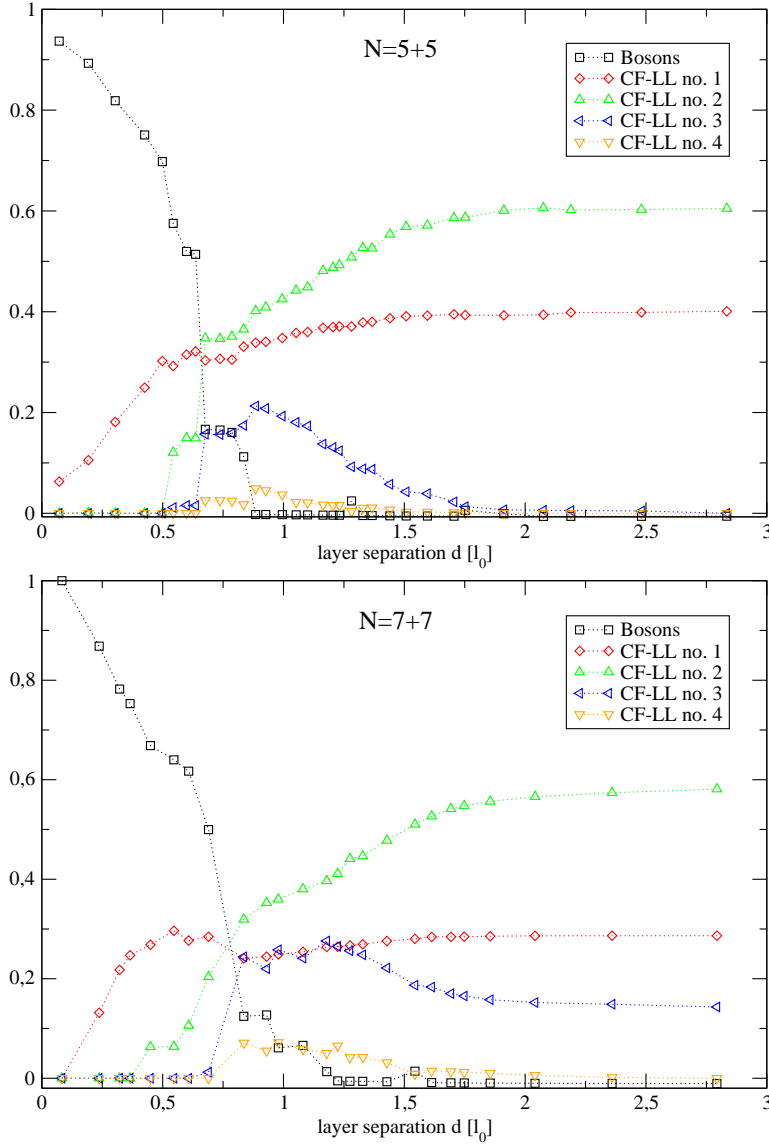


Figure 2.5: Probabilities for a single electron to occupy a given orbital, as obtained from Eq. 2.74. A region of strong pairing, i.e. large probabilities to find an electron in an excited orbital above the would be Fermi-momentum, is found between  $d \sim 0.8 \dots 1.5\ell_0$ . The probability that an electron forms a CB is obtained as  $p_B = 1 - \sum p(n)$ . Note that  $p_B$  practically drops to zero (or slightly below) at  $d \sim \ell_0$ . The kinks in the dependence of  $p_B(d)$  are close to values which are related to the CF shell structure.

which gives some confidence into our method, though it reminds that it is approximate. We need to remark also, that the data is based on calculations for a restricted number of trial states, such that more substantial deviations are likely due to data that does not correspond to the right trial state. The roughness and non-monotonic character of the curves illustrates this. Some of the features in the behavior of  $p_B(d)$  might be caused by filled shell effects, given that kinks are featured at values close to  $1 - n_S/N$  where  $n_S$  CF's yield a filled shell configuration.

Whereas the previous discussion of the occupation probabilities  $p(k)$  provides a qualitative understanding of the character of the CF pairing,  $p(k)$  is a feature of our mathematical description and does not represent a fundamental symmetry of the ground state.

#### 2.2.3.4 Symmetries

This section is devoted to discussing other means of characterizing the mixed fluid trial states—we discuss the broken U(1) symmetry of the 111-state via an appropriate order parameter.

In order to consider the symmetry of our quantum states, it is useful to employ the pseudospin picture. A density-balanced bilayer system is described by a pseudospin field with its values confined to the  $x$ - $y$ -plane. In the ground state the orientation of this pseudospin field is homogeneous and a spontaneous symmetry breaking of the U(1) symmetry for rotations of the pseudospin around the  $z$ -axis occurs such as to select a preferred direction in the  $x$ - $y$ -plane. The operator for the in-plane pseudospin thus yields a measure for detecting the symmetry of a coherent state in the bilayer system. In the second quantized notation, this order parameter describes a flip of the pseudospin at position  $\mathbf{r}$ , noted as  $\mathcal{F}(\mathbf{r})$ :

$$\mathcal{F}(\mathbf{r}) = \mathcal{F}_\uparrow(\mathbf{r}) + \mathcal{F}_\downarrow(\mathbf{r}) \equiv \Psi_\uparrow^\dagger(\mathbf{r})\Psi_\downarrow(\mathbf{r}) + \Psi_\downarrow^\dagger(\mathbf{r})\Psi_\uparrow(\mathbf{r}). \quad (2.77)$$

For the purpose of numerics at fixed particle number  $N_i$  per layer, the operator needs to be further modified such as to conserve  $N_i$ . This is realized by taking the product  $\mathcal{S} = \mathcal{F}(\mathbf{r})\mathcal{F}(\mathbf{r}')$  at two distant points  $\mathbf{r}$  and  $\mathbf{r}'$ . In the limit  $|\mathbf{r} - \mathbf{r}'| \rightarrow \infty$ , one expects to recover the square of the expectation value of  $\mathcal{F}$  in a corresponding grand canonical ensemble. Projected to fixed  $N_i$ ,

$$\mathcal{S} = \lim_{|\mathbf{r}-\mathbf{r}'|\rightarrow\infty} \mathcal{F}_\uparrow(\mathbf{r})\mathcal{F}_\downarrow(\mathbf{r}') + \mathcal{F}_\downarrow(\mathbf{r})\mathcal{F}_\uparrow(\mathbf{r}'). \quad (2.78)$$

One can visualize the action of this operator either as the associated pseudospin flips of two electrons in opposite layers at distant positions, or as the

exchange of the real-space positions of these two particles. This operator can be easily calculated in our Monte-Carlo simulations carrying out this kind of operation on pairs of electrons.

For the 111-state, we have  $\langle 111|\mathcal{S}|111\rangle = -1$ . Conversely,  $\langle \text{CFL}|\mathcal{S}|\text{CFL}\rangle$  yields a very small value provided that the distance  $|\mathbf{r} - \mathbf{r}'|$  is chosen to be large. Any finite geometry imposes a constraint on the limit in (2.78), but numerics confirm that  $\langle \text{CFL}|\mathcal{S}|\text{CFL}\rangle \approx 0$ , in the order of  $10^{-5}$ . Upon calculating  $\mathcal{S}$  for mixed fluid states with filled CF-shells, we found that there is a monotonous relation  $\mathcal{S}(N_{\text{B}}/N_1)$  between the order parameter and the fraction of electrons that have undergone a CB-like flux attachment. Furthermore, results for several different system sizes collapse on a single curve, such that we may estimate finite size effects to be small. We conclude that  $\mathcal{S}$  is a suitable order parameter for the transition between the CFL and the 111-state.

While it is true that increasing the fraction of CB's yields a larger order parameter, this is not the only factor influencing  $\mathcal{S}$ . In particular, nonzero values of the order parameter can be obtained for bilayer states within the paired CF picture, i.e. *without* composite bosons.

Let us discuss this feature in detail by commenting on the dependence  $\mathcal{S}(d)$  extracted from our Monte Carlo simulations by monitoring this order parameter for each of our trial states. We attribute the value obtained for the best trial state at a given  $d$  to represent the value  $\mathcal{S}(d)$ . The data in Fig. 2.6 was obtained following this procedure. Error bars are established by taking into account the values of  $\mathcal{S}$  for trial states, the energies of which are within the range of Monte Carlo errors from the best trial state.

Interestingly the order parameter  $\mathcal{S}$  is non-zero at layer separations  $d$  where we find good trial states without adding composite bosons. For instance, for the system of  $N = 5 + 5$  particles, p-wave paired CF states yield a maximum  $\mathcal{S}$  of about 0.4, 40% the value of the CB condensate. However, for bigger systems we found that this maximal value is smaller. For instance, for  $N = 7 + 7$  its maximal value is no more than 28%. A naïve linear extrapolation over  $N^{-1}$  of these two values would predict that the order parameter for paired states vanishes in the thermodynamic limit. It is also evident that CB's are needed up to higher layer separation  $d^{\text{CB}}$  in order to get good trial states in the larger system. For the system with  $N = 7 + 7$  electrons, we find good paired CF states above  $d^{\text{CB}} \approx 1.1\ell_0$ , whereas  $d^{\text{CB}} \approx 0.9\ell_0$  for  $N = 5 + 5$ .

The question then arises whether the paired CF state still has the symmetry of the 111-state in the thermodynamic limit. Given that the maximal value of the 111 order parameter decreases with  $N$ , it seems that a non-zero  $\langle \mathcal{S} \rangle$  for paired CF states is a vestige of finite size systems. Presumably, the

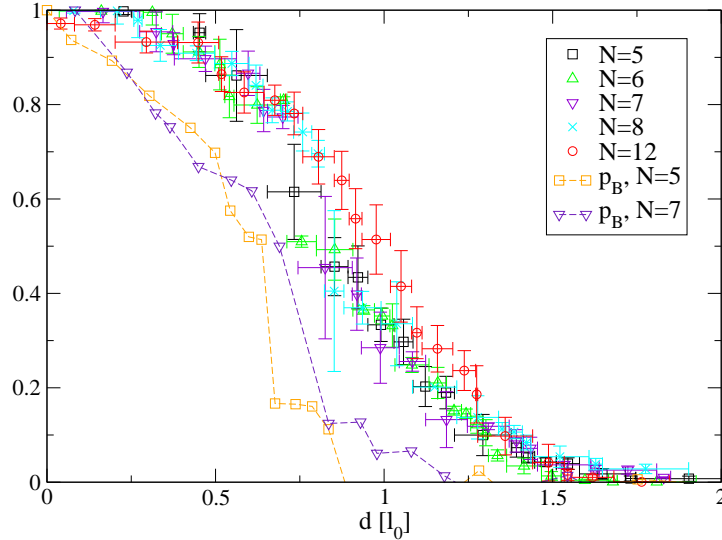


Figure 2.6: A plot of the order parameter  $\mathcal{S}(d)$  for different system sizes according to the legend (symbols with error bars) and the fraction of bosons  $p_B$  as obtained from Eq. 2.74 (dashed lines). Data of system sizes  $N = 8$  and  $N = 12$  is based on a restricted set of MC calculations and we have no according exact calculations available for comparison.

order parameter should vanish in the thermodynamic limit for any state not involving composite bosons. The reason is that interlayer coherence is required for this order parameter to be non-zero. However, it is not clear how the pairing we describe would achieve this. With these precautions, our theory supports a second-order transition between the CB condensate and the paired CF state, as can be argued from the smooth variation of the order parameter. Furthermore, for all system sizes that we examined, we found approximately the same behavior of  $\mathcal{S}(d)$ , which approaches zero at approximately  $d \approx 1.5\ell_0$ . Again, we interpreted the smooth tail of  $\mathcal{S}(d)$  found above this value of the layer separation as finite size effects and presume that the order parameter should approach zero at a precise value  $d_c$  in the thermodynamic limit.

Assuming that the paired CF phase is distinct from the CB phase according to the above hypotheses, there should be a second order parameter that is particular to the paired CF phase. In analogy with BCS theory, one would expect an order parameter of the form  $\Psi_{\uparrow}(r)\Psi_{\downarrow}(r)$ . However, here we consider pairing of composite fermions. The important difference is the Jastrow factors attached to the electrons that make up for the additional



phase factors. Consequently, a guess for the order parameter proceeds by unwrapping these phases such that

$$\Psi_{\uparrow}(z)\Psi_{\downarrow}(z)\exp^{-i\arg[\prod_k(z-z_k)^2]}\exp^{-i\arg[\prod_k(w-w_k)^2]}, \quad (2.79)$$

where  $z$  and  $w$  encode the position  $r$  in the upper and lower layers respectively. However, pairing is in the  $p$ -wave channel and the order parameter is expected to have a phase that forces it to be zero at coinciding points  $z = w$ . A non-zero value might be obtained upon examining operators that are non-diagonal, i.e.  $z \neq w$ . Though, in such cases the order parameter continues to have a phase that makes numerical calculations difficult: averaging a vector rotating arbitrarily in the plane for different configurations gives a vanishing result. One must guess the proper phase of the order parameter, where  $\exp[i\arg(z-w)]$  seems to be the most natural behavior. Thus, we obtain

$$\wp(z, w) = e^{-i\arg(z-w)}\Psi_{\uparrow}(z)\Psi_{\downarrow}(w)e^{-i\arg[\prod_k(z-z_k)^2]}e^{-i\arg[\prod_k(w-w_k)^2]}. \quad (2.80)$$

However, this still needs to be modified since our numerics require an order parameter that conserves the particle number. In principle, one can multiply (2.80) by its hermitian conjugate invoking different positions  $\wp^{\dagger}(z', w')$  to obtain a candidate for an order parameter

$$\mathcal{P} = \wp(z, w)\wp^{\dagger}(z', w'). \quad (2.81)$$

This is a rather complicated operator since it is a function of the four positions  $z$ ,  $w$ ,  $z'$  and  $w'$ . We have not yet succeeded to show that this order parameter, or rather its equivalent on the sphere, has a non-zero expectation value for the paired CF states. On the sphere, an additional difficulty arises as a magnetic monopole charge in the center of the sphere implies the presence of a Dirac string, i.e. a singular point where a flux tube penetrates the surface of the sphere in order to achieve magnetic flux conservation. This then results in Aharonov-Bohm phases for wrapping around this point, which must be taken into account to define  $\mathcal{P}$  properly.

Finally, it is questionable whether the paired CF phase extends out to some finite layer separation  $d_{\text{paired}}$ , where the composite fermion liquid becomes the exact ground state. Alternatively, this could happen only for  $d \rightarrow \infty$ . Almost certainly the nature of such a transition would be a smooth crossover if occurring at finite  $d_{\text{paired}}$ , since the CFL can be formally represented as a paired CF state. However, it remains a possibility that there is a true transition to a CF liquid state at a different shift. This question could be most easily studied on the torus, where all states have the same shift but

different ground state degeneracies. In this context, recent calculations on the torus have not indicated any particularities regarding the ground state degeneracy [Shibata and Yoshioka (2006)].

#### 2.2.4 Conclusion

In conclusion, we have derived a composite particle description for the ground state wave function of the quantum Hall bilayer system at filling factor  $\nu = \frac{1}{2} + \frac{1}{2}$ . This ground state is properly described by interlayer p-wave pairing of composite fermions above a layer separation  $d^{\text{CB}}$ . More precisely, this pairing instability occurs in the positive  $p$ -wave or  $p_x + ip_y$  channel. Below  $d^{\text{CB}}$ , a mixed fluid phase with coexistence of composite bosons and composite fermions develops, and CB's successively replace paired CF's upon diminishing  $d$ . We should emphasize that  $p$ -wave pairing is the only pairing channel that is consistent with such a coexistence.

The precision of the composite particle description has the same order of magnitude as other significantly good trial states in the literature of the quantum Hall effect, notably as the Laughlin-state at  $\nu = \frac{1}{3}$ . The agreement between the trial states and the exact solution was checked using the correlation functions and was found to be similarly in good agreement.

We analyzed the order parameter of the broken U(1) symmetry of the 111-state, and found it to approach zero smoothly at values close to  $d = 1.5\ell_0$  with a tail attributed to finite size effects. We also found it to be non-zero for the pure paired-CF-phase. Though we cannot exclude the contrary with absolute certainty, we believe that this is a phenomenon occurring only in finite size systems. From the shape of the order parameter, we conclude that the phase transition between the 111-state and the paired CF phase is of second order. The precise value of the layer separation where this transition occurs cannot be inferred from our numerics, since the order parameter continues to be non-zero at all layer separations in small systems.

We have also found that correlations between the two layers persist up to layer separations as large as  $3\ell_0$ . It is intriguing if such correlations might still result in drag currents. If the regime of the paired CF phase is limited, a putative transition to the pure CFL phase occurs at very large layer separation. However, given that the CFL can be regarded as a special case of the paired phase, it seems just as likely that this transition occurs only at infinite layer separation.

In the course of this study, we have not explicitly discussed the transport properties of the quantum Hall bilayer system. Two marked phenomena are observed in the bilayer systems: a resonantly enhanced tunneling current between the layers and superfluid counterflow of current. Both occur only in the incompressible low  $d$  phase and can be explained by the presence of

composite bosons. One then argues that superfluid counterflow derives from coherent transport of CB's or charge-neutral interlayer excitons. As these objects have no charge, they also do not couple to the magnetic field and generate no Hall voltage [Eisenstein and MacDonald (2004)]. Furthermore, CB's favor the tunneling between the layers since the electron forming this composite object carries with it a hole in the opposite layer with it, into which it can easily tunnel. Secondly, once a charge transfer has been completed, charge needs to be transported outwards in the layer the electron tunneled into, and inwards in the layer that it has left in order to equilibrate the charge density in both layers. Such an oppositely directed charge transport is again facilitated by the presence of CB's, which have a superfluid mode in this transport channel [Eisenstein (2003)].

The above reasoning is based on considerations regarding the CB condensate. However, our results exclude that the regime of a pure CB condensate is reached in the experiments, given that we find an admixture of paired CF to the 111-state already at very small layer separations  $d$ . In regard to the correlation functions, this is manifest by a less pronounced correlation hole in the interlayer correlation function  $h_{\uparrow\downarrow}$ . Nonetheless, even a fraction of coherent composite bosons is expected to feature the qualitative transport properties of the CB condensate [Simon *et al.* (2003)].

It would be desirable to analyze the transport properties of the paired CF phase in more detail. While we can assure that CF pairing yields a considerable condensation energy, we have not studied the magnitude of the gap of elementary excitations. Pair breaking is a known method for obtaining low-lying neutral excitations. Appropriate trial wave functions can be found in Greiter *et al.* (1992), however, these require an explicit antisymmetrization operation and would be difficult to study numerically. Obtaining these gaps would provide information about the critical temperatures at which the paired phase can exist in a clean system. However, both disorder and layer density imbalance are expected to act as pair breaking agents and could provoke a collapse of the paired phase [Kim *et al.* (2001)]. It would also be interesting to study the transport properties of this paired phase in more detail. For example, one might ask whether this phase could feature coherent transport of CF pairs to generate superfluid co-flow, in contrast to the counter-flow obtained from interlayer excitons.

## 2.3 Paired Hall states in the single layer

In the previous section, we have shown how an accurate description of the ground state wave functions for the quantum Hall bilayer system at total filling one can be achieved by invoking the concept of composite particles. BCS-like pairing of composite fermions across the layers forming Cooper pairs ( $\mathbf{k} \uparrow; -\mathbf{k} \downarrow$ ) was essential for that description. However, the question of whether paired states are at the origin of even denominator states in the single layer has been of long-standing interest [Greiter *et al.* (1991); Moore and Read (1991)].

Though studies of the Chern-Simons theory at half-filling have provided insight into the quantum state at  $\nu = 1/2$  [Halperin *et al.* (1993); Milovanovic and Read (1996); Fradkin *et al.* (1998)], the heuristic argument that led Greiter *et al.* to propose a paired state at half-filling represents a good introduction to the subject matter. Their reasoning was that in order to explain the existence of incompressible FQHE states, one could start from a compressible state and consider an adiabatic process in which homogeneous flux density is slowly traded for statistical flux localized on the particles. Provided that the interactions between particles are such that a gap that is initially present does not close along the line of this process, the endpoint of this evolution will be the ground state of the system. The total changes in magnetic field and the statistical angle are related by:

$$\Delta \frac{\theta}{\pi} = \Delta \frac{1}{\nu}. \quad (2.82)$$

We recognize the close relationship between this idea and the philosophy of Chern-Simons theories where flux is attached to the particles in a singular gauge transform to change the statistics, e.g. from fermionic to bosonic by the attachment of a full flux quantum to each particle. However, Greiter *et al.* have taken advantage of the existence of intermediate statistics that are equally well-defined in two dimensions.

Excluding configurations with particles at coinciding coordinate positions, the worldlines of electrons in the plane may undergo non-trivial winding around each other and provide a realization of the braid group [Leinaas and Myrheim (1977); Goldin *et al.* (1981)]. Unlike *Fermions* and *Bosons* which cause the wave function to pick up a phase of  $\pi$  and 0 respectively for the exchange of two particles, *anyons* are characterized by *any* intermediate statistical angle  $\theta$ , leading to many particle wave functions with a non-trivial monodromy (see Chapter 3).

It is interesting to consider free fermions in zero magnetic field  $\theta = \pi$ ,  $B = 0$  as the starting point for this adiabatic process, which has a pairing

instability even for arbitrarily weak attractive interactions [Cooper (1956)]. If we call  $\pi\epsilon$  the deviation of the statistical angle from the value of fermions, we obtain  $\theta = \pi(1 + \epsilon)$ , and  $B = ne\Phi_0$ . The resulting filling factors attain the points  $\epsilon = 1 \Rightarrow \nu = 1$  (bosons) and finally  $\epsilon = 2 \Rightarrow \nu = 1/2$  (fermions), which are identified as candidates for paired Hall states.

The important question remains of why there would be an effective attractive force that causes a pairing instability in the first place. Greiter *et al.* (1992) argue that a suitable interaction arises from the statistical interaction. Taking into account the Aharonov-Bohm interaction between statistical fluxes, they show in a perturbative calculation for small  $\epsilon$  that there is an attractive velocity-dependent two-body interaction. Starting from the Hamiltonian of free fermions

$$H = \frac{1}{2m} \int d^2r \Psi^\dagger(r) [\hat{p} + a(r)]^2 \Psi(r), \quad (2.83)$$

where particles couple to the vector potential  $a(r)$  resulting from the Aharonov-Bohm interaction of the statistical fluxes and the compensating background magnetic field

$$a(r) = \epsilon \int d^2r' \frac{\hat{z} \times (r - r')}{|r - r'|^2} \{\Psi^\dagger(r') \Psi(r') - \bar{\rho}\}, \quad (2.84)$$

the following two-body interaction can be derived, neglecting second order terms in  $\epsilon$  such that

$$H_{\text{int}} \sim \epsilon \frac{(v \times r) \cdot \hat{z}}{|r|^2}. \quad (2.85)$$

Rewriting the Hamiltonian in Fourier space, this interaction becomes

$$H_{\text{int}} = \sum_{k, k'} V_{kk'} c_{k'}^\dagger c_{-k'}^\dagger c_{-k} c_k, \quad (2.86)$$

with

$$V_{kk'} = 2\pi i \frac{\epsilon}{m} \frac{(k \times k') \cdot \hat{z}}{|k - k'|^2}. \quad (2.87)$$

Treating the problem in the BCS approach, defining the gap parameter  $\Delta_k$ , one is lead to the self-consistency equation

$$\Delta_k = -\frac{1}{2} \sum_{k'} \frac{\Delta_{k'}}{E_{k'}} V_{kk'}, \quad (2.88)$$

where  $E_k = \sqrt{|\Delta_k|^2 + (\epsilon_k - \epsilon_F)^2}$  is the quasi-particle excitation energy. With  $V_{kk'}$  in (2.86) being imaginary, it is immediately clear that there can

be no real solution to the self-consistency relation (2.88). Rather, making the complex Ansatz

$$\Delta_k = |\Delta_k| e^{il \arg(k)}, \quad (2.89)$$

corresponding to  $l$ -wave pairing, Greiter *et al.* (1992) show that the largest gap is expected in the  $p$ -wave channel, i.e. for  $l = 1$ . Whereas this arguments suggests a state with  $p$ -wave pairing at half-filling, this point is out of reach for a perturbative calculation.

A more rigorous approach based upon a Chern-Simons singular gauge transformation considered the effective interactions mediated by the fluctuations of the gauge field [citeHLR]. However, it is questionable to what extent these calculations were well controlled. In this section, we shall approach the discussion of paired states at half-filling via ground state wave functions in the lowest Landau level, exploiting the knowledge gained regarding paired states in the double layer.

### 2.3.1 Paired wave functions

In section 2.2.2.2, we discussed how a paired state can be described as the determinant of a pair wave function  $g(r, r')$  for two component fermions (spin for BCS wave functions, pseudospin for the bilayer case). Here, we search for a suitable wave function for electrons in a single layer. At half-filling, these electrons are subject to a high magnetic field, and we assume them to be entirely spin-polarized (as was supposed for the individual layers of the bilayer system). For scalar fermions, pairing is properly described by the Pfaffian  $\mathfrak{Pf}$  of a pair wave function, the antisymmetrized sum of all possible pairings.<sup>5</sup> Adding appropriate Jastrow factors to obtain a suitable trial wave function for electrons at half-filling, we obtain

$$\Psi_{1/2} = \mathfrak{Pf} [g(z_i - z_j)] \prod_{i < j} (z_i - z_j)^2, \quad (2.90)$$

without writing gaussian factors explicitly. Here,  $g$  must be an odd function. Naturally, the choice of the pair wave function  $g$  determines the nature of the paired state (2.90).

Intuitively, the pair wave function  $g(z)$  is related to the probability of two electrons being at a distance  $|z|$ , though the Jastrow factors modify this. In order to describe a bound state for the pairs, Greiter *et al.* (1991) have argued that  $g$  must be a monotonously decreasing function of the separation.

---

<sup>5</sup>For pairing between two distinguishable species, the Pfaffian is precisely equal to the determinant, cf. Eq. 2.55a. Appendix B.4 gives a brief review of some of the properties of the Pfaffian.

Given that the final wave function is required to be in the lowest Landau level, the choice is restricted to analytic functions, though simple poles may be permitted as long as they are canceled by corresponding terms in the Jastrow factor. The simplest choice that satisfies these criteria is

$$g(z) = 1/z. \quad (2.91)$$

The resulting wave-function is simply known as the Moore-Read Pfaffian state [Moore and Read (1991)]. Greiter *et al.* (1992) argue that this is essentially the only choice.<sup>6</sup> As the final wave function must not have any singularities, no higher odd negative power of  $z$  is possible, such that the general form of the pair wave function can only be

$$g(z) = \frac{1}{z} + p(z), \quad (2.92)$$

where  $p$  is an odd polynomial of degree  $k$ . However, in the thermodynamic limit, adding any polynomial  $p(z)$  of fixed degree  $k$  is irrelevant. To understand why  $p(z)$  is irrelevant, first note that the singular and the non-singular components lead to a totally antisymmetric wave function via two different routes. Equation 2.90 can be decomposed as the symmetric Jastrow factor  $\prod (z_i - z_j)^2$  times the antisymmetric Pfaffian  $\mathfrak{Pf}[g(z_i - z_j)]$ . A pair wave function  $1/z$  leads to a totally antisymmetric wave function by eliminating zeros of the Jastrow factor that it multiplies. However, this is not the case for any harmonic polynomial  $p(z)$ . On the contrary,  $\mathfrak{Pf}[p(z_i - z_j)]$  needs to provide an antisymmetric polynomial on its own. It is known that the lowest degree homogeneous polynomial in  $N$  variables is the Vandermonde determinant  $\prod_{i < j} (z_i - z_j)$ , which is of degree  $d_V = N(N - 1)/2$ . However, the Pfaffian  $\mathfrak{Pf}[p(z_i - z_j)]$  is only of fixed degree  $d_P = kN/2$ . Thus,  $d_P/d_V \rightarrow 0$  and the Pfaffian is bound to vanish in the thermodynamic limit. Similarly, considering the sum of both pair wave functions, one finds that the singular component dominates the majority of terms in the thermodynamic limit.

We concur with Greiter *et al.* (1992), that  $g(z) = 1/z$  is essentially the only *function* that may serve as a pair wave function. We have further observed that its dominance is founded on a particular method for achieving the antisymmetry of the resulting wave function, notably by eliminating zeros of the Jastrow factor. However, we determined that we may construct an *operator* as a pair wave function which may serve to generate wave functions for different paired Hall states.

---

<sup>6</sup>It is also shown that this solution is obtained as the adiabatic extrapolation of the exact ground state of a BCS superconductor with an attractive delta-function potential.

### 2.3.2 Pairing of Composite Fermions

With the development of wave functions for interlayer pairing of composite fermions in the quantum Hall bilayer system (2.55), we introduced a general expression built upon composite fermion orbitals. Analogous to the procedure leading to this wave function, we may express the pair wave function for a single-layer paired state as an expansion of a set of basis functions  $\phi_{\mathbf{k}}$ , however, we need to antisymmetrize the result explicitly here, as the Pfaffian is only defined for antisymmetric matrices. We write

$$g^{\text{CF}}(z_i, z_j) = g^{\text{CF}}(z_i - z_j) = \sum_{\mathbf{k}} g_{\mathbf{k}} \phi_{\mathbf{k}}(z_i) \phi_{-\mathbf{k}}(z_j), \quad (2.93)$$

where  $g_{\mathbf{k}}$  is required to be an odd function to assure that  $g(z)$  is antisymmetric, and in particular  $g(z_i, z_i) \equiv 0$ . The full wave function at half-filling once more requires projection to the LLL, where

$$\Psi_{1/2}^{\text{CF}} = \mathcal{P} \left\{ \mathfrak{P}f [g^{\text{CF}}(z_i - z_j)] \prod_{i < j} (z_i - z_j)^2 \right\}. \quad (2.94)$$

In order to proceed with the projection, we follow the procedure proposed by Jain and Kamilla (1997a) by multiplying the Jastrow factors inside the Pfaffian and projecting matrix element by matrix element. Here, the following identity regarding the Pfaffian is helpful:

$$\mathfrak{P}f [M]^2 = \det[M]. \quad (2.95)$$

This identity reflects the fact that the Pfaffian halves the number of factors in each term with respect to the determinant. Inversely, multiplying the Jastrow factors from (2.93) inside the matrix elements  $M_{ij}$  yields twice as many terms as for a determinant. Multiplying the two resulting one-particle Jastrow factors  $J_j = \prod_{k \neq j} (z_j - z_k)$  to lines and columns of  $M_{ij}$  respectively, it follows that

$$\Psi_{1/2}^{\text{CF}} = \mathcal{P} \{ \mathfrak{P}f [J_i J_j g^{\text{CF}}(z_i - z_j)] \}. \quad (2.96)$$

As in the previous cases, there is precisely one partial Jastrow factor  $J_i$  per basis function  $\phi$ . We may then project all entries of the matrix individually, and in two stages:

$$\mathcal{P} J_i \phi(z_i, \bar{z}_i) J_j \phi(z_j, \bar{z}_j) \sim \mathcal{P} \{ J_i \phi(z_i, \bar{z}_i) \} \mathcal{P} \{ J_j \phi(z_j, \bar{z}_j) \}. \quad (2.97)$$

Denoting the projected orbitals as  $\tilde{\phi}$  according to (2.46), we may express the paired composite fermion wave function as

$$\Psi_{1/2}^{\text{CF}} = \left\{ \mathfrak{P}f \left[ \sum_{\mathbf{k}} g_{\mathbf{k}} \tilde{\phi}_{\mathbf{k}} \tilde{\phi}_{-\mathbf{k}} \right] \prod_{i < j} (z_i - z_j)^2 \right\}. \quad (2.98)$$



Similarly to the bilayer case, this form may be used to describe a variety of paired states, with the pairing channel defined by the short-distance behavior of  $g^{\text{CF}}$  as in (2.56). However, with the motivations cited above, the interesting case is that of negative  $p$ -wave pairing. To attain this case, composite fermion orbitals are required which decrease the total degree of the polynomial by one, precisely as  $1/z$  does. These correspond to composite fermions in negative flux.

As indicated above, (2.98) allows for paired states that are genuinely different from the Moore-Read Pfaffian. The argument given by Greiter *et al.* (1992) that  $g(z) = 1/z$  is essentially the only pair wave function generating LLL wave functions is betrayed by the fact that  $\tilde{\phi}$  are operators.

### 2.3.3 Composite fermions in negative flux

In order to obtain composite fermion wave functions, we need to generalize the derivation of composite fermions in positive flux by Jain and Kamilla (1997a). Whereas composite fermions at positive flux describe the FQHE fractions of the main series  $\nu = p/(2mp + 1)$ , for  $p$  positive, the composite fermions at negative flux formally correspond to the case  $p$  negative. For  ${}^2\text{CF}$  (i.e.  $m = 1$ ), this generates the series of states that are particle-hole conjugates of the respective  $p = 1$  series, which is converging to  $\nu = 1/2$  from above. The first members of this series are  $\nu = \frac{2}{3}, \frac{3}{5}, \frac{4}{7}, \frac{5}{9}$ , etc. It can be shown using particle-hole symmetry in the LLL that the trial wave functions derived from composite fermion wave functions in negative effective flux yield trial wave functions that are about as accurate as those in positive flux. These results are published elsewhere [Möller and Simon (2005)], where the application of these trial wave functions to the series of  $m = 2$ , corresponding to filling fractions around  $\nu = \frac{1}{4}$  is discussed. Here, we restrict the discussion to a short review of the construction of the projected CF orbitals.

With the goal of making comparisons between paired trial states and the results from exact diagonalization, restricted to a limited number of particles, we focus upon the sphere.

The starting point for the composite fermion trial wave functions [Jain and Kamilla (1997a)] are the single particle eigenfunctions of the quantum mechanical problem of a particle in a magnetic monopole field on a sphere. Our nomenclature uses spherical coordinates with the azimuth  $\theta$  ranging from 0 to  $\pi$ , and the longitude  $\phi$  ranging from 0 to  $2\pi$ . The monopole harmonics are given by [Wu and Yang (1976)]

$$Y_{n,m}^q(\Omega) = 2^m M_{q,n,m} (1-x)^{\alpha/2} (1+x)^{\beta/2} P_g^{\alpha,\beta}(x) e^{im\phi} \quad (2.99)$$

with  $\alpha = -q - m$ ,  $\beta = q - m$ ,  $g = |q| + n + m$ ,  $x = \cos \theta$ ,

$$M_{q,n,m} = \sqrt{\frac{2|q| + 2n + 1}{4\pi} \frac{(|q| + n - m)! (|q| + n + m)!}{n! (2|q| + n)!}} \quad (2.100)$$

where  $P_g^{\alpha,\beta}(x)$  are the Jacobi polynomials. This monopole harmonic represents an eigenstate of a particle on a sphere in a radial magnetic field with  $2q$  flux quanta penetrating the sphere, where a positive sign refers to outwards pointing flux. Here, the angular momentum of the eigenstate is  $l = |q| + n$  and the  $z$  component of the angular momentum is  $m \in \{-l, \dots, l\}$ . Furthermore,  $n$  is the positive integer LL index  $n = 0, 1, 2$ , etc. The above expression assumes the Haldane gauge [Haldane (1983)], where the singularities of the vector potential are chosen to be located symmetrically on both the north- and southpoles of the sphere. We focus on the case where  $q < 0$ , since the  $q > 0$  case has already been discussed in detail by Jain and Kamilla (1997a). For our purposes, we assume  $q < 0$ . Expanding the Jacobi polynomials in terms of the spinor coordinates  $u = \cos(\theta/2)e^{-i\phi/2}$  and  $v = \sin(\theta/2)e^{i\phi/2}$ , one obtains

$$Y_{n,m}^{q<0}(\Omega) = (-1)^n M_{q,n,m} (u^*)^{-q+m} (v^*)^{-q-m} \times \sum_{s=0}^n (-1)^s \binom{n}{s} \binom{2|q| + n}{|q| + m + s} (u^* u)^s (v^* v)^{n-s}. \quad (2.101)$$

This expression can equally be obtained from the relationship for complex conjugation of the monopole harmonics [Wu and Yang (1977)] if one corrects Kamilla's formula by replacing  $q$  by  $|q|$  as in (2.101). We can then use the  $Y_{n,m}^q$  as single particle wave functions, written as  $\phi_i$  in the generic expressions, where no geometry is specified, and composite fermionize by attaching Jastrow factors. As discussed previously, many particle composite fermion trial wave functions can be constructed from a basis of projected single particle orbitals defined by  $\tilde{\phi}_i(u_j, v_j) = (J_j^p)^{-1} \mathcal{P}[\phi_i(u_j, v_j, u_j^*, v_j^*) J_j^p]$ . Note that in the spherical geometry, the Jastrow factor becomes

$$J_j = \prod_{k \neq j} (u_k v_j - u_j v_k). \quad (2.102)$$

We added a power  $p$  here, allowing one to consider the attachment of several flux pairs to each composite fermion. Discussion of the details for the projection  $\mathcal{P}$  ensues.

First, we remark that the Jastrow factor  $J_i^p$  is an LLL function, with  $q' = p(N - 1)$  zeros in  $u_i$ , i.e. it is an LLL wave function for flux  $q' > 0$ .

Since  $N$  is generally a large number, we can assume  $q' \gg |q|$ . Therefore, the resulting wave function must be a valid wave function for a total number of flux  $Q = q + q' > 0$ . Secondly, since projection is a linear operation, we may consider the action of projection on each of the basis states  $Y_{0,m'}^{q'}$  separately, by expanding  $J_i^p$  in this basis. In general, multiplication by a basis state  $Y_{n,m}^q$  followed by projection can be described as a linear operator termed hereafter as  $\mathfrak{Y}_{q,n,m}^{q'}$ , where

$$\mathcal{P}Y_{n,m}^q Y_{0,m'}^{q'} = \mathfrak{Y}_{q,n,m}^{q'} Y_{0,m'}^{q'}. \quad (2.103)$$

Since we know the entire basis of the subspace upon which we project, specifically the LLL for flux  $Q$  with states  $|M\rangle$ , and  $|M| \leq Q$ , the projection operator is  $\sum_M |M\rangle\langle M|$ . Below we show how this leads to an expression for  $\mathfrak{Y}_{q,n,m}^{q'}$  as a differential operator in the coordinate representation, in which (2.103) becomes

$$\begin{aligned} \sum_{M=-Q}^Q Y_{0,M}^Q(\Omega) \int d\Omega' Y_{0,M}^{Q*}(\Omega') Y_{n,m}^q(\Omega') Y_{0,m'}^{q'}(\Omega') \\ = \mathfrak{Y}_{q,n,m}^{q'} Y_{0,m'}^{q'}(\Omega). \end{aligned} \quad (2.104)$$

Integration over the longitudinal angle  $\phi$  determines one nonzero scalar product for  $M = m + m'$ , and the one remaining integral over the azimuthal angle  $\theta$  yields a well-known binomial coefficient. Simplifying the normalization factors of  $Y_{0,m'}^{q'}$  on both sides, we obtain:

$$\begin{aligned} (-1)^n M_{q,n,m} \sum_s (-1)^s \binom{n}{s} \binom{2|q| + n}{|q| + m + s} \\ \times (N_{Q,0,M})^2 4\pi \frac{(q' - m' + s)!(q' + m' + n - s)!}{(2q' + n + 1)!} \\ \times u^{q-m+q'-m'} v^{q+m+q'+m'} = \mathfrak{Y}_{q,n,m}^{q'} u^{q'-m'} v^{q'+m'}. \end{aligned} \quad (2.105)$$

Using the explicit form of the normalization

$$(N_{Q,0,M})^2 = \frac{(2Q + 1)!}{4\pi(Q + M)!(Q - M)!} \quad (2.106)$$

and upon noting that the fractions of factorials that are left in this expression equal those that appear by the multiple derivation of a monomial  $u^k$ , where

$$\left(\frac{\partial}{\partial u}\right)^{s-q+m} u^{q'+m'+s} = \frac{(s + q' + m')!}{(Q + M)!} u^{Q+M}, \quad (2.107)$$

we may deduce the operator  $\mathfrak{Y}_{q,n,m}^{q'}$  by comparison of both sides, such that

$$\begin{aligned} \mathfrak{Y}_{q,n,m}^{q'} &= \frac{(2Q+1)!}{(2q'+n+1)!} (-1)^n M_{q,n,m} \times \\ &\quad \sum_{s=0}^n (-1)^s \binom{n}{s} \binom{2|q|+n}{|q|+m+s} \times \\ &\quad \left( \frac{\partial}{\partial u} \right)^{|q|+m+s} u^s \left( \frac{\partial}{\partial v} \right)^{|q|-m+n-s} v^{n-s}. \end{aligned} \quad (2.108)$$

Formally, replacing  $\tilde{\phi}$  with this operator in (2.98) yields a pair wave function with an operator-value that generates paired states fundamentally differing from the Moore-Read state.

The expression (2.108) parallels the known fact that on the plane the projection to the LLL is achieved by moving all  $\bar{z}$ 's to the far left and replacing them with derivatives according to

$$\bar{z} \rightarrow -2 \frac{\partial}{\partial z}. \quad (2.109)$$

On the sphere, we need to perform the same procedure with all occurrences of  $u^*$ 's and  $v^*$ 's, and replace them according to

$$u^* \rightarrow \frac{\partial}{\partial u}, \text{ and } v^* \rightarrow \frac{\partial}{\partial v}. \quad (2.110)$$

However, performing the projection explicitly yields an additional weight factor  $\frac{(2Q+1)!}{(2q'+n+1)!}$  for the different CF Landau levels after projection. When using the composite fermion orbitals for the construction of paired wave functions (2.98), a normalization amounts to a redefinition of  $g_{\mathbf{k}}$ .

It is practical to obtain a form of (2.108) with the derivatives moved to the extreme right, which may be calculated using a straightforward application of the Leibniz rule for multiple derivatives in both  $u$  and  $v$ :

$$\left( \frac{\partial}{\partial v} \right)^\beta v^\gamma = \sum_{\alpha=0}^{\beta} \frac{\beta!}{\alpha!} \binom{\gamma}{\beta-\alpha} v^{\gamma-\beta-\alpha} \left( \frac{\partial}{\partial v} \right)^\alpha. \quad (2.111)$$

This yields a triple sum with the inner summation ranges being dependent on the outer summation index  $s$ . One finds that the summation ranges can be made independent of  $s$  since the summand becomes zero outside of the given intervals. As such, the sum over  $s$  may be evaluated using

$$\sum_{s=0}^n (-1)^s \binom{n-\alpha-\alpha'}{s-\alpha} = (-1)^\alpha \delta_{n,\alpha+\alpha'}. \quad (2.112)$$

Since the result yields a Kronecker delta, one of the remaining sums becomes trivial. After shifting the remaining summation index, the final result is revealed to be exactly like (2.108), with the exception that all derivatives are placed at the very right.

The projected composite fermion wave function is simply this operator applied to the single particle Jastrow factor:

$$Y_{n,m}^q{}^{CF}(\Omega_i) = \mathfrak{Y}_{q,n,m}^{q'} J_i^p. \quad (2.113)$$

In order to perform numerical calculations with this wave function, we must evaluate the derivatives explicitly. One may use Jain and Kamilla's approach [Jain and Kamilla (1997a)], to commute the derivatives through the Jastrow factors as

$$\left(\frac{\partial}{\partial u_i}\right)^s \left(\frac{\partial}{\partial v_i}\right)^t J_i^p = J_i^p [\hat{U}_i^s \hat{V}_i^t 1] \quad (2.114)$$

with

$$\hat{U}_i = J_i^{-p} \frac{\partial}{\partial u_i} J_i^p, \quad \text{and} \quad \hat{V}_i = J_i^{-p} \frac{\partial}{\partial v_i} J_i^p. \quad (2.115)$$

A many-particle wave function may be constructed out of these projected CF wave functions in the form of a Slater determinant. Then the Jastrow factors can be factored out, obtaining a form which resembles single particle wave functions, on a basis of projected states  $\tilde{Y}_{n,m}^q$  with:

$$\begin{aligned} \tilde{Y}_{n,m}^q(\Omega_i) &= \frac{(2Q+1)!}{(2q'+n+1)!} (-1)^n M_{q,n,m} \times \\ &\quad \sum_{s=0}^n (-1)^s \binom{n}{s} \binom{2|q|+n}{|q|+m+s} \times \\ &\quad u_i^s v_i^{n-s} [\hat{U}_i^{|q|+m+s} \hat{V}_i^{|q|-m+n-s} 1]. \end{aligned} \quad (2.116)$$

This appears to be a single-particle wave function, but there is an implicit dependence of the positions of all other electrons in the system hidden in the operators  $\hat{U}_i$  and  $\hat{V}_i$ . Note that the complexity of this expression increases with the total number of derivatives, given by  $N_\partial^{q<0} = 2|q| + n$ . Thus, CF orbitals at negative flux are computationally heavier for negative  $q$  compared to  $N_\partial^{q>0} = n$  for positive effective flux.

However, we wish to obtain a paired wave function at the shift of the Moore-Read Pfaffian state. In pursuit of this, we need to calculate CF orbitals at  $-1$  quantum effective flux, i.e. there is only one additional derivative to be evaluated.

### 2.3.4 Realizations of pairing in the single layer

So far we have discussed possible trial state wave functions in the LLL that incorporate the idea of paired composite fermions. Since the ground state is ultimately defined by the energetics, it is required to analyze the energy of the presented trial states. Again, this analysis will be based on the comparison of numerical diagonalizations of the Coulomb Hamiltonian,

$$\mathcal{H} = \frac{e^2}{\epsilon_0} \sum_{i < j} \frac{1}{|\mathbf{r}_i - \mathbf{r}_j|}, \quad (2.117)$$

and Monte Carlo simulations of the trial states that are thought to yield an appropriate description of the ground state of this Hamiltonian.

#### 2.3.4.1 Pairing in the second LL

Fractional Hall states in higher Landau levels have already been analyzed in this manner. Upon realizing that the structure of Hilbert spaces belonging to higher LL is precisely identical to the structure of the LLL, the problem can be reformulated in the LLL except with an effective interaction which translates the wave function of electrons relative to their guiding center coordinates in higher Landau levels (assuming no LL mixing, i.e. that entirely filled LL's as well as higher LL's are inert at low temperatures). According to Haldane [chapter in Prange and Girvin (1987)], any two body interaction in a strong magnetic field is entirely characterized by the pseudopotential coefficients  $V_m$  equal to the energy of electron pairs at a given relative angular momentum.

$$V_m^n = \int q dq \tilde{V}_c(q) [L_n(q^2/2)]^2 L_m(q^2) e^{-q^2} \quad (2.118)$$

where  $\tilde{V}_c(q)$  is the Fourier transform of the Coulomb interaction and where the presence of the Laguerre polynomials  $[L_n(q^2/2)]^2$  derives from the motion of electrons relative to their guiding center coordinate in the  $n^{\text{th}}$  Landau level.

In this manner, previous studies [Morf (1998); Rezayi and Haldane (2000)] have analyzed the Moore-Read Pfaffian state at filling factor  $\nu = 5/2$ , i.e. half-filling in the second Landau level (the lowest LL consists of two spin-branches, such that the 2<sup>nd</sup> LL is attained only for  $\nu > 2$ ). In particular, manipulating the pseudopotential coefficient  $V_1$  with respect to the values of the Coulomb interaction in the 2<sup>nd</sup> LL, Rezayi and Haldane (2000) have shown that the Pfaffian may have large overlaps with the exact solution if  $V_1$  is enhanced. The groundstate is particularly sensitive to the first coefficients of the pseudopotential expansion, since they express the short-range part of

the interaction. At the pseudopotentials corresponding to the Coulomb interaction the ground state appears to be a striped phase, however, for a slight increase of  $V_1$  a first-order transition to the paired phase takes place<sup>7</sup> as is concluded from a level crossing in the spectrum. This phase is well described by the Moore-Read Pfaffian, though the overlap with the ground state is considerably larger if this state is additionally particle-hole symmetrized. At even larger  $V_1$ , there is a transition to a composite fermion state. In contrast to the previous phase transition, no level crossing is observed in the ground state, indicating a continuous transition.

We can understand the possibility of a crossover between these two states in terms of the paired wave functions (2.98), since we may choose the pair wave function  $g(z)$  to yield either the MR or CF state. Intermediate states can be realized by choosing superpositions:

$$g(z) = c^{\text{MR}} \frac{1}{z} + g^{\text{CF}}[g_{\mathbf{k}}]. \quad (2.119)$$

Therefore, it seems natural to have a smooth crossover between these two states, corresponding to a continuous variation of the coefficients  $c^{\text{MR}}$  and  $g_{\mathbf{k}}$ .

### 2.3.4.2 Pairing in the LLL

As discussed previously, the physics in the lowest and higher Landau levels are essentially identical and differences are reduced to altered pseudopotential coefficients. In the LLL the  $V_m$  are well inside the CF phase, in accordance with the prevailing theory that  $\nu = \frac{1}{2}$  is described as a composite fermion liquid [see also section 2.2.2.1, Halperin *et al.* (1993)]. However, as the CF phase seems to be continuously connected to the strongly paired Pfaffian, there might be a remainder of weak pairing even in the CFL phase [Rezayi and Haldane (2000)].

Analogous to the representation of the Fermi liquid state via CF pairing in the bilayer, obtained with the choice (2.57) for the parameters  $g_{\mathbf{k}}$ , one obtains the Fermi liquid in the single layer in the paired form (2.98) by choosing the same  $g_{\mathbf{k}}$  as in (2.57). More general choices of the parameters  $g_{\mathbf{k}}$ , which encode the shape of the pair wave function, represent non-trivial pairing. Rather than treating these as individual variational parameters, we have chosen an Ansatz for  $g_{\mathbf{k}}$ , inspired by BCS theory and parametrized by

---

<sup>7</sup>Rezayi and Haldane (2000) show that the system might be driven into this regime when taking into account the finite width of the quantum well.

a single ‘gap’ parameter  $\Delta$ , such that

$$g_{\mathbf{k}} \equiv g_k = \frac{1}{\Delta} \left[ \sqrt{\xi_k^2 + \Delta^2} - \xi_k \right], \quad (2.120)$$

where  $\xi_k = \epsilon_k - \epsilon_F$  is the energy relative to the Fermi surface. For  $\Delta = 0$ , this function provides very large values  $g_k \rightarrow \infty$  for  $k < k_F$  and vanishes above  $k_F$ . Finite values smooth this step function, adding a probability for CF’s to occupy orbitals at higher energy.

### 2.3.4.3 Numerical analysis

In this section, we compare Monte Carlo simulations of paired trial states with respect to exact diagonalizations of the Coulomb Hamiltonian in the LLL performed on the sphere. Following the reasoning of Greiter *et al.* (1992), we focus on the case of negative  $p$ -wave pairing. However, to provide further motivation for this particular choice, we first analyzed the spectra of the Coulomb Hamiltonian at various values of the ‘shift’. The ratio of the number of electrons to the number of flux in the system approaches the filling factor only in the thermodynamic limit. ‘Shift’, defined as

$$N_\phi = \nu^{-1}N - \sigma, \quad (2.121)$$

is the offset  $\sigma$  from the aforementioned ratio in finite systems. This is a signature that may serve to distinguish different quantum states at the same filling factor. It can be obtained by flux count arguments, similar to those presented in section 2.2.2.4. For positive  $p$ -wave pairing  $\sigma = 1$ , negative  $p$ -wave pairing yields  $\sigma = 3$ , and for a simple CFL at zero effective flux one obtains the intermediate value  $\sigma = 2$ .

In Table 2.2, we illustrate data regarding these three values of the shift. Note that for states at CFL and positive  $p$ -wave pairing the ground state is situated at  $L = 0$  only for those states which are simultaneously hierarchy states. On the contrary, for states consistent with negative  $p$ -wave pairing the ground state tends to be at  $L = 0$  for  $N$  even, as expected for a paired state—though there are two exceptions to this rule discussed below. Interestingly,  $p-$  has a very pronounced alternating behavior for odd and even  $N$  states in the excitation energy of the lowest energy eigenstate at  $L = 0$  whereas these values have no such period for the other partial waves.

Let us discuss two particular system sizes with  $\sigma = 3$ : there are two instances,  $N = 10$  and  $N = 16$ , where  $L = 0$  is not the ground state but instead a very low-lying excitation. Our claim is that this is due to the particular shell structure of the composite fermion states. At this shift, CF’s



experience an effective flux of minus one quantum of flux. With respect to the eigenstates on the sphere, we have a degeneracy of shells which is  $d_n = 2n + 2$ , with  $n = 0, 1, 2$ , etc. This yields filled shells at  $N = 6$  and  $N = 12$ , those states which we noted as known candidates of the basic hierarchy states  $\nu = p/(2mp \pm 1)$ . However,  $N = 10$  and  $N = 16$  are special as well if we interpret it in terms of CF's at flux  $-1$ . Let us now consider an analogy to electrons in partially filled atomic shells. Empirically, these electrons favor maximizing both their spin and orbital momentum according to Hund's rule. Applying this rule to the system with 10 particles, we find that 4 of them occupy orbitals in the highest CF shell, which is 6-fold degenerate. The angular momenta of these orbital states are  $m = \pm\frac{1}{2}, \pm\frac{3}{2}$ , and  $\pm\frac{5}{2}$ . Thus the state of highest angular momentum that can be constructed from these orbitals has  $L = \frac{5}{2} + \frac{3}{2} + \frac{1}{2} + (-\frac{1}{2}) = 4$ , the angular momentum of the ground state calculated in the exact diagonalizations. If we apply the same reasoning to  $N = 16$ , we find 4 electrons occupying orbitals in the next higher CF shell with 8-fold degeneracy. The state of maximal angular momentum now has  $L = \frac{7}{2} + \frac{5}{2} + \frac{3}{2} + \frac{1}{2} = 8$ , which again yields the proper ground state momentum.

In resuming the results, we have found that the ground states at  $\nu = \frac{1}{2}$  with shift  $\sigma = 3$  seem to be reasonable candidates for paired states since there is a marked odd-even behavior in the particle number. Furthermore, there is a tendency to form a ground state with zero angular momentum which is not observed in the parallel series with different flux. All these findings point towards a paired state with negative  $p$ -wave pairing.

In order to find out whether pairing of composite fermions actually yields a proper description of the ground state of the Coulomb Hamiltonian in the LLL along the line of the flux-particle relation  $N_\phi = 2N - 3$ , we have compared the results of Monte-Carlo simulations of this series. Naturally, the paired states (2.98) are only defined for even particle numbers  $N$ , which coincide with the cases where the actual ground-state is at  $L = 0$ . The trial states (2.98) yield a state with  $L_z = 0$  by virtue of the pairing of orbitals with  $m$  and  $-m$ . Furthermore, the state is by construction rotationally invariant. We conclude that it also must be an eigenstate of  $L^2$  with eigenvalue 0.

For each given system size  $N = 2N_{\text{pairs}}$ , we simulated a number of states with variations of  $g_k$  in (2.98). More precisely, on the sphere  $g_k$  is given by a series of values—one value  $g_n$  for each CF shell.

We defined the 'composite fermion Fermi liquid state' (CFL) as the primary candidate among our trial states. If  $n_F$  is the index of the highest shell in which there are occupied states when filling up shells successively,

$\sigma$	$N$	$N_\phi$	$E_{\text{GS}}$	$L_{\text{GS}}$	$\Delta$	$L_\Delta$	$E_{L=0} - E_{\text{GS}}$
1	4	7	-2.03091	2	0.07834	0	0.07834
	5	9	-2.50171	1	0.07330	0	0.07330
	6*	11	-3.00240	0	0.07505	4	—
	7	13	-3.42690	2	0.05517	5	0.10033
	8	15	-3.88224	4	0.01397	2	0.06031
	9	17	-4.35418	4	0.02358	1	0.07042
	10	19	-4.82136	4	0.01572	2	0.05452
	11	21	-5.29785	2	0.04576	7	0.06230
	12*	23	-5.79167	6	0.05253	6	—
2	4*	6	-2.20039	0	0.11900	2	—
	5	8	-2.60605	2	0.08221	4	0.10264
	6	10	-3.05539	3	0.01870	1	0.01870
	7	12	-3.52557	3	0.02579	1	0.02579
	8	14	-3.99873	2	0.06174	6	0.07035
	9*	16	-4.49266	0	0.06809	5	—
	10	18	-4.92244	3	0.04571	7	0.07421
	11	20	-5.37522	5	0.01432	3	0.01928
	12	22	-5.83883	6	0.01513	4	0.03190
3	4	5	-2.32174	0	0.03637	2	—
	5	7	-2.75033	1	0.10840	2	N/A
	6*	9	-3.23782	0	0.09353	3	—
	7	11	-3.64279	2	0.07988	3	0.12277
	8	13	-4.09816	0	0.00904	4	—
	9	15	-4.54483	4	0.00061	2	0.13865
	10	17	-5.01781	4	0.00245	0	0.00245
	11	19	-5.49315	2	0.05457	7	0.07963
	12*	21	-5.98461	5	0.05955	0	—
	13	23	-6.41538	3	0.04627	8	0.09613
14	25	-6.86981	0	0.00197	6	—	
15	27	-7.32841	7	0.00957	3	0.06636	
16	29	-7.79153	8	0.00545	6	0.01028	

Table 2.2: Results from exact diagonalizations of the Coulomb Hamiltonian on the sphere for states at shift  $\sigma = 1$ ,  $\sigma = 2$  and  $\sigma = 3$ . The energy of the ground state  $E_{\text{GS}}$ , the angular momentum  $L_{\text{GS}}$  at which it occurs, the energy gap  $\Delta$  of the first neutral excitation and its angular momentum  $L_\Delta$  are given. Finally, the excitation energy of the lowest  $L = 0$  eigenstate of the Hamiltonian, if it is not already the ground state is indicated. All energies are in units of  $e^2/\epsilon\ell_0$ . States that can be identified as hierarchy states associated with filled CF shells are marked with an asterisk \*. Some data were taken from the FQHE database [Regnault (b)]. All data were calculated using the DiagHam libraries [Regnault (a)].

the CFL is characterized by

$$g_n = \begin{cases} \text{const.} & , n \leq n_F \\ 0 & , n > n_F \end{cases} . \quad (2.122)$$

For particle numbers that give filled shells of composite fermions and the above choice of parameters, the trial state (2.98) yields a Slater determinant of CF orbitals. However, for particle numbers in between, the resulting wave function is a non-trivial linear combination of different pairings in the highest shell  $n_F$ .

Furthermore trial states are given by the Ansatz (2.120) with varying gap parameters  $\Delta$ . This Ansatz must be complemented by a relation for the quasiparticle energy  $\epsilon_k$ —this is not an a-priori known quantity for CF's since the kinetic energy in the LLL is quenched and all energy arises from interactions. However, for simplicity we shall suppose a behavior that is analogous to the kinetic energy of a free particle. On the sphere, we have  $\epsilon_l \propto l(l+1)$ . For states with a partially filled highest shell, we take the Fermi energy  $\epsilon_F$  at the value of the closest filled shell configuration. Furthermore, one must choose a cut-off of the sum over orbitals with higher momentum. It has proven sufficient to calculate two supplementary CF shells above  $n_F$ .

As a first result, the energies obtained with Monte Carlo simulations from the trial states described above reproduce the ground state energies very closely, even for the states that are not filled shell states. Though this is an achievement in its own right, the question as to whether non-trivial pairing is relevant for the LLL at half-filling cannot be answered from the results of the trial state energies: the energies of the CFL (or  $\Delta = 0$ ) differ from those with finite  $\Delta$  by an amount that is, at most, comparable to the statistical error of Monte-Carlo simulations with  $10^7$  samples.

Therefore, we have resorted to comparisons of the respective correlation functions, which represent a more powerful means for comparing trial states with the exact solution (see section 2.2.3.2). When analyzing the correlation functions, it becomes clear why the CFL and the paired CF states exhibit almost the same energy: the short-distance behavior of the resulting correlation functions is identical. An example for this statement is shown in Fig. 2.7, where we show the correlation functions of the Pfaffian, the CFL as defined above, and the paired state with the  $\Delta$  that gives the best fit to the exact solution. The displayed system size,  $N = 14$ , was chosen as the largest model system in which we found the ground state at  $L = 0$  in exact diagonalizations—larger systems than  $N = 16$  being inaccessible for numerical purposes.

The general shape of the correlation function can be divided into two regions. The short-distance behavior is characterized by a strong correlation

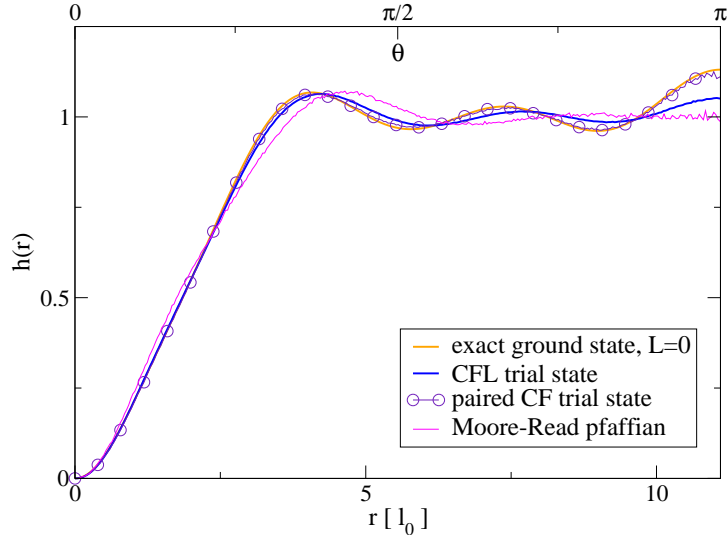


Figure 2.7: Correlation functions for  $N = 14$  electrons on the sphere at  $\nu = 1/2$ —this is the largest system for which we found the exact ground state at  $L = 0$  among those systems accessible to exact diagonalization. We compare the ground state of the Coulomb Hamiltonian to three trial state correlation functions: the Moore-Read Pfaffian, the CFL (2.122) and the paired state with  $\Delta = 0.1$  ( $n_F = 3$ ).

hole that extends to about  $r_{\text{th}} = 4\ell_0$  and a long-distance regime that exhibits oscillations around the asymptotic value for  $r > r_{\text{th}}$ .

As a side note regarding the short-distance behavior, the Moore-Read Pfaffian state exhibits a slightly less pronounced correlation hole. Accordingly, it is irrelevant for the description of  $\nu = 1/2$  and yields considerably higher trial state energies. In the second LL, the situation is inverted and the Pfaffian actually becomes favorable since it takes advantage of the effective interaction that becomes attractive at a short distance.

Now we comment on the long-distance behavior of the correlation functions in Figure 2.7. As expected, the aforementioned Pfaffian is the furthest from the exact solution. Its correlation function reaches the asymptotic regime later, and has slower oscillations of smaller amplitude than the ground state. The CFL-state yields a correlation function that parallels the exact solution for short distances, but then diverges from it to undergo oscillations that are phase-shifted with respect to the ground state. Finally, consider the paired state that is represented in this figure, and that very closely reproduces the correlation function of the exact ground state. Upon closer analysis, one will find that the match is not perfect, but still very

impressive for a one-parameter fit. It is important to note that one might choose a different shape for the coefficients  $g_n$  in the expansion of the pair wave function, and that our Ansatz (2.120) relies on a crude estimation of the quasiparticle energies. Thus, it seems probable that an exact representation of the ground state at  $\nu = 1/2$  in the form of Eq. (2.98) is possible—at least for  $N = 14$  (choosing  $\Delta = 0.1$  as in Fig. 2.7). However, this is not a singular case. To point out that the paired state generally gives the most precise representation of the ground state (or lowest eigenstate with  $L = 0$ ), we have displayed the correlation functions for all examined system sizes in Figure 2.8.

Let us comment on some particularities. In the upper panels, the correlation functions of  $N = 6$  and  $N = 12$  correspond to system sizes which allow for alternative interpretations as hierarchy states, notably at filling factors  $\nu = 2/3$  and  $\nu = 3/5$  respectively. This ambiguity is due to the shift on the sphere: accordingly, a system with a given number of particles at some given flux may have several interpretations for different filling factors  $\nu$ , each associated to a series of states with a different value of the shift  $\sigma$ . The trial wave function derived in the description of the hierarchy states is a simple Slater determinant of CF states, i.e. the CFL. However, even in these two cases the match of the trial state correlation function may be increased by adding pairing. Again, the fit based upon the single gap parameter  $\Delta$  is nearly perfect in respect to the exact ground state.

In the middle panels of Figure 2.8, we find similar behavior for the non-filled shell states at  $N = 4$  and  $N = 8$ . The former case,  $N = 4$ , is special since the Hilbert-subspace with zero angular momentum  $L = 0$  is one-dimensional. Consequently, each of the trial wave functions yields precisely the exact solution, regardless of the choice of the gap parameter  $\Delta$ . This is a numerical confirmation that the trial states (2.98) are true eigenstates of  $L^2$  and  $L_z$  with eigenvalue 0, which we had previously argued by rotational invariance of the state. Moreover, this particular case highlights that the representation of a paired wave function as derived above is not necessarily unique due to the projection to the lowest LL.

In the lower panels we represent the trial wave functions for those system sizes  $N = 10$  and  $N = 16$  where the exact ground state is found at  $L \neq 0$ . Though it is not the ground state, the lowest eigenstate at  $L = 0$  is still best described by the paired states (2.98).

Another question to be asked is the extent to which the best paired trial and CFL states differ. Since the correlation functions are similar, it is expected that both states are similar, as well. A possible way to analyze the differences is to compare the occupation numbers of CF shells according to

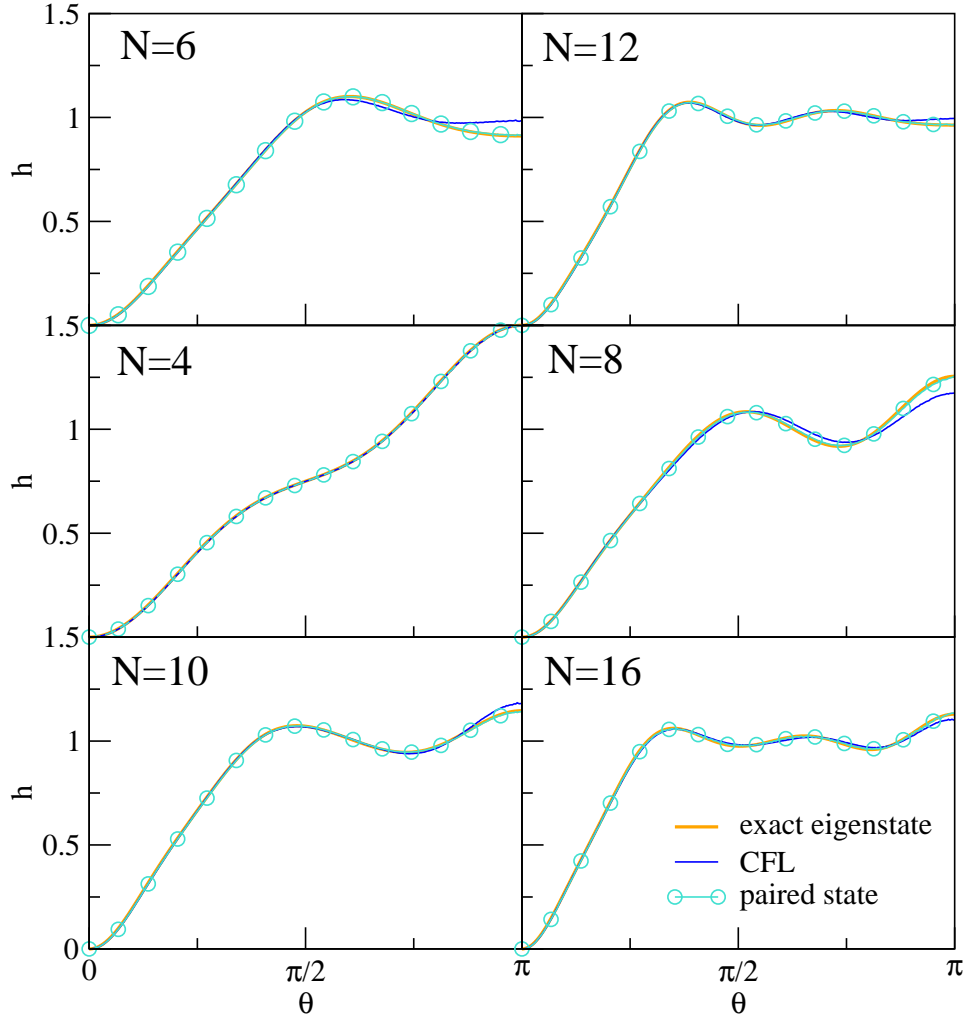


Figure 2.8: Correlation functions  $h(\theta)$  for  $N = 4, 8, 10, 12$  and  $16$  electrons on the sphere at  $\nu = 1/2$ . In the upper panels we display the filled CF shell or hierarchy states at  $N = 6, 12$ . In the second row, the smallest system we examined,  $N = 4$  (left), and  $N = 8$ . In the lower panels, the correlation functions for the lowest excited state at  $L = 0$  for the system sizes  $N = 10$  and  $N = 16$  are shown, where the exact GS is located at  $L \neq 0$ . Distances in magnetic length are related to the indicated angle  $\theta$  as  $r/\ell_0 = \theta \times \sqrt{(2N-3)}/2$ .

$N$	$E_{\text{exact}}$	$E_{\text{CFL}}$	$E_{\text{paired}}$	$\Delta(n_F)$	$\varepsilon_{\Delta}$	$\varepsilon_{\Delta}^{\text{max}}$
6	-3.23782	-3.23472(8)	-3.23778(8)	6(2)	0.0031(1)	0.0031(1)
8	-4.09816	-4.0942(1)	-4.09589(8)	0.1(2)	0.0017(1)	0.0040(1)
10	-5.01781	-5.0129(1)	-5.0149(1)	12(3)	0.0019(2)	0.0049(1)
12	-5.98461	-5.9817(1)	-5.9834(1)	5(3)	0.0017(2)	0.0029(1)
14	-6.86981	-6.8590(2)	-6.8643(2)	0.2(3)	0.0053(3)	0.0108(2)
16	-7.79153	-7.7751(2)	-7.7768(2)	0.25(3)	0.0017(3)	0.0164(2)

Table 2.3: Summary of the total energies in units of the interaction energy  $e^2/\epsilon\ell_0$ . For the two distinct trial states, the composite fermion liquid (CFL) and the paired state, the values were obtained by Monte Carlo with  $5 \times 10^8$  samples. The parameters  $\Delta$  and  $n_F$  specify the form of the pair wave function via the Ansatz (2.120). Estimates for the total condensation energy  $\varepsilon_{\Delta} = E_{\text{CFL}} - E_{\text{paired}}$  and the maximal condensation energy (if the paired state description was exact)  $\varepsilon_{\Delta}^{\text{max}} = E_{\text{CFL}} - E_{\text{exact}}$  were calculated.

(2.74). First, we should note that the sum rule  $\sum p(k) = 1$  is not as well satisfied here as in the bilayer system. Nonetheless, we can conclude with confidence that the occupation of the CF shells above the analogue of the Fermi momentum is minor. Typically, we find occupation probabilities of less than 1% for an electron occupying the  $n_F + 1^{\text{st}}$  CF-LL and probabilities of the order  $10^{-4}$  for the  $n_F + 2^{\text{nd}}$ .

Finally, upon knowing the optimal choice of the variational ‘gap’ parameter  $\Delta$ , we may perform high precision Monte-Carlo in order to compare the condensation energy  $\varepsilon_{\Delta}$  of the CF pairing, the difference between the energy of the CFL (which we write as a paired state) and that of the paired state with actual non-trivial pairing. The condensation energy is a reliable measure compared to the gap parameter  $\Delta$  which is based on phenomenological arguments, in particular, our somewhat artificial Ansatz for the quasiparticle energies.

In Table 2.3, the total energies for the exact solution are given, as well as those of the CFL and the paired states. The paired states here are those with the value of  $\Delta$  that gave the most accurate reproduction of the correlation function. This data reveals that the energy of the paired states is lower than that of the CFL with statistical significance. However, the paired states we calculated did not much improve the relative error. An exception is the system size  $N = 6$ , where the paired state yields almost the exact result. The parametrization of the trial states with  $\Delta$  according to (2.120) yields no coherent behavior of this parameter as a function of  $N$ . These facts lead us to consider the possibility that a different or more general form of  $g_n$  might

still improve the energies obtained for paired states in the form (2.98).

As an upper-bound value for the total condensation energy of the  $N$ -particle system, we may consider the difference between the energy of the CFL and the exact solution  $\varepsilon_{\Delta}^{\max}$ . It should be emphasized that the values given in Table 2.3 represent the total energy of the system. In order for a paired state to exist in the thermodynamic limit, there must be a finite condensation energy per particle. With regard to the states between the filled shell configurations, an at least linear increase of  $\varepsilon_{\Delta}^{\max}$  with  $N$  seems to be present. However, for the filled shell configurations  $N = 6$  and  $N = 12$ , where the CFL is a more precise reference, we obtained approximately the same value of  $\varepsilon_{\Delta}^{\max}$ . This may not be a fundamental problem, since it is known that only a fraction of particles pair in finite size systems, as discussed in the framework of exact solutions of the BCS Hamiltonian by Richardson and Gaudin [Dukelsky *et al.* (2004)]. Therefore, the condensation energy for small systems does not necessarily have to scale as  $N$ .

Furthermore, we should note that the systems that are the particle hole conjugated configurations of the ones discussed here are described by composite fermions in positive flux. As pointed out in the analysis of the validity of CF states at negative flux [Möller and Simon (2005)], trial states at positive flux yield slightly better trial states. These energy differences have similar orders of magnitude as  $\varepsilon_{\Delta}$ . Thus, careful examination of these different representations should be undertaken. Interestingly, if one formulates a paired state for the particle-hole conjugate system, a flux relation of  $N_{\phi} = 2N + 1$  or a shift  $\sigma = -1$  is observed. If this state is described as paired CF's, one obtains positive  $f$ -wave pairing. An analysis of the problem in this viewpoint should be undertaken in the future.

Given the above remarks, it is preferable not to conclude as to whether a paired state might indeed be realized at half-filling in the lowest Landau level.

### 2.3.5 Conclusions

In summary, we studied a general class of paired wave functions in the single layer. Most importantly, we have rebuked the argument by Greiter *et al.* that the Moore-Read Pfaffian is essentially the only paired state in the lowest Landau-level. In effect, we have constructed alternative pair wave functions which are formally operators. The formalism we have presented may be applied to describe pairing in arbitrary pairing channels, though the case of negative  $p$ -wave pairing was found to be particularly attractive, following the heuristic arguments by Greiter *et al.* (1991). Through our analysis of spectra obtained by exact diagonalization of the Coulomb Hamiltonian on



the sphere, we have found that the case of negative  $p$ -wave pairing at half-filling in the lowest LLL, corresponding to a shift  $\sigma = 3$  on the sphere, is unique (up to particle-hole conjugation which yields an identical spectrum). Contrary to the other pairing channels we analyzed, there is a clear odd-even alternating series of ground states, or very low-lying eigenstates, at zero angular momentum. We found that these eigenstates are well described in terms of the paired states (2.98). A paired description is very accurate and possible for any even number of particles  $N$ , in contrast to prior formulations of CF states that were restricted to filled shell configurations or required elaborate constructions of  $L = 0$  eigenstates based on the Wigner vector addition theorems. Even for the filled shell configurations where prior trial states exist, the new description in terms of paired composite fermions at negative effective flux  $N_\phi^{\text{eff}} = -1$  is more accurate. For those system sizes where the exact ground state is not at  $L = 0$ , a description in terms of CF at  $N_\phi^{\text{eff}} = -1$  can predict the appropriate angular momentum of the ground state when invoking Hund's rule for the occupation of orbitals in the highest CF shell.

A conclusion regarding the fate of a pairing gap in the LLL is difficult since no clear indication of a series of gapped states was found in exact diagonalizations. However, we know experimentally that the ground state at half-filling resembles a Fermi liquid [Willett *et al.* (1993)], whereas some of the small systems we have analyzed have a ground state at  $L \neq 0$ , corresponding to a broken translational invariance (i.e. rotational invariance on the sphere). This illustrates that finite size effects certainly play a role, and it is possible, in principle, that a gapped state exists. However, a final conclusion about this issue would require further numerics and an analysis of the particle-hole conjugated states.

## 2.4 Summary

In this chapter we have introduced trial wave functions for paired quantum Hall states and have studied their application to quantum Hall bilayer systems at total filling one and to the half-filled Landau level in a single layer. These wave functions are a synthesis of Jastrow- and BCS-wave functions. The strategy of the Jastrow wave-functions is to introduce good correlations for repulsive interactions by attaching zeros of the many-body wave function to the positions of particles. On the other hand, BCS wave functions describe the superconducting state in normal metals and apply to general situations in which an attractive interaction between Fermions leads to a formation of bound Cooper pairs. The existence of paired composite fermion

states has long been suspected due to the possibility of Chern-Simons gauge field fluctuations to mediate attractive interactions. Our numerical results have confirmed the existence of such a paired CF phase in the bilayer system with considerable condensation energy. At half-filling in the single layer it is less obvious whether such a state might be expressed, however, the weak amplitude of pairing in the single layer emphasizes the importance of our finding a strongly paired phase in the double layer.

## Chapter 3

# Dimensional Reduction on a Sphere

In this chapter, we consider the possibility of a dimensional reduction of the anyon model on a sphere as analogous to the Calogero-Sutherland model on a circle. First, a mapping from the 2D sphere to the 1D chiral circle is established for non-interacting particles. Second, the N-body interacting anyon model is found inadequate for dimensional reduction in its standard formulation, and an alternative, locally anyon-like model is proposed.

The results presented in this chapter were also published under the following reference: G. Möller, S. Matveenko, and S. Ouvry, *Int. J. Mod. Phys. B* **20**, 3533 (2006).

### 3.1 Introduction

One of the most spectacular characteristics of quantum Hall states is the exotic behavior of their excitations, which may have fractional statistics. Whereas these quasi-particle excitations are extended objects emerging from the subtle collective behavior of the underlying interacting many body electron system, we can think of particles with fractional statistics as point-like objects, known as anyons [Leinaas and Myrheim (1977); Goldin *et al.* (1981); Wilczek (1982a,b)]. The two dimensional anyon model has a very complicated spectrum, which is only partially known analytically. Most interestingly, when projecting the model to a subspace of known eigenstates, associated with the LLL-eigenstates of an external magnetic field, the anyon model becomes soluble and furthermore can be related to an integrable one-dimensional model in a particular limit, namely the Calogero model [Calogero (1969, 1971); Sutherland (1971, 1972)].

This problem thus bears similarity with that of the FQHE, where the physical properties of the system can be studied entirely in the particularly simple Hilbert-subspace of the lowest Landau level. The projection to the lowest Landau level has proven to be a useful tool [Jain (1989)] in constructing trial wave functions at filling factors  $\nu = p/(2mp + 1)$  in this context. This is physically motivated, as the quantum Hall effect is observed at such low temperatures  $k_B T \ll \hbar\omega_C$  that the dynamics of the system is dynamically confined to this subspace.

The mapping between the LLL-anyon model and the Calogero-model is different from the case of the quantum Hall effect in that the LLL-projection of the anyon model is not dynamically imposed. Rather, it represents a mathematical tool used to relate these models in order to gain insight concerning their respective structure. In particular, the studies that have addressed this mapping [Hansson *et al.* (1992); Brink *et al.* (1992)] were motivated by the fact that both models describe particles with non standard statistics, which interpolate from Bose-Einstein to Fermi-Dirac statistics. However, both instances of intermediate statistics are typically considered within different theoretical frameworks.

The fractional statistics of anyons are defined via their exchange statistics, i.e. via a phase  $e^{i\pi\alpha}$  that the wave function acquires when exchanging two anyons of statistics parameter  $\alpha$ . This approach requires non-trivial braiding properties of the  $N$ -body configuration space which are specific to two dimensions.

The notion of intermediate statistics applied to the Calogero case is based on Haldane exclusion-statistics [Haldane (1991)], which are further built upon Hilbert space counting arguments. Haldane exclusion-statistics

are defined for systems in which the dimension of the Hilbert space is finite and extensive in the number of particles in the system (excluding, for example, fundamental theories in particle physics). The basic observation leading to the concept of fractional statistics is a paraphrasing of the usual Bose- and Fermi-cases. Take a system with  $N - 1$  particles and consider the one-particle Hilbert space of possible configurations for adding an  $N^{\text{th}}$  particle be of  $d$  dimensions (thus obtaining a completed  $N$ -particle system). In general, this dimension  $d(N)$  is a function of the total particle number, though it must be independent of the particular particle positions. Observing how  $d(N)$  changes reveals the particle statistics. Notably, the difference  $\Delta d = d(N + \Delta N) - d(N)$  allows us to define a statistical interaction  $g$  via the relation

$$\Delta d = -g\Delta N, \quad (3.1)$$

which can be generalized for a statistical interaction between multiple species of particles [Haldane (1991)]. For bosons, the available number of states remains constant such that  $g_{\text{B}} = 0$ , whereas for fermions the number of available one-particle states decreases by one every time a particle is added and  $g_{\text{F}} = 1$ . Thus (3.1) is nothing other than a generalization of the Pauli principle, which allows for intermediate values of  $g$ .

In contrast to the notion of a statistical transformation via the attachment of Chern-Simons flux to the particles, the Hilbert space dimensions are not affected by an additional coupling to the gauge field, and Haldane exclusion statistics remain untouched by such an operation when it is applied to lattice-formulation of the anyon-model which complies with the condition of a finite and extensive Hilbert space [Haldane (1991); Canright *et al.* (1989)].

Regarding the previous remark concerning the relation between the two definitions of fractional statistics discussed in this chapter, one can expect that a rather subtle procedure is required to establish an exact relation between systems realizing these two forms of statistics. Indeed, in order to establish a non-ambiguous relation between the anyon model and the Calogero model [Ouvry (2001); Ouvry and Macris (2002); Ouvry (2002)], several operations are required. First, a long distance regularization must be utilized, which is conveniently achieved by placing the system in a confining harmonic well. Secondly, the anyon model needs to be projected on a particular subspace of the 2D harmonic well Hilbert space to obtain the 1D Calogero model in a harmonic well (Calogero-Moser model). This mapping then relates Haldane exclusion-statistics to anyon-braiding statistics, as already foreseen in the LLL-anyon model [de Veigy and Ouvry (1994, 1995)] where Haldane thermodynamics are realized microscopically. A more intuitive way to look at the harmonic projection is to notice that the 2D har-

monic quantum numbers on which the projection is made would be those of the lowest Landau level if a magnetic field were present. Therefore, the limit a magnetic field approaching zero is taken, which ultimately becomes meaningful via the harmonic well regularization: the vanishing magnetic field limit of the LLL-anyon model is the Calogero model [Ouvry (2001)]. A non-trivial aspect of this mapping is that the dimensionality of the anyon model is effectively reduced to one dimension by projecting to this particular Hilbert subspace [Ouvry (2001)].

In this chapter we discuss whether a similar correspondence can be established with a different regularization scheme, for example by modifying the topology of the 2D plane to a sphere (see also a previous attempt to dimensionally reduce Laughlin wave functions on a cylinder [Rezayi and Haldane (1994)]). For anyons on the sphere, one should obtain a compact anyon model with a discrete spectrum, which might be dimensionally reducible to the Calogero-Sutherland (C-S) model on the circle. Note that a direct relation between the Calogero-Moser and the C-S models has already been discussed by Nekrasov (1997). The C-S model is a prime example of a solvable model with exclusion statistics, and therefore its relation to the anyon model seems natural. This motivates our respective analysis of the anyon model on a sphere of radius  $R$ , which, by projection on a special class of spherical harmonics, might yield the C-S model on a circle of the same radius.

In section 3.2 we will review some basic aspects of the anyon model. As a first step towards a dimensional reduction of a spherical model, the free cases of a quantum mechanical particle on the circle and on the sphere are analyzed in section 3.3. A dimensional reduction scheme from the sphere to a chiral circle is achieved, which mimics the harmonic dimensional reduction scheme. As a second step, the question of defining the anyon model on a sphere is addressed. The anyon model on the sphere has been discussed by various authors [Lee (1989); Iengo and Lechner (1992); Comtet *et al.* (1992); Li (1993); Park *et al.* (1994)]. Yet, basic differences with regard to the C-S model immediately appear. In the latter model, the statistical parameter is a continuous coupling parameter, while in the spherical anyon model, only discrete  $N$ -dependent statistical parameters are allowed due to Dirac quantization of the total flux on the sphere. This restriction may also be regarded as a property of the braid group on the sphere, since a loop made by a particle encircling all others is contractible on the sphere and has trivial braiding properties. Another important difference lies in the scaling of the spectrum with the statistical parameter  $\alpha$ . In the anyon model, the integrable part of the spectrum scales linearly [Comtet *et al.* (1992)], whereas

the spectrum of the C-S model is quadratic in  $\alpha$ . One is thus lead to propose a new anyon-like model on the sphere in section 3.4, whose properties will be discussed. Finally, section 3.5 gives a summary of the results obtained thus far.

## 3.2 Review of the anyon model

Before discussing the main purpose of this chapter, namely to analyze possible relations between quantum mechanical models on the sphere and the circle, some basic facts concerning the anyon model are presented.

### 3.2.1 Multivalued wave functions

For pointlike particles, one may introduce fractional statistics as a generalization of standard quantum statistics. Particles obeying such statistics are described by wave functions which take not just a  $(-)$  sign (as for fermions) or a  $(+)$  sign (as for bosons) under the exchange of two particles, but rather any arbitrary phase

$$\Psi(r_1, r_2) = e^{i\pi\alpha}\Psi(r_2, r_1). \quad (3.2)$$

Accordingly, such particles have been named *anyons* (an alternative notation of the statistical angle is  $\pi\alpha \equiv \theta$ , which was used in section 2.3). We can understand a double exchange of two particles as they return to their initial positions upon orbiting on a path equivalent to one particle completing a closed path around the other. If  $\alpha$  differs from the values that yield bosonic ( $\alpha = 0$ ) or fermionic statistics ( $\alpha = 1$ ), the resulting value differs by a non-trivial phase  $\pm \exp(2\pi i\alpha)$  from the initial value, though particles have returned to the initial positions. The wave function is then multi-valued, and its phase is dependent on the history of the prior movement of the particles. This does not make sense in three or higher dimensions, since the described path can then be contracted to a point, and the phase of the wave function would therefore not be well-defined. In two dimensions, however, it is a sensible concept, since a closed path of a particle around one of its peers leaves a braiding of their world-lines which cannot be trivially unfolded: it represents a topological invariant of the system's history.

### 3.2.2 Lagrangian theory

Particles coupled to a gauge field are described by the Lagrangian

$$\mathcal{L} = \sum_{i=1}^N \frac{1}{2} m \mathbf{v}_i^2 + e[\mathbf{A}(\mathbf{r}_i) \cdot \mathbf{v}_i - A_0(\mathbf{r}_i)] \quad (3.3)$$

for a system of  $N$  particles in two dimensions. Another gauge invariant term that may be added to this Lagrangian is the Chern-Simons term

$$\mathcal{L}_{\text{CS}} = \frac{\kappa}{2} \epsilon_{\mu\nu\rho} \int d^2r A^\mu \partial^\nu A^\rho, \quad (3.4)$$

where  $\epsilon$  is the completely antisymmetric tensor with  $\epsilon_{012} = 1$ . This term contains no metric factors, and is entirely of topological nature. The equations of motion of the time component of this CS-Lagrangian impose that

$$\partial_1 A_2 - \partial_2 A_1 = 0. \quad (3.5)$$

Representing the gauge field as

$$A_i = \partial_i \Lambda + \epsilon_{ij} \partial_j \Upsilon, \quad (3.6)$$

one can see that (3.5) imposes  $\Delta \Upsilon = 0 \Rightarrow \Upsilon = 0$  with according boundary conditions at infinity, and the vector potential is a pure gauge

$$\mathbf{A} = \nabla \Lambda. \quad (3.7)$$

Fixing the gauge as the Coulomb gauge  $\nabla \cdot \mathbf{A} = 0$ , one finds that the gauge parameter is a harmonic function  $\Delta \Lambda = 0$ . Accordingly, this theory does not allow for the propagation of waves, and  $A_\mu$  does not represent an independent dynamical degree of freedom. Studying the full theory with  $\mathcal{L}_T = \mathcal{L} + \mathcal{L}_{\text{CS}}$ , the equation of motion derived from  $A_0$  becomes

$$\kappa(\partial_1 A_2 - \partial_2 A_1) = e \sum_{i=1}^N \delta(\mathbf{r} - \mathbf{r}_i), \quad (3.8)$$

or using the representation (3.6) and keeping the Coulomb gauge

$$\Delta \Upsilon = \frac{e}{\kappa} \sum_{i=1}^N \delta(\mathbf{r} - \mathbf{r}_i). \quad (3.9)$$

We can solve using the 2D Green's function  $\Delta \ln(r) = 2\pi\delta^2(\mathbf{r})$  to obtain

$$\Upsilon = \frac{e}{2\pi\kappa} \sum_{i=1}^N \ln |\mathbf{r} - \mathbf{r}_i|. \quad (3.10)$$

The vector potential deriving from this solution is easily recognized as the Aharonov-Bohm potential of flux tubes located at the positions  $\mathbf{r}_i$  of the particles

$$\mathbf{A}(\mathbf{r}) = \frac{e}{2\pi\kappa} \sum_{i=1}^N \frac{\mathbf{e}_z \times (\mathbf{r} - \mathbf{r}_i)}{|\mathbf{r} - \mathbf{r}_i|^2}. \quad (3.11)$$



The strength of the individual flux tubes, derived by integration around one of the flux tubes gives

$$\Phi = \int_C \mathbf{A} \cdot d\mathbf{l} = \frac{e}{\kappa}. \quad (3.12)$$

### 3.2.3 Hamiltonian theory

Deriving the Hamiltonian associated to the total Chern-Simons Lagrangian  $\mathcal{L}_T$  is particularly simple. Since they are linear in the time derivatives of the gauge field  $\mathbf{A}$ , the corresponding terms cancel in the Hamiltonian. Furthermore,  $A_0$  can be factored out in the remaining terms after partial integration, and the terms it multiplies vanish as imposed by the equations of motion. One is left with the particles as the only dynamical degree of freedom, with a minimal coupling to the gauge field.

$$\mathcal{H} = \sum_{i=1}^N \frac{1}{2m} \mathbf{v}_i^2 = \sum_{i=1}^N \frac{1}{2m} [\mathbf{p}_i - e\mathbf{A}(\mathbf{r}_i)]^2, \quad (3.13)$$

with the vector potential still given by (3.11). Denoting the vectors  $\mathbf{r}_{kl} = \mathbf{r}_k - \mathbf{r}_l$  in a complex notation

$$z_{kl} = r_{kl} e^{i\theta_{kl}}, \quad (3.14)$$

where  $r = |\mathbf{r}|$  and  $\theta$  stands for the angle of the vector with the  $x$ -axis, the function  $\Upsilon$  may be rewritten by realizing that

$$\ln |\mathbf{r}_{kl}| = \Re \ln z_{kl}. \quad (3.15)$$

The vector potential  $\mathbf{A}_i = \mathbf{A}(\mathbf{r}_i)$  at the position of the particle  $i$  can then be written as

$$\mathbf{A}_i \propto \nabla_i \times \sum_{k<l} \Re \ln z_{kl}, \quad (3.16)$$

where  $\nabla_i$  is the gradient with respect to the coordinates of particle  $i$ . Invoking the Cauchy-Riemann equations for the complex logarithm, this can be rewritten as a pure gauge

$$\mathbf{A}_i \propto \nabla_i \sum_{k<l} \Im \ln z_{kl}. \quad (3.17)$$

However, the gauge function

$$\Lambda \propto \Im \sum_{k<l} \ln z_{kl} \equiv \sum_{k<l} \theta_{kl} \quad (3.18)$$

is singular, since the angles are not well defined for coinciding particle positions. Furthermore, this gauge transition does not conserve the magnetic field, and it is immediately clear that the inverse gauge transformation may be used to annihilate the Aharonov-Bohm interactions between the particles.

Starting from interacting bosons with Aharonov-Bohm interactions described by a mono-valued wave function  $\Psi$ , the inverse singular gauge transformation simply yields a free Hamiltonian denoted with the superscript  $o$ , such that

$$\mathcal{H}^o = \sum_{i=1}^N \frac{\mathbf{p}_i^2}{2m}. \quad (3.19)$$

However, the wave function is then a complicated multiple-valued wave function  $\Psi^o$  related to the original one by

$$\Psi^o(\mathbf{r}_1, \dots, \mathbf{r}_N) = e^{i\alpha \sum_{k<l} \theta_{kl}} \Psi(\mathbf{r}_1, \dots, \mathbf{r}_N), \quad (3.20)$$

where the statistics parameter  $\alpha$  is related to the parameters of the Lagrangian model via

$$\alpha = \frac{e^2}{2\pi\kappa} = \frac{e\Phi}{2\pi}. \quad (3.21)$$

The analogy between free anyons and bosons (fermions) coupled via Aharonov-Bohm interactions is one of the central results of the anyon theory and will be discussed next.

### 3.2.4 Anyon spectrum

As mentioned previously, the spectrum of the N-body anyon model is complicated and only partial insight can be gained analytically. Nonetheless, the two-body case can be easily solved. The Hamiltonian in the interacting picture

$$\mathcal{H} = \frac{1}{2m_0} \left[ \mathbf{p}_1 - \alpha \frac{\mathbf{e}_z \times \mathbf{r}_{12}}{r_{12}^2} \right]^2 + \frac{1}{2m_0} \left[ \mathbf{p}_2 - \alpha \frac{\mathbf{e}_z \times \mathbf{r}_{21}}{r_{21}^2} \right]^2 \quad (3.22)$$

decomposes into a free center of mass (CM) term and a relative problem analogous to that of Aharonov-Bohm (a particle in the vector potential of a flux-tube). Upon denoting  $r$  and  $\theta$  as the polar coordinates of the relative position of both particles, and choosing the Ansatz  $\Psi_{\text{rel}} = e^{im\theta} f(r)$ , the radial problem for  $f(r)$  becomes

$$H_{\text{rad}} = \frac{1}{m_0} \left[ -\frac{\partial^2}{\partial r^2} - \frac{1}{r} \frac{\partial}{\partial r} + \frac{(m - \alpha)^2}{r^2} \right]. \quad (3.23)$$

The Bessel functions  $J$  yield the solutions of the respective eigenvalue equation, and one obtains the set of solutions

$$\Psi_{\text{rel}}^{k,m}(r, \theta) = \sqrt{\frac{k}{2\pi}} e^{im\theta} J_{|m-\alpha|}(kr) \quad (3.24)$$

with eigenvalues  $E = k^2/m_0$ . The continuous degeneracy of these eigenfunctions in the quantum number  $k$  makes it difficult to appreciate the nature of this spectrum, and it is instructive to consider the case with an additional harmonic potential. Such a potential acts as a regulator and causes the spectrum to be discrete. The problem still factorizes into the CM and relative problems, and the latter becomes

$$H_{\text{rad}} = \frac{1}{m_0} \left[ -\frac{\partial^2}{\partial r^2} - \frac{1}{r} \frac{\partial}{\partial r} + \frac{(m-\alpha)^2}{r^2} \right] + \frac{1}{4} m \omega^2 r^2. \quad (3.25)$$

The solution involves the Laguerre polynomials  $L_n^\mu$  and reads

$$\Psi_{\text{rel}}^{n,m}(r, \theta) = \mathcal{N} r^{|m-\alpha|} e^{im\theta} L_n^{|m-\alpha|}(\gamma r^2) e^{-\gamma r^2/2}, \quad (3.26)$$

where  $\gamma = m_0\omega/2$  and  $\mathcal{N}$  is some normalization factor. The corresponding spectrum  $E_{n,m} = \omega(2n + |m-\alpha| + 1)$  is related to the spectrum of a two-dimensional harmonic oscillator via the replacement  $m \rightarrow m-\alpha$ . It is important to note that the corresponding wave function  $\Psi^o$  in the free anyon formulation has a short-distance behavior  $\Psi^o \propto z^{|m-\alpha|}$ , which is also present in the known many-particle states. This provides the motivation to consider an effective Hamiltonian  $\tilde{H}$ , in which one prescribes this short distance behavior for the wave function such that  $\Psi^o = z^{-\alpha} \tilde{\Psi}$ . This approach will be exploited below for the anyon-model on the sphere.

### 3.3 Dimensional reduction of free models

As the first step towards a dimensional reduction of a model on the sphere, we have analyzed non-interacting models on the sphere and circle and have established a relation between them. As a reference case, we first discuss a similar relation that applies to harmonically confined particles.

#### 3.3.1 A Reminder: Harmonic Dimensional Reduction

In the case of non-interacting particles, it is known how to map a 2D particle in a harmonic well onto a 1D particle in a harmonic well. The starting point is the 2D Hamiltonian

$$H = -2 \frac{\partial}{\partial \bar{z}} \frac{\partial}{\partial z} + \frac{1}{2} \omega^2 z \bar{z} \quad (3.27)$$

with the common notation for positions in the plane,  $z = x + iy$ , and  $\bar{z}$  its complex conjugate. We can solve for the eigenstates with a calculation analogous to section 3.2.4 by separating the angular and radial part of the equation. The spectrum of the oscillator is obtained as

$$E_{nm} = \omega(2n + |m| + 1), \quad (3.28)$$

where  $n \in \mathbb{N}$  is the radial quantum number and  $m \in \mathbb{Z}$  is the orbital quantum number. The eigenstates are obtained from Eq. (3.26), setting  $\alpha = 0$  and  $\gamma = \omega$ . To establish a mapping with the one-dimensional harmonic oscillator, one needs to specialize to a particular subset of quantum numbers. Here, this subset is obtained by choosing exclusively the state of maximal angular momentum  $l = +|m| \geq 0$  for each degenerate energy level, i.e. the states with radial quantum number  $n = 0$  (see figure 3.1 for a sketch of this situation). We note that these are precisely the LLL quantum numbers if a magnetic field were present. Returning to the complex coordinate notation, these states are

$$\langle z, \bar{z} | 0, l \rangle = z^l e^{-\frac{1}{2}\omega z \bar{z}}, \quad l \geq 0 \quad (3.29)$$

with spectrum

$$E_l = \omega(l + 1). \quad (3.30)$$

One can thus view the action of the harmonic confinement potential as splitting the degeneracy of the LLL states, when starting from an unconfined problem in a magnetic field [Ouvry and Macris (2002)]. Projecting the Hamiltonian on this subspace, assuming wave functions of the form  $\Psi = f(z)e^{-\frac{1}{2}\omega z \bar{z}}$ , leaves us with a simple eigenvalue problem

$$\omega \left( 1 + z \frac{\partial}{\partial z} \right) f(z) = E f(z). \quad (3.31)$$

Note that projection to the subspace with  $n = 0$  and  $l \leq 0$  (which happen to be the complex conjugate eigenfunctions  $\bar{\Psi} = f(\bar{z})e^{-\frac{1}{2}\omega z \bar{z}}$  of the previous ones) yields an equivalent result. The eigenvalue equation then becomes

$$\omega (1 + \bar{z} \bar{\partial}) f(\bar{z}) = E f(\bar{z}). \quad (3.32)$$

In the thermodynamic limit  $\omega \rightarrow 0, l \rightarrow \infty$  with  $\omega l$  fixed, the physical picture of the projection is that it retains only those states with a significant probability density increasingly close to the edge of the 2D plane. These states thus mimic particles on the 1D boundary of the 2D sample.

Equation (3.31) (as well as eq. (3.32)) is identical to an eigenvalue equation for a 1D harmonic well Hamiltonian in the coherent state representation.

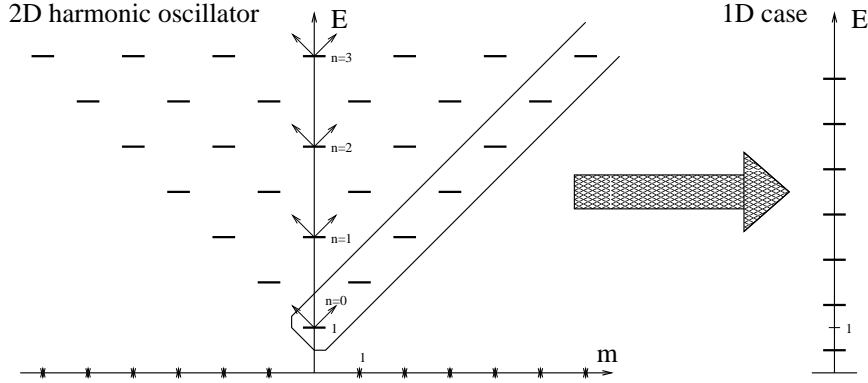


Figure 3.1: A sketch of the eigenstates of the 2D harmonic oscillator involved in the mapping with the spectrum of the 1D harmonic oscillator, established as described in the text via the coherent states that are superpositions of infinitely many 1D eigenstates. Alternatively, the mapping can be performed for the other  $n = 0$  branch of the 2D oscillator eigenstates. Energy scales are indicated in units of  $\omega$ .

Consider the Hamiltonian for a 1D harmonic oscillator

$$H = -\frac{1}{2} \left( \frac{d}{dx} \right)^2 + \frac{1}{2} \omega^2 x^2 = \omega \left( a^\dagger a + \frac{1}{2} \right). \quad (3.33)$$

Its coherent states  $|\alpha\rangle$  [Glauber (1963)] are eigenstates of the annihilation operator

$$a = \sqrt{\frac{\omega}{2}} x + \frac{i}{\sqrt{2\omega}} p_x. \quad (3.34)$$

Applying  $a^\dagger$  to the coherent states  $|\alpha\rangle$  in the canonical basis of energy eigenstates  $|n\rangle$ , such that

$$|\alpha\rangle = e^{-\frac{|\alpha|^2}{2}} \sum_{n=0}^{\infty} \frac{\alpha^n}{\sqrt{n!}} |n\rangle, \quad (3.35)$$

one obtains

$$a^\dagger |\alpha\rangle = \left( \frac{\partial}{\partial \alpha} + \frac{\bar{\alpha}}{2} \right) |\alpha\rangle. \quad (3.36)$$

This leads to the Hamiltonian in the coherent states basis

$$H = \omega \left( \alpha \frac{\partial}{\partial \alpha} + \frac{\alpha \bar{\alpha}}{2} + \frac{1}{2} \right), \quad (3.37)$$

which may be rewritten as (3.31) via the non-unitary transformation (up to a zero-point energy shift) to yield

$$\tilde{H} = e^{\frac{|\alpha|^2}{2}} H e^{-\frac{|\alpha|^2}{2}} = \omega \left( \frac{1}{2} + \alpha \frac{\partial}{\partial \alpha} \right). \quad (3.38)$$

The mapping between the canonical states basis and the coherent states basis (known as the Bargman transform) maps  $\alpha^n$  (the eigenstates in the coherent basis) on the Hermite polynomials  $H_n(x)$  (eigenstates in the configuration space)

$$\alpha^n = \frac{1}{\sqrt{2^n}} \int_{-\infty}^{\infty} dx H_n(x) e^{-x^2 + \sqrt{2}\alpha x - \frac{\alpha^2}{2}}. \quad (3.39)$$

Next, a similar dimensional reduction is outlined which establishes a mapping from a 2D particle on a sphere to a 1D chiral particle on a circle.

### 3.3.2 Free Particle on the Circle

The Hamiltonian of a free particle on a circle is

$$H = \frac{1}{2mR^2} \hat{L}^2, \quad \vec{r} = \cos \phi \vec{e}_x + \sin \phi \vec{e}_y \quad (3.40)$$

where  $\hat{L} = -i\frac{\partial}{\partial \phi}$  is the angular momentum operator in the coordinate representation. For simplicity of notations, one sets  $m = R = 1$ . The eigenstates  $|l\rangle$  with momentum  $l \in \mathbb{Z}$  are

$$\langle \phi | l \rangle = \frac{1}{\sqrt{2\pi}} e^{il\phi} \quad (3.41)$$

with eigenvalues  $E_l = \frac{1}{2}l^2$  ( $l \in \mathbb{Z}$  enforces canonical single valued wave functions, however the case of half integer  $l$  has also been discussed [Kowalski *et al.* (1996)]). One now introduces coherent states on the circle [Kowalski *et al.* (1996)], starting from the unitary operator

$$U = e^{i\hat{\phi}}, \quad (3.42)$$

which defines a ladder operator on the basis  $|l\rangle$

$$U|l\rangle = |l+1\rangle, \quad (3.43)$$

since  $[\hat{L}, U] = U$ . Analogously to both coherent states of the harmonic oscillator and its ladder operator  $a^\dagger$ , which is of the form ‘position’ +  $i$ ·‘momentum’, one may introduce an operator  $\Xi$  that is built from a similar expression

$$\Xi = \exp\{i(\hat{\phi} + i\hat{L})\} = U \exp\left\{-\hat{L} - \frac{1}{2}\right\}. \quad (3.44)$$

Its eigenstates,  $|\xi\rangle$ , are the desired coherent states [Kowalski *et al.* (1996)]. In the canonical basis  $\{|l\rangle\}$ , they have the form

$$|\xi\rangle = \sum_l \xi^{-l} e^{-\frac{1}{2}l^2} |l\rangle. \quad (3.45)$$

The action of the angular momentum operator on  $|\xi\rangle$  can be calculated such that:

$$\hat{L}|\xi\rangle = \sum_l l \xi^{-l} e^{-\frac{1}{2}l^2} |l\rangle = -\xi \frac{\partial}{\partial \xi} \sum_l \xi^{-l} e^{-\frac{1}{2}l^2} |l\rangle = -\xi \frac{\partial}{\partial \xi} |\xi\rangle. \quad (3.46)$$

Thus, the representation of the Hamiltonian in the basis of coherent states is

$$H = \frac{1}{2} \left( \xi \frac{\partial}{\partial \xi} \right)^2, \quad (3.47)$$

with eigenstates  $\psi_l(\xi) = \xi^l$  and eigenvalues  $E_l = \frac{1}{2}l^2$  with  $l \in \mathbb{Z}$ .

In analogy to the Bargman transform (3.39) that establishes a relation between the energy eigenstates and the coherent eigenstates of the 1D harmonic well, we can find a mapping from the basis of angular momentum eigenstates to the coherent eigenstates on the circle. This mapping is obtained as the equation of two different expressions of the scalar  $\langle l|\xi\rangle$ , either evaluated directly or after insertion of the completeness relation  $I = \frac{1}{\pi} \int d\phi |\phi\rangle\langle\phi|$  for the coherent states [Bargmann *et al.* (1971); Perelomov (1971)]. One then obtains

$$\xi^l = \frac{1}{2\pi^2} e^{\frac{1}{2}l^2} \int_0^{2\pi} d\phi e^{-il\phi} \theta_3 \left( \frac{1}{2}(\phi + i \ln \xi) \middle| \frac{i}{2\pi} \right). \quad (3.48)$$

### 3.3.3 Free Particle on the Sphere

The Hamiltonian of a free particle on the sphere is (3.40) except the angular momentum operator of the particle confined on a sphere of radius  $R$  is 2D instead of 1D. As above, we set  $m = R = 1$ . The eigenstates are the spherical harmonics  $Y_l^m(\theta, \phi) = \langle \theta, \phi | l, m \rangle$ , with  $l = 0, 1, 2, \dots$  and  $-l \leq m \leq l$ . Their energies are degenerate in  $m$  with the eigenvalue equation

$$H|l, m\rangle = \frac{1}{2}l(l+1)|l, m\rangle. \quad (3.49)$$

On the circle, the spectrum has a twofold degeneracy on each energy level (except at  $l = 0$ ). A subspace of the 2D Hilbert space  $\{|l, m\rangle, l \in \mathbb{N}, |m| \leq l\}$  should be selected to establish a mapping on the circle. Naturally, this

subspace has to be characterized by a single quantum number. It is natural to consider either  $\{|l, l\rangle\}$  or  $\{|l, -l\rangle\}$  in analogy with the two subspaces discussed for the harmonic well in Sec. 3.3.1. In configuration space, these eigenstates have the form

$$\langle \theta, \phi | l, l \rangle = Y_l^l(\theta, \phi) = \sin^l \theta e^{il\phi} \quad \text{or} \quad \langle \theta, \phi | l, -l \rangle = Y_l^{-l}(\theta, \phi) = \sin^l \theta e^{-il\phi}. \quad (3.50)$$

Note that these states correspond to a probability density increasingly close to the equator of the sphere with growing  $l$ . The physical picture that arises is that the 2D system mimicks an effectively one-dimensional system: particles on the equatorial circle.

To achieve a relationship with the coherent state representation on the circle, the Hamiltonian on the sphere can be rewritten in stereographic coordinates  $(z, \bar{z})$ , with  $z = \cot(\theta/2)e^{i\phi}$  such that

$$H = -\frac{1}{2}(1 + z\bar{z})^2 \frac{\partial}{\partial z} \frac{\partial}{\partial \bar{z}}. \quad (3.51)$$

The wave functions (3.50) can be rewritten as

$$\langle z, \bar{z} | l, +l \rangle = \left( \frac{z}{1 + z\bar{z}} \right)^l \equiv u^l, \quad \text{and} \quad \langle z, \bar{z} | l, -l \rangle = \left( \frac{\bar{z}}{1 + z\bar{z}} \right)^l \equiv \bar{u}^l. \quad (3.52)$$

Note that in the thermodynamic limit  $R \rightarrow \infty$ ,  $u^l$  or  $\bar{u}^l$  reproduces the states of the lowest Landau level in the presence of a magnetic monopole. This becomes obvious if one considers the explicit  $R$ -dependence of these states

$$u = \frac{z}{1 + \frac{z\bar{z}}{4R^2}} \xrightarrow{R \rightarrow \infty} z, \quad \text{and} \quad \bar{u} \rightarrow \bar{z}.$$

Projecting on these particular Hilbert spaces  $\{|l, +l\rangle\}$  or  $\{|l, -l\rangle\}$  means that the Hamiltonian acts singularly on functions of  $u$  or  $\bar{u}$ . Therefore, one may obtain either

$$H = \frac{1}{2} \left( u^2 \left( \frac{\partial}{\partial u} \right)^2 + 2u \frac{\partial}{\partial u} \right) \quad (3.53)$$

or

$$H = \frac{1}{2} \left( \bar{u}^2 \left( \frac{\partial}{\partial \bar{u}} \right)^2 + 2\bar{u} \frac{\partial}{\partial \bar{u}} \right). \quad (3.54)$$

These Hamiltonians match (3.47), up to a zero point shift for the energy and the angular momentum

$$H_w = \frac{1}{2} \left[ \left( w \frac{\partial}{\partial w} + \frac{1}{2} \right)^2 - \frac{1}{4} \right] = \frac{1}{2} \left[ \left( \hat{L}_w + \frac{1}{2} \right)^2 - \frac{1}{4} \right], \quad (3.55)$$



where  $w$  is either  $u$  or  $\bar{u}$ . Their spectrum is  $E_l = \frac{1}{2}((l + \frac{1}{2})^2 - \frac{1}{4})$  with  $l \in N$ . Therefore, the chiral Hilbert subspaces allow for a dimensional reduction from the two-dimensional problem on the sphere to the one-dimensional chiral problem on the circle, as can be seen from (3.40) and (3.55), with spectra that are both quadratic in the single quantum number of either problem.

### 3.4 A Generalized Aharonov-Bohm Model on the Sphere

As discussed in the introduction, we are interested in a model on the sphere, which may be dimensionally reducible to the Calogero-Sutherland model. Since the latter features exclusion statistics [Isakov (1994)], a connection with the anyon model appears possible, though there seems to be a mismatch of the spectra which we wish to relate via a mapping. The integrable part of the spectrum of the anyon model as defined by Leinaas and Myrheim (1977), Goldin *et al.* (1981), and Wilczek (1982a,b) scales linearly with the interaction parameter, whereas the C-S spectrum scales quadratically.

As reviewed previously, anyons on the plane are defined either by the nontrivial monodromy of the  $N$ -body wave function with a free Hamiltonian or related via a singular gauge transformation by a mono-valued  $N$ -body wave function (bosonic by convention). This wave function has an interacting  $N$ -body Aharonov-Bohm Hamiltonian which describes a situation where each particle carries a (statistical) flux line of strength  $\Phi = \alpha\Phi_0$  (where  $\Phi_0$  is the flux quantum). In this section, we construct a model on the sphere beginning with the Aharonov-Bohm problem and the principle of flux attachment, which can be traced back to a geometrical definition of the statistical phase between two particles.

The standard Aharonov-Bohm problem consists of a particle coupled to a single flux-tube which pierces the plane at the origin. The Aharonov-Bohm problem on the sphere, first considered by Kretzschmar (1965), consists of a particle coupled to a flux that pierces the sphere at the south pole and exits at the north pole. Given that the total flux through the sphere sums to zero, there is no Dirac quantization condition and the coupling parameter  $\alpha$  is a continuous variable. Furthermore, the spectrum of this Aharonov-Bohm problem is quadratic in  $\alpha$ .

### 3.4.1 Symmetric single-particle case

The canonic single-particle Aharonov-Bohm problem as considered by Kretzschmar (1965) is begun with a charged particle on a sphere interacting with a flux line  $\Phi$  entering the sphere at the south pole and exiting at the north pole. In order to obtain the vector potential  $\mathbf{A}$  describing this situation, its circulation of along each azimuthal circle<sup>1</sup> (constant  $\theta$ ) must be equal to the flux  $\Phi$ . Therefore,

$$\mathbf{A} = \frac{\Phi}{2\pi} \nabla\phi. \quad (3.56)$$

The Aharonov-Bohm (A-B) Hamiltonian  $H^{AB}$  is obtained by substitution of the multi-valued phase  $\exp(i\alpha\phi)$  in the free Hamiltonian  $H^o = -\frac{1}{2R^2}\Delta$  (in units  $\hbar = m = 1$ ), i.e.,  $\Psi_o = \exp(i\alpha\phi)\Psi$ , with  $\Phi = \alpha\Phi_o$  (up to  $\delta$  contact terms at the north and south poles). This yields

$$H^{AB} = -\frac{1}{2R^2} \left[ \frac{1}{\sin\theta} \frac{\partial}{\partial\theta} \sin\theta \frac{\partial}{\partial\theta} + \frac{1}{\sin^2\theta} \left( \frac{\partial}{\partial\phi} + i\alpha \right)^2 \right]. \quad (3.57)$$

The eigenfunctions of (3.57) found by Kretzschmar (1965) are given by

$$\Psi = e^{im\phi} P_\lambda^{-\mu}(x), \quad (3.58)$$

with  $x = \cos\theta$ . The associated Legendre functions  $P_\lambda^{-\mu}(x)$  are related to the hypergeometric functions via

$$P_\lambda^{-\mu}(x) = \frac{1}{\Gamma(1+\mu)} \left( \frac{1-x}{1+x} \right)^{\frac{\mu}{2}} F_H \left( -\lambda, \lambda+1; \mu+1; \frac{1-x}{2} \right), \quad (3.59)$$

where  $\mu = |m + \alpha|$ , and  $m$  is the angular quantum number of  $L_z$ . Vanishing boundary conditions for the wave function are imposed at the north and south poles where the flux line pierces the sphere. Equation (3.59) satisfies these conditions for  $\lambda = \mu + k$  where  $k$  is a positive integer. The spectrum is described by  $E_\lambda = \lambda(\lambda + 1)$  and contains terms quadratic in  $\alpha$ , which are also present in the Calogero-Sutherland spectrum.

The stereographically projected coordinates  $(z, \bar{z})$  on the projective plane containing the south pole turn out to be useful. When  $r$  is the distance from the south pole in the projective plane we define a rescaled radial coordinate  $\rho = r/(2R) = \cotg(\theta/2)$  and we set the radius of the sphere  $R$  equal to unity, thus giving

$$z = \rho e^{i\phi}, \quad (3.60)$$

---

<sup>1</sup>We use the common spherical coordinates with a polar angle  $\theta$  and azimuthal angle  $\phi$

$$\cos \theta = \frac{\rho^2 - 1}{\rho^2 + 1}, \quad \sin \theta = \frac{2\rho}{\rho^2 + 1}, \quad \rho^2 = \frac{1+x}{1-x}, \quad (3.61)$$

as well as

$$\frac{1-x}{2} = \frac{1}{1+z\bar{z}} \quad \text{and} \quad \frac{1+x}{2} = \frac{z\bar{z}}{1+z\bar{z}}. \quad (3.62)$$

If we look at (3.58), and start from the free Hamiltonian in projective coordinates, we get

$$H^o = -\frac{1}{2}(1+z\bar{z})^2 \partial \bar{\partial}, \quad (3.63)$$

such that the eigenstates are

$$\Psi^o = e^{i(m+\alpha)\phi} \tan(\theta/2)^{|m+\alpha|} \frac{1}{\Gamma(1+\mu)} F_H \left( -\lambda, \lambda+1; \mu+1; \frac{1-x}{2} \right), \quad (3.64)$$

which can be expressed either in the form ,

$$\Psi^o = F^{m+\alpha} \frac{1}{\Gamma(1+\mu)} F_H \left( -\lambda, \lambda+1; \mu+1; \frac{1-x}{2} \right), \quad (3.65)$$

if  $m+\alpha \geq 0$  or alternatively as

$$\Psi^o = \bar{F}^{-m-\alpha} \frac{1}{\Gamma(1+\mu)} F_H \left( -\lambda, \lambda+1; \mu+1; \frac{1-x}{2} \right), \quad (3.66)$$

if  $m+\alpha \leq 0$ . In equations (3.65) and (3.66),  $F = 1/\bar{z}$  simultaneously encodes the A-B-phase and the analog of a “short distance” behavior on the sphere: it defines the south→north pole Aharonov-Bohm problem (on the plane, one has  $F = z$  for the A-B problem with a vortex at the origin).

The appearance of  $F$  in the eigenstates is not accidental. With  $\phi$  being a harmonic function on the sphere, the Cauchy-Riemann equations yield the function  $F = |F| \exp(i\phi)$ . In the local coordinate system spanned by the vectors  $\partial_\theta \leftrightarrow \partial_x$  and  $\partial_\phi / \sin \theta \leftrightarrow \partial_y$ ,

$$\partial_\theta \ln |F| = \frac{1}{\sin \theta} \quad \frac{1}{\sin \theta} \partial_\phi \ln |F| = 0 \quad (3.67)$$

are obtained. Therefore,  $|F| = \tan \frac{\theta}{2}$  and  $F = \tan \frac{\theta}{2} \exp(i\phi) = 1/\bar{z}$ .

As an illustration of (3.64), consider the simple case  $k = 0$ , such that  $\lambda = |m+\alpha|$ , where the hypergeometric function rewrites as

$$F_H \left( -\lambda, \lambda+1; \lambda+1, \frac{1-x}{2} \right) = \left( 1 - \frac{1-x}{2} \right)^\lambda = \left( \frac{1+x}{2} \right)^\lambda = \left( \frac{z\bar{z}}{1+z\bar{z}} \right)^\lambda. \quad (3.68)$$

If  $m + \alpha \geq 0$

$$\Psi^o = \left( \frac{z}{1 + z\bar{z}} \right)^{m+\alpha}, \quad (3.69)$$

whereas if  $m + \alpha \leq 0$

$$\Psi^o = \left( \frac{\bar{z}}{1 + z\bar{z}} \right)^{-m-\alpha}, \quad (3.70)$$

and the eigenvalues of the latter states are  $E = |m + \alpha|(|m + \alpha| + 1)$ . Within the standard interval for the statistic parameter  $-1/2 < \alpha \leq 1/2$ , the ground state is either (3.70) with  $m = 0$ , if  $-1/2 < \alpha < 0$  or (3.69) with  $m = 0$ , if  $0 < \alpha < 1/2$ .

One explicitly sees that although  $F$  is singular at the south pole, the wave function is still regular both at the south and north poles because of appropriate terms in the hypergeometric function.

Proceeding as on the plane, one can bypass the A-B Hamiltonian and define a new Hamiltonian  $\tilde{H}$ , directly obtained from  $H^o$  by extracting  $F^\alpha$  (or  $\bar{F}^{-\alpha}$ ) in  $\Psi^o$ , i.e.,  $\Psi^o = F^\alpha \tilde{\Psi}$ . Consequently,

$$\tilde{H} = -\frac{1}{2}(1 + z\bar{z})^2 (\partial\bar{\partial} - \alpha \frac{1}{z} \partial). \quad (3.71)$$

Or, upon taking advantage of (3.69) (or (3.70)), one can define a Hamiltonian  $\tilde{H}'$  obtained from  $H^o$  by extracting  $(\frac{z}{1+z\bar{z}})^\alpha$  (or  $(\frac{\bar{z}}{1+z\bar{z}})^{-\alpha}$ ), i.e.,  $\Psi^o = (\frac{z}{1+z\bar{z}})^\alpha \tilde{\Psi}'$ , which yields

$$\tilde{H}' = -\frac{1}{2}(1 + z\bar{z})^2 \left( \partial\bar{\partial} + \alpha \frac{1}{z(1+z\bar{z})} \bar{\partial} - \alpha \frac{z}{1+z\bar{z}} \partial \right) + \frac{1}{2} \alpha(\alpha + 1). \quad (3.72)$$

Both  $\tilde{H}$  and  $\tilde{H}'$  have a simple form.

### 3.4.2 Tilted single-particle case

In order to generalize to the  $N$ -body problem, consider a particle at position  $z_i$  coupled to a vortex  $\Phi$  entering the sphere at a point with stereographic coordinate  $z_j$  and exiting the sphere at its antipode  $-1/\bar{z}_j$ . This problem is identical to the preceding one and in particular, the spectrum is unchanged. We must still rewrite the wave functions and the corresponding function  $F_{ij}$  which generalizes  $F$  in the appropriate coordinates  $z_i$  and  $z_j$ .

It turns out that the A-B phase on the sphere has a geometric interpretation analogous to the one on the plane as depicted in Fig. 3.2. One obtains

$$\cot \phi_{ij} = \frac{\cos \theta_i \sin \theta_j - \sin \theta_i \cos \theta_j \cos(\phi_i - \phi_j)}{\sin \theta_i \sin(\phi_i - \phi_j)}, \quad (3.73)$$

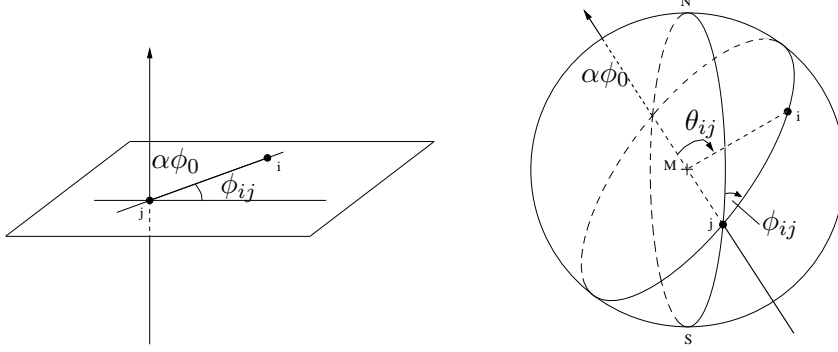


Figure 3.2: On the plane, the relative angle  $\phi_{ij}$  of a vortex  $z_j$  and a particle  $z_i$  is the angle between two geodesics (straight lines), one defined as the horizontal line passing through the vortex  $z_j$ , and the second defined as the geodesic passing through both the vortex  $z_j$  and the particle  $z_i$ . On the sphere,  $\phi_{ij}$  is again the angle between two geodesics, one defined as the great circle passing through both poles and the vortex  $z_j$  and the second defined as the geodesic passing through both the vortex  $z_j$  and the particle  $z_i$ . These geodesics have a second intersection at the point  $-1/\bar{z}_j$  at the antipode of  $z_j$ . Equivalently, one can consider the azimuthal angle of the particle  $i$  in the coordinate system where the south→north axis coincides with the flux line  $j$ : this is again  $\phi_{ij}$ , up to a constant.

or in a different form,

$$\phi_{ij}(z_i, z_j) = \frac{1}{2i} \ln \frac{(\bar{z}_i z_j + 1)(z_i - z_j)\bar{z}_j}{(z_i \bar{z}_j + 1)(\bar{z}_i - \bar{z}_j)z_j}. \quad (3.74)$$

This function is harmonic with respect to  $z_i$  and  $z_j$ . The Cauchy Riemann equations yield the “short distance” behavior

$$|F_{ij}| = \sqrt{\frac{(1 + z_i \bar{z}_j)(1 + \bar{z}_i z_j)}{(z_i - z_j)(\bar{z}_i - \bar{z}_j)}}. \quad (3.75)$$

This leads to the function

$$F_{ij} = \sqrt{z_j \bar{z}_j} \frac{\bar{z}_i + \frac{1}{z_j}}{\bar{z}_i - \bar{z}_j}. \quad (3.76)$$

In the limiting case where  $(z_i = z, z_j \rightarrow 0)$ , (3.76) coincides with  $F = 1/\bar{z}$  up to a constant shift in the phase. Clearly, this function describes a vortex-antivortex pair on the projected plane, at position  $z_j$  and  $-1/\bar{z}_j$ , which are

unsurprisingly the positions where the vortex pierces the sphere. Starting from the free Hamiltonian  $H_i^o$  for particle  $i$ , which is given by

$$H_i^o = -\frac{1}{2}(1 + z_i \bar{z}_i)^2 \partial_i \bar{\partial}_i, \quad (3.77)$$

one may obtain the according Aharonov-Bohm Hamiltonian by substitution of the phase  $\exp(\phi_{ij}(z_i, z_j))$  in  $\Psi_i^o$ . Instead, one can directly construct the Hamiltonian  $\tilde{H}_i$  by substitution of the function (3.76), i.e.,  $\Psi_i^o = (F_{ij})^\alpha \tilde{\Psi}_i$ , such that

$$\begin{aligned} \tilde{H}_i &= F_{ij}^{-\alpha} H_i^o F_{ij}^\alpha \\ &= -\frac{(1 + |z_i|^2)^2}{2} \left\{ \partial_i \bar{\partial}_i + \alpha(\partial_i \ln F_i) \bar{\partial}_i + \alpha(\bar{\partial}_i \ln F_i) \partial_i \right. \\ &\quad \left. + \alpha^2(\partial_i F_i)(\bar{\partial}_i F_i) + \alpha \partial_i \bar{\partial}_i F_i \right\} \\ &= -\frac{(1 + |z_i|^2)^2}{2} \left\{ \partial_i \bar{\partial}_i - \alpha \frac{1 + z_j \bar{z}_j}{(1 + \bar{z}_i z_j)(\bar{z}_i - \bar{z}_j)} \partial_i \right\}. \end{aligned} \quad (3.78)$$

The eigenfunctions are deduced from Eqs. (3.65) and (3.66) upon replacing  $F$  by  $F_{ij}$  and the argument of the hypergeometric function  $x$  by  $x_{ij}$  which equals

$$x_{ij} = \cos \theta_{ij} = \frac{2|z_i - z_j|^2}{(1 + z_i \bar{z}_i)(1 + z_j \bar{z}_j)} - 1. \quad (3.79)$$

We note that

$$\frac{1 + x_{ij}}{2} = \frac{|z_i - z_j|^2}{(1 + z_i \bar{z}_i)(1 + z_j \bar{z}_j)}, \quad \text{and} \quad \frac{1 - x_{ij}}{2} = \frac{|1 + z_i \bar{z}_j|^2}{(1 + z_i \bar{z}_i)(1 + z_j \bar{z}_j)}. \quad (3.80)$$

A particular subset of the solutions possesses a simple analytic form when  $\lambda = \mu$  (i.e.,  $k = 0$ ), such that

$$\Psi_i^o = \begin{cases} (F_{ij})^{m+\alpha} \left(\frac{1+x_{ij}}{2}\right)^{m+\alpha} &= \left(\frac{(1+\bar{z}_i z_j)(z_i - z_j)}{(1+z_i \bar{z}_i)(1+z_j \bar{z}_j)}\right)^{m+\alpha}, & m + \alpha > 0 \\ (\bar{F}_{ij})^{-m-\alpha} \left(\frac{1+x_{ij}}{2}\right)^{-m-\alpha} &= \left(\frac{(1+z_i \bar{z}_j)(\bar{z}_i - \bar{z}_j)}{(1+z_i \bar{z}_i)(1+z_j \bar{z}_j)}\right)^{-m-\alpha}, & m + \alpha < 0, \end{cases} \quad (3.81)$$

which are deformations of (3.69) and (3.70). Upon taking advantage of (3.81), one can define a Hamiltonian  $\tilde{H}_i'$  by means of the substitution  $\Psi_i^o =$

$\left(\frac{(1+\bar{z}_i z_j)(z_i - z_j)}{(1+z_i \bar{z}_i)(1+z_j \bar{z}_j)}\right)^\alpha \tilde{\Psi}'_i$ . This yields

$$\begin{aligned} \tilde{H}'_i = & -\frac{(1+z_i \bar{z}_i)^2}{2} \left\{ \partial_i \bar{\partial}_i + \alpha \frac{1+\bar{z}_i z_j}{(1+z_i \bar{z}_i)(z_i - z_j)} \bar{\partial}_i - \alpha \frac{z_i - z_j}{(1+z_i \bar{z}_i)(1+\bar{z}_i z_j)} \partial_i \right\} \\ & + \frac{1}{2} \alpha (\alpha + 1). \end{aligned} \quad (3.82)$$

### 3.4.3 Generalization to the N-Body Case

Consider now a system of  $N$  identical particles of charge  $e$  and with flux tubes of strength  $\alpha\phi_0$  (now with  $\alpha \in [-1, 1]$ ) attached to them, that are piercing the sphere at the positions of the particles and exiting at their antipodes. In this spherical model, the total flux through the sphere is null, thus there is no Dirac quantization condition on  $\alpha$ . Locally, the relative phase of two particles (3.73) is anyon-like, however globally—and in contrast to the planar anyon model, where  $\phi_{ij} = \phi_{ji} + \pi$ —the phase between two particles is not symmetric. Consequently, it is not possible to intuitively establish a global phase for the many-particle wave function. Nonetheless, each particle must see all the fluxes carried by the other particles. Thus, the phase for particle  $i$  is

$$\phi_i = \sum_{j \neq i} \phi_{ij}. \quad (3.83)$$

Consequently, the A-B Hamiltonian  $H_i^{AB}$  for particle  $i$  coupled to all other particles can be obtained from  $H_i^o$  by extracting the multi-valued phase  $\exp(i\alpha\phi_i)$ . The global A-B Hamiltonian of the system is obtained as the sum of the  $H_i^{AB}$ 's such that

$$H^{AB} = \sum_i H_i^{AB}. \quad (3.84)$$

Contrary to the phase, the “short-distance” behavior (the absolute value of (3.76)) is symmetric under the exchange of particles,  $|F_{ij}| = |F_{ji}|$ , as is expected for a “distance”. One can thus substitute in the A-B Hamiltonian  $H^{AB}$  a global “short-distance” behavior  $\prod_{i < j} |F_{ij}|^\alpha$  (here one restricts to  $\alpha \in [0, 1]$ ) to obtain a global  $\tilde{H}$  Hamiltonian. Equivalently, one can start directly from the free Hamiltonian  $H_i^o$  for particle  $i$  and substitute  $\prod_{j, j \neq i} F_{ij}^\alpha$  to obtain

$$\tilde{H}_i = -\frac{1}{2}(1+z_i \bar{z}_i)^2 \left\{ \partial_i \bar{\partial}_i - \alpha \sum_{j \neq i} \frac{1+z_j \bar{z}_j}{(1+\bar{z}_i z_j)(\bar{z}_i - \bar{z}_j)} \partial_i \right\}. \quad (3.85)$$

Then  $\tilde{H} = \sum_i \tilde{H}_i$ . Or, similar to the considerations above Eq. (3.82),  $\prod_{j,j \neq i} \left( \frac{(1+\bar{z}_i z_j)(z_i - z_j)}{(1+z_i \bar{z}_i)(1+z_j \bar{z}_j)} \right)^\alpha$  can be substituted to obtain  $\tilde{H}'_i$ . The  $N$ -body generalization then reads

$$\begin{aligned} \tilde{H}'_N = \sum_i \tilde{H}'_i = & -\frac{1}{2} \sum_i^N (1 + z_i \bar{z}_i)^2 \partial_i \bar{\partial}_i + \frac{\alpha}{2} \sum_i^N (1 + z_i \bar{z}_i)^2 \times \\ & \left\{ \alpha \sum_{j \neq i} \frac{z_i - z_j}{(1 + \bar{z}_i z_j)(1 + z_i \bar{z}_i)} \partial_i - \alpha \sum_{j \neq i} \frac{1 + \bar{z}_i z_j}{(z_i - z_j)(1 + z_i \bar{z}_i)} \bar{\partial}_i \right\} \\ & + \frac{\alpha(\alpha + 1)}{2} N(N - 1) + \frac{1}{2} \alpha^2 \sum_i \sum_{\substack{j,k \\ j \neq i, k \notin \{i,j\}}} \frac{(1 + \bar{z}_i z_k)(z_i - z_j)}{(z_i - z_k)(1 + \bar{z}_i z_j)}. \end{aligned} \quad (3.86)$$

This Hamiltonian has a complicated structure, as can be seen in particular for the 3-body  $\alpha^2$  term.

### 3.4.4 The Two-Body Case and its Ground State

In the 2-anyon case things simplify, since the  $\alpha^2$  term is now merely a c-number:

$$\begin{aligned} \tilde{H}'_2 = & -\frac{1}{2} (1 + z_1 \bar{z}_1)^2 \partial_1 \bar{\partial}_1 - \frac{1}{2} (1 + z_2 \bar{z}_2)^2 \partial_2 \bar{\partial}_2 \\ & - \frac{\alpha}{2} (1 + z_1 \bar{z}_1)^2 \left\{ \frac{1 + \bar{z}_1 z_2}{(1 + z_1 \bar{z}_1)(z_1 - z_2)} \bar{\partial}_1 - \frac{z_1 - z_2}{(1 + z_1 \bar{z}_1)(1 + \bar{z}_1 z_2)} \partial_1 \right\} \\ & - \frac{\alpha}{2} (1 + z_2 \bar{z}_2)^2 \left\{ \frac{1 + \bar{z}_2 z_1}{(1 + z_2 \bar{z}_2)(z_2 - z_1)} \bar{\partial}_2 - \frac{z_2 - z_1}{(1 + z_2 \bar{z}_2)(1 + \bar{z}_2 z_1)} \partial_2 \right\} \\ & + \alpha(\alpha + 1). \end{aligned} \quad (3.87)$$

It is immediately determined that the ground state is  $\tilde{\Psi}_{GS} = 1$ , with energy  $E_{GS} = \alpha(\alpha + 1)$ , i.e., for the A-B Hamiltonian

$$\Psi_{GS}^{AB} = \left( \frac{|1 + \bar{z}_1 z_2| |z_1 - z_2|}{(1 + z_1 \bar{z}_1)(1 + z_2 \bar{z}_2)} \right)^\alpha. \quad (3.88)$$

Note that when  $\alpha \rightarrow 1$ , the 2-body wave function has a fermionic behavior: when  $z_1 \simeq z_2$ ,  $\Psi_{GS}^{AB}$  vanishes as  $|z_1 - z_2|$  (also when  $z_1 \simeq -1/\bar{z}_2$ ,  $\Psi_{GS}^{AB}$  vanishes as  $|1 + \bar{z}_1 z_2|$ ). Likewise, note that  $\phi_{12} \simeq \phi_{21}$  up to a constant, which confirms that the model is locally anyon-like.



### 3.5 Conclusion

A dimensional reduction scheme has been proposed which relates a quantum mechanical particle on the sphere of radius  $R$  to a chiral particle on a circle of the same radius. This projection parallels the projection between a 2D particle in a harmonic well and a 1D particle in a harmonic well. In both cases, a coherent state representation is essential for the projection. A relationship between the coherent states on the circle and the canonical eigenstates of the sphere was established. An identity that parallels the Bargman transform has been derived in this context.

A generalized Aharonov-Bohm model on the sphere has been defined, with regard to its dimensional reduction to the Calogero-Sutherland model. This model was found to have an anyon-like character and interesting properties: it allows for continuous values of its coupling parameter  $\alpha$ , since it is not subject to any Dirac quantization condition. We have found that the corresponding  $N$ -body Hamiltonian may be expressed in a simple form via stereographic projection coordinates. Its construction follows a geometrical analogy with the plane case: a gauge field defining the interactions between the particles is deduced from the relative phases arising from winding the particles around the flux tubes attached to the other particles. Adding up the vector potentials in this interacting description yields the total Aharonov-Bohm Hamiltonian. This new model implements an interesting modification of the usual properties of anyon exchange statistics, which follows a global phase asymmetry  $\phi_{ij} \neq \phi_{ji}$  that is due to the non-trivial topology of the sphere. In particular, the limit  $\alpha = 1$  does not correspond to free fermions, in this case. As a new property, the model possesses locally anyon-like statistics: at short distances, the phase is symmetric  $\phi_{ij} \simeq \phi_{ji}$ , and can be tuned to an arbitrary fraction of  $2\pi$  as two particles circle around each other at a small separation. We have found evidence of this locally anyon-like character in the fermionic short distance behavior of the 2-body ground state.

## Chapter 4

# Frustrated Magnetic Systems and Spin Ice

In this chapter, we study magnetic spin systems with dipolar interactions in two dimensions. This work was motivated by a study of arrays of magnetic islands recently manufactured using lithographic technology. Though the analysis presented here is motivated mainly by the experimental realization of the system, it has emerged from the stimulating field of frustrated magnetic systems that has given rise to important theoretical developments in recent years. Our results were published in print under the following reference:

G. Möller and R. Moessner, *Phys. Rev. Lett.* **96**, 237202 (2006).  
This article was also selected for the *Virtual Journal of Nanoscale Science & Technology*: Volume 13, Issue 25 (2006).

## 4.1 Introduction

The starting point of quantum Hall physics is a macroscopically degenerate ground state in the single particle picture, where the kinetic energy is quenched, and therefore effectively eliminated as an energy scale. Consequently, electronic interactions that could often be neglected or treated in a mean-field picture or perturbatively, acquire the central role in determining the ground state properties, giving rise to the field of strongly correlated systems. As has been the case for the rich physics that governs the regime of the (fractional) quantum Hall effect, one may hope to find equally interesting effects in other systems with the fundamental property of a macroscopically degenerate ground state manifold.

In the world of the quantum Hall effect, interesting physics results from a large number of degenerate one particle states, when interactions between these particles are such as to cause the ground-state to be gapped, i.e. well-separated from the excitation spectrum. On the contrary, the peculiarity of frustrated magnetic systems is that a macroscopically degenerate ground state manifold arises only from the interactions of its elementary constituents, and there is a large number of such ground states. The idea of such systems, where a large number of ground states is accessible thermodynamically, was first envisioned in Pauling's work on ice [Pauling (1945)]. However, the term 'frustrated' to designate this class of systems was coined only about 30 years thereafter [Toulouse (1977); Villain (1977)].<sup>1</sup> While macroscopic degeneracy plays a somewhat different role in the quantum Hall and frustrated systems, common techniques are used in both fields. For instance, the projection to the ground state manifold is among the mathematical tools which give access to the relevant physics at low temperatures in both cases.

The macroscopic degeneracy of the ground state in ice has also been proposed as a three-dimensional realization of fractional statistics [Ihm (1995)], where fractional statistics are understood in the sense of exclusion statistics [Haldane (1991)]. In the framework proposed there, a mapping between the statistics of the hydrogen configurations under the ice constraint and fractional exclusion statistics is established by assigning the maximal degeneracy in the absence of the ice rules  $d_{\max} = 2^N$  to bosonic statistics and the opposite limit of a totally determined system with  $d_{\min} = 1$  to fermionic statistics. In the presence of the ice-rule constraints, an intermediate statis-

---

<sup>1</sup>Though these two papers are the first time "frustration" appears in print, the word is attributed to P.W. Anderson who supposedly wrote on an Aspen blackboard in 1977 "Frustration is the name of the game."

tics parameter  $\alpha \approx 0.867$  is obtained [Ihm (1995)]. We should note that these counting arguments do not imply the existence of actual particles or excitations of the ground state that exhibit fractional statistics.

Though frustration may appear in different types of physical systems, the archetypal representation of such systems is probably in spin systems. Examples of such frustrated systems are geometrically frustrated antiferromagnets composed of units, each of which does not allow its constituent spins to satisfy all bonds. For instance, take the antiferromagnetic Ising-model on the triangular lattice [Wannier (1950); Houtappel (1950)]. The frustration of the system becomes maximal for lattices with elementary units that are merely site-sharing, such as the *kagomé* lattice [Husimi and Syôzi (1950); Syôzi (1950)], as all constraints are then independent. The solid state community has also shown interest in systems with nearly degenerate ground states with the advent of spin glasses. In contrast to simple antiferromagnetic spin systems, spin glasses have large energy barriers separating local minima in the energy landscape resulting in slow, glassy dynamics.

#### 4.1.1 A historical perspective

Let us take a historic perspective and recapitulate on how ice gave the first impetus to the field of frustrated systems. In the 1930s, the entropy of water at 298K was measured by two different methods: spectroscopically and by integration of the heat capacity from  $T = 15K$  upwards [Giauque and Stout (1936)]. The two results showed a discrepancy of about 0.82 cal/mol·K, very close to the residual entropy of water of  $R \ln 3/2 = 0.81$  cal/mol·K, that Pauling had calculated. Analyzing the unusual structure of ice (see Fig. 4.1), in which oxygen atoms occupy the sites of a wurzite structure and four hydrogen atoms are located around each oxygen atom and on the links between these, Pauling observed that the O-H distance (0.96 Å), essentially the same as in liquid water, is significantly less than half of the O-O distance (2.76 Å). Furthermore, configurations where two hydrogen atoms occupy the same bond between two oxygens are energetically unfavorable and strongly suppressed in real ice at moderate negative temperatures on Celsius' scale. It follows that those configurations with exactly two hydrogens close by each oxygen-site and the other two close to the nearest neighbor oxygen are energetically favored. By virtue of the asymmetry mentioned above, these configurations are distinguishable. The number of possible arrangements satisfying the above rules is large—a naïve count neglecting the lack of independence of constraints yields a macroscopical number of them: for an ice crystal of  $N$  water molecules, there are twice as many hydrogen atoms, and a total of  $2^{2N}$  configurations they may occupy. Considering the constraints

on the four hydrogen bonds around a given oxygen atom, there are a total of  $2^4 = 16$  possible configurations of which only 6, i.e. a fraction of  $3/8$  satisfy the ‘ice rules’. Pauling’s estimate of the zero point entropy [Pauling (1935, 1945)] was based on the approximation that the ice constraint may be imposed independently for each of the  $N$  hydrogen atoms, resulting in a total entropy of  $S = k_B \ln[2^{2N} (\frac{3}{8})^N] = Nk_B \ln \frac{3}{2}$ .

### 4.1.2 Spin Ice

Configurations of ice may be mapped on the configurations of a particular spin-system [Anderson (1956)]. To do so, spins are arranged on the center points of the oxygen-oxygen bonds of the above sketched wurzite structure, yielding a structure of corner-sharing tetrahedra known as the pyrochlore lattice (see Fig. 4.1). Furthermore, preferred orientations or easy-axes for these spins are introduced such that each spin may point either in or out of the two tetrahedra with which it is associated. The mapping between ice and this spin system is such that the displacement of each hydrogen atom from the mid-point of the two neighboring oxygen atoms indicates the direction for the spin on this link.<sup>2</sup> Due to this similarity of water ice and the pyrochlore structure, the spin system just described is also known as spin ice.

The ground state manifold of ice is characterized by the ‘ice-rules’, namely that there be two spins pointing into and two spins pointing out of each tetrahedron, or in water language, that there be exactly two hydrogen atoms adjacent to each oxygen.

To formalize the previous description in a model, a Hamiltonian describing this physics can be written in terms of Ising pseudo-spins  $\sigma = \pm 1$ , with a fixed axis oriented according to the symmetry of the easy axis at the corresponding lattice site. Vector spins  $\mathbf{S}$  are then written as  $\mathbf{S}_{i\alpha} = \sigma_{i\alpha} \mathbf{e}_\alpha$ , where  $\alpha$  is the sublattice index indicating which of the four lattice sites within each unit cell the spin is associated with, and elementary cells are indexed with  $i$ . An appropriate spin Hamiltonian encoding the ice-rules in its ground state is given by

$$\mathcal{H} = J_0 \sum_{\langle(i,\alpha),(j,\beta)\rangle} (\sigma_{i\alpha} \mathbf{e}_\alpha) \cdot (\sigma_{j\beta} \mathbf{e}_\beta), \quad (4.1)$$

where  $\langle \cdot, \cdot \rangle$  notes the sum over nearest neighbor sites. The pyrochlore lattice can be viewed as a face centered cubic lattice with a four site basis and easy axes  $\mathbf{e}_1 = (-1, -1, -1)/\sqrt{3}$ ,  $\mathbf{e}_2 = (1, -1, 1)/\sqrt{3}$ ,  $\mathbf{e}_3 = (1, 1, -1)/\sqrt{3}$  and

<sup>2</sup>Defects with double or void hydrogen occupancy of a link are not represented in the spin-analogue of ice sketched here, but these defects are also very rare in water ice.

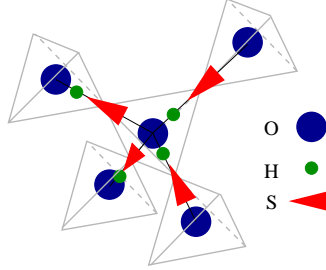


Figure 4.1: Mapping between water ice ( $I_h$ ) and spin ice: in ice, oxygen atoms are arranged on a wurzite lattice, where neighboring oxygens are located on a tetragonal structure. Hydrogen atoms are found on the O-O links, and shifted from its center towards one of the oxygen atoms. This defines the orientations of spins associated with each O-O-bond in the corresponding spin model. The sites of these spins are thus arranged on a lattice of corner-sharing tetrahedra, a structure also known as the pyrochlore lattice. In spin ice, the spins are assigned easy-axes linking the center points of their tetrahedra, i.e. neighboring oxygen sites.

$\mathbf{e}_4 = (-1, 1, 1)/\sqrt{3}$ . In this language, the ice-rules are expressed as a local constraint for each tetrahedron of the lattice:

$$\sum_{(i\alpha) \in \text{tet.}} \sigma_{(i,\alpha)} = 0 \quad (4.2)$$

Note that the scalar product between any pair of the pyrochlore easy axes  $\mathbf{e}_i$  is equal to  $-1/3$ , such that the Hamiltonian (4.1) may be rewritten making explicit use of this fact

$$\mathcal{H} = J \sum_{(i,\alpha),(j,\beta)} \sigma_{i\alpha} \mathcal{J}_{i\alpha,j\beta} \sigma_{j\beta}, \quad (4.3)$$

Here  $\mathcal{J}_{i\alpha,j\beta}$  is the adjacency matrix, and  $J$  represents the effective coupling between neighboring spins. No further geometric factors enter this Hamiltonian.

### 4.1.3 Emergent gauge structure in spin ice

In order to explore the properties of spin ice, it is convenient to consider this model reinterpreting once more its underlying degrees of freedom by means of another mapping [Isakov *et al.* (2004)]. Think of the spins as lattice fluxes forming a flux-field  $\mathbf{S}$ , then a spin-state satisfying the ice-rules (4.2) equivalently obeys the condition

$$\nabla \cdot \mathbf{S} = 0, \quad (4.4)$$

where  $\nabla$  is the appropriate lattice divergence. Contrary to the local constraint (4.2), the field constraint (4.4) may be used to formulate a long-wavelength theory for ice, simplifying the partition sum

$$Z = \sum_{\mathbf{S}} \delta_{\nabla \cdot \mathbf{S}, 0} \quad (4.5)$$

Such a procedure has been used to calculate the correlations in spin ice [Isakov *et al.* (2004)]. The idea is to coarse grain the structure of the underlying crystal and ask what occurs on a larger scale after an effective block-spin transformation  $\mathbf{S} \rightarrow \tilde{\mathbf{S}}$ . Besides the constraint (4.4), the second ingredient required to formulate an effective field theory for  $\tilde{\mathbf{S}}$  is the number of microscopic configurations that correspond to a given value of the field. Observing the number of different ways of arranging the lattice fluxes, one finds that configurations with spins forming closed loops contribute multiple micro-states to a coarse grained configuration. Also, closed loop configurations result in a low field  $\tilde{\mathbf{S}}$  (obtained by averaging over several unit cells): in a closed loop, every magnetic flux is canceled by a peer in the opposite direction, the total flux averaging to zero. As the simplest possible analytic expression that reflects these aspects, a quadratic energy functional is introduced to obtain the effective partition sum:

$$\tilde{Z} = \int \mathcal{D}\tilde{\mathbf{S}} \delta(\nabla \cdot \tilde{\mathbf{S}}) e^{-\frac{\gamma}{2} \int d^3r \tilde{\mathbf{S}}^2}. \quad (4.6)$$

As in magnetostatics the condition of vanishing divergence may be trivially fulfilled expressing  $\mathbf{S}$  as a function of a vector potential  $\mathbf{S} = \nabla \times \mathbf{A}$ . As a result, one obtains a simple Gaussian theory, and the correlators obtained from the latter are familiar expressions from magnetostatics with a dipolar form:

$$\langle \tilde{\mathbf{S}}_z(0) \tilde{\mathbf{S}}_z(r) \rangle \propto \frac{1}{r^3} (3 \cos \theta - 1). \quad (4.7)$$

#### 4.1.4 Spin Ice Materials

While the mapping between ice and spin ice as outlined in section 4.1.2, and the corresponding Hamiltonian (4.3) are derived in a few lines, the question whether magnetic materials with such an arrangement of spins exist in nature has proven to be more difficult to answer [Bramwell and Gingras (2001)]. The first evidence for spin ice behavior in real materials was reported by Harris *et al.* (1997). The material they analyzed was holmium titanate, the rare earth compound  $\text{Ho}_2\text{Ti}_2\text{O}_7$ , in which only the  $\text{Ho}^{3+}$  ions have magnetic moments and occupy lattice sites forming a pyrochlore lattice. Neutron scattering experiments showed that there is no magnetic order

down to temperatures of 0.05 K [Harris *et al.* (1997)]. A strong easy axis anisotropy of these magnetic moments, with their preferred axes pointing towards the center of every tetrahedron of spins, was also reported there, thus relating this system to Ice.

Subsequent precision measurements of this material's heat capacity revealed a zero point entropy corresponding to the magnetic degrees of freedom in spin ice materials which equals that of Ice [Ramirez *et al.* (1999)], confirming the Ice-hypothesis. Nonetheless, an important aspect remained to be understood, namely why the nearest neighbor interaction (4.3) gave a consistent description of the newly discovered spin ice materials, in which one finds long-ranged dipolar interactions between the magnetic sites [Siddharthan *et al.* (1999)]. Moreover, an exchange interaction of the form (4.3) is present between nearest neighbors. The total Hamiltonian that describes the magnetic behavior of spin ice materials is

$$\mathcal{H} = \sum_{(i,\alpha),(j,\beta)} \sigma_{i\alpha} [J\mathcal{J}_{i\alpha,j\beta} + D\mathcal{D}_{i\alpha,j\beta}] \sigma_{j\beta}, \quad (4.8)$$

with the exchange interaction  $J$  between nearest neighbors and the dipole interaction strength  $D = \mu_0\mu^2/4\pi$ . The shape of the long range dipolar interaction is coded by the matrix

$$\mathcal{D}_{i\alpha,j\beta} = \frac{\mathbf{e}_\alpha \cdot \mathbf{e}_\beta}{|\mathbf{r}_{i\alpha,j\beta}|^3} - \frac{3(\mathbf{e}_\alpha \cdot \mathbf{r}_{i\alpha,j\beta})(\mathbf{e}_\beta \cdot \mathbf{r}_{i\alpha,j\beta})}{|\mathbf{r}_{i\alpha,j\beta}|^5}, \quad (4.9)$$

where we note  $\mathbf{r}_{i\alpha,j\beta} = \mathbf{r}_{j\beta}\mathbf{r}_{i\alpha}$  as the vector separating spins  $\mathbf{S}_{i\alpha}$  and  $\mathbf{S}_{j\beta}$ .

#### 4.1.5 Projective Equivalence

The question of why the long range dipolar interactions in spin ice yield essentially the same behavior as nearest neighbor interactions has been elegantly answered by Isakov *et al.* (2005). The starting point of the analysis is a mean field description of the Hamiltonian in which the equivalence of the ground states is manifest [den Hertog and Gingras (2000)]. Transforming this Hamiltonian in Fourier space yields a four by four matrix (according to the number of sublattices or sites per unit cell). Upon a subsequent diagonalization, four bands in Fourier space are obtained with the size of the Brillouin zone defined by the dimensions of unit cells  $k_{\text{BZ}} = \pi/a$ .

For the pure nearest-neighbor interaction (4.3), the lowest two eigenvalues  $\epsilon_{1,2}$  are degenerate, independent of  $\mathbf{k}$ , and are set equal to zero by convention. This degenerate pair of flat bands reflects the macroscopic degeneracy of the ground state manifold: by linearity of the Hamiltonian, each



state that can be written as a Fourier sum of states within these two bands is a ground state. The two remaining bands have some finite dispersion but the low temperature physics depends solely on the low-lying bands. As a consequence, any interaction that only differs in the eigenvalues of these higher bands  $\epsilon_{3,4}$  yields precisely the same low temperature physics for the system (as long as the eigenvectors of the flat bands remain untouched). In particular, upon choosing  $\epsilon_{3,4} \equiv 1$ , one obtains an interaction  $\mathcal{P}$  that is a simple projector [Isakov *et al.* (2005)]

$$\mathcal{P} = \mathcal{P}^2 = \sum_{\mu=3}^4 |v_{\mu}(\mathbf{q})\rangle\langle v_{\mu}(\mathbf{q})|. \quad (4.10)$$

The crucial point is that the dipolar interactions in (4.8) happen to be asymptotically proportional to the projector (4.10). Deviations from this proportionality were found to be of order  $\mathcal{O}(r_{i\alpha,j\beta}^{-5})$  [Isakov *et al.* (2005, 2004); den Hertog and Gingras (2000)], i.e. (4.8) and (4.10) share the same long-distance behavior. The consequence is that, again due to small perturbations, the full spin ice Hamiltonian (4.8) has a pair of nearly flat bands, thus describing a frustrated magnetic system at temperatures  $T$  larger than the residual band-width of the lower band  $\omega$  —as observed in recent experiments [Harris *et al.* (1997); Ramirez *et al.* (1999)]. Experiments have not yet unveiled the ordering transition expected at  $T < \omega$ . This is believed to be explained as a dynamic inability to find this unique ordered state [Snyder *et al.* (2001); Matsuhira *et al.* (2001); Siddharthan *et al.* (2001)].

#### 4.1.6 Square Ice

In two dimensions, the analogue of the ice-model is also known as square-ice. This model is realized by pseudo-ising spins on the links of a square lattice with nearest-neighbor  $J_1$  and next-nearest-neighbor interactions  $J_2$  of equal strength (see Figure 4.2). A mean-field analysis of the Hamiltonian reveals that this model shares the property of displaying a flat band in its spectrum, related to a finite zero point entropy of  $\frac{3}{4} \ln \frac{4}{3}$  per site, that has been determined using the Bethe Ansatz [Lieb (1967a)]. Locally, this macroscopic degeneracy of the ground state may be displayed by the fact that six different spin configurations minimize the interaction energies of spins on one vertex of the square lattice. It then becomes clear that the ground states of square ice relate to the configurations of the six-vertex model. Similarly to the three dimensional case, when considering spins as lattice fluxes, ground state configurations satisfy flux conservation. Consequently, as in 3D, a corresponding gauge theory can be formulated that yields algebraic spin

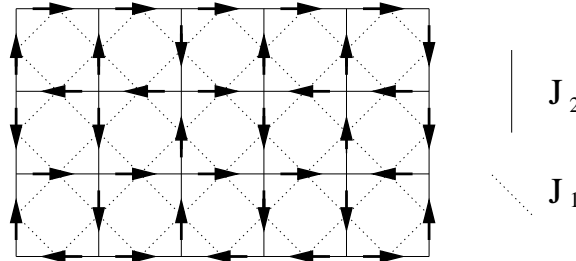


Figure 4.2: A visualization of the square ice model: spins reside on the links of a square lattice. There are interactions  $J_1$  between nearest neighbors, i.e. along diagonals between a pair of spins belonging to the same lattice unit, as indicated with dotted lines. Next nearest neighbor interactions  $J_2$  act between spins linked by solid lines, i.e. those belonging to the same sublattice in adjacent lattice units. In order to obtain square-ice  $J_1 = J_2 = J$ ; in the case of inequality, the so-called F-model is obtained instead. The spin-configuration depicted here satisfies the ice-rules: at each vertex of the square lattice flux is conserved. Thus, six different spin configurations with minimal energy are possible for each vertex. These are frustrated since only four out of six bonds are satisfied.

correlations. The history of this model would still allow for numerous facts to be cited here, among which one finds exact solutions of related models, quantum magnetism and unusual dynamics.

## 4.2 Artificial spin ice

As outlined in section 4.1 and its subsections, spin ice has given an impetus to a large number of experimental and theoretical investigations. Materials which realize this geometrically frustrated structure have been composed using the combinatorial richness of the periodic table of elements. While this provides a certain range of control parameters, the advent of nanotechnology holds the promise to attain the skills to custom-tailor degrees of freedom in condensed matter systems with even more flexibility. Recent proposals for manufactured structures with many interacting degrees of freedom have included a topologically protected quantum computer based on Josephson junction arrays [Ioffe *et al.* (2002)] as well as submicron superconducting rings that provide effective spin- $\frac{1}{2}$  degrees of freedom [Davidovic *et al.* (1996); Hilgenkamp *et al.* (2003)].

Motivated by the rich features unearthed during the history of the square ice model, and since appropriate techniques for manufacturing 2D systems are available, Wang *et al.* (2006) have attempted to realize this model in an

artificial structure.

The starting point for their system is the fact that sufficiently small islands of a magnetic material represent a single magnetic domain and may mimic a single spin with relatively large magnetic moment. Choosing an anisotropic shape for these domains, rectangular in the study of Wang *et al.* (2006), these spins acquire a preferential orientation and thus act like pseudo Ising spins. This behavior is a property of the dipole interactions (4.9). The interaction energy of a pair of aligned spins  $\mathbf{S}_i \cdot \mathbf{S}_j = 1$  is negative if they point parallel to the vector relating their positions. However, it is positive if they point in the direction perpendicular to this line.

$$E_{\text{dipole}}(\mathbf{S}_i, \mathbf{S}_j) = \begin{cases} -2J/r_{ij}^3 & , \text{ if } \mathbf{r}_{ij} \parallel \mathbf{S}_{i,j} \\ +J/r_{ij}^3 & , \text{ if } \mathbf{r}_{ij} \perp \mathbf{S}_{i,j} \end{cases} \quad (4.11)$$

Note that the energy gain by alignment in the former of these two cases is twice stronger than the energy loss for alignment in the latter case. Assuming for example a uniform spin polarization of an elliptic magnetic domain, the interaction energy is minimized for the alignment of spins along the long axis of this shape.

Arrays of ferromagnetic islands with such an anisotropy were fabricated placing permalloy structures ( $\text{Ni}_{0.81}\text{Fe}_{0.19}$ ) on a silicon substrate [Wang *et al.* (2006)] using lithographic methods [Martín *et al.* (2003)]. An atomic force microscopic image of one of the samples is given in Fig. 4.3(a). Several such arrays were examined, which had different lattice constants  $a$  ranging from 320nm to 800nm, while the size of the magnetic islands forming individual dipoles was kept constant at 80nm×220nm laterally and 25nm wide, resulting in magnetic moments of  $\mu \approx 3 \cdot 10^7 \mu_0$ . Thus, the strength of nearest-neighbor interactions was tuned in a large interval—for the given dimensions they ranged from about 3000 to  $10^5$  Kelvin.

Magnetic configurations were found to be stable at room temperature, thus an experimental protocol was devised to introduce dynamics into the system, which consisted in rotating the sample at 1000 r.p.m. in an in-plane magnetic field that was gradually stepped down in amplitude from an initial field of 1300 Oerstedt. Since this initial field is well above the coercive field of the islands, one may hope that this initially generates a random spin configuration.<sup>3</sup> Upon “cooling down”, spins will feel the interactions between

---

<sup>3</sup>This statement is based on the hypothesis that ‘spin-flips’ are induced frequently by the quickly rotating field, but not so quickly that the magnetization of all domains is permanently pointing in the direction of the external field. The actual behavior of the permalloy islands might be much more complicated than this, especially since some islands might be much more susceptible to changing their magnetization than others due to disorder of their shape.

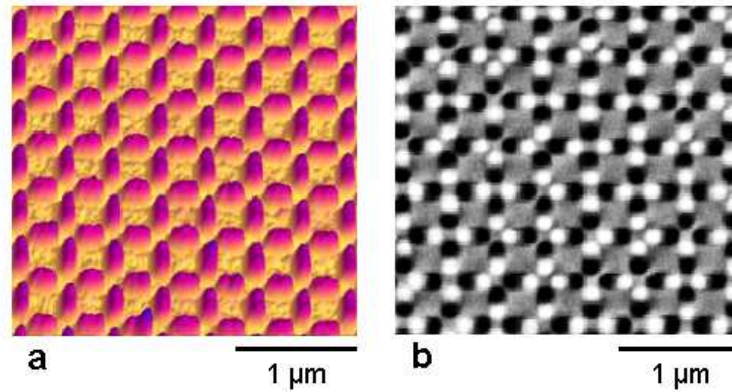


Figure 4.3: (a) An AFM picture of one of an array of magnetic permalloy islands that realizes a two dimensional spin model. The dimensions of a single island are about 80nm times 220 nm, with a thickness of 25nm; the lattice spacing is 400nm. (b) Magnetic states of single islands, as recorded by atomic force microscopy (after Wang *et al.* (2006)). Black and white coloring corresponds to north- and south-poles of local dipoles respectively. It is evident that all islands are in a dipole configuration, allowing only a reversal of the direction of magnetization. More complicated magnetic states within single permalloy islands are absent.

islands and develop non-trivial correlations.

After undergoing this procedure, resulting spin configurations were examined by magnetic force microscopy, a method giving access to the state of individual ‘spins’, as confirmed by a sample result of such measurements represented in Fig. 4.3(b). Finally, these results were evaluated with respect to spin correlations and the frequency with which different vertex types occur: four spins adjacent to a crossing of second neighbor bonds allow for spin configurations with  $2^4 = 16$  possible micro-states. These fall in four classes distinguished by their respective energies (see Tab. 4.1), since nearest-neighbor interactions  $J_1$  and next-nearest-neighbor interactions  $J_2$  differ in this system of interacting dipoles.

Wang *et al.* (2006) reported that nearest- and next-nearest-neighbor correlations in the analyzed arrays increased upon decreasing the lattice spacing of dipoles, i.e. upon increasing the interactions. Wang and colleagues also counted the statistics of vertex types and found increased incidence of Type I and Type II vertices, the ‘ice-rule’ vertices, whereas the occurrence of Type III and Type IV vertices decreased with respect to a random distribution. However, further neighbor correlations were found to vanish rapidly. Some

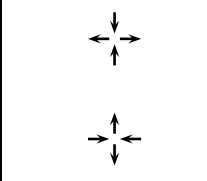
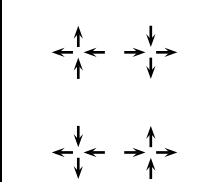
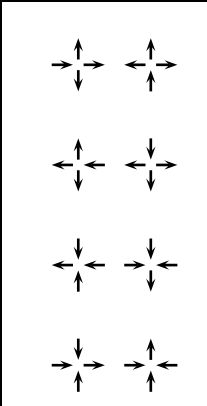
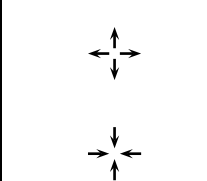
Type	Configurations	$E$	$\nabla \cdot \mathbf{S}$	$\boldsymbol{\mu} = \sum_i \boldsymbol{\mu}_i$	Weight
I		$-4J_1 + 2J_2$	0	0	12.5%
II		$-2J_2$	0	$2\boldsymbol{\mu}(\pm \mathbf{e}_1 \pm \mathbf{e}_2)$	25%
III		0	$\pm 1$	$2\boldsymbol{\mu}(\pm \mathbf{e}_{1,2})$	50%
IV		$4J_1 + 2J_2$	$\pm 4$	0	12.5%

Table 4.1: Vertex types and their characteristics: energy, ‘charge’ (equal to the lattice divergence, interpreting spins as flux), total magnetic moment, and the weight of these spin configurations in configuration space. If  $J_1 = J_2$  the energies of Type I and Type II vertices are degenerate. These are also the configurations of the six-vertex model which satisfy the ice-rule  $\nabla \cdot \mathbf{S} = 0$ .

of their experimental results can be found in Figure 4.12 where they are compared against those obtained from theoretical models we examined.

### 4.3 Models for artificial square ice and related dipolar arrays

The pioneering study by Wang *et al.* (2006), described in section 4.2, raises a number of important theoretical questions, further motivating the theoretical examination outlined in the remainder of this chapter. First, we would like to stress that the techniques used to manufacture the arrays presented in this study represent a powerful tool which opens up new paths for exploring the properties of spin systems. Thus, the cited study is most probably the prelude to a series of increasingly more sophisticated investigations of this kind. Consequently, we seek to understand the properties of the experimental system with the intent of exploring possibilities to extend and improve its design approach. In particular, the question of whether a two dimensional system with long range dipolar interactions can be modeled by the short-range (square) ice model is addressed in analogy to the three dimensional case outlined previously in Section 4.1.5. Since the experiment by Wang *et al.* (2006) utilized an external perturbation in the form of a rotating magnetic field to induce dynamics in their dipolar arrays, we also tried to shed light on the properties of these dynamics.

#### 4.3.1 Spectra in Fourier space

As a starting point, we consider point-like dipoles on the links of a square lattice and analyze the spectrum of the corresponding Hamiltonian in a mean field theory [Melko *et al.* (2001)]. The permalloy islands in the experiment [Wang *et al.* (2006)] are sufficiently large that the resulting magnetic moments clearly can be treated as classical variables. In particular, remaining at the level of a classical system for the discussion of this model, there is no exchange interaction between nearest neighbor islands: interactions are purely dipolar. Since each magnetic island allows for only two possible configurations, as in (4.8), the Hamiltonian of our dipolar model may be written in terms of Ising pseudo-spin variables. The structure is modeled as two distinct sublattices with spins pointing in the horizontal direction forming the first, and those disposed vertically forming the second sublattice.

For a finite lattice with  $N$  unit cells,

$$\mathcal{H} = D \sum_{i,j=1}^N \sum_{\alpha,\beta=1}^2 \sigma_{i\alpha} \mathcal{D}_{i\alpha,j\beta} \sigma_{j\beta}. \quad (4.12)$$

The interaction matrix is defined again as in (4.9), and the locations of lattice sites are decomposed as a vector to the unit cell (indexed with the roman index  $i = 1 \dots N$ ) and a relative displacement for each sublattice (second, greek index  $\alpha$ ).

$$\mathbf{r}_{i\alpha} = \mathbf{r}_i^0 + \boldsymbol{\rho}_\alpha \quad (4.13)$$

For convenience, all length scales on the lattice are taken dimensionless, and the corresponding scaling of the interaction energies absorbed in  $D$  such that  $D = \mu_0 \mu^2 / (4\pi a^3)$ . Upon referencing the unit cells of the square lattice by their lower left corner, the appropriate sublattice vectors are

$$\boldsymbol{\rho}_1 = \frac{1}{2} \mathbf{e}_x, \text{ and } \boldsymbol{\rho}_2 = \frac{1}{2} \mathbf{e}_y. \quad (4.14)$$

As a first step towards obtaining the spectrum of the Hamiltonian, a Fourier transform is performed separately for each sublattice. The conventions for this transformation are chosen as

$$\sigma_{\mathbf{q}\alpha} = \sum_j \sigma_{j\alpha} e^{-i\mathbf{q}\cdot\mathbf{r}_j^\alpha}, \quad (4.15)$$

and for the inverse transform

$$\sigma_{j\alpha} = \frac{1}{N} \sum_{\mathbf{q}} \sigma_{\mathbf{q}\alpha} e^{i\mathbf{q}\cdot\mathbf{r}_j^\alpha}. \quad (4.16)$$

The Hamiltonian obtained after Fourier transformation is

$$\mathcal{H} = \frac{1}{2N} \sum_{\mathbf{q}} \sigma_{\mathbf{q}\alpha} V_{\mathbf{q}}^{\alpha\beta} \sigma_{-\mathbf{q}\beta}, \quad (4.17)$$

where the interaction  $V_{\mathbf{q}}^{\alpha\beta}$  is a real and symmetric  $2 \times 2$  matrix, and summation over repeated indices is implied by convention. As the final step,  $V_{\mathbf{q}}^{\alpha\beta}$  must be diagonalized to yield the energy eigenvalues. To cite an example, consider the first two possible terms for a general interaction with nearest-neighbor interactions of amplitude  $J_1$  relating different sublattices and longitudinal next-nearest-neighbor interactions (as present in the ice model) of amplitude  $J_2$ . The former connects different sublattices and thus generates off-diagonal elements, and the latter connect spins within the same

sublattice and yields diagonal ones. The example Fourier-transformed interaction is then:

$$V_{\mathbf{q}} = - \begin{pmatrix} J_2 \cos q_x & J_1 \left[ \cos \frac{q_x+q_y}{2} - \cos \frac{q_x-q_y}{2} \right] \\ J_1 \left[ \cos \frac{q_x+q_y}{2} - \cos \frac{q_x-q_y}{2} \right] & J_2 \cos q_y \end{pmatrix} \quad (4.18)$$

Changing the basis to new effective spin variables

$$\tilde{\sigma}_{\alpha} = (A^T)_{\alpha\alpha'} \sigma_{\alpha'} \quad (4.19)$$

a diagonal form of the interaction matrix is achieved

$$(\tilde{V}_{\mathbf{q}}^n)_{\alpha\beta} = (A^T)_{\alpha\alpha'} V_{\mathbf{q}}^{\alpha'\beta'} A_{\beta\beta'} \equiv J_n(\mathbf{q}) \delta_{\alpha\beta}. \quad (4.20)$$

Note that we introduced  $J_n(\mathbf{q})$  as an alias of the diagonal form of  $V_{\mathbf{q}}$ . The adjoint matrix  $A$  is formed by the eigenvectors  $\mathbf{v}_n$  of the original interaction matrix  $V_{\mathbf{q}}^{\alpha\beta}$ , notably  $A_{n\alpha} = (\mathbf{v}_n)_{\alpha}$ .

**Eigenvalues of square ice:** As an instructive example, we will calculate the eigenvalues and eigenvectors of square ice. In the latter part of this section, different models will be compared against these results. The Fourier space interaction matrix of square ice is given by (4.18) with  $J_1 = J_2 \equiv J$ . It is then convenient to express the matrix elements in terms of  $u = \sin(q_x/2)$  and  $v = \sin(q_y/2)$ :

$$V_{\mathbf{q}}^{\text{ice}} = -J \begin{pmatrix} 1 - 2u^2 & -2uv \\ -2uv & 1 - 2v^2 \end{pmatrix} \quad (4.21)$$

The eigenvalues yield the following band structure with indices  $n = l$  marking the lower band, and  $n = u$  the upper one:

$$J_l^{\text{ice}}(\mathbf{q}) = 0 ; J_u^{\text{ice}}(q) = 2J(u^2 + v^2) = 2J \left( \sin^2 \frac{q_x}{2} + \sin^2 \frac{q_y}{2} \right). \quad (4.22)$$

For convenience, the energy of the lower flat band has been defined as the zero point of the energy scale. It is the flatness of this lower branch that indicates the frustration of this Ising-ice model. The corresponding eigenvectors are:

$$\mathbf{v}_l^{\text{ice}}(\mathbf{q}) = \frac{1}{\sqrt{u^2 + v^2}} \begin{pmatrix} v \\ -u \end{pmatrix} ; \mathbf{v}_u^{\text{ice}}(\mathbf{q}) = \frac{1}{\sqrt{u^2 + v^2}} \begin{pmatrix} u \\ v \end{pmatrix} \quad (4.23)$$

In order for a model to have the same low-temperature physics as this ice model, it is required that its lower branch be flat and that it shares the eigenvectors of the Ising-ice model.



**Eigenvalues of nearest-neighbor interaction:** For the dipole interaction, the nearest-neighbor interaction is increased with respect to further neighbor terms that fall off as  $r^{-3}$ . As a didactic example that exaggerates this behavior, we shall first consider a model where only the nearest-neighbor interactions persist and all others vanish, i.e. we set  $J_2 = 0$  in (4.18). The result is a symmetric pair of bands

$$J_{l,u}^{\text{NN}}(\mathbf{q}) = \mp 2J \left| \sin \frac{q_x}{2} \sin \frac{q_y}{2} \right|. \quad (4.24)$$

While this is a rather simple result, analyzing the eigenvector reveals a surprise: though the eigenvalues are very different from those of Ising-ice, the overlaps of the eigenvectors of these two models are rather large. First, let us note that the eigenvectors of the lowest band  $J_l(\mathbf{q})$  are discontinuous in  $\mathbf{q}$ , since there is a crossing of two analytic bands  $2J \sin \frac{q_x}{2} \sin \frac{q_y}{2}$  at the coordinate axes:

$$\mathbf{v}_l^{\text{NN}}(\mathbf{q}) = \begin{cases} \frac{1}{\sqrt{2}} \begin{pmatrix} 1 \\ -1 \end{pmatrix} & , \text{ if } q_x q_y > 0 \\ \frac{1}{\sqrt{2}} \begin{pmatrix} 1 \\ 1 \end{pmatrix} & , \text{ if } q_x q_y < 0 \\ \text{any} & , \text{ if } q_x q_y = 0 \end{cases} \quad (4.25)$$

As a result, the scalar product of the eigenvectors is given by

$$|\mathbf{v}_l^{\text{NN}} \cdot \mathbf{v}_l^{\text{ice}}| = \frac{|u| + |v|}{\sqrt{2(u^2 + v^2)}} \geq \frac{1}{\sqrt{2}}. \quad (4.26)$$

The eigenvectors of the Ising-ice and the nearest-neighbor model never form an angle of more than  $\frac{\pi}{4}$ . Moreover, along the diagonals of the Brillouin zone with  $|q_x| = |q_y|$  the eigenvectors are identical.

**Eigenvalues of the ‘F-model’:** In the sequence of simple spin-models on the square lattice the F-model deserves to be mentioned, which is a deformation of the six-vertex model where the vertices that are named Type II vertices in Wang *et al.* (2006) and the present document (see Table 4.1) acquire an energy larger than the Type I [Lieb (1967b)]. To be precise, the configurations of the F-model consist of all spin configurations involving only these two types of vertices, whereas the spin-model discussed in this paragraph allows arbitrary spin configurations. Nonetheless, thermodynamic configurations at low temperature are expected to consist primarily of Type I and Type II vertices. In this sense, an ‘F-model’ can be obtained by detuning  $J_1$  and  $J_2$  with respect to the ice-model. The case that we are

interested in here is when these two interactions take the values that correspond to those of the dipolar interaction (4.9). Namely, for this dipolar interaction with a very short cut-off, we have  $J_1 = 3\sqrt{2}$  and  $J_2 = 2$ . As for the nearest-neighbor model discussed in the previous paragraph, it continues to be true that the eigenvectors of this interaction are identical along the diagonals of the Brillouin zone. This fact arises from a particular structure of the interaction matrix. Since the interaction is isotropic and invariant under lattice symmetries, the value of the interaction matrix  $V_{\mathbf{q}}$  is the same at all inverse lattice vectors that are related by such symmetry operations up to a sign. In particular, all points with  $|q_x| = |q_y| = q$  satisfy this property, and a particular element of the corresponding symmetry group realizes an exchange of the  $x$  and  $y$ -axes. But this also exchanges both sublattices, thus  $V_{11}(q_x, q_x) = V_{22}(q_x, q_x)$ . Consequently, along the diagonals of the Brillouin zone

$$V(q_x, \pm q_x) \propto \begin{pmatrix} a & b \\ b & a \end{pmatrix} \quad (4.27)$$

The eigenvector corresponding to the lowest eigenvalue of this matrix is

$$\mathbf{v}_l = \frac{1}{\sqrt{2}} \begin{cases} \mathbf{e}_x - \mathbf{e}_y & , \text{ for } b > 0 \\ \mathbf{e}_x + \mathbf{e}_y & , \text{ for } b < 0 \end{cases} . \quad (4.28)$$

Thus, a sufficient condition for eigenvectors of the two interactions to be the same is that the sign of the off-diagonal terms is identical. Since only the prefactor was changed, this holds true.

In addition, the eigenvectors of the ice-model and the F-model are also identical along the momentum axes  $q_{x,y}$ : in this case, the off-diagonal terms of the interaction matrix (4.18) vanish for both interactions.

**Eigenvalues of the dipolar interaction:** The spectrum for a dipolar interaction is intermediate between the two spectra discussed before. The full dipolar interaction (4.9) is long-range, and the entries of the interaction matrix now become sums of numerous cosine terms. As before, interaction terms relating spins on different sublattices yield an off-diagonal term of the interaction matrix. The diagonal terms are those relating spins on the same sublattice. With the structure of the dipolar interaction (4.9), the first summand is the only contribution for diagonal terms. As for the F-model interaction, we obtain  $V_{11}(q_x, q_x) = V_{22}(q_x, q_x)$  along the diagonals such that the symmetry of the interaction matrix (4.27) also holds for the general dipolar interaction. As the off-diagonal elements of the interaction

matrix may be written as

$$J_{12}(\mathbf{q}) = \sum_{u_x > 0, u_y > 0} J(\mathbf{u}) [\cos(u_x q_x + u_y q_y) - \cos(u_x q_x - u_y q_y)], \quad (4.29)$$

along the diagonal, the sign of these interaction elements equals that of  $J_{12}$  in the ice model:

$$\cos((u_x + u_y)q) - \cos((u_x - u_y)q) = -2 \sin(u_x q) \sin(u_y q). \quad (4.30)$$

Thus, it still holds true that the eigenvectors of the lower band are identical to those of the ice-model  $\mathbf{v}_l^{\text{ice}}$  along the diagonals of the Brillouin zone as well as along the coordinate axes.

Regarding the shape of the band structure for small  $k$ , i.e. regarding the long-distance behavior of the interactions, it is instructive to consider the interaction between spins in two distant unit cells. The discrete character of the lattice is then negligible, and the relative position of the unit cells considered is given in polar coordinates  $(r, \theta)$ . As above, we write the interactions of spins on various sublattices as an interaction matrix

$$\mathcal{D} = \frac{D}{r^3} \begin{pmatrix} 1 - 3 \cos^2 \theta & -3 \cos \theta \sin \theta \\ -3 \cos \theta \sin \theta & 1 - 3 \sin^2 \theta \end{pmatrix}. \quad (4.31)$$

Diagonalizing this matrix, we find eigenvalues that have no angular dependence (whereas eigenvectors depend on  $\theta$ ). The Fourier transform of the remaining radially symmetric function  $1/r^3$  is readily obtained by dimensional analysis. In  $d$  dimensions, for a general power of  $r$  and in the continuum limit

$$\int d^d r e^{i\mathbf{k}r} r^{-n} = k^{n-d} \int dx d\Omega e^{ix \cos \theta} x^{d-n-1} = k^{n-d} \pi^{n-\frac{d}{2}} \frac{\Gamma(\frac{d-n}{2})}{\Gamma(\frac{n}{2})} \quad (4.32)$$

For the current problem with  $d = 2$ , we find a dispersion as  $E \propto k$  for small  $k$ . We may also compare to the results of Isakov *et al.* (2005) with  $d = 3$ , who analyzed the corresponding case with  $d = 3$  and found a series of flat bands and an upper band with a discontinuity as a Kronecker delta at  $k = 0$ .

Further analysis calls for a numerical calculation of the spectra and eigenvectors. A cut-off distance  $r_{\text{max}}$  needs to be introduced to this end, such as to reduce the summation over elements as (4.29) to a finite number of terms. Three-dimensional plots of the spectrum for the dipolar interaction with  $r_{\text{max}} = 10$ , and the simple models discussed in the previous paragraphs are shown in Figure 4.4. None of the spectra shown here resemble the spin ice spectrum; the latter is the only one which exhibits a flat band that can

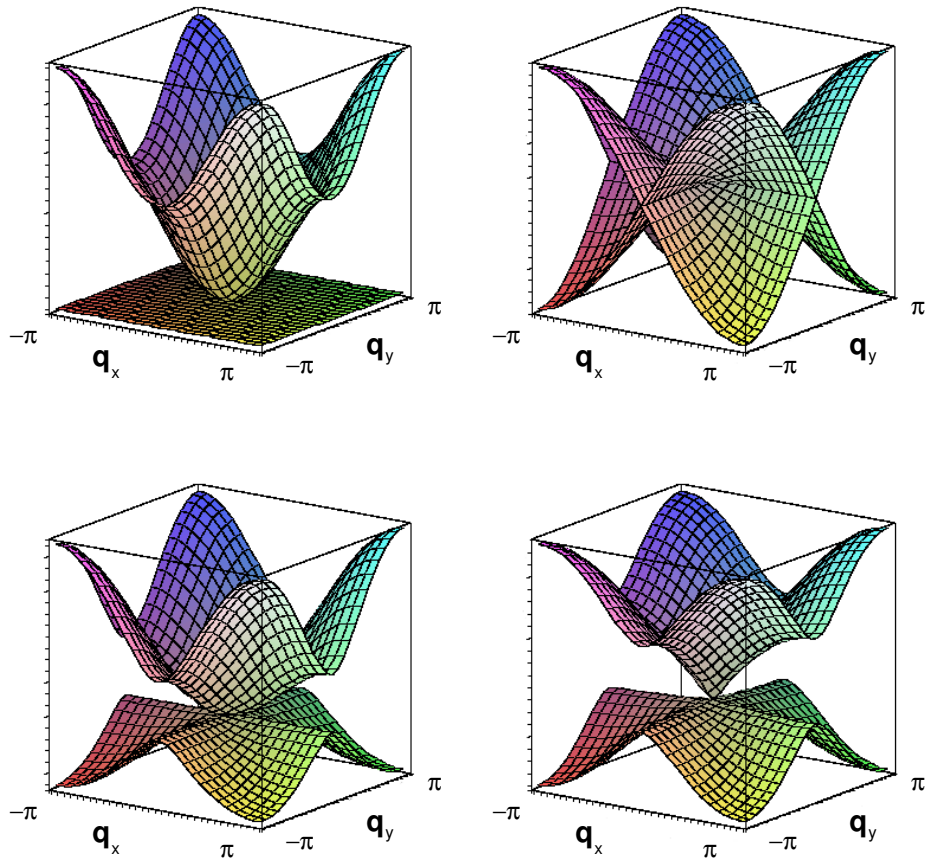


Figure 4.4: Spectra for spin models with pseudo-Ising spins on the bonds of a square lattice. The Ising-ice model (top left), the nearest-neighbor interaction (top right), the F-model with nearest- and next-nearest-neighbor interactions as in the ice-model detuned to the values of the dipolar interaction (bottom left) and the dipolar model with a cut-off distance of  $r_{\max} = 10$  (bottom right).

be associated with a macroscopic ground state degeneracy. Roughly, the dispersion of the nearest-neighbor model gives the dominant contribution for the dipolar interaction. When taking into account the longitudinal second neighbors, as in the F-model, a lower band is obtained that is very similar to the one observed for the dipolar interaction with cut-off  $r_{\max} = 10$ . The most marked difference between the F-model and the dipolar interaction is the shape of the upper band: the latter develops a central part shaped as a reversed cone as expected from 4.32. The lower band accounts for approximately one third of the total bandwidth in both cases.

Besides the requirements of a flat lower band, the second condition that is required for an interaction to yield the same low temperature physics as the ice model is that the eigenvectors of the Hamiltonian are the same for both interactions. Above, we have seen how some symmetries cause these eigenvectors to be identical along certain symmetry axes in the Brillouin zone. In order to obtain a larger view of this feature, we have numerically examined the overlap, i.e. the square of the scalar product of corresponding eigenvectors in the lower band  $|\mathbf{v}_l^{\text{ice}}(\mathbf{q}) \cdot \mathbf{v}_l^{\text{other}}(\mathbf{q})|^2$ . We find that this value varies smoothly as a function of  $\mathbf{q}$  and consequently, since this value is forced to be one along the main symmetry axes, only small deviations from 1 are found. This is displayed in Figure 4.5. From this point of view, the dipolar interaction in a two-dimensional array represents a very favorable candidate for projective equivalence with the ice-model.

In order to analyze how the spectrum of the dipolar interaction evolves as a function of the cut-off distance  $r_{\max}$ , we chose a more elementary graphical representation. To this end, note that the spectra in Figure 4.4 are well characterized by their aspect along the high symmetry axes, given here by the coordinate axes  $q_i$  and the diagonals of the Brillouin zone where  $|q_x| = |q_y|$ . Therefore, in Figure 4.6 the eigenvalues of the Hamiltonian are shown for different values of the cut-off, with  $J_{\mathbf{q}}$  given along a path in the Brillouin zone (BZ) that successively follows these two axes from a center point of the BZ boundary  $X = (0, \pi)$  to the center 0 and then towards the corner  $K = (\pi, \pi)$  (as depicted in the top part of this figure). The top part of Figure 4.6 focuses on the development of the interaction for small values of  $r_{\max}$ . The dispersion of both bands changes quite noticeably for  $r_{\max} \lesssim 10$ , but successive terms have significant influence only in the center region of the Brillouin zone (see the bottom part). The relatively rapid convergence of the Fourier sum leading to these spectra is not surprising, since a Fourier sum of a  $1/r^3$  interaction in two dimensions is absolutely convergent

$$\int_a^R r dr d\varphi \frac{1}{r^3} \propto \frac{1}{R} - \frac{1}{a}, \quad (4.33)$$

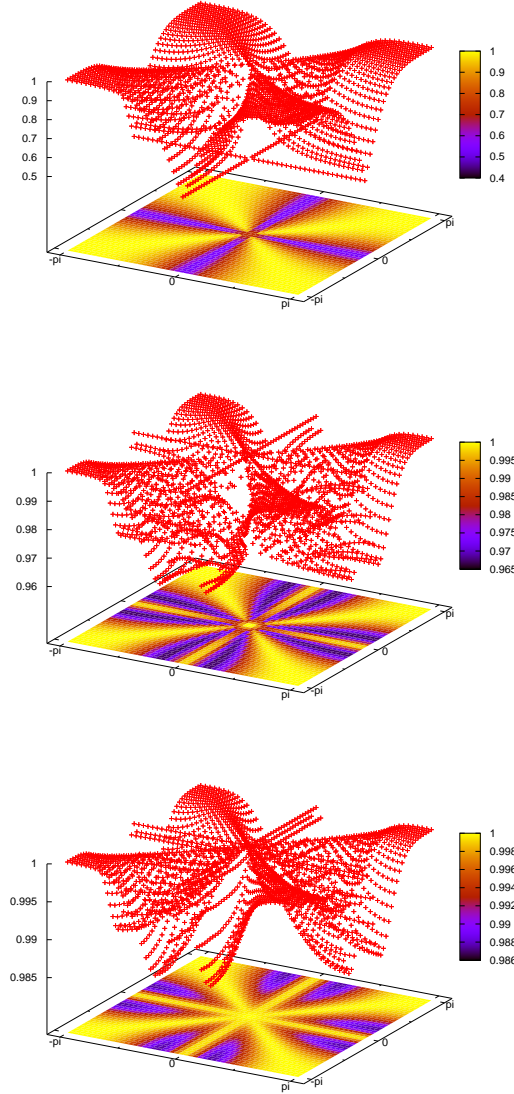


Figure 4.5: Overlap of the eigenvectors in the lower band of different interactions with respect to the ice-interaction  $|\mathbf{v}_l^{\text{ice}}(\mathbf{q}) \cdot \mathbf{v}_l^{\text{other}}(\mathbf{q})|^2$ . From top to bottom, the nearest-neighbor interaction, the F-model interaction and the dipolar interaction with cut-off  $r_{\text{max}} = 10$  are chosen for the second model. Note that the scale of the  $z$ -axis changes: whereas the minimal overlap is 0.5 for the NN-model, its deviation from 1 is only  $\sim 3.5\%$  for the NN-interaction and a mere  $\sim 1.5\%$  for the dipolar one.

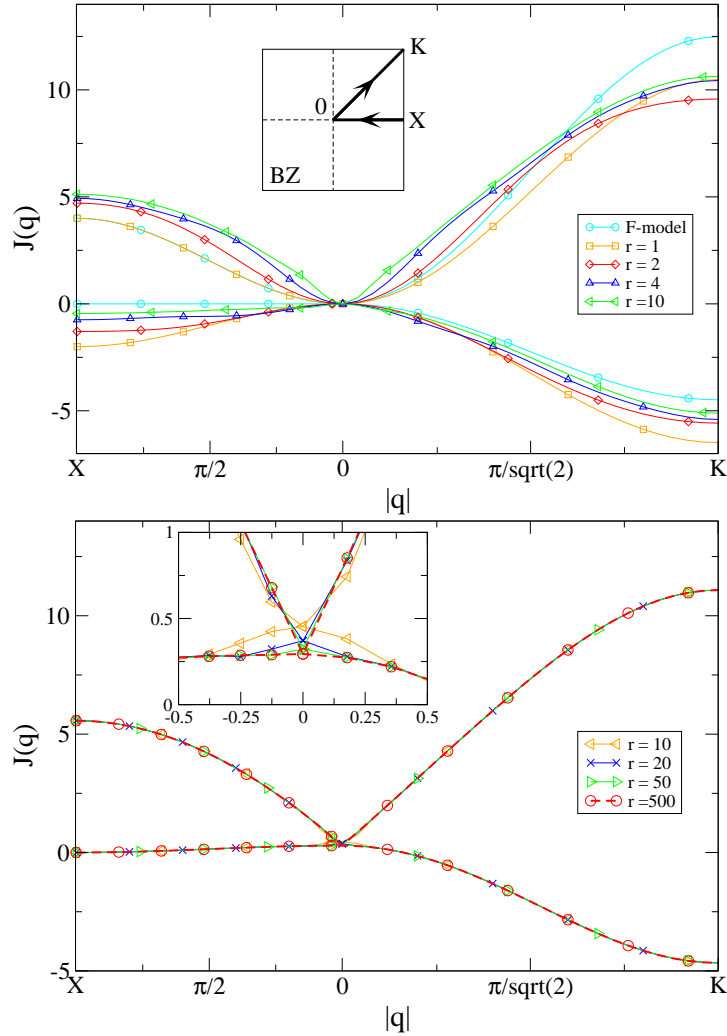


Figure 4.6: Top: Evolution of the spectrum of ‘artificial ice’ as a function of the cut-off  $r$ . Eigenvalues of the Hamiltonian  $J_n(\mathbf{q})$  along the main symmetry axes, following the path in the Brillouin zone as indicated in the inset. For better visibility, the spectra are shifted such that  $J(\mathbf{q} = 0) = 0$ . Note that overall shape of the dispersion of the lower band remains very similar to that of the F-model, taking into account only the first two interaction terms of the dipolar model. Bottom: Eigenvalues of the Hamiltonian  $J_n(\mathbf{q})$  along the same path, but for larger values of the cut-off  $r$ . For sufficiently large  $|\mathbf{q}|$ , the development of the interaction has already converged for the smallest cut-off displayed here,  $r_{\max} = 10$ . To display this effect, spectra are shifted such that the values at large  $|\mathbf{q}|$  coincide. Successive terms of the development shape the center region of the Brillouin zone, such that the lower band appears to be flat and the upper band resembles a cone for small  $|\mathbf{q}|$  (see magnification of the part around the BZ center in the inset).

where the lattice constant  $a$  is the natural infrared cut-off for lattice problems. Additionally, the dipolar interaction has a non-trivial angular dependence,  $V(\varphi) \propto (3 \cos^2 \varphi - 1)$ , for parallel spins that contributes to the fast convergence observed. Knowledge about the approximate convergence of the Fourier sum for  $V_{\mathbf{q}}$  will be useful to the numerical simulations presented below.

From the analysis of the discussed spectra, we may conclude that a thermodynamic transition to an ordered phase is expected for the dipolar interaction. This ordered phase, found at  $\mathbf{q} = (\pm\pi, \pm\pi)$  in momentum space corresponds to forming closed loops of spins around the unit cells of the square lattice. This can also be interpreted as a tiling of the square lattice with Type I vertices exclusively. On each of the sublattices, spins then form a perfect antiferromagnetic order or Néel state. Before analyzing the thermodynamics of this transition, we shall demonstrate that a flat lower band can indeed be achieved with dipolar interactions in two dimensions via slight modifications in the geometry of the model system.

**Flat bands with dipolar interactions on a square lattice** From the above analysis, we conclude that the main cause for the dipoles on the bonds of a square lattice yielding only a weakly frustrated magnetic system is the inequality of the nearest-neighbor interactions  $J_1$  and next-nearest-neighbor interactions  $J_2$ : the dispersion of the lower band of the dipolar interaction essentially remains like that of the F-model, as outlined in the preceding paragraphs. This can be seen in contrast to spin ice in three dimensions, where the interactions between four spins forming a vertex are all equivalent. One then has to ask, how the interactions between the spins of a vertex of the two-dimensional square lattice can be tuned such as to equal one another. In other words, how does one achieve equal energies of Type I and Type II vertices?

In view of the geometry of samples in the experiment [Wang *et al.* (2006)] that motivated the work presented here, we shall model the magnetic islands with a finite extension. The energy of a magnetic dipole is given as the integral over local dipole densities

$$H = \iint d\vec{r}_i d\vec{r}_j \frac{\vec{\mu}(\vec{r}_i) \cdot \vec{\mu}(\vec{r}_j) - 3[\vec{\mu}(\vec{r}_i) \cdot \hat{r}_{ij}][\vec{\mu}(\vec{r}_j) \cdot \hat{r}_{ij}]}{r_{ij}^3}, \quad (4.34)$$

where  $\vec{\mu}(\vec{r}_i)$  is the dipole moment at position  $\vec{r}_i$ , and  $r_{ij} = |\vec{r}_i - \vec{r}_j|$ .

More specifically, we suppose that the magnetic islands may be regarded as uniform, mono-domain thin needles of finite length  $l$ . Then for a magnetic domain of length  $l$  and total magnetic moment  $\mu$ , the local magnetic



moment is written as  $\vec{\mu}(\vec{r}_i) = (\mu/l)d\ell\sigma_i\vec{e}_{\alpha(i)}$  where only one linear variable  $\ell$  is integrated over, and  $\sigma_i$  and  $\vec{e}_{\alpha}$  are the pseudo-spin variable and sublattice orientation as before. In this approach, the extension of the dipoles in the transverse direction is still neglected, but nonetheless this gives the necessary ingredients to a more realistic study of the interactions found in the real system. A change of  $l$  causes the ratio of  $J_1$  and  $J_2$  to vary, however, the former of these two interactions always remains larger.

Note that for very large  $l$  (i.e.  $l/a \rightarrow 1$ ) the interaction energy between neighboring magnetic islands comes essentially from their tips. Defining  $\epsilon = 1 - l/a$ , the dominant contribution to the energy scales as  $1/\epsilon$ , just like the Coulomb interaction. This can be interpreted as the interaction of pairs of monopoles. Here one can draw an analogy to electrostatics where electric dipoles are modeled by a pair of opposite point charges. Conversely, the interaction of distant magnetic islands remains nearly unaffected by their finite extension. Consequently,  $\epsilon$  provides a parameter which controls the relative magnitude of the immediate- and further neighbor interactions in our model.

The route towards equal interactions among the spins of a vertex involves a slight change of the array geometry: for a square lattice all that needs to be done is to give all spins of one sublattice a height offset  $h/a$  with respect to the other sublattice. In the formalism used in this chapter, this corresponds to modifying the sublattice vectors (4.14) to yield

$$\boldsymbol{\rho}_1 = \frac{1}{2}\mathbf{e}_x - \frac{h}{2}\mathbf{e}_z, \text{ and } \boldsymbol{\rho}_2 = \frac{1}{2}\mathbf{e}_y + \frac{h}{2}\mathbf{e}_z. \quad (4.35)$$

Consequently,  $J_1$  decreases with  $h$ , whereas  $J_2$  remains unaffected. This allows us to tune their ratio at will. The interaction strength within the model of needle dipoles (4.34) are readily obtained by a double integration over two linear dipoles. For two spins on sublattice 1, with the first spin belonging to the unit cell at the coordinate origin and the second one to the unit cell at  $\mathbf{n} = (n_x, n_y)$  (for simplicity, we measure all lengths in units of the lattice constant  $a$ , i.e.  $a = 1$ , such that this is a vector of integers), the interaction is given by

$$J^{11}(\mathbf{n}) = \frac{D}{l^2} \left[ \frac{2}{\sqrt{n_x^2 + n_y^2}} - \frac{1}{\sqrt{(n_x + l)^2 + n_y^2}} - \frac{1}{\sqrt{(n_x - l)^2 + n_y^2}} \right]. \quad (4.36)$$

When the second spin belongs to sublattice 2, with the same conventions

$$J^{12}(\mathbf{n}) = \frac{D}{l^2} \sum_{s_1=\pm 1} \sum_{s_2=\pm 1} \frac{s_1 s_2}{\sqrt{(n_x - \frac{1+s_1 l}{2})^2 + (n_y + \frac{1+s_2 l}{2})^2 + h^2}}. \quad (4.37)$$

As before, the constant setting the dimensions of the coupling strength is  $D = \mu_0 \mu^2 / (4\pi a^3)$ , and  $h$  is measured in units of  $a$ .

With the above formulae, a target region for the height offset  $h_{\text{ice}}$  required to obtain equality of  $J_1$  and  $J_2$  as a function of the dipoles' extension can be derived. The question remains whether this will be technologically feasible, since lithographic processes for manufacturing such arrays become more difficult when introducing such a three-dimensional aspect to the structure. The same applies to the subsequent detection of the magnetic states of individual islands that are measured bringing a magnetic force probe to the sample surface. However, the required height offset is relatively small and appears to be reconcilable with such potential technical difficulties. For point-like dipoles ( $l \rightarrow 0$ ), this value is

$$h_{\text{ice}} = \sqrt{\left(\frac{3}{8}\right)^{2/5} - \frac{1}{2}} \approx 0.419 \quad (4.38)$$

and taking into account the finite extension of the dipoles lowers the required height offset. For instance, for  $l = 0.7$ ,  $h_{\text{ice}} \approx 0.207$ . In principle, for  $1 - l/a \equiv \epsilon \rightarrow 0$ ,  $h_{\text{ice}} \sim \sqrt{2}\epsilon \rightarrow 0$ . However, in this ideal limit the effects of disorder, finite transverse width, and a possible internal structure of the dipoles will all play a role. For a global overview of the ratio  $J_2/J_1$  as a function of  $h$  and  $l$ , refer to Figure 4.7. There a target region for realistic values of the island aspect ratio is also indicated. We note that this target region is relatively narrow, especially for  $l/a \rightarrow 1$ . This poses a real challenge for an experimental realization of a system with balanced  $J_1$  and  $J_2$ . In order to achieve this, the geometry of the magnetic islands has to be controlled very precisely, otherwise fluctuations of the couplings will represent an important source of disorder.

Having fixed the short-distance trouble by introducing the modulation in height, the question remains what happens to the long-distance part of the dipolar interaction, which in  $d = 3$ , turned out to leave the ice regime intact [Siddharthan *et al.* (2001); Melko *et al.* (2001)]. However, the mechanism responsible for this equivalence in  $d = 3$  [Isakov *et al.* (2005)] is not operational in  $d = 2$ , as it requires the dimensionality of the dipolar interaction to coincide with that of the underlying lattice. Here, however, we have a  $d = 3$ ,  $1/r^3$  dipolar interaction in a  $d = 2$  array. Nonetheless, as stated above, the present situation is relatively benign, as the Fourier sum of a  $1/r^3$  interaction in  $d = 2$  is absolutely convergent (obviating the need for an Ewald sum).

Further neighbor terms can be suppressed parametrically in the ideal limit of  $l \rightarrow 1$ . The ratio  $J_{n \geq 3}/J_{1,2}$  vanishes as  $\epsilon \rightarrow 0$ , thus yielding the

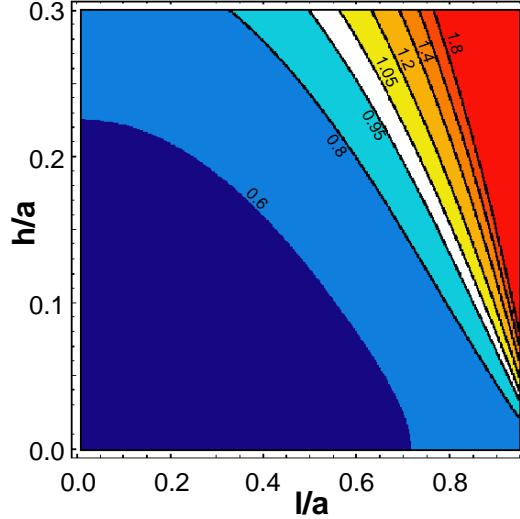


Figure 4.7: Map of the ratio  $J_2/J_1$  of the second to the first nearest neighbor interactions for different values of lattice constant,  $a$ , and sublattice height offset,  $h$ . Numbers indicate the ratio at the closest solid line. In the white zone,  $|J_2/J_1 - 1| < 5\%$ . In the left (blue) region, the ordered state is antiferromagnetic, whereas it is ferromagnetic in the right (yellow-red) area.

ideal Ising-ice model. As  $l$  is reduced, the flat band initially acquires only a small dispersion. To demonstrate this, in Figure 4.8 we have plotted the mode spectrum for  $l = 0.7$ , which corresponds to the extension of dipoles  $a = 320\text{nm}$  sample from Wang *et al.* (2006), but with a supplementary height offset of  $h = 0.207$ . The overlap of its eigenvectors with those of the Ising-ice model, also displayed in this Figure, differs from 1 by less than  $5 \times 10^{-5}$  over the entire Brillouin zone. On top of the parametric suppression of further neighbor terms with increasing  $l$ , the very low residual bandwidth of the lower band (of less than 1.5% in the case displayed in Fig. 4.8) is also due to a tendency of self-screening of the dipolar interaction. A self-screening potential is a potential which mimics its nearest-neighbor interaction component [Isakov *et al.* (2005)]. Figure 4.9 displays this behavior for the lower band of the spectrum discussed in this paragraph: the F-model part of the interaction, i.e. its nearest-neighbors components, yields an almost flat band (which might be chosen to be exactly flat). The transverse interaction ( $r = 1$ ) adds an important dispersion to this band, but successive terms compensate this influence and yield increasingly better approximations to a flat band. This demonstrates that an ice-regime can be obtained by this

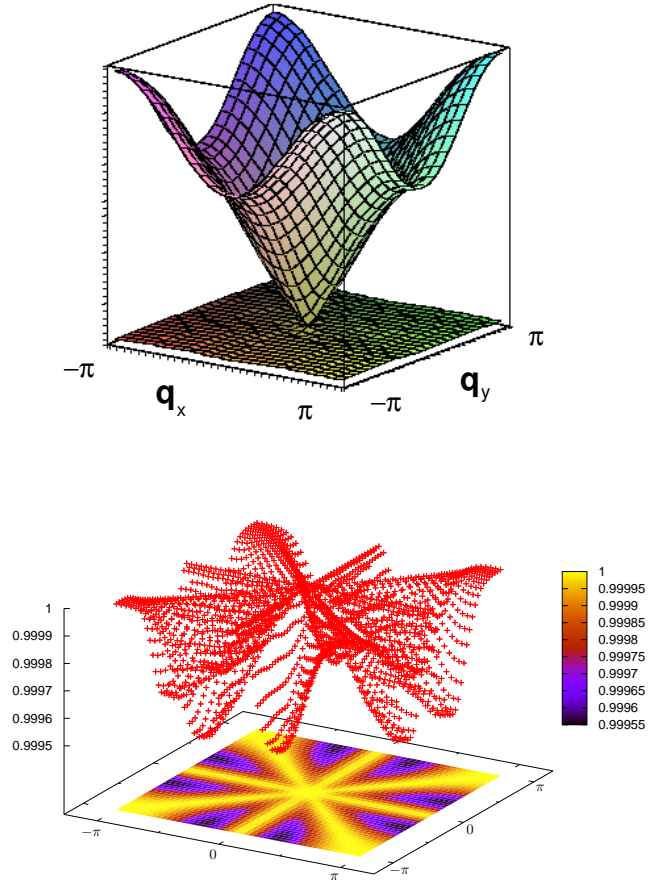


Figure 4.8: Top: Spectrum of the dipolar interaction on the square lattice for dipoles with finite extension  $l/a = 0.7$  and with a height offset  $h/a = 0.207$  between the two sublattices. The lower band becomes almost flat with less than 1.5% of the total bandwidth. Bottom: The overlap of the eigenvectors with square ice for this modified interaction shows almost complete agreement.

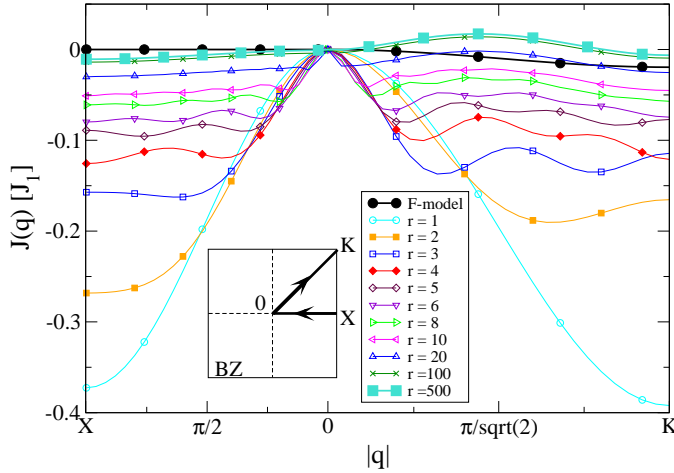


Figure 4.9: Lowest eigenvalue of the interaction matrix  $J_{\mathbf{q}}$  for the needle model (4.34) with  $l = 0.7$  and  $h = 0.207$ . Its values are indicated along a path following the main symmetry axes as in Fig. 4.6. Note that the final spectrum yields an almost flat band, as does the F-model with interaction strengths according to the parameters  $h$  and  $l$ . Perturbations introduced by further neighbor terms are leveled out with increasing cut-off  $r$ : the interaction is approximately self-screening.

route. To study the properties of an ice-regime of this model, we turn to analyzing its thermodynamical properties in the following section.

**Kagomé Ice** The ground states of antiferromagnetic Ising spins on the kagomé lattice define what is known as kagomé ice, with the ‘ice rules’ requiring each triangle to have one spin pointing in and two out, or vice versa [Wills *et al.* (2002)]. Since the sites of the kagomé lattice correspond to the links of the honeycomb lattice, one can pose the question whether a dipolar array forming a honeycomb lattice will display a kagomé ice regime.

The case of kagomé ice has the advantage that the three bonds of the triangle are equivalent, unlike the six bonds of the square. This means that the nearest-neighbor Hamiltonian does not require any fine-tuning through a height offset to allow for an ice regime. Furthermore, using the above limit of  $\epsilon \rightarrow 0$ , we can again parametrically suppress the importance of further neighbor interactions, and hence obtain a representation of kagomé ice. The vestiges of the further neighbor terms will again give rise to an ordering transition, terminating the ice phase on its low- $T$  side. We note that kagomé ice is a phase distinct from square ice in that its long-wavelength theory is different—its correlations are not algebraic, but exponentially short-ranged

even at zero temperature.

### 4.3.2 Mean Field Theory

As the spectrum of artificial spin ice, i.e. dipoles on the links of a square lattice, exhibits a dispersive lower band, the question at which temperature  $T_{\text{af}}$  an ordering transition occurs is addressed next. For three-dimensional spin systems, a self consistent mean field theory has been elaborated [Garanin and Canals (1999)]. We shall apply this approach to the two-dimensional systems discussed here.

First, as reviewed by Moshe and Zinn-Justin (2003), one replaces scalar spins by many component spins. The spin degrees of freedom may then be considered as soft spins, i.e. continuous variables rather than as discrete pseudo-Ising spins. Subsequently a constraint is enforced on the length of these soft spins. However, we will see that this constraint is trivially satisfied in the limit of infinite components  $\mathcal{N} \rightarrow \infty$ , so that the theory is well controlled in this limit.

In order for the notation to remain easily readable, we will note the pair of unit-cell-index and sublattice-index ( $i\alpha$ ) in a simplified fashion as  $i$ , to be understood as the prior combination. Many component spins will then be noted as

$$\mathbf{S}_i = S_i^a, \text{ with } |\mathbf{S}_i| = \mathcal{N} \quad (4.39)$$

with the upper index indicating the component  $a \in 1 \dots \mathcal{N}$ . The coupling matrix relating these multi-component spins remains the same as in (4.12)

$$\mathcal{H} = \sum_{i,j=1}^{2N} \mathbf{S}_i \mathcal{J}_{i,j} \mathbf{S}_j, \quad (4.40)$$

and by convention the ground state energy is shifted to zero. The partition function at the inverse temperature  $\beta = 1/T$  for the above system is then written as a path integral over  $\mathcal{N}$ -component continuous field variables  $\phi_i^a$

$$\mathcal{Z} = \int \mathcal{D}[\phi_i] \mathcal{D}[\lambda_i] \exp\{-\mathcal{S}(\phi, \lambda)\}, \quad (4.41)$$

enforcing the length at each lattice site via a Lagrange multiplier  $\lambda_i$ . The full action is then

$$\begin{aligned} \mathcal{S}(\phi_i, \lambda_i) &= \sum_{i,j} \sum_{a=1}^{\mathcal{N}} \left\{ -\beta \phi_i^a \mathcal{J}_{ij} \phi_j^a + i \frac{\lambda_i}{2} \delta_{i,j} (\phi_i^a \phi_i^a - \mathcal{N}) \right\} \\ &\equiv \sum_{i,j} \sum_{a=1}^{\mathcal{N}} \left\{ -\frac{1}{2} \phi_i^a M_{ij} \phi_j^a - i \mathcal{N} \frac{\lambda_i}{2} \delta_{i,j} \right\}, \end{aligned} \quad (4.42)$$

with  $M_{ij} = 2\beta\mathcal{J}_{ij} + i\lambda_i\delta_{i,j}$ . Since the action (4.42) is quadratic in the fields, the Gaussian integrals over  $\phi_i$  in (4.41) may be performed and evaluated to

$$\mathcal{Z} = \int \mathcal{D}\lambda_i \left( \frac{1}{\sqrt{\det M}} \right)^{\mathcal{N}} \exp \left\{ i\mathcal{N} \frac{\lambda_i}{2} \sum_{i,j} \delta_{i,j} \right\}. \quad (4.43)$$

By translational invariance of the coupling matrix  $\mathcal{J}_{ij}$  the local Lagrangian multipliers  $\lambda_i$  are all identical and can be replaced by a single global value  $\lambda$ . The remaining effective action depends on  $\lambda$  only, and can be written as

$$\mathcal{S}(\lambda) = \frac{\mathcal{N}}{2} \text{Tr} \ln(M_{ij}) - i\mathcal{N}\mathcal{N} \frac{\lambda}{2}, \quad (4.44)$$

where  $N$  is the number of sites. The number of spin components  $\mathcal{N}$  now factorizes and it is clear that in the limit  $\mathcal{N} \rightarrow \infty$ , the saddle point approximation  $\frac{d}{d\lambda}\mathcal{S}(\lambda) = 0$  becomes exact. Also, this limit implies by virtue of the central limit theorem that fluctuations from the constraint on the length of individual spins vanish and the mean field approach additionally becomes exact in this sense. The trace may be favorably evaluated in the diagonal representation of the Hamiltonian (4.20), and with this, the saddle point equation reads

$$\frac{1}{N} \sum_{\mathbf{q},n} \frac{1}{\frac{J_n(\mathbf{q})}{T} - i\lambda} = 1. \quad (4.45)$$

This is a self-consistency relation for the soft-spin mean field theory exposed here, in which the dimensionality of the problem comes into play via  $\sum_{\mathbf{q}}$ , contrasting the general idea that a mean field theory is independent of the dimension.

Obviously, and in contrast to the three-dimensional case, the theory fails to predict an ordering transition in two dimensions. Since the soft-spin approach represents a situation with continuous degrees of freedom in two dimensions, this case falls under the premises of the theorem by Mermin and Wagner (1966) which states the absence of an ordering transition. To show this, a simple example assuming a single quadratic band  $J_{\mathbf{q}} = \gamma q^2$  is sufficient. For  $d$  dimensions,

$$\frac{1}{N} \sum_{\mathbf{q}} \rightarrow \int q^{d-1} dq \quad (4.46)$$

**d=2:** The self-consistency relation (4.45) becomes, with some cut-off  $\Lambda$  for the momentum:

$$1 = \int_0^\Lambda \frac{q dq}{\frac{\gamma q^2}{T} + \lambda} = \frac{T}{2\gamma} \ln \left[ \frac{\gamma\Lambda^2}{\lambda T} + 1 \right]. \quad (4.47)$$

This relation can always be satisfied, and for low  $T$  the expression for  $\lambda$  becomes

$$\lambda = \frac{\gamma\Lambda^2}{T} \exp\left[-\frac{2\gamma}{T}\right]. \quad (4.48)$$

On the contrary, a phase transition would correspond to a case where the self-consistency relation (4.45) cannot be fulfilled without adding a supplementary term accounting for condensation in a single mode or in other words an ordering transition. Note that, while the self consistent Gaussian approximation does not properly describe the ordering transition we expect, it was used successfully to describe the antiferromagnetic model on the kagomé lattice, where no ordering is observed down to zero temperature [Garanin and Canals (1999)].

**d=3:** Just to make an example for the case just mentioned, let us consider the same trivial band structure in three dimensions. We then have from (4.45) and (4.46)

$$1 = \int_0^\Lambda \frac{q^2 dq}{\frac{\gamma q^2}{T} + \lambda} = \lambda^{\frac{1}{2}} \left(\frac{T}{\gamma}\right)^{\frac{3}{2}} \left[ \sqrt{\frac{\gamma}{T\lambda}} - \arctan x \right]_0^{\Lambda\sqrt{\frac{\gamma}{T\lambda}}} \quad (4.49)$$

For low temperatures  $\sqrt{\frac{\gamma}{T\lambda}} \rightarrow \infty$ , and one can simplify the arctan part such that

$$\lambda^{\frac{1}{2}} = \frac{2}{\pi} \left(\frac{\gamma}{T}\right)^{\frac{3}{2}} \left[\frac{T}{\gamma} - 1\right] \quad (4.50)$$

This equation can only be fulfilled if  $T > \gamma$ . We thus conclude that at  $T_c \approx \gamma$ , a transition towards an ordered phase occurs. Note that the critical temperature predicted by this theory is proportional to the assumed band curvature. However, this must be seen as a relict of the soft spin theory, whose fundamental excitations are spin waves with long wave-length or small  $q$ . Thus, the ordering transition is given by the local properties of the band-structure around the minimum in the BZ. On the contrary, for hard spins no collective low-energy modes exist: just above the ordering transition one finds domain walls between ordered domains. As these are located in real-space, their Fourier-space representation is delocalized and extends over the whole BZ.

### 4.3.3 Thermodynamics: Numerical Algorithms

Given the failure of the mean field approach discussed above, further insight from numerical work on the spin systems seemed desirable. To this end, we



simulated the thermodynamic properties of the previously discussed systems resorting to the well-established Monte-Carlo approach [Metropolis *et al.* (1953); Binder (1986); Kertesz and Kondor (1998)].

The general principle of Monte-Carlo (MC) algorithms is outlined in Appendix A, as these concepts are used throughout this thesis. Here, we focus on the particular algorithms tailored for the different spin models we wanted to investigate. All simulations performed were executed on a lattice with an equal number of unit cells in either direction  $L = L_x = L_y$  and periodic boundary conditions, such as to obtain a finite system without strong boundary effects. In order to obtain estimates of particular thermodynamic properties, it was required to observe the scaling with the lattice size  $L$  and extrapolate for  $L \rightarrow \infty$ .

**Single-Spin-Flip Monte-Carlo** As a particularity of the experimental system underlying this study [Wang *et al.* (2006)], the samples were disposed such that an external magnetic field was needed to induce the reversal of individual permalloy islands' dipoles. We assumed that such reversals for individual domains occur essentially independently from their neighbors. To translate into spin language: we assume successive attempts for individual spin-flips to be uncorrelated. Consequently, a single-spin-flip Monte-Carlo algorithm seems to be appropriate to analyze artificial ice. In such an algorithm, the next configuration is generated from the last one by the attempted reversal of a single spin that is chosen at random, and the move is accepted so as to respect the relation of detailed balance.

The most important result from our analysis following this method was that this type of artificial dynamics are sufficient for the system to order. The ordered configurations of the dipolar model on the square lattice are particular members of the set of spin ice configurations. They satisfy the condition of zero lattice divergence, but are made up exclusively of Type I vertices and exhibit perfect long range order. Such an ordered state fills the whole lattice with closed loops around each unit cell (an example is shown in Fig. 4.2), and there is a total of two such states possible on the lattice if its size  $L$  is even. For odd  $L$ , no commensurate tiling is possible and there will be a boundary line along which all bonds are broken. As this is clearly a finite size effect, we restrict our study to even values of  $L$ . The twofold ground state degeneracy observed for even  $L$  strongly the two ferromagnetic states of a simple two-dimensional Ising model. Indeed, there is an exact mapping between the latter and the nearest-neighbor model as follows:

$$S_k = (-1)^{i_1 - i_2 + \alpha} \sigma_i^\alpha, \quad (4.51)$$

with spins  $S_k$  residing at the positions of the pseudo-Ising spins  $\sigma_i^\alpha$ . These points define a square lattice tilted by  $\pi/4$  with respect to the initial one, and with lattice spacing  $a' = 1/\sqrt{2}a$ . Further, consider that spins  $S_k$  are oriented along the  $y$ -axis of this new lattice. By virtue of this mapping, the critical temperatures of the two models are identical, and this temperature is known exactly for the Ising model:

$$T_c^{\text{NN}} = T_c^{\text{Ising 2D}} = \frac{2}{\ln(1 + \sqrt{2})} J \approx 2.269 J \quad (4.52)$$

However, for the long-range dipolar interactions, a numerical calculation is required. It is well known that the discussed single-spin-flip algorithm fails when approaching the critical temperature from above due to a diverging correlation length. For a proper treatment of this behavior, a cluster algorithm is required [Swendsen and Wang (1987); Wolff (1989)] in which large clusters of spins with the same orientation are reversed simultaneously. As the central goal of this study was to explore the properties of the spin ice regime rather than the critical behavior related to the ordering transition, the algorithm will not be elaborated upon here. Instead, we restrict ourselves to giving estimates of the transition temperatures for the different regimes based on the single spin-flip algorithm. The results of this analysis are represented in Figure 4.10. Although we know that the algorithm used is not ergodic just above the ordering transition, the exact value of the transition temperature (4.52) is recovered rather precisely in our simple simulations. Thus, the following estimates for the respective ordering transitions of the F-model and the dipolar model might be expected to be similarly accurate.

Simulations of the dipolar interaction were carried out with different cut-offs such as to estimate its influence on the transition temperature. As the transition is ruled (mainly) by the environment of the minima in the Brillouin zone, and convergence was reached quite quickly around these points (see Fig. 4.6), a weak influence of the cut-off on the value of  $T_c$  is expected. This is indeed borne out in our simulations. Once the dipolar interactions are summed up to a cut-off  $r_{\text{max}} \gtrsim 8a$ , further neighbor terms give minor corrections. Also, since the regression of the critical temperature over the inverse system size yields very small slopes, we concluded that finite size effects are weak. Based on these arguments, the estimated transition temperature is  $T_c^{\text{Dipole}} = 1.69(3)J_1$ .

A result to be stressed at this point is that the ordering temperature of the dipole model is only slightly reduced with respect to the nearest-neighbor model. From the numbers given in Figure 4.10, we have  $T_c^{\text{Dipole}} \approx 0.75 T_c^{\text{NN}}$  (for  $J = J_1$ ). However, regarding the spectra in Figure 4.4 this is not very surprising, given that the thermodynamics close to the ordering transition

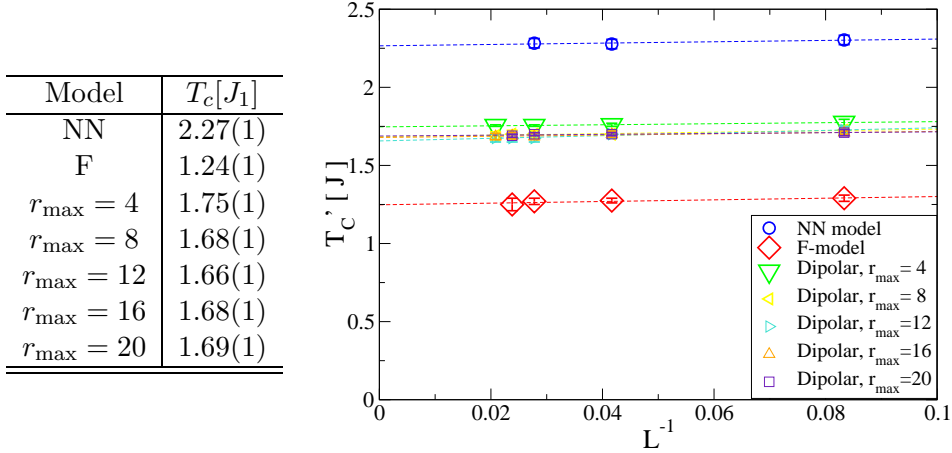


Figure 4.10: Critical temperatures estimated from numerical calculations based on a single spin flip algorithm and corrected by finite size scaling. For each given system size, the transition temperature was estimated as the position of the maximum in the heat capacity  $T'_C$  such that  $C(T'_C) = \max_T[C(T)]$ . A finite size scaling over the inverse linear system size  $L$  was carried out, as represented in the figure.

are dominated by the behavior of the lowest energy eigenvalue. As a rough estimate, we may take the relative band-width of the lower band as the relevant energy scale determining the transition temperature. This value is reduced from  $1/2$  for the F-model to approximately  $1/3$  of the dipolar model, leading to the naïve estimate of a 66% reduction for the ordering temperature.

The fact that the single-spin-flip algorithm loses ergodicity when approaching the ordered regime of the above models does not seem to harm the estimate of the respective transition temperatures. It also fails to describe the spin ice regime. When simulating the square-ice model, the dynamics of the single-spin-flip algorithm freeze at low temperatures (having attained a configuration among those of the ice ground state-manifold). Yet, it is the very property of square-ice that its spin configurations do not freeze at any finite temperature. The failure of the algorithm is due to the fact that once a spin ice configuration is reached, flipping a single spin always results in leaving the ground state manifold—this represents a finite energy cost. At low temperatures, the probability of accepting such moves becomes exponentially small. These energy barriers are separating distinct ground states. To circumvent this problem, a more elaborate algorithm with non-local moves is required.

**Loop Algorithms** The strategy of any good Monte Carlo algorithm is to propose moves that will be accepted with high probability, and affect a large number of degrees of freedom, such as the celebrated cluster algorithms [Swendsen and Wang (1987); Wolff (1989)]. For square-ice, similar algorithms exist [Barkema and Newman (1998); Newman and Barkema (1999)] that exploit the fact that all degenerate ground states of square-ice feature closed loops of spins. A loop is to be understood as a closed chain of spins that have the same orientation with respect to the underlying path. Upon reversing all spins within such a loop, another ground state configuration (with identical energy) is reached. The only requirement necessary to fulfil the relation of detailed balance in a loop algorithm constructed on this feature is that the probability of selecting a given loop depends on its length only, and is independent of its orientation.

In fact, by appropriate mappings these loop algorithms may apply to different problems as coloring models, random surface models, or fully loop-covered lattices [Barkema and Newman (1998)]. Here we will focus on its application to spin ice and next discuss how appropriate loops are constructed.

**Long-loop algorithm** As mentioned above, the ice-rules are equivalent to a zero divergence of the lattice flux, i.e. two spins point towards and two point away from each vortex. First, suppose that we start from a ground state configuration satisfying these constraints. In order to construct a loop in which all spins point in the same orientation, these rules are followed:

1. choose an arbitrary spin and reverse it, creating two defects or vertices with a ‘charge’  $\nabla \cdot \mathbf{S} = \pm 1$
2. choose one of the vertices where defects have been introduced and reverse one of the two spins that reestablishes the ice rule (not the one previously flipped), thus moving the defect one site further.
3. continue to the vertex that now carries the defect and iterate this procedure until the initial vertex site that carries a defect of opposite polarity is reached.

This algorithm can be viewed as a defect moving around the lattice until it annihilates with an oppositely charged defect. Accordingly, on a finite lattice in two dimensions the algorithm always returns back to the initial site and terminates there. The result is that all spins along the loop will have been reversed. Such loops may be arbitrarily long, even taking into account the possibility of visiting individual sites several times. For the ice-model

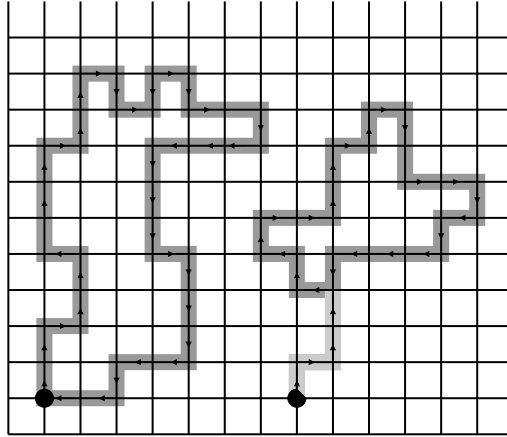


Figure 4.11: Long and short loops formed by the Newman and Barkema algorithm [Barkema and Newman (1998)] on a square ice lattice. Each lattice line between two crossings carries a spin. For clarity, only spins which are included in the loops are shown, however all vertices visited by the loop are required to obey to the ice rules for the depicted moves to be valid. Starting vertices are indicated by large black dots. On the left an example of a long loop is given, which is completed upon encountering its own starting vertex. On the right an example short loop is depicted, which is complete when it crosses itself at any point. Dark gray lines outline completed loops. The excluded tail of the short loop is shown in light gray (adapted from Melko *et al.* (2004)).

where starting configurations satisfy the ice-rules this is not a problem, since long loops also have the ability to flip a larger number of spins. However, since our aim is to simulate a model that exhibits such defects (namely Type III and Type IV vertices), the above rules have to be extended by the following clause: whenever a defect (other than the one created initially) is encountered, abort the loop move and return to the initial configuration. With this addition, the so-called long-loop algorithm risks wasting a lot of computation time before arriving to a defect position. It then becomes more favorable to use a variant, called the short-loop algorithm.

**Short-loop algorithm** The short-loop algorithm modifies the condition for the termination of a loop according to the above rules. Here, a loop is considered complete whenever it meets a vertex that it has previously visited. At that point the ensemble of reversed spins corresponds to a closed loop of spins and an additional tail from the start of the orbit to

the point where the loop closes. Thus, all spins belonging to this tail have to be reversed a second time after the loop closes, such as to obtain a valid move. Contrarily to the long-loop algorithm, the length of the loops it creates remains finite and does not grow with the lattice size. To display the difference between this and the previously discussed type of loop moves, a representation of two example moves is given in Figure 4.11.

**Loop algorithms for non-ice models** When the ice states are not exactly degenerate, the above algorithms have to be extended once more. For the F-model, an appropriate way to adapt the probability of choosing the path can be found which does not require rejecting any moves [Barkema and Newman (1998)]. However, for long-range interactions, the easiest means to keep the condition of detailed balance intact is to proceed in analogous fashion to single-spin-flips: accept the move if it lowers the energy, or otherwise accept it with a probability corresponding to the ratio of the Boltzmann factors  $\exp[\beta(E^{\text{initial}} - E^{\text{final}})]$ . Furthermore, a loop move is abandoned each time that it meets a non-ice ‘defect’ vertex. When rejecting supplementary moves in this way, it seems obvious that the short loop algorithm becomes favored in comparison to the long-loop algorithm. For the long-loop algorithm, the probability that the move will be abandoned by meeting a defect vertex is higher, and it is very questionable if the larger fraction of spins that may be affected by a single (but rare) move may outweigh this risk (which could be checked numerically).

A supplementary problem now arises: the energy difference between the initial and final configuration has to be calculated. It would be very inefficient to calculate the energy for the whole lattice before and after performing the loop move, but how does one know which interactions to sum in order to obtain the energy for the whole loop, especially for long-rang interactions? Given that the energy (4.12) is linear in the spin variables, a local field  $\mathcal{F}_k$  can be defined such that the energy of a given spin  $\sigma_k$  is

$$E_k = \sigma_k \mathcal{F}_k \equiv \sigma_k \left[ \sum_l J_{kl} \sigma_l \right]. \quad (4.53)$$

The energy change reversing spin  $\sigma_k$  is then

$$\Delta E_k = E_k^{\text{final}} - E_k^{\text{initial}} = -2\sigma_k \mathcal{F}_k. \quad (4.54)$$

A proper implementation in the short-loop algorithm that obtains the total loop energy is obtained upon adding the following rule to the above procedure: before flipping a spin  $\sigma_k$ , add its energy difference  $\Delta E_k$  to the total

energy difference  $E_{\text{total}}$ . Once the loop is complete, continue to add the individual energies of the spins that were initially flipped but do not belong to the loop, following the path until it reaches the beginning site. This way, only interactions between spins within the loop and spins that do *not* belong to the loop are counted. For a pair of spins  $\sigma_{l_1}$  and  $\sigma_{l_2}$  belonging to the loop, the respective interactions  $J_{l_1 l_2}$  are summed twice but with opposite signs since the first of the two has been reversed. For those spins in the tail of the path that do not belong to the loop, the interaction terms for spins which were not reversed in the meanwhile are compensated. On the other hand, those interactions with spins that were reversed are then properly taken into account.

Even for the ice-model, there are many defects to the ice-rules in the high temperature regime, therefore making the loop algorithms ineffective. In particular, they never destroy any defects since they only operate on vertices that already satisfy the ice-rules. Thus, we utilized a mixed algorithm which intermingles single-spin-flips and loop-moves. The ratio of attempted moves of each type can be adapted with respect to the simulated temperature. Typically, at high temperature few ice-rule vertices exist and loop moves are thus aborted quickly. The mixed algorithm is then only slightly less efficient than the algorithm based exclusively on single-spin-flips. At low temperatures, the same argument holds true for the roles of both types of MC-moves inverted.

#### 4.3.4 Thermodynamics: Observed quantities

For the whole spectrum of interactions studied, Monte Carlo simulations were run stepwise, ‘cooling down’ the system from a high temperature and averaging the desired thermodynamic quantities over  $10^5$  to  $10^6$  configurations before proceeding to the next temperature. In the case of elementary quantities as the energy, magnetization or correlation functions were computable directly from the respective spin configurations. Since we wished to compare results to those of experiments Wang *et al.* (2006), we included the distribution of vertex-types in the collection of observed quantities which are described in Table 4.1. Other quantities were derived from the fluctuation such as the magnetic susceptibility  $\chi$  which requires the evaluation of the fluctuation in the magnetization  $M$ . The latter is obtained from the partition function  $Z$  derived with respect to the external magnetic field  $B$

$$M = \frac{1}{\beta} \frac{\partial \ln Z}{\partial B}. \quad (4.55)$$

Thus, for the susceptibility, we have

$$\chi(T) = \frac{\partial M}{\partial B} = \frac{1}{\beta} \left[ \frac{1}{Z} \frac{\partial^2 Z}{\partial B^2} - \frac{1}{Z^2} \left( \frac{\partial Z}{\partial B} \right)^2 \right] = \beta [\langle M^2 \rangle_T - \langle M \rangle_T^2], \quad (4.56)$$

where  $\langle \cdot \rangle_T$  denotes thermodynamic averages at temperature  $T$ . Similarly, the specific heat  $C$  is obtained using the second moment of the energy  $E$

$$C(T) = \beta^2 [\langle E^2 \rangle_T - \langle E \rangle_T^2]. \quad (4.57)$$

Finally, the entropy is a quantity that requires another step of processing. The entropy difference between two different temperatures may be obtained through evaluating

$$S(T_2) - S(T_1) = \int_{T_1}^{T_2} \frac{C(T)}{T} dT. \quad (4.58)$$

Since the entropy is an extensive measure, it is favorable to use the entropy per degree of freedom instead, which we continue to call  $S$  by abuse of notations. For the Ising-spin systems examined, we may choose the reference temperature as  $T \rightarrow \infty$ , where the entropy per spin is trivially given by  $S = \ln 2$ . Further, it is possible to interpolate the behavior of the heat capacity at temperatures that exceed the typical interaction, since then  $C(T) \sim T^{-2}$ , as follows from (4.57).

To test the validity of the numerical results, we performed a number of checks. For a small system of  $3 \times 3$  unit cells, an analytical calculation was performed for the ice-model with the help of mathematics software. The corresponding numerical results compared favorably with the exact ones. Another check was already given in section 4.3.3 above, namely that the transition temperature for the nearest-neighbor model reproduced the exact known  $T_c$  of the 2D Ising model.

### 4.3.5 Thermodynamics: Results

Having shown the discrepancies between spin ice and ‘artificial spin ice’ based on the spectral analysis of the Hamiltonians of the ice- and the dipolar model, the aim of the numerical study was twofold. First, we hoped to analyze the experimental results in comparison with the thermodynamic properties of the dipolar model. The experiments in Wang *et al.* (2006) required an external excitation with a magnetic field in order to stimulate spin-transitions in the experimental dipolar arrays. We then posed the question of whether such an excitation could be represented by an effective



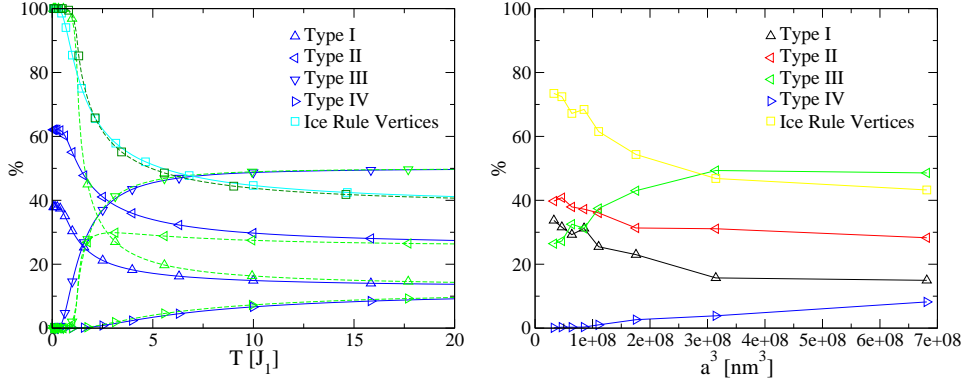


Figure 4.12: On the left, the distribution of vertices among the four types introduced in Table 4.1, for the Ice-model (solid lines) and for artificial ice (dotted lines) on the square lattice as a function of the temperature in units  $J$ . On the right, the experimental results given as a function of  $a^3$  which scales roughly as  $J^{-1}$ .

temperature for the system. Secondly, we wished to establish in more detail the notion of an ice regime in a dipolar array.

In Figure 4.12, the thermodynamic distribution of vertex types in the target model and the dipolar model is represented, paired with the experimental results from Wang *et al.* (2006). These experiments were designed such that all samples were composed of magnetic islands with constant size, and the lattice spacing was varied to manipulate their interactions. The rotating magnetic field used to induce their dynamics also remained the same for all samples. In the case that this procedure succeeds in simulating a thermodynamic equilibrium in the samples, one should be able to find a match for each set of experimental results with a given temperature of the thermodynamic results. Yet, such a match cannot be easily found. The ice-model and the dipolar model, though their respective low temperature behavior is very different, yield quite similar fractions of type III and type IV vertices. One might conclude that these values would represent a good gauge to fix an effective temperature for the experimental system. When trying to match the experimental results with this criterion, it became obvious that the distribution between type III and type IV vertices was slightly different in the experimental setup. At high temperatures or large lattice spacing, all vertices were present according to their weight among the microstates. As a general tendency, when lowering the (effective) temperature, the non-ice vertices or ‘defects’ became successively suppressed and ice-rule vertices accumulated. However, upon comparing the relative abundance of

Type III and Type IV vertices in the experimental data and both of our thermodynamic simulations, we found that Type IV vertices are relatively more strongly suppressed in the experiments. Any attempt to deduce an effective temperature from the experimental data resulted in a compromised fit either according to one or the other species of vertices. We conclude that such a procedure remains unsatisfactory.

In the preceding discussion, we did not turn our attention to the relative distribution between the two species of ice-rule vertices. Important differences are found between thermodynamic simulations and experimental data. In order to understand these differences, consider the results for the two distinct models given in the left part of Figure 4.12. Whereas type I and type II vertices are both present down to the lowest temperatures in the ice-model, the dipolar model undergoes an ordering transition. We can determine from the distribution of vertex types that the ordered phase of this model corresponds exclusively to a tiling of the lattice with type I vertices. The critical temperature for this transition is most easily obtained by observing the heat capacity, rather than focusing on the distribution of vertex types. More results regarding this issue are discussed later. We now turn back to our comparison of the experimental results with the model simulations. For the dipolar model with point-like dipoles (that we think of as a first approximate description of the experimental system), the fraction of type II vertices remains approximately constant before the ordering transition sets in, where they are essentially entirely suppressed. No similar behavior is observed experimentally for the dipolar arrays: there is no indication of an ordering transition. Rather, a moderate increase of type I and type II vertices is observed, a behavior which is closer to that of the ice-model while a large fraction of type III ‘defects’ remains present even at the strongest interactions. Specifically, note that the fraction of type II vertices rises to values well above the maximum reached by the model for point-like dipoles.

A possible source for this disparity might be that the ratio between first- and second-neighbor interactions in the experimental system is not well captured by the point-like model. Similarly, simulations for the needle-dipole model (4.34) also exhibited this feature. Wang *et al.* (2006) proceeded through a finite-element simulation for the interaction energies of their permalloy islands. They analyzed their results denoting  $\mathcal{E}_{ij} = \frac{E_i - E_I}{E_j - E_I}$ , where  $E_i$  is the energy of an isolated Type  $i$  vertex. From their simulations, they found  $\mathcal{E}_{32} > 2$ ,  $\mathcal{E}_{42} > 6$  for  $l/a = 0.7$ . Let us now compare these values to those obtained for point-like dipoles and the needle Hamiltonian (4.34). For point-like dipoles, we found  $\mathcal{E}_{32} \approx 1.45$ , and  $\mathcal{E}_{42} \approx 3.78$ , where the values

are much lower than those calculated by Wang *et al.* (2006), indicating that the energies of the two species of ice-rule vertices are not as strongly separated from the non-ice rule ones as in the experimental setting. With the interactions (4.34) this continues to be true and one obtains  $\mathcal{E}_{32} = 1.7$  and  $\mathcal{E}_{42} = 4.9$ . To fairly compare results we trimmed  $J_2$  by hand, reducing the value of  $|J_1 - J_2|$  by 30% with respect to Eq. 4.34. This allowed the energy ratios to grow to  $\mathcal{E}_{32} = 2.25$ ,  $\mathcal{E}_{42} = 7$ , even exaggerating the calculations by Wang *et al.* (2006). However, even then, thermodynamic simulations never yielded a fraction of 40% type II vertices as was observed in experiments. We conclude that the array configurations observed in the experiments do not correspond to thermodynamic equilibrium states. It would therefore be desirable to develop an alternative model for the dynamics of these systems. Such a model is discussed in the next section. In the remainder of the present section, more Monte Carlo results for thermodynamics are discussed.

Figure 4.13 displays a number of thermodynamic quantities for the ice model, as well as the fraction of accepted Monte Carlo moves, and Figure 4.14 provides that same information for a dipolar-needle model on the square lattice with needles of length  $l/a = 0.7$  and one sublattice shifted such as to match  $J_1$  and  $J_2$ . This value of  $l/a$  corresponds to the geometry of the sample with the largest interactions in Wang *et al.* (2006). The high temperature behavior of these two models is very similar. This can be discussed in reference to the distribution of vertex-types. Non-ice defects are increasingly suppressed with decreasing temperature. Type IV vertices are almost entirely suppressed for the shown temperature range of  $T < 3J_1$ , and Type III vertices are present with less than 1% of all sites for  $T_u \lesssim 0.45J_1$ . This point coincides with the temperature at which the acceptance rate for single-spin-flips practically vanishes, displaying the property that single spin-flips applied to a spin ice-state imply leaving the ground state manifold.

Below the temperature  $T_u$ , the physics observed is essentially that of spin ice or the 6-vertex model. Naturally, this regime extends to zero temperature for the spin ice model, evidenced also by the acceptance rate for loop-moves going to one. For the dipole model, the ice-regime is terminated at a finite temperature related to the residual dispersion of the lower band. For the example cited here, this transition temperature is encountered at  $T_l \sim 0.13J_1$ . This value is very sensitive to the parameters  $l$  and  $h$  of the interaction as well as to the cut-off  $r_{\max}$  used in the simulation. Consistent with the details of the band structure as a function of the cut-off (see Fig. 4.9), we found that our simulations yielded even lower estimates for the ordering temperature  $T_l$  as  $r_{\max}$  is increased. For a very precise estimate of this transition temperature, a re-summation of the dipolar interaction using an Ewald sum might

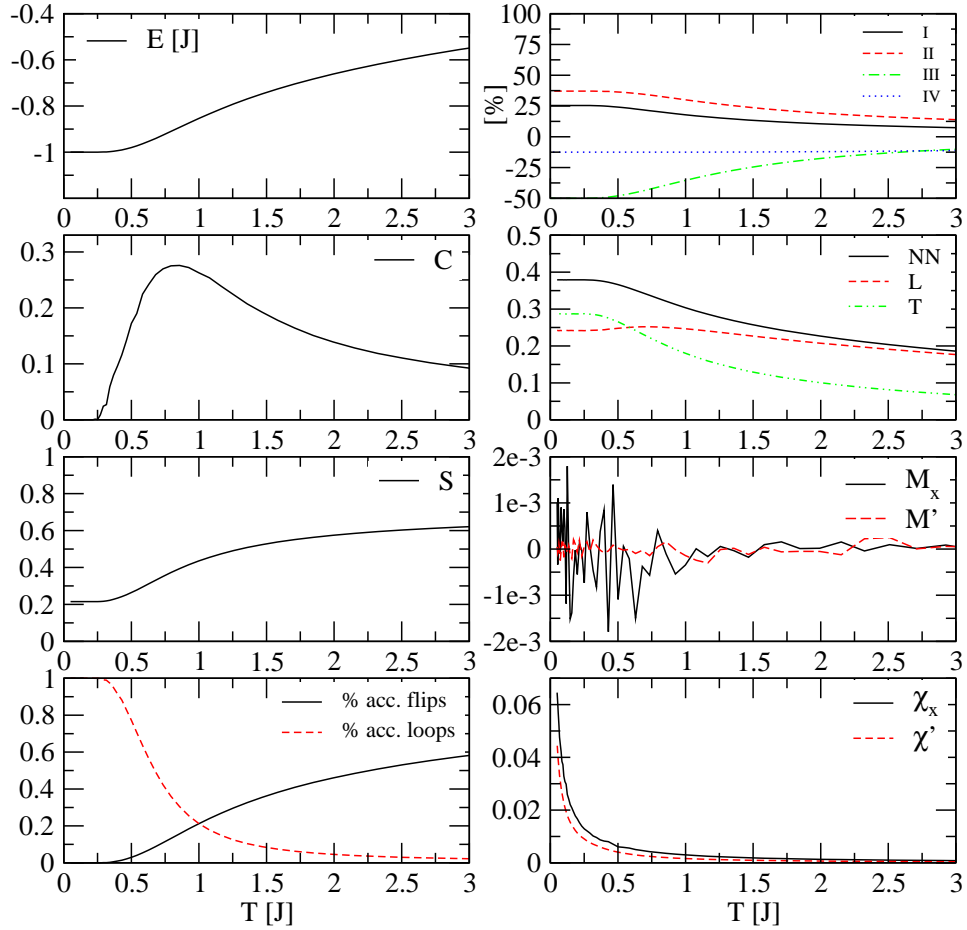


Figure 4.13: Thermodynamic quantities for a simulation of the Ice-model. Represented are the energy  $E$ , heat capacity  $C$ , entropy  $S$ , the ratio of accepted single-spin-flips and loop moves, the excess distribution of vertex-types with respect to a random configuration of spins, the three nearest-neighbor correlations (see Fig. 4.16 for an explanation), magnetization along the  $x$ -direction  $M_x$  and the staggered magnetization  $M' = \langle (-1)^{i_x - i_y + \alpha} \sigma_{i\alpha} \rangle_T$ , and the respective susceptibilities for these two magnetization channels. Extensive quantities are given per spin degree of freedom. The simulation was performed on a square lattice with periodic boundary conditions and  $24 \times 24$  unit cells.

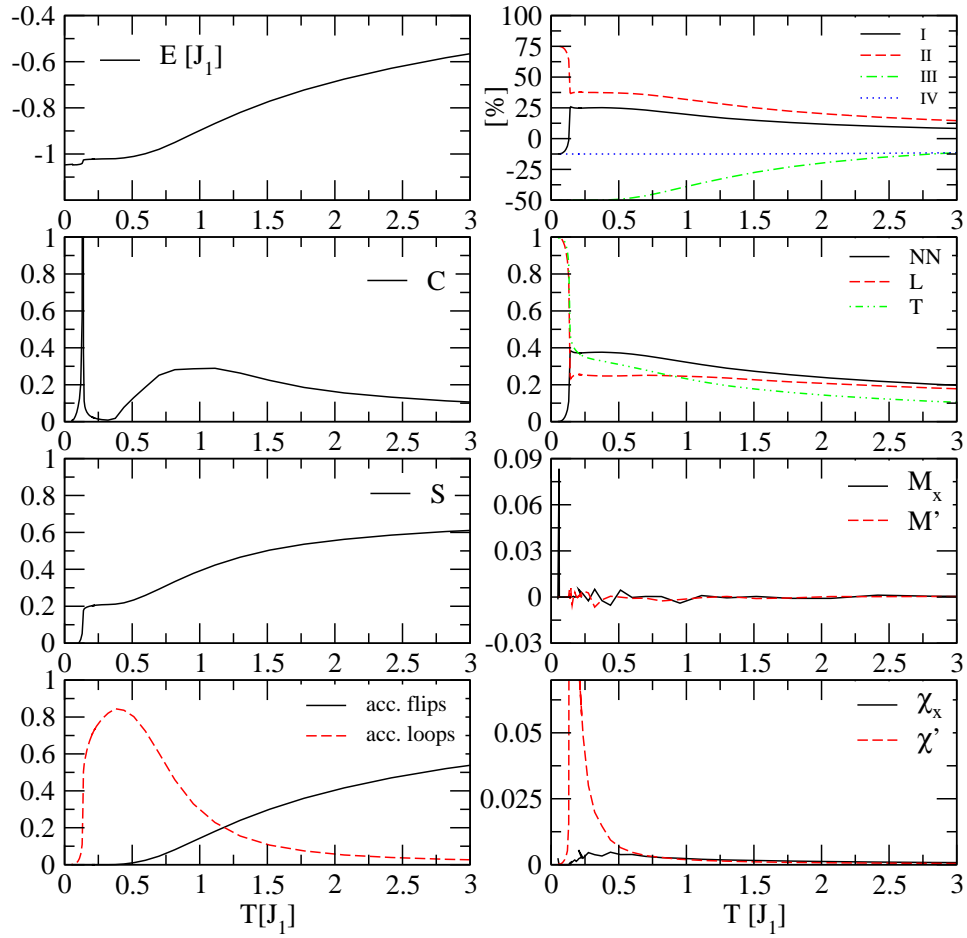


Figure 4.14: Thermodynamic quantities (see caption of Figure 4.13 for details) for a simulation of the needle-dipole model with  $l/a = 0.7$  and a finite height-offset of one sublattice of spins  $h/a = 0.207$ , calculated with a cut-off  $r_{\max} = 4a$ .

be desirable. Apart from these details, our simulations confirmed that there is a relatively wide temperature range between the two temperatures  $T_l$  and  $T_u$  in which the dipolar model exhibits an effective ice-regime, corresponding to a separation of energy scales for the ordering transition (dispersion of the lower band) and for attaining the spin ice regime (band separation, low lying fraction of the upper band). As for the ice-model, this is related to a high (but noticeably smaller than 1) acceptance rate for loop moves in our Monte Carlo simulations. Also, we found that the internal energy  $E(T)$  is close to constant in the interval  $[T_l, T_u]$ , which gives one more indication for an extended ice regime. Naturally, the peak in the heat capacity at the ordering transition was found to be accompanied by a step-like feature of  $E(T)$ , both of which are features of a first order phase transition.

For the model interaction displayed in Figure 4.14, we found an ordering transition to a ferromagnetic state with alignment of spins along the lattice directions. However, this does not result in a macroscopic magnetic moment, as neighboring chains of this type are arranged in opposite directions so as to optimize the transverse dipolar interactions. The staggered magnetization  $M'$  indicated in the figures is an order parameter for the antiferromagnetic phase and would be equal to one if the system ordered in a state built out of type I vertices. Though this state is obviously not the ground state for the set of parameters displayed in 4.14, it seems to be competing with the actual ground state.

Upon close analysis of the different thermodynamic quantities just above the ordering transition in Figure 4.14, one notices that they are non-monotonic, which can be interpreted as the interplay of energy and entropy of the two competing ordered states described above.

Concerning the magnetizations shown in Figures 4.13 and 4.14, we propose a different behavior of the susceptibility  $\chi_x$  associated with the magnetization  $M_x$  along the  $x$ -axis. This is contrary to spin ice where the two displayed susceptibilities diverge as  $1/T$ , and with amplitudes proportional to the fraction of type I vertices ( $\chi'$ ) and type II vertices ( $\chi_x$ ). For the dipolar model, similar divergence of the staggered susceptibility  $\chi' \sim 1/(T - T_c)$  is observed. However, the fluctuations of  $M_x$  (see Eq. 4.56) appear strongly suppressed there, as no such divergence is present for  $\chi_x$ . This is noticeable even far above the ordering transition, so the system seems to somewhat anticipate how it is going to order at lower temperature.

As mentioned in section 4.3.1, the geometrical parameters for dipolar spin ice may equally be adjusted so as to obtain an antiferromagnetic ordering transition. Figure 4.15 gives an account for this behavior in term of vertex-types. In this figure, the  $x$ -axes have been scaled such that the high

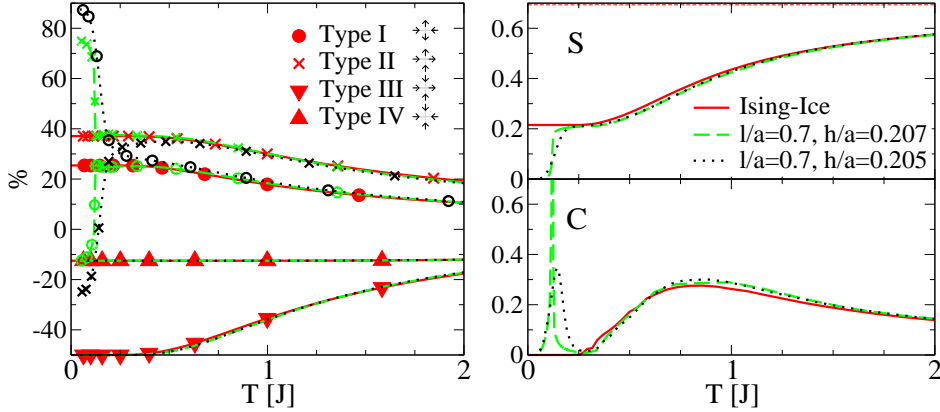


Figure 4.15: Ising-ice vs. dipolar arrays: frequency of vertex types (% deviation from values obtained for a random distribution of spins, which yields  $\frac{1}{8}$ ,  $\frac{1}{4}$ ,  $\frac{1}{2}$  and  $\frac{1}{8}$  for Types I-IV, respectively), entropy ( $S$ ), and heat capacity ( $C$ ) from Monte Carlo simulations.  $X$ -axes were scaled for high- $T$  asymptotics to coincide. The fraction of non-ice-rule vertices is below 1% for  $T < 0.42J$  for all depicted systems. At low  $T$ , the ice regime, which widens with increasing  $l/a$ , is terminated by either ferro- (dashed) or antiferromagnetic (dots) orders for varied  $h$ .

temperature parts of all depicted curves coincide. It then becomes obvious that the entropy of dipolar ice yields a plateau at the value corresponding to square ice,  $\frac{3}{4} \ln \frac{4}{3} \approx 0.21576$ , in the indicated temperature interval. This concludes our evidence that an ice regime can be obtained by this route.

### 4.3.6 Models for Dynamics and Annealing

We have shown, based on theoretical arguments and numerical evidence, that a dipolar spin ice model can be realized. Yet, the discussion of the thermodynamics has not given a satisfactory explanation of the experimental results of Wang *et al.* (2006). Given the impossibility of thermally equilibrating the arrays in these experiments, a rotating magnetic field  $B_{\text{ext}}$ , gradually stepped down, was used to speed up the dynamics [Cowburn (2002)]. The question whether such an ‘algorithm’ can be efficiently used to find the ground state of a system has been discussed in the context of spin glasses [Zarand *et al.* (2002)]. However, in the case of an ice regime, the question is somewhat simpler, namely whether it is possible to find one of *exponentially* many ice configurations.

An analysis of the orders of the energy scales present in the experiment [Wang *et al.* (2006)] may serve as a starting point. For our model of dipolar

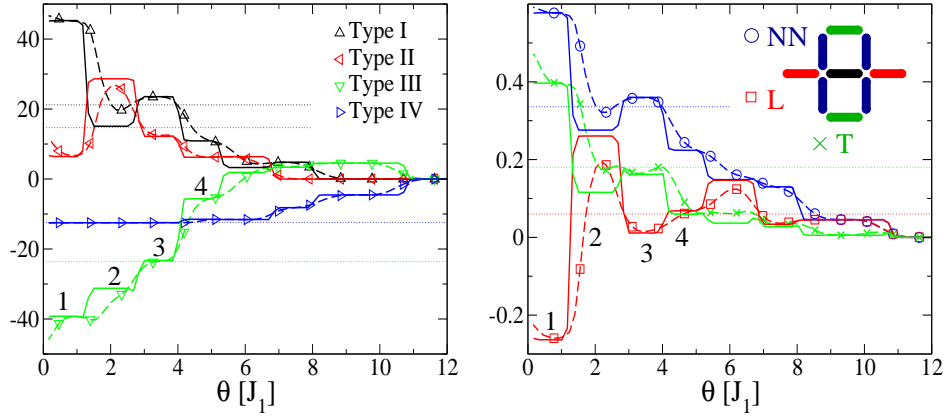


Figure 4.16: Simulation of the ‘downhill’ algorithm: zero-temperature Monte Carlo dynamics subject to an energy barrier  $\theta$  for its moves. Displayed are the results for the dipole model without height offset between the sublattices for extended dipoles with  $l/a = 0.7$  (dashed lines) corresponding to the sample with  $a = 320\text{nm}$  in Wang *et al.* (2006) and for  $l/a = 0.95$  displaying the development of discrete steps in the distribution of vertices when the interaction becomes effectively more local. The dotted lines indicate the experimental results of the  $a = 320\text{nm}$  sample. The greedy dynamics give a very good agreement with the plateau found for  $\theta/J_1 \in [3, 4]$ . On the right, the correlations that were measured in the experiment [Wang *et al.* (2006)] are shown. Note that the nearest-neighbor (NN) and longitudinal (L) correlations may be obtained directly from the distribution of vertex-types. Only the transversal correlations represent an independent measurement.

needles, the corresponding energy scales are:

$$\begin{aligned} \text{‘Zeeman’ energy} &: |\mu \cdot B_{\text{ext}}| \leq 2.6 \times 10^6 \text{K} \\ \text{‘Exchange’} &: J_1^{880\text{nm}} \sim 3.6 \times 10^3 \text{K} \leq J_1 \leq 1.1 \times 10^5 \text{K} \sim J_1^{320\text{nm}} \end{aligned} \quad (4.59)$$

Were the arrays in thermodynamic equilibrium, antiferromagnetic long-range order should be present at room temperature.

**A simple ‘greedy’ algorithm** Since this behavior is not observed, we considered a phenomenological model for the dynamics. First, with the experimental temperatures well below the interaction strengths, we used a form of zero-temperature Monte Carlo dynamics. Secondly, we noted that vertices violating the ice rules were experimentally present throughout. As such defect vertices can be removed using single spin flips only, we imposed a constraint on our single-spin-flip dynamics: for a flip to be accepted, the energy gain must be above a threshold  $\theta$ .



Simulations of this ‘downhill’-algorithm are started by initializing a spin system with a random configuration proceeded by arbitrarily flipping chosen spins if the threshold condition is fulfilled. This process is repeated until no further moves are possible. Measurements are taken as averages over a number of such runs.

We can define different types of moves associated with flipping a single spin depending on the types of its neighbor vertices. An example move would be (III,IV)  $\rightarrow$  (I,III). The downhill algorithm allows us to explore a different set of possible moves according to the value of the threshold chosen. For dipolar interactions which are long-ranged, whether a move is allowed or rejected thus depends not merely on the types of the neighboring vertices, but also on the configuration of distant spins. As we noticed before, in the limit of very extended spins  $\epsilon \rightarrow 0$ , the weight of further neighbor terms is effectively suppressed and the limiting threshold for allowing a given type of move becomes more and more sharply defined as a function of  $\theta$ . The vertex distributions from simulations for moderate and very large values of  $l/a$  are shown in Figure 4.16.

Since the samples in Wang *et al.* (2006) were designed such that the properties of the individual spins in all samples were kept constant for all different lattice spacings, the question arises whether a single (absolute) value of the threshold  $\theta$  can be found such that the model predicts the experimental results. Varying  $J_1$  (experimental values differ by a factor of about 30) locates different points on the curves as those shown in Fig. 4.16. Such an approach works well for the samples with large interaction strength, indicating that there might indeed be a threshold that inhibits the annihilation of further defects, which could explain the relatively large fraction of Type III vertices that have been observed. On the other hand, this trivial model has different characteristics in the regime of weak correlations, requiring another explanation.

**A phenomenological model** To extend the previous greedy ‘downhill’ scheme, we add one more ingredient motivated by the experimental protocol: the rotating field present in the experiments is modeled by a field of random orientation. The choice of a random field orientation is appropriate to represent the rotating field used in experiments if the frequency of spin-flips is sufficiently low (consistent with the results shown below), since the field then always points in a different direction at the instant when a spin flips.

This phenomenological model then has two free parameters: the threshold  $\theta$  and the speed with which the field is ramped down  $\kappa$ . We fixed

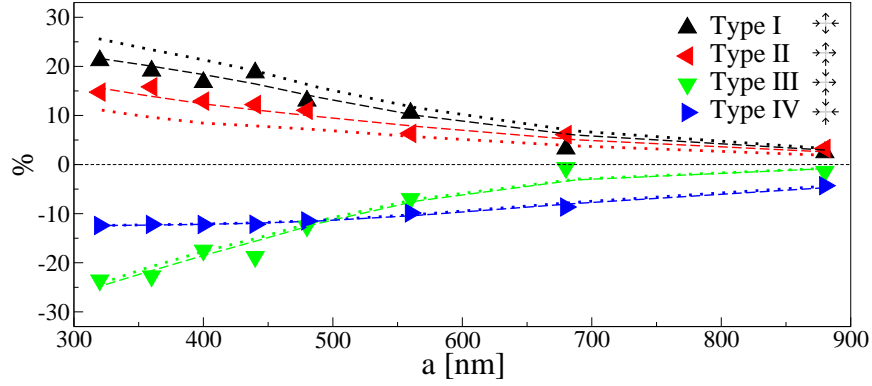


Figure 4.17: Frequency of vertex types (as explained in Table 4.1). Interaction energies scale approximately as  $1/a^3$ , a factor of 30 between extremes. Experiments (symbols) are shown against dynamics simulations for needle dipoles (Eq. 4.34, dotted), and for increased  $J_2$  (dashed, see text).

these parameters to be the same for all arrays, and fit them to obtain the best agreement with the experimental measurements of the local correlations (longer-range correlations in the experiment were very weak) [Wang *et al.* (2006)]. The best fit was obtained for  $\theta = 2.3 \times 10^5$  Kelvin and  $\kappa = 87$  Tesla $^{-1}$  attempted flips per spin during ramp-down (Fig. 4.17).

This algorithm gives semi-quantitative agreement with experimental results over a range of interaction energies differing by a factor of 30 (see Eq. 4.59). However, we systematically overestimate the frequency of Type I vertices compared to those of Type II (similar to what we found above). Again, this appears to be due to our needle model (Eq. 4.34) overestimating the ratio  $J_1/J_2$ . Therefore, we proposed to boost the next-nearest-neighbor interactions  $J_2$  to comply with the finite element calculations from Wang *et al.* (2006) (see Section 4.3.5). This results in reducing the value of  $|J_1 - J_2|$  from Eq. 4.34 by 30%. The resulting fit (Fig. 4.17, dashed lines) appears noise-limited. Furthermore, note that such a change also *reduces* the height offset  $h_{\text{ice}}$  required to obtain equality of  $J_1$  and  $J_2$ .

While our dynamical model obtains an agreement with the experimental findings, the mechanism we propose may not govern the behavior of the dipolar arrays at a microscopic level. We believe that its success relies on properly capturing the effects of a reduced dynamics of defect annealing in the samples of Wang *et al.* (2006). Therefore, even for the strongest interactions, approximately 25% (non-ice-rule) defects, Type III vertices persist. Whereas it is easy to remove pairs of appropriately oriented neighboring

defects by flipping the spin which joins them, such an annihilation process occurs with low probability once these defects are sparse: they first need to diffuse around until they encounter a partner. Such diffusion requires a higher mobility of defects than what was experimentally realized.

This idea can be tested by analyzing the results of the downhill algorithm. As mentioned earlier, each of the plateaus that are visible in Figure 4.16 corresponds to a number of ‘decay’ or ‘annihilation’ processes between vortices that are allowed, whereas others remain forbidden. We remind the reader that this algorithm consists of taking a random initial configuration, which is modified by single spin flips (at random positions) as long as we can find spins that will lower the energy of the system if they are flipped. As a first approximation, this energy depends on the nearest neighbors and these belong to the two neighboring vertices of the flipped spin. In the following paragraphs a discussion of the frequency of certain combinations of neighbor vertices encountered as well as the state of the vertices upon flipping is provided. Such moves are described by the four numbers indicating these vertex types before ( $i$ ) and after ( $f$ ) the spin-flip  $(V_1^i, V_2^i) \rightarrow (V_1^f, V_2^f)$ . For the plateau which best matches the experimental data of the  $a = 320\text{nm}$  array (numbered as plateau n° 3 in Fig. 4.16), the following processes remain forbidden, while one becomes very important in plateau n° 1.

Move (Initial) $\rightarrow$ (Final) $(V_1^i, V_2^i) \rightarrow (V_1^f, V_2^f)$	Relative Frequency	
	Plateau 3 [%]	Plateau 1 [%]
(I,III) $\rightarrow$ (I,III)	0	0.21
(II,III) $\rightarrow$ (I,III)	0	37.71
(II,III) $\rightarrow$ (II,III)	0	0.48
(III,IV) $\rightarrow$ (III,IV)	0	0.04

The relative frequency corresponds to the ratio of the typical number of moves of the given type over the total number of moves during the downhill process. These numbers do not add up to 100%, since those moves which were present at higher  $\theta$  were omitted. All of the above moves (that contribute to a stronger ordering, see Fig. 4.16) are similar in that they involve Type III vertices in their initial and final state and correspond to diffusion processes of these. Since the downhill algorithm only allows moves which lower the total energy, only those of the above decay channels which lower the energy noticeably give a non-negligible contribution to the total number of moves. Where initial and final vertex types are the same, such energy gains are due exclusively to further-neighbor interactions. Moreover, the relatively large weight of the one process that is an exception to this remark,

(II,III) $\rightarrow$ (I,III), confirms the idea that the restricted diffusion of Type III vertices is at the origin of the large fraction of these defects that remain present in the experiments.

In our phenomenological model, due to the external excitation that it simulates, there is no strict suppression of the discussed diffusion processes. Nonetheless, the energetically most favorable processes are those that freeze in last, when tuning down the external excitation, i.e. the magnetic field. Consequently, when the system is annealed more slowly (i.e. choosing a larger  $\kappa$ ), a more ordered state is reached. This, however, does not seem to be the case in the experimental system [Schiffer (2006)]. Note also that our model does not necessarily give a single best fit to the experimental data. In principle, there are several possible combinations of the parameters  $\theta, \kappa$ . However, the values indicated above yield the best fit, and the value  $\theta = 2.3 \times 10^5$  Kelvin we obtained for the threshold is larger than the nearest-neighbor interactions, which is consistent with the finding that any arrangement of the spins remains stable—no spontaneous spin-flips are observed [Schiffer (2006)].

**Disorder** The above discussion indicates that the good agreement of our model with experiment might be due to its correct reproduction of the dynamical bottleneck, and not the detailed microscopic dynamics. An important aspect not taken into account by our dynamical model is disorder, which is expected to have substantial influence on the dynamical behavior even of single islands [Martín *et al.* (2003)]; the inability of the defects to ‘find’ one another may simply be due to their becoming pinned.

Disorder also impacts the ice regime, as the size of the leading perturbation sets the scale for its termination at low temperature. Especially for fine-tuned  $h \sim h_{\text{ice}}$ , disorder may dominate (over  $J_1 \neq J_2$  and further-neighbor interactions), by selecting some ice configurations over others. Strong disorder might even lead to the presence of defects at any temperature.

To expand this analysis, experimental input would be desirable. What is the variance of the islands’ geometrical properties? Are there some islands that freeze at much higher fields than others? Are defects usually located at the same positions, and what is their spatial distribution? How do correlations evolve during the ramp-down of the external field?

## 4.4 Summary and Outlook

We have presented models for the dynamics and thermodynamics of frustrated dipolar arrays, including ways of stabilizing ice regimes. Perhaps the

most interesting direction of further study involves their dynamics, in the presence of varying degrees of disorder.

In particular, can other protocols [Zarand *et al.* (2002)], perhaps involving the use of AC magnetic fields, be used to speed up the dynamics? Note that in present samples, the largest interaction energies are more than two orders of magnitude above room temperature, so that further miniaturization is possible without resorting to cryogenics.

Better equilibration might then open the door for an experimental study of constrained classical [Das *et al.* (2003)] and perhaps eventually even quantum dynamics [Davidovic *et al.* (1996); Hilgenkamp *et al.* (2003)] (and quantum ice [Moessner *et al.* (2004)]). Even though this will require a substantial experimental effort, there appears to be no fundamental obstacle to obtaining at least a classical ice regime.

The results obtained through experimental efforts should provide insights into how the physics of frustration can lead to new ways of effectively suppressing interactions between neighboring magnetic islands and limits imposed by disorder, a topic of special interest to applications in memory storage [Martín *et al.* (2003)]. Therefore, we are optimistic that dipolar nanoarrays will provide an interesting field for further studies.

# Appendix A

## Monte Carlo Algorithms and the Detailed Balance

### A.1 General Principle

Whether applied to statistical physics or to calculations of averages in a quantum mechanical ensemble, the purpose of the Monte Carlo (MC) algorithm is to replace such averages over an available configuration space with a given weight by an average over a number of properly weighted selected configurations. The question of how typical configurations may be obtained in a practical way is answered by the Monte-Carlo- or Metropolis algorithm [Metropolis *et al.* (1953)]. Starting from some arbitrary initial configuration, subsequent configurations  $\sigma_i$  are obtained by a series of moves  $\sigma_i \rightarrow \sigma_{i+1}$ .

In order for the ensemble of generated configurations to be properly distributed according to the desired probability law  $P(\sigma)$ , it is sufficient that:

- Single moves obey the condition of detailed balance, i.e. the transition probabilities  $p(\sigma_i \rightarrow \sigma_j)$  satisfy

$$\frac{p(\sigma_i \rightarrow \sigma_j)}{p(\sigma_j \rightarrow \sigma_i)} = \frac{P(\sigma_j)}{P(\sigma_i)}. \quad (\text{A.1})$$

- Assure that the entire ensemble of configurations may be reached via subsequent moves, i.e. the process must be ergodic.

A particularly simple choice that verifies the equation (A.1) is one from the initial paper by Metropolis *et al.* (1953), who proposed:

$$p(\sigma_i \rightarrow \sigma_j) = \begin{cases} 1 & , P(\sigma_j) \geq P(\sigma_i) \\ \frac{P(\sigma_j)}{P(\sigma_i)} & , \text{otherwise.} \end{cases} \quad (\text{A.2})$$

The algorithm just described may be used to calculate averages  $\langle \cdot \rangle$  over the statistical ensemble  $P(\sigma)$ . With the above conditions, it is granted that the Monte-Carlo average  $\langle \cdot \rangle_{\mathcal{N}}$  over  $\mathcal{N}$  configurations converges to its true value in the thermodynamic limit

$$\lim_{\mathcal{N} \rightarrow \infty} \langle \mathcal{O} \rangle_{\mathcal{N}} = \langle \mathcal{O} \rangle \quad (\text{A.3})$$

for any observable quantity  $\mathcal{O}$ , where, again, the Monte Carlo average is a simple average of the  $\mathcal{O}$  over the series of configurations

$$\langle \mathcal{O} \rangle_{\mathcal{N}} = \frac{1}{\mathcal{N}} \sum_{i=1}^{\mathcal{N}} \mathcal{O}(\sigma_i). \quad (\text{A.4})$$

According to the central limit theorem, statistical fluctuations of the observable  $\langle \mathcal{O} \rangle_{\mathcal{N}}$  will vanish as  $1/\sqrt{\mathcal{N}}$ . Actually, this would be strictly true if the configurations  $\sigma_i$  were independent, which they are not—since they were generated by a process with memory, as a series of subsequent manipulations of the initial state.

We conclude that a well designed Metropolis algorithm will firstly grant that the configurations it generates are as uncorrelated as possible, and secondly assure that a large number of these may be generated efficiently.

## A.2 Applicability

One might ask why Monte Carlo simulations have become such a popular means despite their relatively slow convergence. This is due to the fact that this development of the statistical uncertainty holds true regardless of the number of degrees of freedom in the system. Indeed, the average on the right hand side of equation (A.3) may be expressed as an integral

$$\langle \mathcal{O} \rangle = \int d[\sigma] P(\sigma) \mathcal{O}(\sigma), \quad (\text{A.5})$$

where  $[\sigma]$  represents the entirety of variables that may describe a physical configuration of the system. Contrarily to the behavior of Monte Carlo integration, numerical methods for the evaluation of multiple-dimensional integrals based upon analytic developments for the calculations typically produce errors that scale according to the degrees of freedom. Thus, whenever integrals in high dimensions must be evaluated, a probabilistic calculation is preferable.

Since MC is applied mostly to systems with many degrees of freedom, it then becomes a challenge to find an algorithm that implements moves which allow passing from a given configuration to an entirely uncorrelated one.

Take the example of the two-dimensional Ising spin system. Whereas the easiest way to satisfy the requirements of detailed balance and ergodicity is given by local moves attempting to flip a single spin, this procedure becomes very inefficient for large systems, particularly upon approaching a critical point where the correlation length diverges.

### A.3 Towards efficient MC algorithms

Any computer program realizing the Metropolis algorithm will actually proceed in two stages. First, it proposes a new move, and second it will test whether that move can be accepted. The probability to generate a given move  $m = \sigma_i \rightarrow \sigma_j$  can then favorably be thought of as the composition of these two probabilities: the a-priori probability for a move to be proposed  $p_a(m)$  and the acceptance probability once a move has been proposed  $p_b(m)$  [Kertesz and Kondor (1998)]. Trivially,  $p(m) = p_a(m)p_b(m)$  follows.

The most efficient and most elegant class of MC algorithms are those which satisfy the conditions of detailed balance solely with the a-priori probabilities. Such algorithms propose only acceptable moves, i.e.  $p_b(m) \equiv 1$  and  $p(m) = p_a(m)$ .

#### A.3.1 Ising Spin Systems

Ising Spin systems are the simplest models of magnetic systems. In these models, one considers elementary degrees of freedom with a finite number of discrete values. In particular spin- $\frac{1}{2}$  Ising spins may take merely two values  $\pm 1$ . For this class of models, example algorithms are known which follow the strategy to generate moves that (i) satisfy the principle of detailed balance uniquely with the a-priori probabilities and (ii) affect a large number of degrees of freedom with a single move. These examples are the cluster algorithm for 2D Ising spins on a square lattice close to criticality [Swendsen and Wang (1987); Wolff (1989)], as well as the loop-algorithms applied to the six-vertex model [Barkema and Newman (1998)]. The latter are discussed in the context of chapter 4 and explained in section 4.3.3. Both algorithms apply to spin-systems with particular short range interactions. Proposing MC moves that involve many spins and whose a-priori probabilities directly fulfil the detailed balance condition remains a design approach that cannot be easily implemented for other systems. A generalization of



the loop-algorithm to 2D spin-systems with long range dipolar interactions is possible (as discussed in section 4.3.3) at the price of calculating the energies of the initial and final configuration and accepting loop moves according to (A.2), where  $P(\sigma)$  is given by the Boltzmann distribution

$$P(\sigma) = \exp(-\beta E(\sigma)). \quad (\text{A.6})$$

### A.3.2 Strongly Correlated Electron Systems

An important field of application for Monte Carlo algorithms lies in the study of variational wave functions for quantum mechanical systems. In contrast to the prior case (A.6), the probability distribution for configurations is given by the square of the wave function

$$P(\sigma) = |\Psi(\sigma)|^2, \quad (\text{A.7})$$

where  $\sigma$  now stands for an ensemble of coordinates for the quantum mechanical system.

This strategy is widely applied to calculations of the quantum Hall wave functions [Fano *et al.* (1986)]. However, similar Monte Carlo techniques are also widely used in different areas such as electronic structure calculations in atoms [Umrigar *et al.* (1988)].

For strongly correlated systems, it is not possible to develop algorithms that save computation time through moves involving many degrees of freedom, or even to match the a-priori probabilities to fulfil the principle of detailed balance. Quantum Hall wave functions for example reflect the strong interactions among all particles. Consequently, it is very difficult to predict the behavior of  $|\Psi|^2$  under the manipulation of a coordinate change.

In order to speed up calculations, a different scheme is used in this context. Note that every observation  $i$  will require the knowledge of the wave function for the present configuration  $\Psi(\sigma_i)$ . However, subsequent configurations are correlated, and it is useless to make observations for configurations that are much closer than the autocorrelation time of the desired variable. This leads the way to the idea of correlated sampling. Rather than generating a sequence of configurations according to the probability (A.7) based on the wave function itself, one may instead use a computationally less complex probability distribution  $P(\sigma) = F(\sigma)$  and proceed through a re-weighting of the obtained configurations.  $F$  is called the sampling function. Common sampling functions for Quantum Hall systems are based on simple Jastrow factors. To cite an example, let us note the positions of electrons in such a two-dimensional system with  $N$  electron by their complex coordinates

$z_l = x_l + iy_l$ , such that  $\sigma = \{z_1, z_2, \dots, z_N\}$ . A possible sampling function at filling factor  $\nu = \frac{1}{m}$  would be

$$F(\sigma) = \prod_{k < l} (z_k - z_l)^{2m}, \quad (\text{A.8})$$

which is identical to  $|\Psi|^2$  for the Laughlin wave functions for fermions with  $m = 3, 5$ , etc. However, it is certainly a valid sampling function even for  $m = 2$ , or  $\nu = \frac{1}{2}$ , since it describes the appropriate short-distance behavior despite the fact that it does not have the proper symmetry. As discussed in section 2.3.1, the true wave function at  $\nu = \frac{1}{2}$  is much more complicated than  $\prod_{i < j} (z_i - z_j)^2$ .

An operator  $\mathcal{O}$  evaluated as an average of configurations  $\sigma^F$  sampled according to  $F(\sigma)$  yields an estimate of the integral

$$\lim_{\mathcal{N} \rightarrow \infty} \frac{1}{\mathcal{N}} \sum_{i=1}^{\mathcal{N}} \mathcal{O}(\sigma_i^F) = \langle \mathcal{O} \rangle_F = \int d[\sigma] F(\sigma) \mathcal{O}(\sigma), \quad (\text{A.9})$$

as stated in Eq. (A.5). Thus, in order to recover the desired expectation value  $\langle \mathcal{O} \rangle_{|\Psi|^2}$  of the operator  $\mathcal{O}$  in the trial state  $\Psi$ , one needs to evaluate the average of the operator

$$\mathcal{O}' = \frac{|\Psi|^2}{F} \mathcal{O} \quad (\text{A.10})$$

which corresponds to a re-weighting of measurements. Substituting this operator in (A.9) formally yields the proper expectation value. However, note that care must be taken so that sampling with  $F$  ergodically covers the typical configurations of the distribution according to  $|\Psi|^2$ . Otherwise, if very few configurations with large  $|\Psi|^2$  occur in the sequence  $\{\sigma_i^F\}$ , convergence of the average will be slow or never be reached.

In the optimal case, sampling with  $F$  will permit exploration of the relevant configuration space much more efficiently than sampling with  $|\Psi|^2$ , since the more complicated expression  $\Psi$  is calculated only after a number of micro-steps  $\Delta N$ , to be chosen in the order of the autocorrelation time  $\tau$  of micro-configurations.

For variational calculations where  $\Psi = \Psi(\vec{c})$ , with  $\vec{c} = (c_1, \dots, c_{n_{\text{param}}})$  spanning the space of variational parameters, operators may be evaluated for several choices  $\vec{c}_i$  of these parameters simultaneously. The additional cost is that  $\Psi(\vec{c}_i)$  must be evaluated for all different ensembles of parameters  $\vec{c}_i$ , while the effort for sampling remains the same. This procedure is known as correlated sampling. It is a known fact in correlated sampling that averages

evaluated for neighboring choices of parameters remain to some degree correlated, i.e. the error of differences is statistically smaller than sum of the individual errors.

$$\delta|\mathcal{O}(\vec{c}_i) - \mathcal{O}(\vec{c}_j)| < \sqrt{(\delta\mathcal{O}(\vec{c}_i))^2 + (\delta\mathcal{O}(\vec{c}_j))^2}. \quad (\text{A.11})$$

Such correlations are helpful within optimization algorithms that aim to reach the maximization of some operator  $\mathcal{O}$  over  $\vec{c}$ .

For example, a very naïve optimization algorithm, similar to a steepest descent method, would calculate configurations  $\vec{c}_k = \vec{c}_0 + \delta c_k \mathbf{e}_k$ ,  $k = 1, \dots, n_{\text{param}}$  with an initial guess  $\vec{c}_0(t)$  for the parameters and

$$\vec{c}(t+1) = \vec{c}_k(t) |_{\mathcal{O}(\vec{c}_k) = \min_k \mathcal{O}(\vec{c}_k)}. \quad (\text{A.12})$$

In general, it is very important to estimate the statistical error for measurements obtained from Monte-Carlo calculations. This issue will be discussed in the next section.

## A.4 Estimation of errors

As mentioned above, errors are expected to scale as  $1/\sqrt{\mathcal{N}}$  for a Monte Carlo calculation over  $\mathcal{N}$  observations. However, in practice, the scaling of the error is even lower, as the effective number of independent measurements is smaller than  $\mathcal{N}$  due to autocorrelations. Thus, the error of the calculation is intimately linked to the ‘time’-correlation function, i.e. the correlation of succeeding samples when visualizing the generation of samples as a process in time.

### A.4.1 Time-correlation function

In Binder and Heermann (1988), a procedure of error estimation for a sequence  $\mathcal{O}_\mu, \mu = 1, \dots, \mathcal{N}$  of observations of a quantity  $\mathcal{O}$  can be found. Noting the exact value of the average as  $\langle \mathcal{O} \rangle$ , the error  $\delta\mathcal{O}$  is:

$$\begin{aligned} \langle (\delta\mathcal{O})^2 \rangle &= \left\langle \left[ \frac{1}{\mathcal{N}} \sum_{\mu=1}^{\mathcal{N}} \mathcal{O}_\mu - \langle \mathcal{O} \rangle \right]^2 \right\rangle \\ &= \frac{1}{\mathcal{N}^2} \sum_{\mu=1}^{\mathcal{N}} \langle (\mathcal{O}_\mu - \langle \mathcal{O} \rangle)^2 \rangle + \frac{2}{\mathcal{N}^2} \sum_{\mu_1=1}^{\mathcal{N}} \sum_{\mu_2=\mu_1+1}^{\mathcal{N}} (\langle \mathcal{O}_{\mu_1} \mathcal{O}_{\mu_2} \rangle - \langle \mathcal{O} \rangle^2). \end{aligned} \quad (\text{A.13})$$

Performing the summation over  $\mu$  and  $\mu_1$ , one obtains

$$\langle(\delta\mathcal{O})^2\rangle = \frac{1}{\mathcal{N}} \left[ \langle\mathcal{O}^2\rangle - \langle\mathcal{O}\rangle^2 + 2 \sum_{\mu=1}^{\mathcal{N}} \left(1 - \frac{\mu}{\mathcal{N}}\right) (\langle\mathcal{O}_0\mathcal{O}_\mu\rangle - \langle\mathcal{O}\rangle^2) \right] \quad (\text{A.14})$$

For large sequences of samples, the above sum can be transformed into an integral over the time correlation function of the sequence, interpreting each sample as corresponding to a given time interval  $\delta t$ , which may be one Monte-Carlo microstep or some multiple of this, giving

$$\langle(\delta\mathcal{O})^2\rangle = \frac{1}{\mathcal{N}} (\langle\mathcal{O}^2\rangle - \langle\mathcal{O}\rangle^2) \left( 1 + \frac{2}{\delta t} \int_0^{t_{\mathcal{N}}} \left(1 - \frac{t}{t_{\mathcal{N}}}\right) \frac{\langle\mathcal{O}(0)\mathcal{O}(t)\rangle - \langle\mathcal{O}\rangle^2}{\langle\mathcal{O}^2\rangle - \langle\mathcal{O}\rangle^2} dt \right). \quad (\text{A.15})$$

We expect the normalized relaxation function, defined as

$$\phi_{\mathcal{O}}(t) = \frac{\langle\mathcal{O}(0)\mathcal{O}(t)\rangle - \langle\mathcal{O}\rangle^2}{\langle\mathcal{O}^2\rangle - \langle\mathcal{O}\rangle^2}, \quad (\text{A.16})$$

to decay to zero quickly as a function of  $t$  such that the integral of this function gives a finite result,  $\tau_{\mathcal{O}} = \int_0^{\infty} \phi_{\mathcal{O}}(t) dt$ . As a general rule, the prefactor  $(1 - t/t_{\mathcal{N}})$  is approximately one for a large observation time and rapidly decreasing  $\phi_{\mathcal{O}}$ . Thus,

$$\langle(\delta\mathcal{O})^2\rangle = \frac{1}{\mathcal{N}} [\langle\mathcal{O}^2\rangle - \langle\mathcal{O}\rangle^2] \left(1 + 2\frac{\tau_{\mathcal{O}}}{\delta t}\right). \quad (\text{A.17})$$

Two limiting behaviors are worth mentioning: if  $\delta t \gg \tau_{\mathcal{O}}$ , then  $1 + 2\frac{\tau_{\mathcal{O}}}{\delta t}$  is one to a very good approximation. In the inverse case, the one can be neglected, and we find a behavior that is reciprocal in the total observation time  $\tau_{\text{obs}} = \mathcal{N}\delta t$ :

$$\langle(\delta\mathcal{O})^2\rangle = 2\frac{\tau_{\mathcal{O}}}{\tau_{\text{obs}}} [\langle\mathcal{O}^2\rangle - \langle\mathcal{O}\rangle^2]. \quad (\text{A.18})$$

This yields the important result that the statistical error estimate is independent of the choice of the time interval  $\delta t$  as long as the requirement  $\mathcal{N} \gg 1$  is met. It solely depends on the ratio of relaxation and total observation time.

In practice, it is not easy to directly calculate the relaxation or autocorrelation time. To do so, one needs to calculate the normalized relaxation function (A.16). However, this is a relatively time-consuming numerical task, and the evaluation is not trivial since the time-correlation function itself introduces statistical errors. These errors are manifest through a decay

of the relaxation function that does not converge to zero, but rather leads to a noisy background. Consequently, the integral of the relaxation function is generally not finite. In order to extract the autocorrelation time, we find empirically that the initial part of the relaxation function is well-fit by an exponential  $\phi_{\mathcal{O}}(t) = \exp(-t/\tau_{\mathcal{O}})$ , such that the relaxation time may be obtained by regression from a semi-logarithmic plot.

#### A.4.2 Binning

Autocorrelation functions are somewhat tedious to calculate, and the evaluation might not always be easy. Thus, a different approach for the estimation of errors is desirable. One possibility is to consider rebinning of data. This consists in taking averages over series of measurements into  $M = \mathcal{N}/b$  ‘bins’ of size  $b$ , which gives

$$\mathcal{O}_j^b = \frac{1}{b} \sum_{\mu=(j-1)b+1}^{jb} \mathcal{O}_{\mu}. \quad (\text{A.19})$$

From  $\mathcal{O}_j^b$ , one obtains a new standard deviation

$$\sigma(b) = \sqrt{\frac{\langle (\mathcal{O}^b)^2 \rangle - \langle \mathcal{O}^b \rangle^2}{M-1}}, \quad (\text{A.20})$$

which is a function of  $b$ . The idea is that  $\sigma(b)$  underestimates the error as long as  $b < \tau_{\mathcal{O}}$ , since the formula for the standard deviation supposes independent measurements (which they are not). Upon averaging over successive measurements that do not contribute new information,  $\sigma(b)$  increases and finally reaches an asymptotic regime for large  $b > \tau_{\mathcal{O}}$ . Thus, we estimate the MC error as

$$\delta\mathcal{O} = \lim_{b \gg \tau_{\mathcal{O}}} \sigma(b), \quad (\text{A.21})$$

while respecting  $M \gg 1$ . Such an asymptotic value exists, since the values of different bins fluctuate less and less with larger  $b$ , at exactly the same rate as the denominator  $\sqrt{M-1}$  in the expression of  $\sigma(b)$  decreases. Finally, this method also allows estimation of the autocorrelation time of measurements as the bin-size where the asymptotic regime is reached.

## Appendix B

# Appendices to Chapter 2

### B.1 Paired CF wave functions on the sphere

The geometry chosen for our numerical calculations is the sphere, which has the benefit of avoiding boundary effects for finite-size systems. For our purposes, the most suitable coordinates are the spinor coordinates

$$u = \cos(\theta/2)e^{-i\phi/2} \text{ and } v = \sin(\theta/2)e^{i\phi/2}. \quad (\text{B.1})$$

We introduced new conventions for designating the layer index on the sphere, and have noted particle coordinates with two indices: the upper index indicates the pseudospin and designates the layer to which it belongs, whereas the lower index indicates the particle number. Thus,  $(u_i^\sigma, v_i^\sigma) \equiv \Omega_i^\sigma$  describes the location of particle  $i$  with pseudospin  $\sigma$ , where the abbreviated notation  $(\Omega)_i^\sigma$  is used in function arguments. The external magnetic field is represented by a magnetic monopole of strength in the center of the sphere, and it is useful to work in the Haldane gauge [Haldane (1983)]. In this gauge, singular flux tubes of half the total flux penetrate the sphere in a symmetrical fashion at the north- and south-poles. This choice circumvents possible problems regarding the phase of the eigenstates of the angular momentum operator in the presence of a magnetic monopole on the sphere. In particular, using the formalism of the stereographic projection between the plane and the sphere [Fano *et al.* (1986)], one then obtains wave functions on the sphere which can be expressed entirely in the  $u$ 's and  $v$ 's and contain no additional phase factors. Our purposes require the translation of Jastrow factors to the new spinor coordinates on the sphere. A coordinate  $z$  translates to pseudospin up ( $\uparrow$ ) and a coordinate  $w$  translates to pseudospin down ( $\downarrow$ ), e.g.,

$$(z_i - w_k) \rightarrow (\Omega_i^\uparrow - \Omega_k^\downarrow) \equiv (u_i^\uparrow v_k^\downarrow - u_k^\downarrow v_i^\uparrow). \quad (\text{B.2})$$

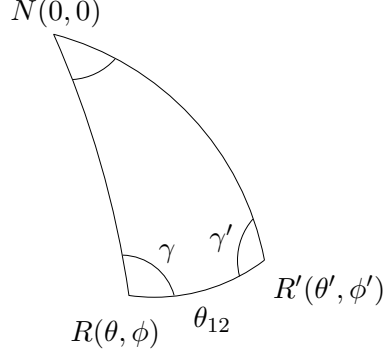


Figure B.1: Definition of the different angles for Eq. B.5 taken from Wu and Yang (1977), adapted to our notations. Points  $R$  and  $R'$  indicate the positions of two electrons, and the third reference point,  $N$ , is the north pole of the sphere. Generally, the reference point is given by the singular point of the section for a given representation of the monopole harmonics [Wu and Yang (1976)]. In the Haldane gauge [Haldane (1983)] used for our simulations, both the north- and the south-pole may be chosen to this end.

Furthermore, the knowledge of a complete set of eigenstates  $\phi_i$  is required to describe (2.55a) on the sphere. These eigenstates are given by the monopole harmonics [Tamm (1931); Wu and Yang (1976, 1977)] written as  $Y_{q,l,m}$  for a total flux  $N_\phi = 2q$ , and the angular momentum quantum numbers  $l = |q| + n$  and  $|m| \leq l$ . These orbitals are organized in a shell structure related to the Landau levels on the plane. The LL-index takes integer values  $n = 0, 1, 2$ , etc. Contrarily to the plane, the degeneracy  $d_n$  of these ‘Landau levels’ is not constant but increasing with  $n$  as

$$d_n = 2(|q| + n) + 1. \quad (\text{B.3})$$

The proper pair correlation function on the sphere might be deduced entirely from the requirements of its antisymmetry and the condition imposed on the flux-count for the resulting bilayer wave function (2.55a) to be commensurable with the 111-state. Nonetheless, let us discuss the symmetry of this two-point function (before projection to the LLL) in more general terms. A general pair wave function on the sphere may be expanded in terms of monopole harmonics, such that

$$g(\Omega_i^\uparrow, \Omega_j^\downarrow) = \sum_n \sum_m g_{n,m} Y_{\frac{1}{2}, \frac{1}{2}+n, m}(\Omega_i^\uparrow) Y_{\frac{1}{2}, \frac{1}{2}+n, -m}(\Omega_j^\downarrow). \quad (\text{B.4})$$

Here, the pair  $(\mathbf{k}, -\mathbf{k})$  has been replaced by its analogue on the sphere  $[(n, m), (n, -m)]$ . Rotational invariance of (B.4) imposes that  $g_{n,m} \equiv g_n$  independent of  $m$ . In the case of  $p$ -wave pairing, we must deal with a slightly more complicated case, since the phase of the pair correlation function is then not rotationally invariant, but rather acquires a phase. This is reflected by a less restrictive condition  $|g_{n,m}| = g_n$ . The angular behavior of (B.4) may then be analyzed according to Eq. 25 from Wu and Yang (1977). This equation expresses the sum over the angular momentum quantum number  $m$  of a product of two monopole harmonics in terms of an amplitude depending solely upon their distance on the sphere, and a phase depending on several angles. For our purposes, we need to set  $q = q'$ , and then take into account the relationship for the complex conjugation of the monopole harmonics, (Eq. 1 in the paper by Wu and Yang (1977)) in order to deduce the relationship

$$\begin{aligned} & \sum_m (-1)^{q+m} Y_{q,l,m}(\theta', \phi') Y_{q,l,-m}(\theta, \phi) \\ &= \sqrt{\frac{2l+1}{4\pi}} Y_{q,l,q}(\theta_{12}, 0) e^{iq(\phi+\phi')} e^{-iq(\gamma-\gamma'+\pi)}. \end{aligned} \quad (\text{B.5})$$

This equation holds independently for each shell  $n$ . The angles  $\phi, \phi', \gamma$  and  $\gamma'$  occurring in this expression are named according to our own conventions and indicated in Fig. B.1. The third point of this triangle is a reference point, that is given by the singular point of the section on which the monopole harmonics are defined. The phase  $\delta\varphi$ , accumulated when taking the two particles around each other with a small angular separation, may be deduced from the last term in (B.5). For a half rotation (i.e. changing the position of both particles), both  $\gamma$  and  $\gamma'$  vary by  $\pi$ , but with different signs, whereas  $\phi$  and  $\phi'$  merely change roles. We then have  $\delta\varphi = 2\pi q$ . Thus, pair wave functions expanded in monopole harmonics  $Y_{q,l,m}$  correspond to  $2q$ -wave pairing, following the analogy with (2.56). The choice of  $q = \frac{1}{2}$  for the mixed fluid bilayer wave functions is coherent with the phase of the pair wave function found in the 111-state. Analogously, this may also be concluded from the flux-count argument introduced at the end of section 2.2.2.4: naturally, an orbital  $Y_{q,l,m}$  adds a number  $N_\phi = 2q$  flux to this count. Thus, with  $q = \frac{1}{2}$ , we recover the previous result that a mixed CF-CB fluid requires  $p$ -wave pairing of composite fermions. To resume the previous results, we have explained how to derive the mixed fluid wave function with paired CF on the sphere. Taking into account the above considerations, the explicit expression upon adding the projection to the LLL [Jain and Kamilla (1997a)]



is:

$$\Psi^{\text{CF-CB}}(\{g_n\}) = \det \left[ \frac{J_i^{zw} J_j^{wz}}{u_i^\uparrow v_j^\downarrow - u_j^\downarrow v_i^\uparrow} + \right. \\ \left. J_i^{zz} J_j^{ww} \sum_{n,m} (-1)^{q+m} g_n \tilde{Y}_{\frac{1}{2}, \frac{1}{2}+n, m}(\Omega_i^\uparrow) \tilde{Y}_{\frac{1}{2}, \frac{1}{2}+n, -m}(\Omega_j^\downarrow) \right]. \quad (\text{B.6})$$

As a reminder, arguments  $(\Omega_i^\sigma)$  denote the coordinates particle  $i$  with pseudospin  $\sigma$ . Jastrow factors must be expressed following the replacement rule (B.2).

## B.2 Numerical results for mixed CF-CB states with filled CF shells

The analysis of the mixed fluid bilayer states with CF pairing presented in section 2.2.3 has shown that, in general, the ground state features non-trivial CF pairing. However, the precise shape of the pairing potential has been found by optimization over a small set of variational parameters. Since this requires a considerable numerical effort, it is interesting to analyze a particular subclass of the bilayer states: those states with filled CF shells. Using the term ‘shells’, we refer to the spherical geometry, as discussed in Appendix B.1. These filled shell states are obtained following the choice of parameters (2.66) for the  $g_n$ , i.e. choosing very large coefficients up to a reduced Fermi momentum  $(k_F)_F$  to force the respective number of electrons into CF orbitals. Remaining electrons then occupy CB states, since all fermionic orbitals obey the Pauli exclusion principle.

Given the degeneracy of CF shells on the sphere (B.3), with  $q = \frac{1}{2}$  for the mixed fluid states, this yields a small number of possible filled shell states for each system size  $N$ . Explicitly, the series of possible CF numbers per layer for  $n_s$  filled CF shells is given by

$$N_{1F}(n_s) = n_s(n_s + 1) = 0, 2, 6, 12, 20, \dots \quad (\text{B.7})$$

Though these filled shell states are known not to be ground states of the bilayer system, they represent intermediate states between the 111-state and the CFL, and are better approximations of the ground state than either of the latter two states for intermediate layer separations.

As an example,  $|2 \text{ Fermions}\rangle$  as described in the paper by Simon *et al.* (2003) is such a filled shell state. In order to show that our calculation reproduces exactly the state  $|2 \text{ Fermions}\rangle$  for large  $g_0$ , and  $g_n = 0, \forall n \geq 1$ ,

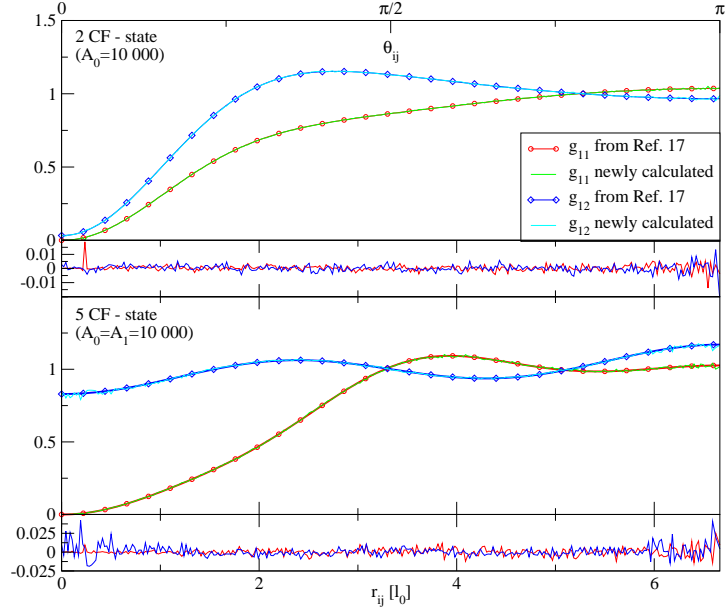


Figure B.2: Intralayer correlation functions  $h_{\downarrow\downarrow}(r)$  and interlayer correlation functions  $h_{\uparrow\downarrow}(r)$  for the states with 2 and 5 composite fermions, respectively  $|2 \text{ Fermions}\rangle$  and  $|5 \text{ Fermions}\rangle$  from Simon *et al.* (2003) and the corresponding states with  $g_0$  large,  $g_n = 0$  otherwise (2F) or  $g_0, g_1$  large,  $g_n = 0$  otherwise (5F), showing perfect agreement. The differences of correlation functions calculated from Monte Carlo and by explicit calculation of the given state, displayed beneath the respective plots, show typical statistical fluctuations inherent to Monte Carlo algorithms, which become larger close to the edges of the plots due to a smaller number of measurements  $\mathcal{N} \propto \sin \theta_{ij}$ .

we have represented the correlation functions from a Monte-Carlo simulation along with the exact one and the respective difference in Fig. B.2. The agreement we have found supports our interpretation of the  $g_n$  and their relation to the occupation probability of the respective CF shell. Note that when choosing  $g_n$  to be large, this means that the respective CF states are inert. It is then without any influence, whether the pair correlation function is chosen symmetric or antisymmetric.

In the case of filled CF shells, one can argue that our paired CF description and the mixed fluid picture developed by Simon *et al.* (2003) are identical. However, we also find perfect agreement for the state where all electrons occupy CF orbitals,  $|5 \text{ Fermions}\rangle$ , which is not a filled shell configuration. To distinguish this from the previous case, note first that to obtain

this agreement, it is required that the pair correlation function  $g_F$  is antisymmetrized (see Appendix B.1). Also, we cannot exclude the possibility that this agreement is possible only by virtue of the relative small size of the Hilbert subspace with  $L = 0$ , which amounts to 29 dimensions (see also Table 2.1).

Since the fraction of CFs and CBs is known for the mixed fluid states, these represent a testing ground for the validity of Eq. 2.74. Numerical evaluation indeed confirms that the correct fraction of CFs  $p(n_s) = N_F(n_s)/N_1$  is obtained from (2.74) within a less than one percent error. Typically, when calculating a Fermi liquid state,  $\sum_{n_s} p(n_s)$  is slightly larger than one but remains within the same error margin.

Having clarified that the filled CF shell states represent a subclass of the mixed fluid states [Simon *et al.* (2003)], but with the advantage that the representation (B.6) is computationally easier to evaluate, we may study this class of states up to very large system sizes.

We have studied larger systems, focusing our attention to system sizes of the sequence (B.7). For a system size corresponding to  $n_s$  filled shells, we may construct  $n_s + 1$  different trial states, notably the 111-state and the states with  $1, 2, \dots, n_s$  filled shells. The state with all shells filled (i.e. the CF Fermi liquid) gives us a criterion to test whether the parameters  $g_n$  have been chosen large enough to transform all particles to composite fermions. Such a state features no interlayer correlations and, consequently, its interlayer correlation function should be constant. All one needs to do is to tune the  $g_n$  until this situation is reached. Empirically, we have found that values  $g_n \gtrsim 1000$  satisfy this criterion.

The biggest system analyzed in this way has  $N = 42 + 42$  particles. A plot resuming the energies for the  $n_s = 0$  to  $n_s = 6$  filled shells is shown in Fig. B.3. Here, we have plotted energy differences with respect to the best of the selected trial states, given that the exact ground state energy is not known for systems this large.

At zero layer separation, the 111 state is the exact ground state. Interestingly, note that states with a small number of CFs are so close in energy that our simulations cannot resolve the absolute difference. However, we have found a general tendency such that states with CFs have lower energy at increasing  $d$ . This evokes the question of whether a finite fraction of CF would eventually be favorable at any finite  $d$  in the thermodynamic limit. Below  $d \sim \frac{1}{2}\ell_0$ , the energy gain for creating CF correlations is not well resolved in our numerics due to statistical uncertainties of our Monte Carlo result. However, going to larger layer separation, states with subsequently more filled CF-LLs clearly become the most favorable trial states.

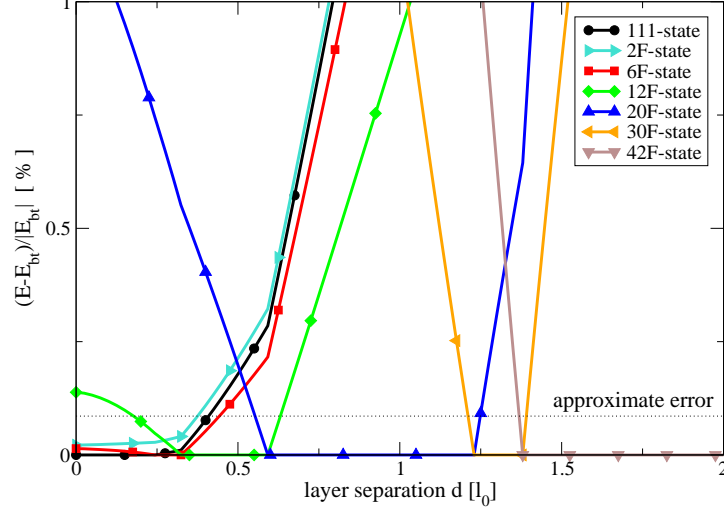


Figure B.3: Energies  $E(d)$  of trial states with filled shells of composite fermions with respect to the energy of the best trial state at the given layer separation  $E_{bt}(d)$  as a function of layer separation. Energies were normalized as  $[E(d) - E_{bt}(d)]/E_{bt}(d)$ . The data was obtained by Monte Carlo simulations for a spherical system with 42 electrons per layer. The most favorable number of CF increases with the layer distance  $d$  until saturation. Note that the formation of CF becomes favorable at very small  $d$ , though the overlaps of states with a small number of CF and the 111 state remain large.

The layer separations  $d_{n_s}^\times$ , where we have observed a level crossing between the state with  $n_s - 1$  filled CF shells and that where  $n_s$  shells are filled are well separated, and range from  $d_0^\times \lesssim 0.4\ell_0$  to  $d_5^\times \sim 1.375$ . As stated before, neither of the filled shell states describes the ground state of the system at the point of their level crossing. Nonetheless, the  $d_{n_s}^\times$  provide an estimate of the range of  $N_F/N$  that one expects to observe in the ground state at this layer separation. Supposing that in the ground state,

$$\frac{N_F(n_s - 1)}{N} \lesssim \frac{N_F|_{d_{n_s}^\times}}{N} \lesssim \frac{N_F(n_s)}{N}, \quad (\text{B.8})$$

we may collect the data from level crossings at different system sizes, and display the results in a common graphical representation. In Fig. B.4 (see page 180), we have represented the complementary ratio of composite bosons  $N_B/N = 1 - N_F/N$ , since this ratio is related to the order parameter  $\mathcal{S}$  via a monotonously growing function for the filled shell states (see inset of Fig. B.4).

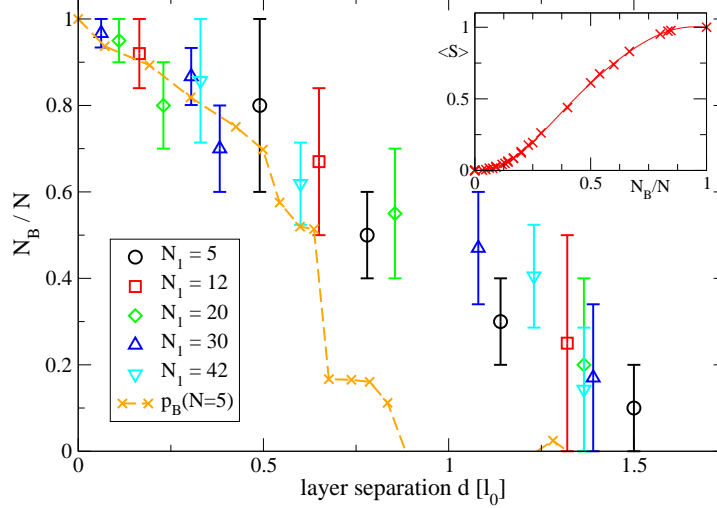


Figure B.4: Intersections of the energy levels of filled CF shell states allow deduction of estimates for the range of the most favorable fraction of CB at the layer separation  $d^*$  of the point of intersection. The results for various system sizes represented collectively in this plot show good coherence. Note that CF are formed in the system at very small  $d$ . A rough linear extrapolation of these result to the right seems to indicate that the ratio  $N_B/N$  will vanish at approximately  $d = 1.7l_0$ , the value at which two independent Fermi liquids would be formed with no composite bosons. The inset shows the monotonous relationship between the order parameter  $\langle S \rangle$  and the fraction of bosons for data from various filled shell states at different  $N$ . The occupation probability of the boson orbitals for  $N_1 = 5$  is given for comparison.

Given that CF pairing predominantly lowers the energy of states that contain an important fraction of CFs, the range for  $N_B/N$  indicated in Fig. B.4 should be seen as an estimate for the upper bound of the fraction of bosons. This is most drastically illustrated by the occupation probability of CB orbitals  $p_B$  that is given for reference in this figure. At low layer separations, where the mixed fluid description is at work, this curve is within the error bars deduced from the filled shell analysis. However, once the paired regime is approached, the true occupation of boson orbitals drops rapidly and the estimate made here clearly overestimates the actual value.

### B.3 Numerical Methods

As mentioned in section 2.2.3, the aim of our numerical simulations of the bilayer states (2.64) was to show that they potentially represent the ground

state. However, to achieve an explicit representation of the ground state at a given layer separation  $d$ , one must find the corresponding set of variational parameters  $\{g_n, c_B\}_d = \gamma_d$  that minimizes the energy. This is a non-trivial optimization problem. In general, optimization algorithms require a large number of function evaluations before obtaining a good ‘guess’ of the optimal solution. Furthermore, our calculations were based upon Monte Carlo simulations, a statistical method which yields statistical errors vanishing only as the inverse square root of the number of samples. This means that any optimization method is bound to make a trade-off between the uncertainty it allows for the function evaluations and the number of such evaluations it requires.

In principle, each set  $\gamma = \{g_n, c_B\}$  requires a separate Monte-Carlo simulation, though it is possible to simulate several choices of these parameters at the same time using correlated sampling. This may be used, for example, to numerically evaluate local derivatives with respect to the variational parameters. Best results for our calculations were achieved by using a self-consistent sampling function  $F$  —an expression obtained as a Jastrow product form exploiting the correlation functions  $h_{\sigma\sigma'}^\gamma$ , calculated in the same run (let the superscript  $\gamma$  be a reference of a distinct trial state). This yields

$$F = \prod_{i<j} h_{\uparrow\uparrow}^\gamma(z_i - z_j) \prod_{i<j} h_{\downarrow\downarrow}^\gamma(w_i - w_j) \prod_{i,j} h_{\uparrow\downarrow}^\gamma(z_i - w_j), \quad (\text{B.9})$$

where  $h_{\uparrow\uparrow}(r) = h_{\downarrow\downarrow}(r)$  by symmetry.

As a first approach, a random sampling of the relevant parameter space was performed. Since all LLL wave functions can be written as polynomials with real coefficients,  $g_n$  was considered real. Once an initial sampling was performed, the best trial states were located using a graphical representation as in Fig. 2.3. The resulting parameters  $\gamma$  may serve as an input to one of the discussed optimization methods.

Due to the statistical errors that underly the Monte-Carlo simulations, computation time increases as the inverse square of the required precision, such that any optimization scheme using local derivatives of the energy is condemned to failure. However, we have successfully employed a more subtle optimization method [Umrigar] based on iterated diagonalization of the Hamiltonian in the space spanned by the present trial state  $|\Psi_0\rangle$  and its derivatives with respect to the variational parameters  $|\Psi_i\rangle = \frac{\partial}{\partial \gamma_i} |\Psi_0\rangle$ . The trial-state representation for the next iteration can be represented as the Taylor expansion

$$|\Psi\rangle = \sum_{i=0}^{n_c} c_i |\Psi_i\rangle, \quad (\text{B.10})$$

where  $c_i$  is the proposed change in the parameters. The values  $c_i$  may be obtained as the solution of the generalized eigenvalue problem in this non-orthogonal and incomplete basis

$$H|\Psi\rangle = ES c, \quad (\text{B.11})$$

where  $S$  is the overlap matrix  $S_{ij} = \langle \Psi_i | \Psi_j \rangle$ . Even better results were obtained using a slightly different basis which was additionally chosen to be semi-orthogonalized with respect to  $|\Psi_0\rangle$ , such that  $\langle \Psi_0 | \Psi_i \rangle = 0, i = 1, \dots, n_c$ .

Mixed energy and variance optimization might also be promising [Umrigar and Filippi (2005)], but was not implemented within our study. In some cases, the prior optimization method may fail to yield satisfactory results. The question then arises whether this is due to the particular optimization procedure or due to the ground-state being not properly represented by the wave functions (2.64) proposed in this thesis.

To answer this question, we took advantage of the supplementary information which we have extracted from exact diagonalization calculations for small systems: Contrary to the energy that typically varies by a small amount upon a small change of  $g_n$ , the evolution of the correlation functions tends to be well expressed. Thus, we have analyzed the correlation functions as explained below. Given the spherical geometry, it is useful to analyze the difference of the correlation functions noted as

$$\Delta h_{\sigma\downarrow}(\theta) = h_{\sigma\downarrow}^{\gamma}(\theta) - h_{\sigma\downarrow}^G(\theta), \quad \sigma = \uparrow, \downarrow \quad (\text{B.12})$$

by performing a Legendre expansion:

$$c_l^{\sigma} = \frac{1}{2l+1} \int d(\cos\theta) P_l(\theta) \Delta h_{\sigma\downarrow}(\theta). \quad (\text{B.13})$$

The idea is to then study the linear perturbations around a given configuration  $\gamma = \{g_n\}$ , supposing

$$h_{\sigma\downarrow}^{\gamma+\delta\gamma}(\theta) = h_{\sigma\downarrow}^{\gamma}(\theta) + \sum_n \frac{\partial h_{\sigma\downarrow}^{\gamma}}{\partial g_n} \delta g_n. \quad (\text{B.14})$$

The latter are obtained from evaluating the derivatives in a linear approximation. Finally, one must solve the linear system

$$c_l^{\sigma} + \sum_n \frac{\partial c_l^{\sigma}}{\partial g_n} \delta g_n = 0. \quad (\text{B.15})$$

Since the required number of variational parameters  $g_n$  is small, the system (B.15) is over-determined, even if one restricts the Legendre expansion to a few terms (the first equation with  $l = 0$  is trivially satisfied, since it merely reflects the normalization of  $h_{\sigma\sigma'}$ ). Since the system was obtained from noisy data, one cannot expect that (B.15) has an exact solution. Approximate solutions should take into account a select set of equations that appear to be the least noisy. Assuming that the absolute errors of the  $c_l^\sigma$  are approximately independent of  $l$ , these equations are those with large coefficients: these yield the best signal to noise ratio. One may thus attempt to find a least squares solution of (B.15) by defining a weight that reflects the statistical confidence according to the latter statement. Finally, one often obtains propositions for large steps in parameter space solving (B.15) in this fairly naïve manner. To stabilize the procedure one should take the relative direction as an indication, and obtain the optimal length of the step from an intermediate evaluation of several points towards that direction before iterating.

## B.4 The Pfaffian

For an antisymmetric  $2N \times 2N$  matrix, the Pfaffian is defined as

$$\mathfrak{Pf}[M] = \sum_{\text{pairings } p} (-1)^{\text{sgn}(p)} \prod_{i=1}^N M_{p_{2i-1}, p_{2i}} \quad (\text{B.16})$$

where  $\text{sgn}(p)$  is  $+1$  for pairings that can be realized as even permutations of the indices and  $-1$  in the odd case. Maybe the most important property of the Pfaffian is that its square yields the determinant of the matrix  $M$

$$\mathfrak{Pf}[M]^2 = \det[M]. \quad (\text{B.17})$$

If it is not necessary to know the sign of the Pfaffian, this relation can be exploited for a numerical calculation of its absolute value based on standard algorithms for the determinant.

In case the sign is required, the following relationship is helpful. Upon transforming an antisymmetric matrix  $A$  to an adjunct form, the Pfaffian transforms as

$$\mathfrak{Pf}[BAB^T] = \det B \mathfrak{Pf}[A]. \quad (\text{B.18})$$

Then, in order to calculate the Pfaffian numerically, one must choose a transformation  $R$ , that yields a representation of the matrix  $M$  such that

$$M = R^T J R, \quad (\text{B.19})$$



where  $J$  is a matrix for which the Pfaffian becomes trivial. One such matrix is

$$J = \begin{pmatrix} 0 & I_N \\ -I_N & 0 \end{pmatrix}, \quad (\text{B.20})$$

where  $I_N$  is the identity matrix in  $\mathbb{R}^N$ . Notably, its Pfaffian is  $\mathfrak{Pf}[J] = 1$ . It has been shown that for any antisymmetric matrix  $M \in \mathbb{R}^{2n} \times \mathbb{R}^{2n}$ , such a decomposition exists, where  $R$  is a permuted triangular matrix [Benner *et al.* (2000)]. In that same paper, an algorithm is given that allows construction of this matrix. With (B.18), the Pfaffian then evaluates to  $\mathfrak{Pf}[M] = \det R$ .

# Bibliography

- P. W. Anderson, Phys. Rev. **102**, 1008 (1956).
- D. Arovas, J. R. Schrieffer, and F. Wilczek, Phys. Rev. Lett. **53**, 722 (1984).
- J. Bardeen, L. N. Cooper, and J. R. Schrieffer, Phys. Rev. **108**, 1175 (1957).
- V. Bargmann, P. Butera, L. Girardello, and J. R. Klauder, Rep. Math. Phys. **2**, 221 (1971).
- G. T. Barkema and M. E. J. Newman, Phys. Rev. E **57**, 1155 (1998).
- J. G. Bednorz and K. A. Müller, Z. Physik **64**, 189 (1986).
- P. Benner, R. Byers, H. Fassbender, V. Mehrmann, and D. Watkins, Elec. Trans. Num. Anal. **11**, 85 (2000).
- K. Binder (ed.), *Monte Carlo Methods in Statistical Physics* (Springer Verlag, Berlin, 1986).
- K. Binder and D. W. Heermann, *Monte Carlo Simulations in Statistical Physics* (Springer, 1988).
- P. Bonderson, A. Kitaev, and K. Shtengel, Phys. Rev. Lett. **96**, 016803 (2006a).
- P. Bonderson, K. Shtengel, and J. K. Slingerland, Phys. Rev. Lett. **97**, 016401 (2006b).
- N. E. Bonesteel, Phys. Rev. B **48**, 11484 (1993).
- N. E. Bonesteel, I. A. Macdonald, and C. Nayak, Phys. Rev. Lett. **77**, 3009 (1996).
- S. T. Bramwell and M. J.-P. Gingras, Science **294**, 1495 (2001).

- L. Brink, T. H. Hansson, S. Konstein, and M. A. Vasiliev, Nucl. Phys. B **401**, 591 (1992), and references therein.
- M. Büttiker, Phys. Rev. Lett. **57**, 1761 (1986).
- J. M. Caillol, D. Levesque, J. J. Weiss, and J. P. Hansen, J. Stat. Phys. **28**, 325 (1982).
- F. Calogero, J. Math. Phys. **10**, 2191 (1969).
- F. Calogero, J. Math. Phys. **12**, 419 (1971).
- G. S. Canright, S. M. Girvin, and A. Brass, Phys. Rev. Lett. **63**, 2291 (1989).
- J. T. Chalker and P. D. Coddington, J. Phys. C **21**, 2665 (1988).
- S. B. Chung and M. Stone, Phys. Rev. B **73**, 245311 (2006).
- R. G. Clark, J. R. Mallett, S. R. Haynes, J. J. Harris, and C. T. Foxon, Phys. Rev. Lett. **60**, 1747 (1988).
- A. Comtet, T. Jolicoeur, S. Ouvry, and F. David (eds.), *Topological aspects of low-dimensional systems, Les Houches*, vol. LXIX (EDP Sciences, 1998), see in particular the chapter by S. Girvin.
- A. Comtet, J. McCabe, and S. Ouvry, Phys. Rev. D **45**, 709 (1992).
- J. R. Cooper, W. Kang, P. Auban, G. Montambaux, D. Jérôme, and K. Bechgaard, Phys. Rev. Lett. **63**, 1984 (1989).
- L. N. Cooper, Phys. Rev. **104**, 1189 (1956).
- R. P. Cowburn, Phys. Rev. B **65**, 092409 (2002).
- D. Das, J. Kondev, and B. Chakraborty, Europhys. Lett **61**, 506 (2003).
- S. Das Sarma, M. Freedman, and C. Nayak, Phys. Rev. Lett. **94**, 166802 (2005).
- D. Davidovic, S. Kumar, D. H. Reich, J. Siegel, R. C. T. S. B. Field, R. Hey, and K. Ploog, Phys. Rev. Lett. **76**, 815 (1996).
- P. G. de Gennes, *Superconductivity of Metals and Alloys* (Benjamin, New York, 1966).
- A. D. de Veigy and S. Ouvry, Phys. Rev. Lett. **72**, 600 (1994).

- A. D. de Veigy and S. Ouvry, *Mod. Phys. Lett. A* **10**, 1 (1995).
- B. C. den Hertog and M. J. P. Gingras, *Phys. Rev. Lett.* **84**, 3430 (2000).
- M. R. Douglas and N. A. Nekrasov, *Rev. Mod. Phys.* **73**, 977 (2001).
- J. Dukelsky, S. Pittel, and G. Sierra, *Rev. Mod. Phys.* **76**, 643 (2004), for a review on the Richardson-Gaudin model.
- A. Einstein, *Ann. d. Phys.* **17**, 132 (1905a).
- A. Einstein, *Ann. d. Phys.* **17**, 891 (1905b).
- A. Einstein, *Ann. d. Phys.* **17**, 549 (1905c).
- J. Eisenstein, *Solid St. Comm.* **127**, 123 (2003).
- J. P. Eisenstein, G. S. Boebinger, L. N. Pfeiffer, K. W. West, and S. He, *Phys. Rev. Lett.* **68**, 1383 (1992).
- J. P. Eisenstein and H. L. Stormer, *Science* **248**, 1461 (1990).
- J. P. Eisenstein and A. H. MacDonald, *Nature* **432**, 691 (2004).
- G. Fano, F. Ortolani, and E. Colombo, *Phys. Rev. B* **34**, 2670 (1986).
- A. B. Fowler, F. F. Fang, W. E. Howard, and P. J. Stiles, *Phys. Rev. Lett.* **16**, 901 (1966).
- E. Fradkin, C. Nayak, A. Tsvelik, and F. Wilczek, *Nucl. Phys.* **B516**, 704 (1998).
- D. A. Garanin and B. Canals, *Phys. Rev. B* **59**, 443 (1999).
- W. F. Giaque and J. W. Stout, *J. Am. Chem. Soc.* **58**, 1144 (1936).
- J. N. Ginocchio and W. C. Haxton, *Phys. Rev. Lett.* **77**, 1568 (1996).
- S. M. Girvin and A. H. MacDonald, *Phys. Rev. Lett.* **58**, 1252 (1987).
- S. M. Girvin, A. H. MacDonald, and P. M. Platzman, *Phys. Rev. Lett.* **54**, 581 (1985).
- R. J. Glauber, *Phys. Rev.* **131**, 2766 (1963).
- M. O. Goerbig, P. Lederer, and C. de Morais Smith, *Phys. Rev. B* **69**, 155324 (2004).

- G. A. Goldin, R. Menikoff, and D. H. Sharp, *J. Math. Phys.* **22**, 1664 (1981).
- K. L. Graham, S. S. Mandal, and J. K. Jain, *Phys. Rev. B.* **67**, 235302 (2003).
- M. Greiter, X.-G. Wen, and F. Wilczek, *Phys. Rev. Lett.* **66**, 3205 (1991).
- M. Greiter, X. G. Wen, and F. Wilczek, *Nucl. Phys. B* **374**, 567 (1992).
- F. D. M. Haldane, *Phys. Rev. Lett.* **51**, 605 (1983).
- F. D. M. Haldane, *Phys. Rev. Lett.* **67**, 937 (1991).
- E. H. Hall, *Am. J. Math.* **2**, 287 (1879).
- B. I. Halperin, *Helv. Phys. Acta* **56**, 75 (1983).
- B. I. Halperin, *Phys. Rev. Lett.* **52**, 1583 (1984).
- B. I. Halperin, P. A. Lee, and N. Read, *Phys. Rev. B* **47**, 7312 (1993).
- S. T. Hannahs, J. S. Brooks, W. Kang, L. Y. Chiang, and P. M. Chaikin, *Phys. Rev. Lett.* **63**, 1988 (1989).
- T. H. Hansson, J. M. Leinaas, and J. Myrheim, *Nucl. Phys. B* **384**, 559 (1992).
- M. J. Harris, S. T. Bramwell, D. F. McMorrow, T. Zeiske, and K. W. Godfrey, *Phys. Rev. Lett.* **79**, 2554 (1997).
- O. Heinonen (ed.), *Composite Fermions* (World Scientific, 1998), for a review of CF's.
- H. Hilgenkamp, Ariando, H.-J. H. Smilde, D. H. A. Blank, G. Rijnders, H. Rogalla, J. R. Kirtley, and C. C. Tsuei, *Nature* **422**, 50 (2003).
- T.-L. Ho, *Phys. Rev. Lett.* **75**, 1186 (1995).
- R. M. F. Houtappel, *Physica* **16**, 425 (1950).
- B. Huckestein, *Rev. Mod. Phys.* **67**, 357 (1995), for a review of the scaling theory of the IQHE.
- K. Husimi and I. Syôzi, *Prog. Theor. Phys.* **5**, 177 (1950).
- R. Iengo and K. Lechner, *Phys. Rep.* **213**, 179 (1992).
- J. Ihm, *J. Phys. A: Math. Gen.* **29**, L1 (1995).

- Y. Imry and R. Landauer, *Rev. Mod. Phys.* **71**, S306 (1999), for a short review of ballistic transport theory.
- L. B. Ioffe, M. V. Feigel'man, A. Ioselevich, D. Ivanov, M. Troyer, and G. Blatter, *Nature* **415**, 503 (2002).
- S. B. Isakov, *Int. J. Mod. Phys. A* **9**, 2563 (1994).
- S. V. Isakov, K. Gregor, R. Moessner, and S. L. Sondhi, *Phys. Rev. Lett.* **93**, 167204 (2004).
- S. V. Isakov, R. Moessner, and S. L. Sondhi, *Phys. Rev. Lett.* **95**, 217201 (2005).
- J. K. Jain, *Phys. Rev. Lett.* **63**, 199 (1989).
- J. K. Jain, *Phys. Rev. B* **41**, 7653 (1990).
- J. K. Jain and R. K. Kamilla, *Phys. Rev. B* **55**, R4895 (1997a).
- J. K. Jain and R. K. Kamilla, *cond-mat/9704031*, starting p. 26 (1997b).
- Y. N. Joglekar, A. V. Balatsky, and A. H. MacDonald, *Phys. Rev. Lett.* **92**, 086803 (2004).
- Y. N. Joglekar and A. H. MacDonald, *Phys. Rev. B* **64**, 155315 (2001).
- B. A. Joyce, *Rep. Prog. Phys.* **48**, 1637 (2001), for a review on MBE techniques.
- C. L. Kane and M. P. A. Fisher, *Phys. Rev. B* **51**, 13449 (1995).
- M. Kellogg, J. Eisenstein, L. N. Pfeiffer, and K. W. West, *Phys. Rev. Lett.* **90**, 246801 (2003).
- M. Kellogg, I. B. Spielman, J. Eisenstein, L. N. Pfeiffer, and K. W. West, *Phys. Rev. Lett.* **88**, 126804 (2002).
- J. Kertesz and I. Kondor (eds.), *Advances in Computer Simulation*, chap. by W. Krauth, "Introduction To Monte Carlo Algorithms" (Springer Verlag, 1998).
- Y. B. Kim, C. Nayak, E. Demler, N. Read, and S. D. Sarma, *Phys. Rev. B* **63**, 205315 (2001).
- A. Kitaev, *Russian Math. Survey* **52**, 1191 (1997).

- H. Kjønsgberg and J. Myrheim, *Int. J. Mod. Phys. A* **14**, 537 (1999).
- K. Kowalski, J. Rembieliński, and L. C. Papaloucas, *J. Phys. A* **29**, 4149 (1996).
- M. Kretzschmar, *Z. f. Physik* **185**, 97 (1965).
- L. D. Landau and E. M. Lifshitz, *Course on theoretical physics, Statistical physics, part II*, vol. 9 (Pergamon, 1980).
- R. Landauer, *J. Phys.: Cond. Mat.* **1**(43), 8099 (1989).
- R. B. Laughlin, *Phys. Rev. Lett.* **50**, 1395 (1983).
- K. Lee, *Anyons on spheres and tori*, preprint BU/HEP-89-28 (1989).
- J. M. Leinaas and J. Myrheim, *Nuovo Cimento* **37**, 1 (1977).
- D. Li, *Nucl. Phys. B* **396**, 411 (1993).
- E. H. Lieb, *Phys. Rev. Lett.* **18**, 692 (1967a).
- E. H. Lieb, *Phys. Rev. Lett.* **18**, 1046 (1967b).
- A. Lopez and E. Fradkin, *Phys. Rev. B* **44**, 5246 (1991).
- H. C. Manoharan, Y. W. Suen, T. S. Lay, M. B. Santos, and M. Shayegan, *Phys. Rev. Lett.* **79**, 2722 (1997).
- J. I. Martín, J. Nogués, K. Liu, J. L. Vicent, and I. K. Schuller, *J. Mag. and Mag. Mat.* **256**, 449 (2003), for a review on lithographic methods.
- K. Matsuhira, Y. Hinatsu, and T. Sakakibara, *J. Phys. Condens. Matter* **13**, L737 (2001).
- S. Das Sarma and A. Pinczuk (eds.), *Perspectives in Quantum Hall effects* (Wiley, New York, 1997).
- R. G. Melko, B. C. den Hertog, and M. J. P. Gingras, *Phys. Rev. Lett.* **87**, 067203 (2001).
- R. G. Melko, M. Enjalran, B. C. den Hertog, and M. J. P. Gingras, *J. Phys. Cond. Mat.* **16**, R1277 (2004).
- N. D. Mermin and H. Wagner, *Phys. Rev. Lett.* **17**, 1133 (1966).
- N. Metropolis, A. W. Rosenbluth, M. N. Rosenbluth, A. H. Teller, and E. Teller, *J. chem. Phys.* **21**, 1087 (1953).

- M. Milovanovic and N. Read, Phys. Rev. B **53**, 13559 (1996).
- R. Moessner, O. Tchernyshyov, and S. L. Sondhi, J. Stat. Phys. **115**, 1769 (2004).
- G. Möller, S. Matveenko, and S. Ouvry, Int. J. Mod. Phys. B **20**, 3533 (2006).
- G. Möller and R. Moessner, Phys. Rev. Lett. **96**, 237202 (2006).
- G. Möller and S. H. Simon, Phys. Rev. B **72**, 045344 (2005).
- K. Moon, H. Mori, K. Yang, S. M. Girvin, A. H. MacDonald, L. Zheng, D. Yoshioka, and S.-C. Zhang, Phys. Rev. B **51**, 5138 (1995).
- G. Moore and N. Read, Nucl. Phys. **B360**, 362 (1991).
- R. H. Morf, Phys. Rev. Lett. **80**, 1505 (1998).
- T. Morinari, Phys. Rev. Lett. **81**(17), 3741 (1998).
- T. Morinari, Phys. Rev. B **59**, 7320 (1999).
- M. Moshe and J. Zinn-Justin, Phys. Rep. **385**, 69 (2003).
- S. Q. Murphy, J. P. Eisenstein, G. S. Boebinger, L. N. Pfeiffer, and K. W. West, Phys. Rev. Lett. **72**, 728 (1994).
- G. Murthy and R. Shankar, Rev. Mod. Phys. **75**, 110 (2003).
- N. Nekrasov, *On a Duality in Calogero-Moser-Sutherland Systems*, hep-th/9707111 (1997).
- M. E. J. Newman and G. T. Barkema, *Monte Carlo Methods in Statistical Physics* (Clarendon Press, Oxford, 1999).
- K. Nomura and D. Yoshioka, Phys. Rev. B **66**, 153310 (2002).
- S. Ouvry, Phys. Lett. B **510**, 335 (2001).
- S. Ouvry, Int. J. Mod. Phys. B **16**, 2065 (2002).
- S. Ouvry and N. Macris, in *Proceedings of the Third Sakharov Conference* (Lebedev Institute, Moscow, 2002).
- K. Park, Phys. Rev. B **69**, 045319 (2004).
- N. W. Park, C. Rim, and D. S. Soh, Phys. Rev. D **50**, 5241 (1994).



- L. C. Pauling, J. Am. Chem. Soc. **57**, 2680 (1935).
- L. C. Pauling (Cornell University Press, Ithaca, NY, 1945).
- A. M. Perelomov, Teor. Mat. Fiz. **6**, 213 (1971).
- L. N. Pfeiffer, E. Schubert, K. W. West, and C. Magee, Appl. Phys. Lett. **58**, 2258 (1991).
- V. L. Pokrovsky and A. L. Talapov, J. Phys. C **18**, L691 (1985).
- R. E. Prange and S. M. Girvin (eds.), *The Quantum Hall Effect* (Springer, 1987).
- A. P. Ramirez, A. Hayashi, R. J. Cava, R. Siddharthan, and B. S. Shastry, Nature **399**, 333 (1999).
- N. Read, Semi Cond. Sci. Tech. **9**, 1859 (1994).
- N. Read, Phys. Rev. B. **58**, 16262 (1998).
- N. Regnault, *DiagHam homepage*, <http://www.phys.ens.fr/~regnault/diagham/> (a).
- N. Regnault, *The fractional quantum Hall effect numerical database*, <http://www.phys.ens.fr/~regnault/qhe/> (b).
- E. H. Rezayi and F. D. M. Haldane, Bull. Am. Phys. Soc. **32**, 892 (1987).
- E. H. Rezayi and F. D. M. Haldane, Phys. Rev. B **50**, 17199 (1994).
- E. H. Rezayi and F. D. M. Haldane, Phys. Rev. Lett. **84**, 4685 (2000).
- P. Schiffer, private communication (2006).
- J. Schliemann, Phys. Rev. B **67**, 035328 (2003).
- J. Schliemann, S. M. Girvin, and A. H. MacDonald, Phys. Rev. Lett. **86**, 1849 (2001).
- E. Schrödinger, Ann. d. Phys. **79**, 361 (1926a).
- E. Schrödinger, Phys. Rev. **28**, 1049 (1926b).
- N. Shibata and D. Yoshioka, J. Phys. Soc. Jpn. **75**, 043712 (2006).
- R. Siddharthan, B. S. Shastry, and A. P. Ramirez, Phys. Rev. B **63**, 184412 (2001).

- R. Siddharthan, B. S. Shastry, A. P. Ramirez, A. Hayashi, R. J. Cava, and S. Rosenkranz, Phys. Rev. Lett. **83**, 1854 (1999).
- J. A. Simmons, H. P. Wei, L. W. Engel, D. C. Tsui, and M. Shayegan, Phys. Rev. Lett. **63**, 1731 (1989).
- S. H. Simon, N. Bonesteel, M. H. Freedman, N. Petrovic, and L. Hormozi, Phys. Rev. Lett. **96**, 070503 (2006).
- S. H. Simon, E. H. Rezayi, and M. V. Milovanovic, Phys. Rev. Lett. **91**, 046803 (2003).
- J. Snyder, J. S. Slusky, R. J. Cava, and P. Schiffer, Nature **413**, 48 (2001).
- I. B. Spielman, J. Eisenstein, L. N. Pfeiffer, and K. W. West, Phys. Rev. Lett. **84**, 5808 (2000).
- I. B. Spielman, J. Eisenstein, L. N. Pfeiffer, and K. W. West, Phys. Rev. Lett. **87**, 036803 (2001).
- I. B. Spielman, M. Kellogg, J. P. Eisenstein, L. N. Pfeiffer, and K. W. West, Phys. Rev. B **70**, 081303 (2004).
- I. Stanic and M. V. Milovanovic, Phys. Rev. B **71**, 035329 (2005).
- F. Steglich, J. Aarts, C. D. Bredl, W. Lieke, D. Meschede, W. Franz, and H. Schäfer, Phys. Rev. Lett. **43**, 1892 (1979).
- A. Stern and B. I. Halperin, Phys. Rev. Lett. **88**, 106801 (2002).
- A. Stern and B. I. Halperin, Phys. Rev. Lett. **96**, 016802 (2006).
- A. Stern, B. I. Halperin, F. von Oppen, and S. H. Simon, Phys. Rev. B. **59**, 12547 (1999).
- Y. W. Suen, J. Jo, M. B. Santos, L. W. Engel, S. W. Hwang, and M. Shayegan, Phys. Rev. B **44**, 5947 (1991).
- B. Sutherland, Phys. Rev. A **4**, 2019 (1971).
- B. Sutherland, Phys. Rev. A **5**, 1372 (1972).
- R. H. Swendsen and J.-S. Wang, Phys. Rev. Lett **63**, 86 (1987).
- I. Syôzi, Prog. Theor. Phys. **5**, 341 (1950), *ibid*, **6**, 306 (1951).
- I. Tamm, Z. Physik **71**, 141 (1931).

- G. Toulouse, Commun. Phys. **2**, 115 (1977).
- S. A. Trugman and S. Kivelson, Phys. Rev. B **31**, 5280 (1985).
- D. C. Tsui, H. Stormer, and A. C. Gossard, Phys. Rev. Lett. **48**, 1559 (1982).
- C. J. Umrigar, private Communication; to be published ().
- C. J. Umrigar and C. Filippi, Phys. Rev. Lett. **94**, 150201 (2005).
- C. J. Umrigar, K. G. Wilson, and J. W. Wilkins, Phys. Rev. Lett. **60**, 1719 (1988).
- K. v. Klitzing, Séminaire Poincaré **2**, 1 (2004).
- K. v. Klitzing, G. Dorda, and M. Pepper, Phys. Rev. Lett. **45**, 494 (1980).
- J. Villain, J. Phys. C **10**, 1717 (1977).
- R. F. Wang, C. Nisoli, *et al.*, Nature **439**, 303 (2006).
- G. H. Wannier, Phys. Rev. **79**, 357 (1950).
- F. Wilczek, Phys. Rev. Lett. **48**, 1144 (1982a).
- F. Wilczek, Phys. Rev. Lett. **49**, 957 (1982b).
- R. Willett, J. P. Eisenstein, H. L. Störmer, D. C. Tsui, A. C. Gossard, and J. H. English, Phys. Rev. Lett. **59**, 1776 (1987).
- R. L. Willett, R. R. Ruel, K. W. West, and L. N. Pfeiffer, Phys. Rev. Lett. **71**, 3846 (1993).
- A. S. Wills, R. Ballou, and C. Lacroix, Phys. Rev. B **66**, 144407 (2002).
- U. Wolff, Phys. Rev. Lett **62**, 361 (1989).
- T. T. Wu and C. N. Yang, Nucl. Phys. **B107**, 365 (1976).
- T. T. Wu and C. N. Yang, Phys. Rev. D **16**, 1018 (1977).
- J. Xia, W. Pan, *et al.*, Phys. Rev. Lett. **93**, 176809 (2004).
- K. Yang, K. Moon, L. Belkhir, H. Mori, S. M. Girvin, A. H. MacDonald, L. Zheng, and D. Yoshioka, Phys. Rev. B **54**, 11644 (1996).
- G. Zarand, F. Pazmandi, K. F. Pal, and G. T. Zimanyi, Phys. Rev. Lett. **89**, 150201 (2002).
- S. C. Zhang, T. H. Hansson, and S. Kivelson, Phys. Rev. Lett. **62**, 82 (1989).



## Abstract

For a description of the low-temperature physics of condensed-matter systems, it is often useful to work within dynamically reduced spaces. This philosophy equally applies to quantum Hall bilayer systems, anyon systems, and frustrated magnetic spin systems - three examples studied in this thesis.

First, we developed a new class of wave functions based upon paired composite fermions. These were applied to analyze the physics of the quantum Hall bilayer system at total filling one. Studying these via variational Monte Carlo methods, we concluded that the compressible to incompressible transition in the bilayer system is of second order. Furthermore, we pursued the longstanding question of whether pairing in the single layer might cause an incompressible quantum state at half filling. We then considered schemes of dimensional reduction for quantum mechanical models on the sphere. We achieved a mapping from non-interacting particles on the sphere to free particles on the circle. We proposed that an analogous mapping might exist for interacting anyons, and an appropriate anyon-like model on the sphere was introduced. Lastly, we performed an analysis of frustrated spin systems on two-dimensional lattices addressing the question of whether spin-ice can be realized in the presence of long-range dipolar interactions.

## Résumé

Pour la description des propriétés de basse température des systèmes en physique de la matière condensée, il est souvent utile de travailler dans un espace dynamique réduit. Cette philosophie s'applique aux systèmes bicouches à effet Hall quantique comme aux systèmes d'anyons et aux systèmes magnétiques frustrés qui représentent les exemples discutés dans cette thèse.

On introduit une classe générale d'états appariés de fermions composites. Ces fonctions d'onde sont exploitées pour analyser l'état fondamental des systèmes bicouches à effet Hall quantique pour un facteur de remplissage total valant un. A partir d'une étude de Monte Carlo variationnel nous concluons que la transition de phase compressible à incompressible observée dans ce système est du deuxième ordre. Nous étudions également la question de l'existence d'un état apparié à remplissage valant un demi dans les simples couches. Ensuite nous considérons des schémas de réduction dimensionnelle de systèmes bidimensionnels sur la sphère vers des systèmes unidimensionnels sur le cercle. Un tel mapping est établi pour des systèmes libres et un candidat pour un système d'anyons généralisé est proposé en vue de sa réduction dimensionnelle vers le modèle de Calogero-Sutherland. Finalement, nous analysons les systèmes de spins frustrés sur réseaux bidimensionnels et discutons si un état de glace de spins peut exister en présence d'interactions dipolaires à longue portée.